Delft University of Technology

Challenge the future

FACULTY OF CIVIL ENGINEERING

MASTER THESIS

3D Finite Element Analysis of a Scaled Trapezoidal 3-story Reinforced Concrete Structure on a Shaking Table

Author:
D.A. LABIB

Supervisors:
Prof. Dr. Ir. J.G. ROTS
Dr. Ir. G.M.A. SCHREPPERS
Dr. Ir. M.A.N. HENDRIKS
Ir. J. MANIE
Dr. Ir. E. LOURENS

September 17, 2014

Abstract

This master thesis is about finite element analyses of a 3D model of a $1/4^{th}$ scaled trapezoidal 3-story reinforced concrete mock-up on a shaking table which is part of SMART 2013 international benchmark. The idea of this benchmark is to asses and predict the dynamic behavior of the reinforced concrete mock-up with respect to seismic loading using finite element method software. In this master thesis, the finite element method software DIANA is used to asses and predict the dynamic behavior of the scaled mock-up with respect to seismic loading.

In order to make reliable assessment and prediction of the dynamic behavior of the reinforced concrete mock-up it is important to work step by step. That is why research questions are formulated which divide this master thesis into 3 stages where the main focus of this thesis lies in stage 2 and stage 3. The research questions that are formulated and answered throughout this thesis are given below together with their answers:

1. What kind of a finite element model has to be developed for the reinforced concrete mock-up on the shaking table? A 2D or a 3D model? What kind of elements are suitable to model concrete, reinforcement, additional masses and the shaking table?
2. Which material models are suitable to model the material behavior of concrete, reinforcement and steel, knowing that the model will be loaded repeatedly?

Questions 1 and 2 are treated in stage 1. Although stage 1 is not the main focus of this thesis, it is important to treat these questions because they are the basis of all analyses. Without having a model with suitable elements and material models, it is not possible to perform reliable analyses.

3. What needs to be done in order to make good predictions about the dynamic behavior of the mock-up using the finite element model?
4. What are the natural characteristics (natural frequencies and the corresponding mode shapes) of the model?
5. How good is the prediction of the dynamic response of the finite element model when performing (non)linear transient analysis?
6. How can the predictions of the finite element analyses be assessed in how good these predictions are?
7. How useful are response spectrum and pushover analysis when investigating the dynamic behavior of the finite element model?
8. When investigating the dynamic behavior of the model, where do the highest stresses in the model occur? How does the crack pattern look like when the model cracks? Where in the model does the reinforcement yield?

Questions 3 - 8 are treated in stage 2 and stage 3.

In stage 1 of this thesis the finite element model is developed. This finite element model consists of the model of concrete, reinforcement, additional masses and the shaking table. The concrete is modeled with solid elements. The reason why concrete is modeled with solid elements is because it is chosen to mimic the real concrete mock-up from the laboratory as good as possible. In order to mimic the dynamic behavior of the real concrete mock-up as good as possible, accurate results from the finite element analyses are necessary and with solid elements and a fine mesh of the model (where the model has a fine mesh in this thesis) it is possible to get accurate results from the finite element analyses.

The reinforcement is modeled with embedded reinforcement. In the real mock-up reinforcement bars are used and to mimic the reality as good as possible it is chosen to model

the reinforcement with embedded reinforcement. It is also interesting to know that in finite element analysis embedded reinforcement add only stiffness to the finite element model. These embedded reinforcement are embedded in the elements in which they are located and do not allow relative slip

Distributed translational mass elements are used to model the additional masses on each floor. These elements add mass to the finite element model without influencing the stiffness of the model. These elements are only active when performing a dynamic analysis.

The shaking table in the laboratory consists of plates and these plates are modeled with curved shell elements. It is chosen to model this shaking table in order to simulate the real mock-up + shaking table system as good as possible. In stage 2 it will be shown that it is important to model the shaking when performing eigenvalue analyses to calibrate the finite element model.

After developing the finite element model, material models are assigned to concrete, reinforcement and the shaking table plates. These material models describe the behavior of these materials. The total strain rotating crack model, with Hordijk softening and Thorenfeldt crushing, is chosen to model the behavior of concrete. The Menegotto-Pinto model describes the cyclic behavior of the reinforcement and the Von Mises plasticity model describes the behavior of the shaking table plates. In the past, the just mentioned material models have shown that they are suitable to model the nonlinear behavior of concrete and steel when subjected to cyclic loading like earthquakes. After choosing the material models, one-element tests are performed in order to validate these material models. The results of these validations look good and can be found at the end of stage 1.

To calibrate the finite element model with the reinforced concrete mock-up, eigenvalue analyses are performed. These analyses are performed in stage 2. In the eigenvalue analyses, the numerical natural frequencies of the model together with the corresponding mode shapes for the first three modes are compared with the provided experimental natural frequencies of the mock-up together with the corresponding mode shapes. The eigenvalue analyses are performed for the following three cases:

1. the mock-up is fixed at the lower face of the foundation and is not loaded with additional masses,
2. the mock-up is fixed at the lower face of the foundation and is loaded with additional masses,
3. the mock-up is linked to the shaking table and is loaded with additional masses.

After the eigenvalue analyses for all three cases, it appeared that the numerical natural frequencies for case 3 made the best match with the provided experimental natural frequencies where the mode shapes of the model for all three cases were the same.

For the linear transient analysis, comparisons are made between the numerical responses (in terms of displacements and accelerations) of the model to RUN6 and RUN7 with the experimental responses of the mock-up to RUN6 and RUN7 on floor 3 in point D. The match between the numerical responses and the experimental responses was good as shown in the previous sections of this stage.

It appears that it is important to calibrate the finite element model as good as possible with the real mock-up in order to make reliable predictions of the dynamic behavior of the mock-up. The match between the numerical responses and the experimental responses to RUN6 and RUN7 showed that the match was good. This nice match was only possible be-

cause of the calibration of the finite element model using the results of the eigenvalue analyses.

At last, response spectrum analyses are performed to calculate the tensile stresses in the model. These calculated tensile stresses show how big the tensile stresses in the model are. With this information it is possible to see where the concrete model will crack (when the concrete cracks) and where the reinforcement will yield (when the reinforcement yields) when nonlinear transient analyses for each RUN are performed. So this information obtained from RSA is very useful.

In stage 3 the nonlinear dynamic response of the model is evaluated by performing nonlinear transient analyses and pushover analyses. For the nonlinear transient analyses different seismic excitations are used where for the pushover analyses only the first three mode shapes are taken into account.

The pushover analyses predicted that the model can withstand RUN9, RUN11 and RUN21. And indeed, these predictions were right. Because of the pushover analysis it is known why RUN17, RUN19 and RUN23 diverged. These RUNs diverged because the model could not withstand these RUNs. The pushover analyses showed where the model would crack (as a result of high tensile stresses) when the model is loaded to its capacity according to its first three mode shapes by giving the crack patterns. These crack patterns give an indication of where the model might crack when performing nonlinear transient analyses. The pushover analyses also showed where the reinforcement will yield which give an indication of where the reinforcement might yield when the reinforcement yields when performing nonlinear transient analyses. It is also important to mention that the predictions of the pushover analyses are not 100% accurate of how the model will behave when performing a nonlinear transient analysis. The reason for this is that when performing a nonlinear transient analysis, the model vibrates arbitrarily in every direction at various range of frequencies where in a pushover analysis the model is loaded only at one mode shape at a time. In this thesis, for the pushover analysis only the first three mode shapes are taken into account which also limits the prediction power of the pushover analysis. Having the previous said, a pushover analysis is a useful nonlinear dynamic analysis with certain limitations. This limitation may be reduced by taking more than three mode shapes into account.

During the study of the crack patterns of the nonlinear transient analyses, the stress distributions of the model according to the response spectrum analyses were considered to see if these stress distribution could say anything about the crack patterns of the model in the nonlinear transient analyses. These stress distributions were very useful in showing where the model might crack when performing nonlinear transient analysis. In places where the tensile stresses are much higher then the tensile strength of concrete in the contour plots from RSA, the model showed cracks in the contour plots from the nonlinear transient analyses. It is important to mention that the results of response spectrum analysis are less accurate in comparison with the results of the nonlinear transient analysis which is quite logical because a nonlinear transient analysis gives the exact response of the model due to seismic loading as a response spectrum analysis gives the maximum linear response of the model due to seismic loading. Because the RSA is a linear dynamic analysis, the model will not crack in this analysis. And the tensile stress contour plots which are shown in the previous sections of this stage show very high tensile stresses in areas where the model shows cracks in the nonlinear transient analysis. Also the tensile stresses spread which cover big areas of the model, from the area where the tensile stresses are much higher then the tensile strength of concrete. So a response spectrum analysis is also a useful dynamic analysis with certain limitations.

During the comparisons of the numerical responses of the model and the experimental responses of the mock-up with respect to all RUNs, there were some good matches between

these two responses. The responses due to RUN9, RUN11 and RUN13 were close to each other. The match between the numerical and experimental responses due to RUN17 and RUN19 were quite good but after some time the amplitudes of the experimental responses became much higher then the numerical responses. A reason for this could be that the damage history of the finite element model was not taken into account while the damage history of the real mock-up was taken into account. Only the responses due to RUN21 and RUN23 did not show a good match. This is possibly because of the damage that is experienced by the real mock-up with respect to RUN9, RUN11, RUN13, RUN17 and RUN19 while the damage history of the finite element model is not taken into account.

The story from above is a short summry of this master thesis. A more detailed version can be found in stage 1, stage 2 and stage 3 of this thesis.

Acknowledgments

Contents

1   Introduction

Recent events occurred in the world have shown the need to assess the dynamic behavior of reinforced concrete structures with respect to seismic loading. This issue remains an open question and motivates the scientific community for the last decades in improving design methods regarding the seismic risk. Especially, in the case of reinforced concrete structures exhibiting complex coupled torsional flexural behavior, a better understanding of the dynamic behavior under seismic loading is needed. That is why an experimental campaign, the SMART [1] 2013 international benchmark, has been launched, supported by Commissariat a l´Energie Atomique et aux Energies Alternatives (CEA) and Electricite de France (EDF). This benchmark investigates the dynamic behavior of a $(1/4^{th})$ scaled 3-story trapezoidal reinforced concrete mock-up on a shaking table. The dynamic behavior of this scaled reinforced concrete mock-up is investigated using finite element software. Several parties around the world has participated in this benchmark to investigate the dynamic behavior of this scaled mock-up using their own finite element software. Beside investigating the dynamic behavior of the scaled mock-up, also predictions are made of the dynamic behavior of the scaled mock-up using finite element software. Next to the finite element analyses, experimental analyses are performed in the laboratory with the real reinforced concrete mock-up. To verify the predictions of the finite element analyses of the dynamic behavior of the scaled mock-up, comparisons are made between the results obtained from the experiment from the laboratory and the results obtained from the finite element analyses.

To assess the dynamic behavior of this scaled mock-up, the SMART 2013 benchmark has been divided into the following 4 stages:

Stage 1: With the help of the provided geometric data and the material properties, the numerical model (geometry, mesh, models, materials and targeted seismic inputs) will be developed.
Stage 2: The low intensity seismic inputs and the corresponding experimental results are provided. This stage is meant to calibrate the numerical model based on the linear structural behavior of the model.
Stage 3: One is focused on the nonlinear dynamic behavior of the reinforced concrete structure. The seismic inputs are provided. This stage aims at quantifying the performance and the relevancy of constitutive laws used, when working in their non-linear range.
Stage 4: This stage is focused on the probabilistic evaluation of the model vulnerability. The determination of the fragility curves with respect to prescribed criteria is the main objective of this stage. In particular, the effects of the variability of the concrete tensile strength and those related to the spatial variability of the aforementioned parameters will be studied.

This master thesis is focused on stage 2 and stage 3 of the SMART 2013 benchmark. For the sake of completeness also stage 1 of the SMART 2013 benchmark is treated.

---

[1]**S**eismic design and best estimate **M**ethods **A**ssesment for **R**einforced concrete buildings subjected to **T**orsion and non-linear effects

It is handy to know how this thesis is set up. The figure below shows the global set-up of this master thesis.
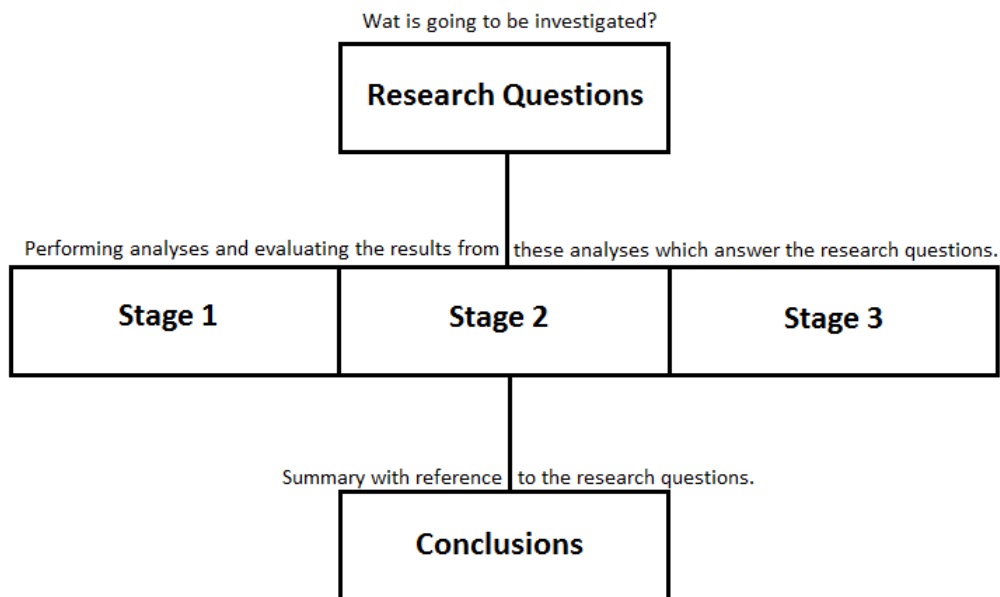

Figure 1.1: Set-up of this master thesis.

According to this global set-up, first the research questions are formulated. After that the analyses are performed in stage 1, stage 2 and stage 3 which are used to answer the research questions. At the end the conclusions are given which summarize this thesis, taking the research questions into account.

2 Glossary

In this section, terms are explained which are necessary to understand the contents of this thesis.

Model refers to the finite element model. **Mock-up** refers to the real structure in the laboratory.

Dynamic analysis is a type of structural analysis which covers the behavior of structures subjected to dynamic loading. When a structure has a loading which varies with time, it is reasonable to assume its response will also vary with time. In such cases, a dynamic analysis may have to be performed which reflects both the varying load and response.

Eigenvalue analysis is a type of dynamic analysis which is performed when the natural frequencies of vibration are of interest. This is probably the most common type of dynamic analysis. In addition to the natural frequencies, the mode shapes of vibration which arise at the natural frequencies are also of interest. These are the *undamped free vibration response* of the structure caused by an initial disturbance from the static equilibrium position.

Transient analysis, also called *time history analysis*, is a type of dynamic analysis which will be performed when the loading is arbitrary and time-dependent like an earthquake loading. This arbitrary time-dependent load is also called a transient load. Transient analysis is used to determine the time-varying displacements, strains and stresses in the structure as it responds to a transient load.

Response spectrum is a plot of the maximum response (displacement, velocity or acceleration) of a series of linear single degree of freedom (SDOF) oscillators with different natural frequencies at a certain damping ratio, to a certain ground motion. So a response spectrum is a convenient way of describing earthquake motion in terms of the maximum response of a linear SDOF system of arbitrary natural frequency and damping ratio. Each data point on the response spectrum curve represents the peak response from a time history analysis of the earthquake applied to the linear SDOF oscillators with different natural frequencies at a certain damping ratio. The vertical axis of the response spectrum gives the *spectral response* which is the same as the peak response of the SDOF oscillator. The horizontal axis gives the natural frequency at which the oscillator is tuned. The horizontal axis can also be the natural period of the oscillator which is the inverse of the natural frequency.

Response spectrum analysis is a linear dynamic analysis where the response spectrum of a certain earthquake is used as input. With the response spectrum analysis it is possible to calculate the maximum response (accelerations, velocity, displacements, stresses, strains, reaction forces) of the model for each mode that is considered. Then the maximum responses of all considered modes are summed up according to the absolute sum (ABS) rule, Complete Quadratic Combination (CQC) rule or the Square Root of Sum of Squares (SRSS) rule. In thesis, the SRSS rule is used to sum up the responses of all considered modes.

Pushover analysis is non-linear static analysis using a specified load pattern, applied to a model with nonlinear properties, which starts from zero load and incrementally increases to an ultimate load where the model reaches its capacity.

Accelerogram is a complete history of a component (horizontal or vertical) of ground motion described in terms of acceleration versus time. The velocity and displacement histories of the earthquake can be obtained by integrating the acceleration record. In general, acceleration records have rapidly changing accelerations and broadband frequency content.

Peak ground acceleration (PGA) is the largest earthquake acceleration on the ground. It can be expressed in g where $1\ g = 9.81\ \text{m/s}^2$.

Discrete Fourier transform (DFT) transforms a signal in the time domain to a signal in the frequency domain.

3 Research Questions

The research questions which logically arise are formulated as follows:

1. How is the dynamic behavior of the finite element model with respect to seismic loading?
2. How good is the prediction of the finite element analysis for the dynamic behavior of the reinforced concrete 3-story trapezoidal mock-up?

These two research questions are broadly formulated. In order to treat these questions it is necessary to also formulate the corresponding sub-questions. These sub-questions are given below:

1. What kind of a finite element model has to be developed for the reinforced concrete mock-up and the shaking table? A 2D or a 3D model? What kind of elements are suitable to model concrete, reinforcement, additional masses and the shaking table?
2. Which material models are suitable to model the material behavior of concrete, reinforcement and steel, knowing that the model will be loaded repeatedly?

Sub-questions 1 and 2 are treated in stage 1, although this is not part of this thesis, but it is important to treat these questions because they are the basis of all analyses. Without having a model with suitable elements and material models, it is not possible to perform reliable analyses.

3. What needs to be done in order to make good predictions about the dynamic behavior of the mock-up using the finite element model?
4. What are the natural dynamic characteristics (natural frequencies and the corresponding mode shapes) of the model?
5. How good is the prediction of the dynamic response of the finite element model when performing (non)linear transient analysis?
6. How can the predictions of the finite element analyses be assessed in how good these predictions are?
7. How useful are response spectrum and pushover analysis when investigating the dynamic behavior of the finite element model?
8. When investigating the dynamic behavior of the model, where do the highest stresses in the model occur? How does the crack pattern look like when the model cracks? Where in the model does the reinforcement yield?

Questions 3 - 8 are treated in stage 2 and stage 3.

When these sub-question are treated then the two broadly formulated research questions are automatically answered. In section *conclusions* 8 of this thesis, the answers to all these research questions are given after performing finite element analyses and analyzing the results of these analyses.

4 Project Description

This section gives a description of the SMART 2013 International Benchmark. The description comes from the report that has been provided by the SMART 2013 organizing committee [3].

4.0.1 Geometry

The $(1/4^{th}$ scaled) mock-up to be studied is a trapezoidal, 3-story reinforced concrete structure. This structure is representative to a typical simplified half part of an electrical nuclear building. A plan view and elevation views of the specimen are shown below.
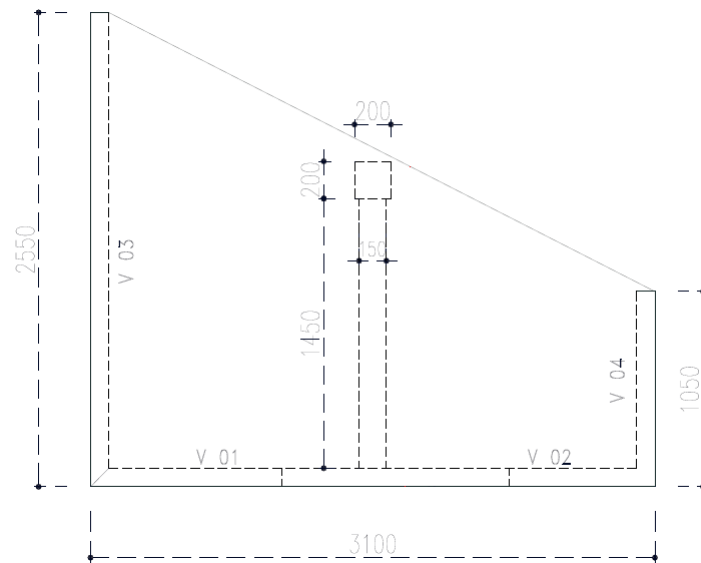
Figure 4.1: Plan view - dimensions in mm.
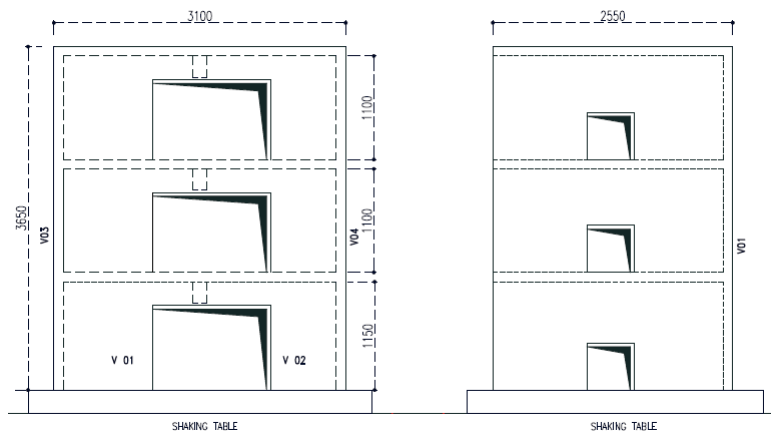
Figure 4.2: Elevation lateral views - dimensions in mm.
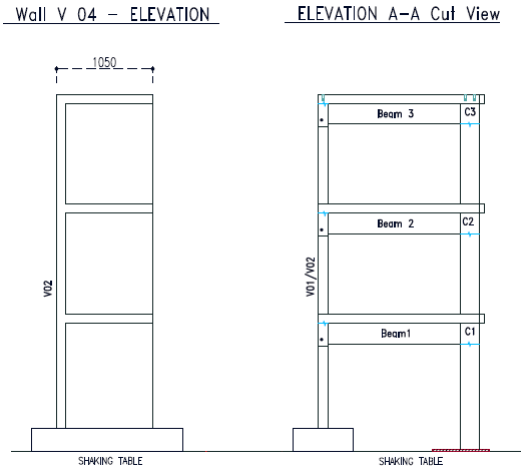
Figure 4.3: Elevation front views - dimensions in mm.

The dimensions of the structural components of the mock-up are given in table 4.1.

Table 4.1: Dimensions of the structural components of the mock-up.

Structural component	Length [mm]	Thickness [mm]	Height [mm]
Wall (V01 + V02)	3100	100	3650
Wall V03	2550	100	3650
Wall V04	1050	100	3650
Beams	1450	150	325
Columns	200	200	3900

4.0.2 Geometry of the Foundation

The foundation is made of a continuous reinforced concrete footing. The footing is 650 mm wide and 250 mm high. A layer made of mortar is used between the bottom of the foundation and the shaking table in order to limit planarity defaults. This layer has a thickness of 20 mm. The column is fixed on the shaking table by a steel plate that is 20 mm thick. A sketch of the anchorage system of the foundation is given in the figure below.
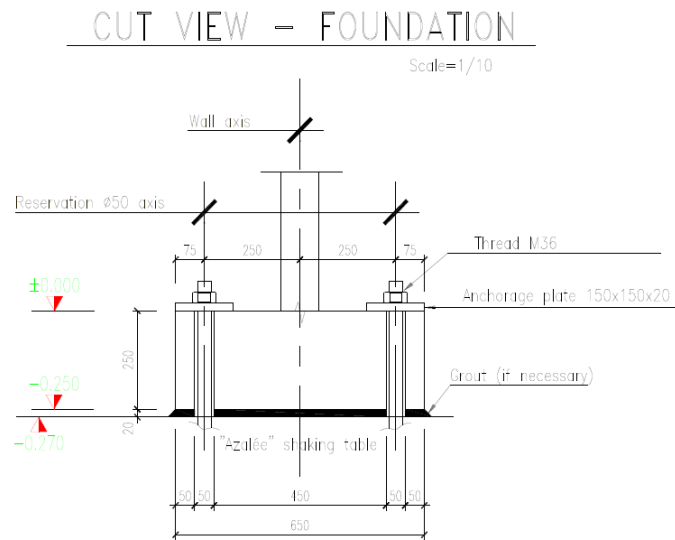
Figure 4.4: Anchorage system of the foundation on the shaking table - dimensions in mm.

Figures 4.5 and 4.6 show how the reinforced concrete mock-up looks like.

Figure 4.5: Foundation of the mock-up.

Figure 4.6: Reinforced concrete mock-up and additional masses.

Figure 4.6 shows that each floor is loaded by steel blocks. These steel blocks are called the additional masses. These additional masses are fixed at each floor.

4.0.3 Reference Coordinate System

The axis system is described in the following two figures.

Figure 4.7: Axis system for the mock-up in the plane (x,y).
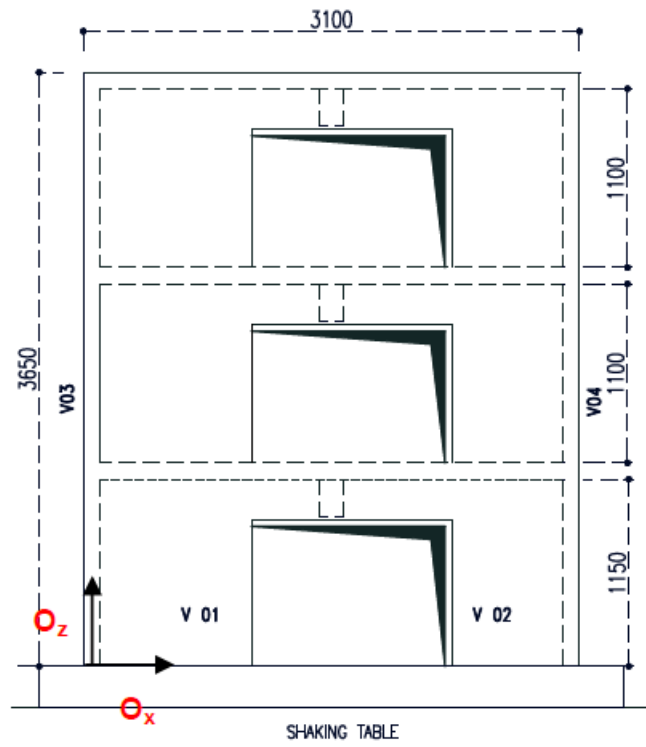
Figure 4.8: Axis system for the mock-up in the plane (x,z).

The origin point is located at the junction of the walls V01 and V03. The top face of the foundation is considered to be located in the plan defined by z=0. This axis system is used and the results will be expressed with respect to it.

4.1 Material Parameters: Concrete and Steel

To model the reinforced concrete mock-up it is important to have material parameters. The material parameters for concrete and steel which are used to model the mock-up are given in tables 4.2 and 4.3.

Table 4.2: Material parameters for concrete.

Structural component	Young's modulus [MPa]	Poisson's ratio	f_c [MPa]	f_t [MPa]	G_f^I [J/m^2]	ρ_c [kg/m^3]
Foundation	25400	0.17	30	2.4	270	2300
Walls cast 1	28700	0.19	30	2.4	270	2300
Walls cast 2	25700	0.19	30	2.4	270	2300
Walls cast 3	29500	0.18	30	2.4	270	2300
Floor 1	28200	0.18	30	2.4	270	2300
Floor 2	24700	0.17	30	2.4	270	2300
Floor 3	24400	0.18	30	2.4	270	2300

In this table, only the Young's moduli and Poisson's ratios are measured values. The values for the compression strengths, tensile strengths, fracture energies and the densities are design values.

Table 4.3: Material parameters for reinforcement steel.

Structural component	Young's modulus [MPa]	Poisson's ratio	f_y [MPa]	ρ_c [kg/m^3]
Reinforcement	210000	0.3	500	7800

These material parameters for steel are all design values.

4.2 Mass of the Mock-up and Additional Masses

The weight of the additional masses on each floor is given in table 4.4.

Table 4.4: Additional masses.

Floor	Mean value [tons]
At +1.250 m	11.45
At +2.450 m	12.17
At +3.650 m	10.32

The mass of the mock-up without the additional masses is equal to 11.890 tons. The overall mass (mock-up and additional masses) is close to 45 tons. The spatial distribution of the additional masses is given in figures 4.9, 4.10 and 4.11.
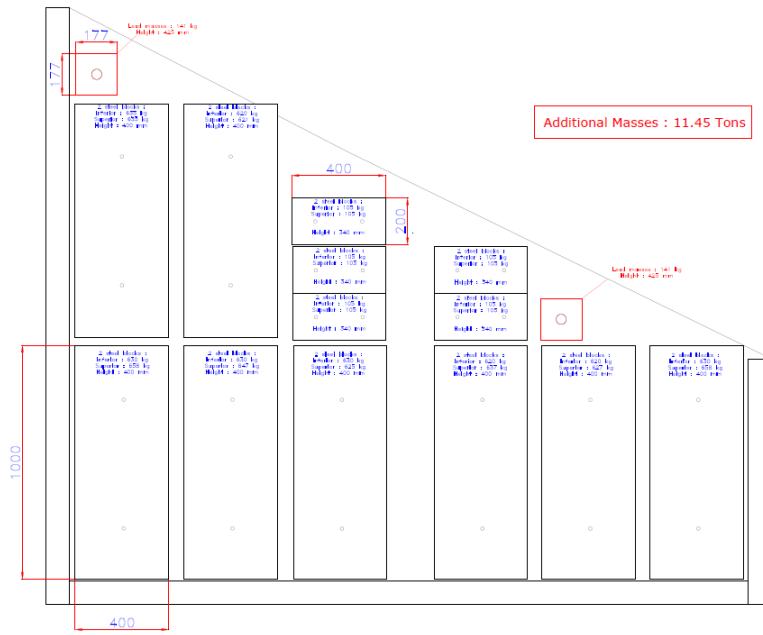
Figure 4.9: Additional masses 1st slab (+1250 mm).
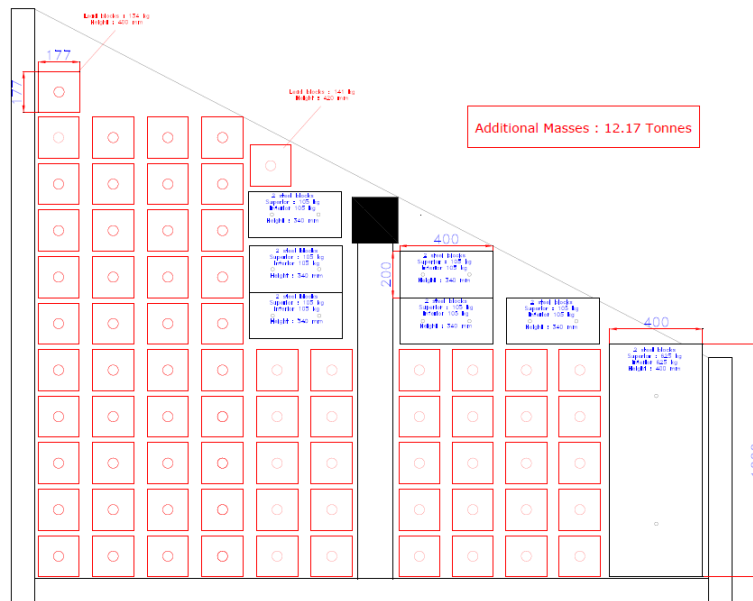
Figure 4.10: Additional masses 2nd slab (+2450 mm).

Figure 4.11: Additional masses 3rd slab (+3650 mm).

4.3 Shaking Table

The shaking table can be considered as a semi-rigid block with a total mass of 25 tons fixed to 8 hydraulic actuators, 4 in the horizontal direction and 4 in the vertical direction. The plan view and elevation view are shown in the figures below.
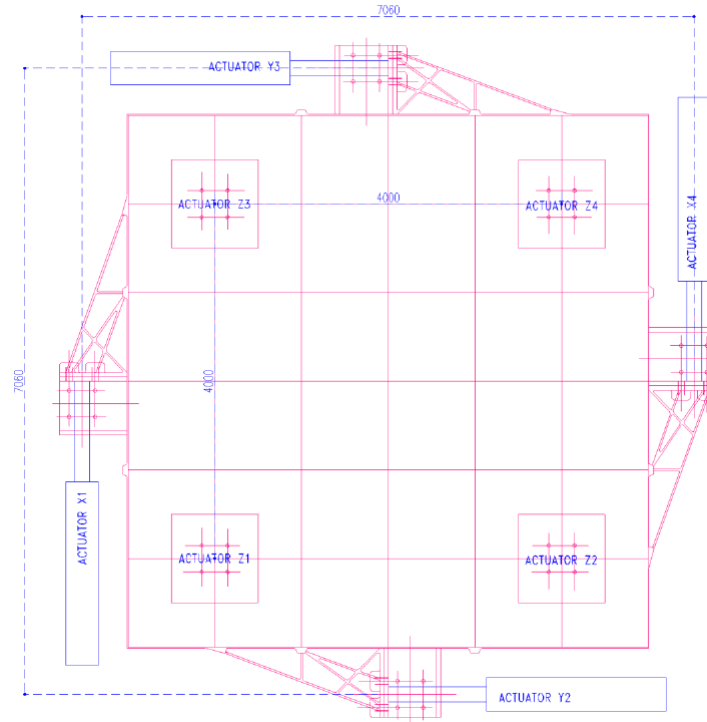
Figure 4.12: Plan view of the shaking table, dimensions in mm.
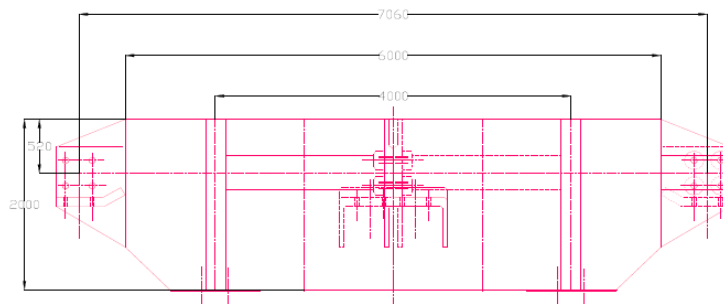
Figure 4.13: Elevation view of the shaking table, dimensions in mm.

The distance between two vertical actuators is 4000 mm. The distance between 2 horizontal actuators is 7060 mm. The axes of the horizontal actuators are located at 520 mm below the upper face of the shaking table. In order to control the boundary conditions in an efficient way, the following data will be provided in stage 2 (for low intensity inputs) and in stage 3 (for high intensity inputs):

- the acceleration and the displacement time history at the table level (point T_0),
- the acceleration and the displacement time history at each actuator levels (points X1, X4, Y2, Y3, Z1, Z2, Z3 and Z4),
- the natural frequencies of the specimen under various boundary conditions.

It is recommended to prescribe the displacement time histories at the actuator levels instead of prescribing the equivalent force field induced by the measured accelerations. This methodology ensures that the rigid body movements of the shaking table are taken into account.

The shaking table is modeled by using the data from the figures below.

Description	Type of finite element	Type of constitutive law	Young's modulus (Pa)	Poisson ration	Mass density (kg.m-3)	Thickness (m)	Mesh picture
Topmost horizontal plate	4 node-shell	Isotropic linear elastic	7.24E+10	0.3	2739.8	0.05	
Horizontal plates excepting the topmost one	4 node-shell	Isotropic linear elastic	4.0E+10	0.3	2739.8	0.02	
Lateral plates	4 node-shell	Isotropic linear elastic	3.2E+10	0.3	2739.8	0.01	
Diagonal plates	4 node-shell	Isotropic linear elastic	3.2E+10	0.3	2739.8	0.01	
Part #1 of the ear #1	4 node-shell	Isotropic linear elastic	3.298E+10	0.3	2739.8	0.02	
Part #2 of the ear #1	4 node-shell	Isotropic linear elastic	3.298E+10	0.3	2739.8	0.05	

Part #3 of the ear #1	4 node-shell	Isotropic linear elastic	3.298E+10	0.3	2739.8	0.1	
Part #4 of the ear #1	4 node-shell	Isotropic linear elastic	3.298E+10	0.3	2739.8	0.05	
Part #5 of the ear #1	4 node-shell	Isotropic linear elastic	3.298E+10	0.3	2739.8	0.05	
Part #6 of the ear #1	4 node-shell	Isotropic linear elastic	3.298E+10	0.3	2739.8	0.1	
Part #1 of the ear #2	4 node-shell	Isotropic linear elastic	3.298E+10	0.3	2739.8	0.02	
Part #2 of the ear #2	4 node-shell	Isotropic linear elastic	3.298E+10	0.3	2739.8	0.05	
Part #3 of the ear #2	4 node-shell	Isotropic linear elastic	3.298E+10	0.3	2739.8	0.1	
Part #4 of the ear #2	4 node-shell	Isotropic linear elastic	3.298E+10	0.3	2739.8	0.05	
Part #5 of the ear #2	4 node-shell	Isotropic linear elastic	3.298E+10	0.3	2739.8	0.05	
Part #6 of the ear #2	4 node-shell	Isotropic linear elastic	3.298E+10	0.3	2739.8	0.1	
Part #1 of the ear #3	4 node-shell	Isotropic linear elastic	3.298E+10	0.3	2739.8	0.02	
Part #2 of the ear #3	4 node-shell	Isotropic linear elastic	3.298E+10	0.3	2739.8	0.05	
Part #3 of the ear #3	4 node-shell	Isotropic linear elastic	3.298E+10	0.3	2739.8	0.1	
Part #4 of the ear #3	4 node-shell	Isotropic linear elastic	3.298E+10	0.3	2739.8	0.05	

Part #5 of the ear #3	4 node-shell	Isotropic linear elastic	3.298E+10	0.3	2739.8	0.05	
Part #6 of the ear #3	4 node-shell	Isotropic linear elastic	3.298E+10	0.3	2739.8	0.1	
Part #1 of the ear #4	4 node-shell	Isotropic linear elastic	3.298E+10	0.3	2739.8	0.02	
Part #2 of the ear #4	4 node-shell	Isotropic linear elastic	3.298E+10	0.3	2739.8	0.05	
Part #3 of the ear #4	4 node-shell	Isotropic linear elastic	3.298E+10	0.3	2739.8	0.1	
Part #4 of the ear #4	4 node-shell	Isotropic linear elastic	3.298E+10	0.3	2739.8	0.05	
Part #5 of the ear #4	4 node-shell	Isotropic linear elastic	3.298E+10	0.3	2739.8	0.05	
Part #6 of the ear #4	4 node-shell	Isotropic linear elastic	3.298E+10	0.3	2739.8	0.1	
Boundary condition – Actuator Y2	4 node-shell	Isotropic linear elastic	3.298E+10	0.3	2739.8	0.1	
Boundary condition – Actuator X4	4 node-shell	Isotropic linear elastic	3.298E+10	0.3	2739.8	0.1	
Boundary condition – Actuator Y3	4 node-shell	Isotropic linear elastic	3.298E+10	0.3	2739.8	0.1	
Boundary condition – Actuator X1	4 node-shell	Isotropic linear elastic	3.298E+10	0.3	2739.8	0.1	
Boundary condition – Actuator Z1	4 node-shell	Isotropic linear elastic	4.0E+10	0.3	2739.8	0.02	
Boundary condition – Actuator Z2	4 node-shell	Isotropic linear elastic	4.0E+10	0.3	2739.8	0.02	
Boundary condition – Actuator Z3	4 node-shell	Isotropic linear elastic	4.0E+10	0.3	2739.8	0.02	
Boundary condition – Actuator Z4	4 node-shell	Isotropic linear elastic	4.0E+10	0.3	2739.8	0.02	

Figure 4.14: Data of the shaking table.

4.4 Position of the Mock-up on the Shaking Table

The reinforced concrete mock-up is placed on the shaking table such as its center of mass corresponds approximately to the one of the table. The coordinates of both centers of mass are given in table 4.5 and are expressed with respect to the global axis system that has been defined. A sketch of the mock-up positioned on the shaking table is shown in figure 4.15 below.
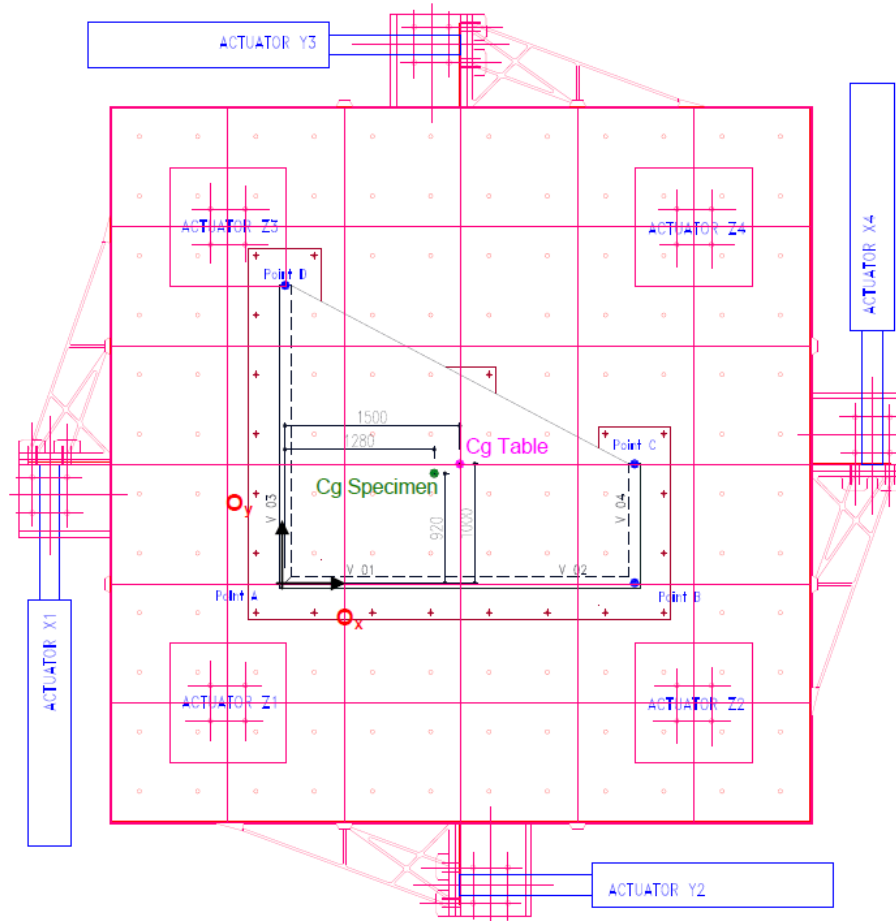

Figure 4.15: Position of the reinforced concrete mock-up on the shaking table.

Table 4.5: Center of mass.

Component	x [m]	y [m]
Shaking table	1.5	1
Mock-up	1.28	0.92

5 Stage 1 - Development of the Finite Element Model

The modeling of the reinforced concrete mock-up on the shaking table consists of the following 3 parts:

- the discretization of the geometry (the finite element mesh),
- the modeling of the physical behavior of the materials which are applied in the structure, for example concrete and reinforcing steel,
- the modeling of the structural effects which influence the behavior of the structure, for example large displacements or time dependent behavior.

For the discretization of the geometry, FX^+ is used. To model the physical behavior of the material, it is important to know which failure mechanisms can occur in the structure. In the case of reinforced concrete structures (like here), the behavior is mainly influenced by cracking and crushing of the concrete and yielding of the reinforcement. And as mentioned before, structural effects are phenomena which influence the behavior of the structure.

Stage 1 of this thesis focuses on the development of the finite element model. Information about the finite element model developed and specific information about the material models are presented in this stage. Geometric data and material properties are provided by the SMART 2013 benchmark committee. These data are used to develop the model.

5.1 Mesh of the Finite Element Model

In this section the mesh of the finite element model is presented. After presenting the mesh of the finite element model, it is explained where the finite element model consists of and what kind of elements are used to develop the model. The information about the elements which are given in this section are coming from the *element library* of DIANA manual [4].

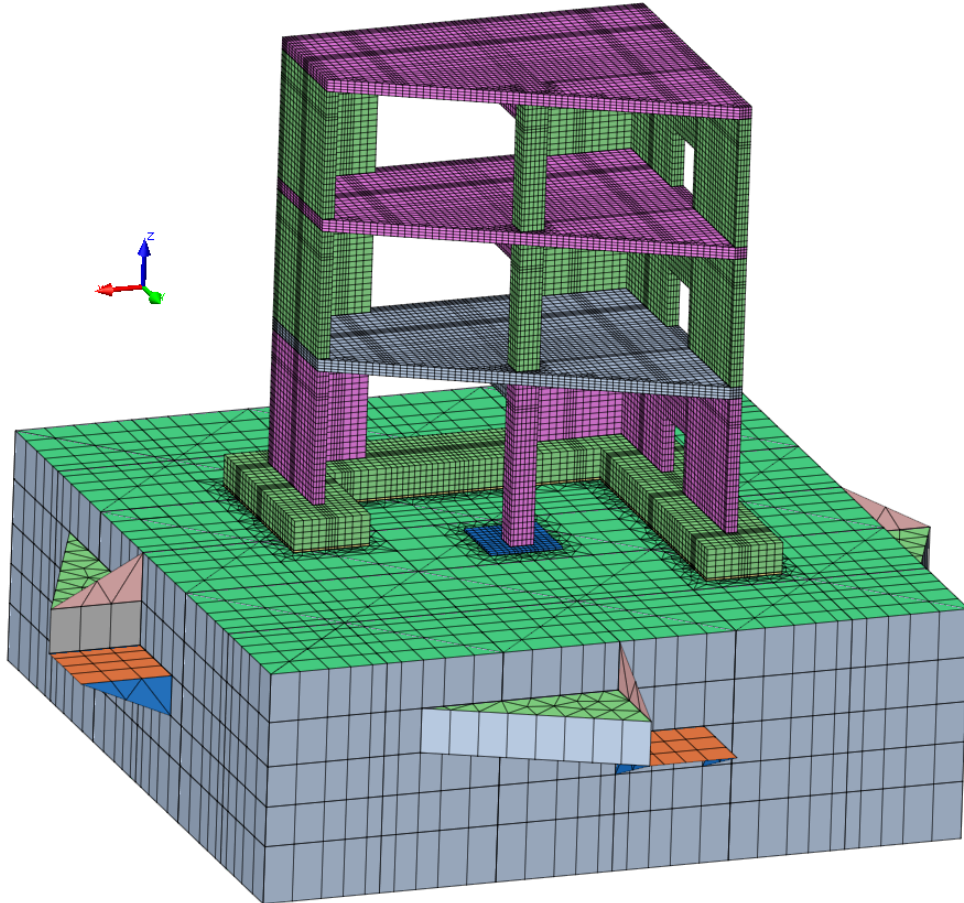Figure 5.1 shows how the finite element model looks like. This model is developed in FX$^+$.

Figure 5.1: Finite element model developed in FX+.

As can be seen in figure 5.1, this model consists of a model of the reinforced concrete mock-up and the shaking table. The model of the mock-up is a 3D finite element model which means that it consists of 3D solid elements. The reason why a 3D model is chosen above a 2D model is because it is assumed that with a 3D model it is possible to mimic the real mock-up in a good and reliable way. This means that the results of the dynamic analyses will be more accurate and the predictions of the dynamic behavior of the mock-up, using the finite element model, will also be more reliable. The same reason applies to why the shaking table is also modeled together with the mock-up, to mimic the reality as good as possible.

5.1.1 Mesh of the Concrete Structure

The mesh of the mock-up alone looks as follows.
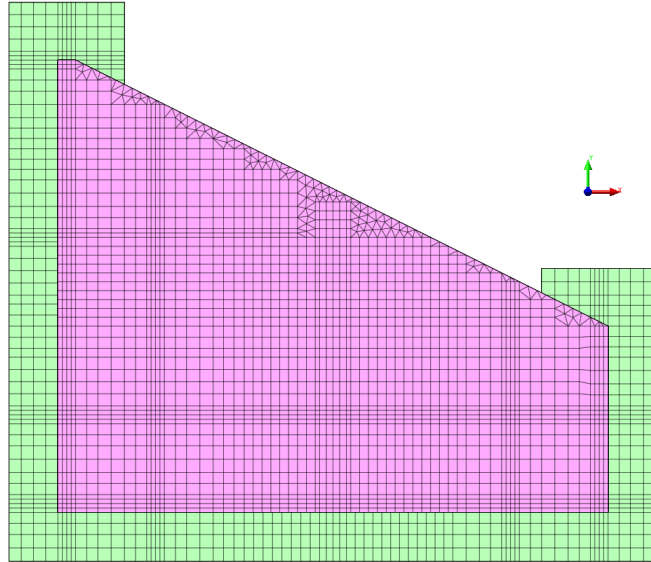
Figure 5.2: Top view of the mock-up model.
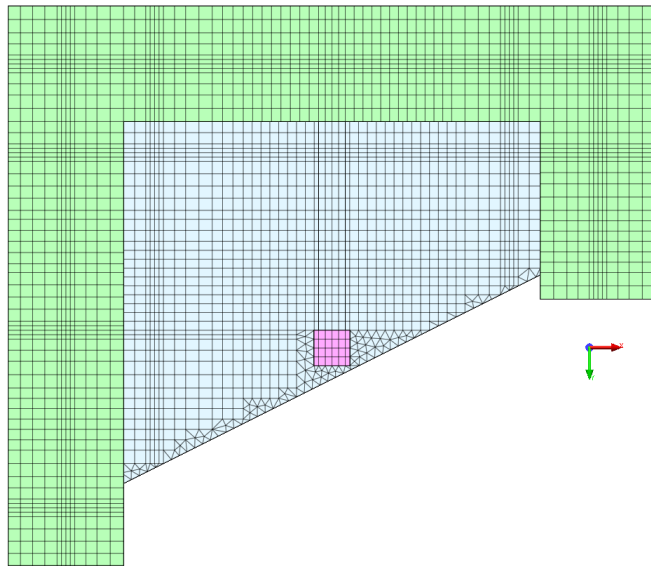
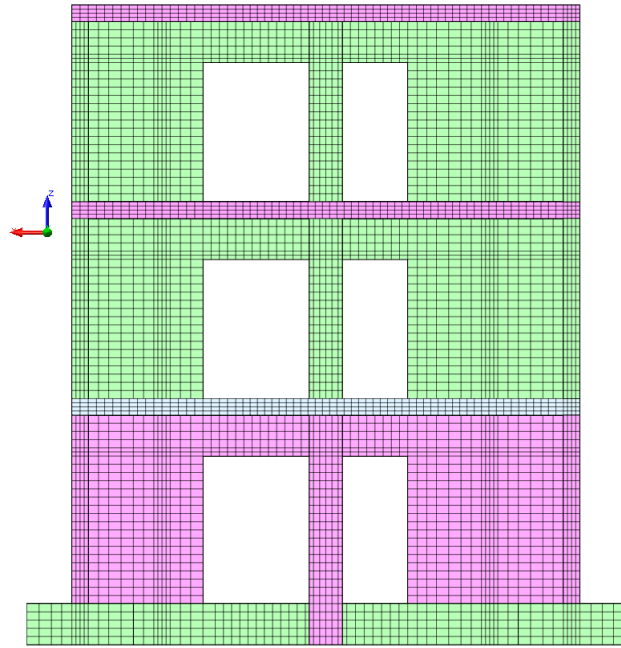Figure 5.3: Bottom view of the mock-up model.

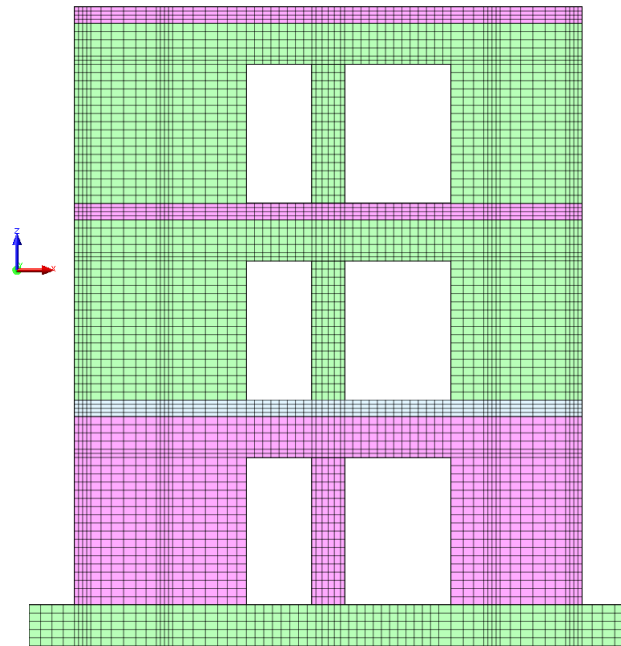Figure 5.4: Front view of the mock-up model.

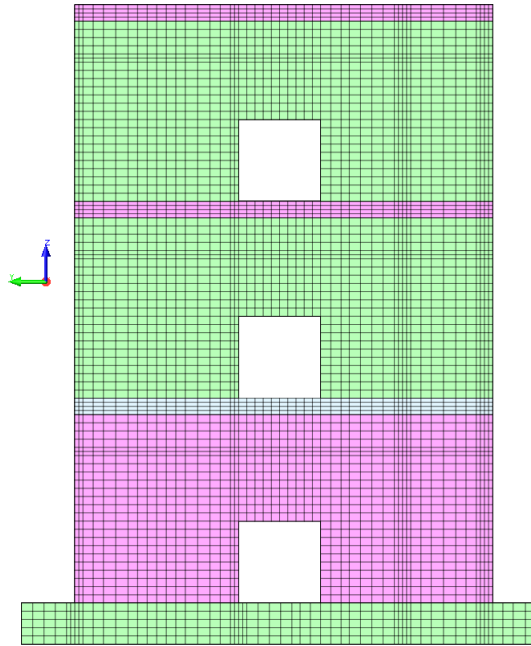Figure 5.5: Rear view of the mock-up model.
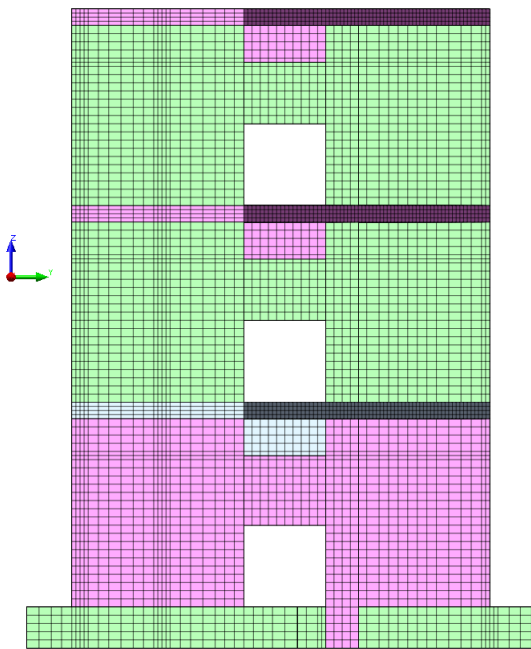
Figure 5.6: Left side view of the mock-up model.
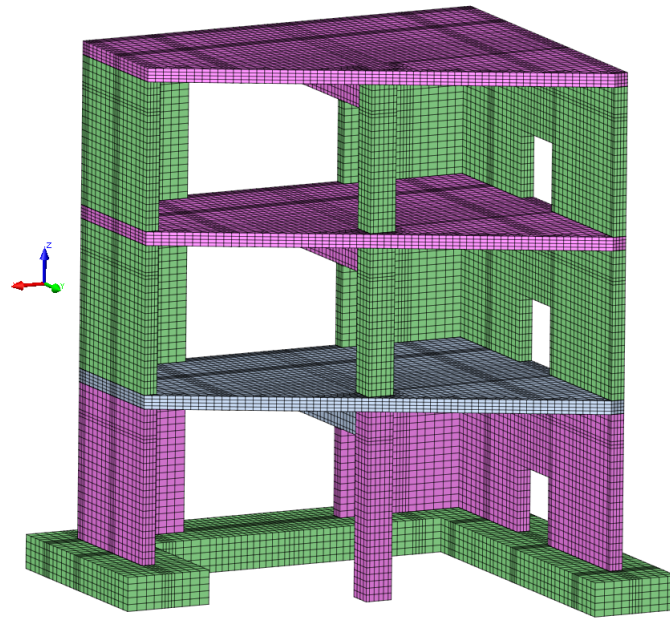

Figure 5.7: Right side view of the mock-up model.
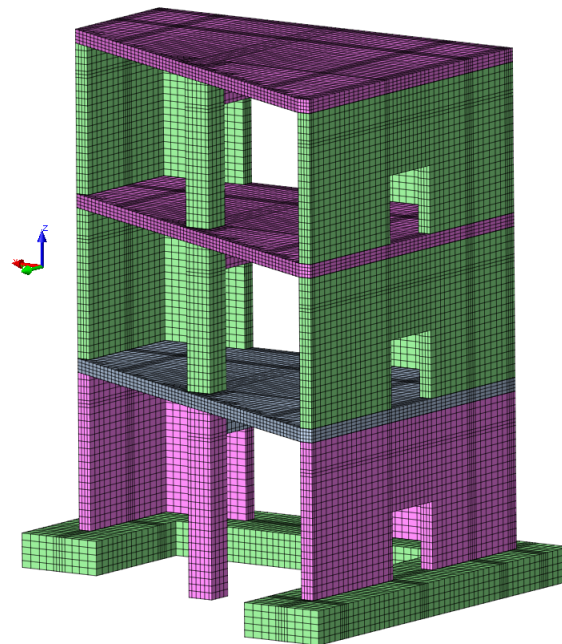
Figure 5.8: Reinforced concrete mock-up model.

Figure 5.9: Reinforced concrete mock-up model.

The figures show that the mesh of the model is quite fine. The thickness of the walls and the floors are for example divided into four elements. The model of the mock-up is build out of *solid elements*. Solid elements are general purpose elements. These type of elements are usually applied only when other elements are unsuitable or would produce inaccurate analysis results. It is already known that in stage 2 and stage 3 (non)linear transient analyses are performed and in order to get accurate results from these analyses it is chosen to have solid elements instead of 2D elements. With solid elements and a fine mesh of the model it is

25

possible to mimic the concrete mock-up as good as possible. The figure below shows how a solid element may look like.
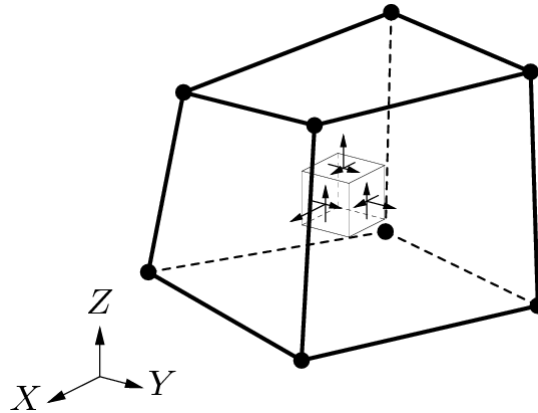

Figure 5.10: Characteristics of solid elements.

Solid elements have the following properties: the stress situation is 3-dimensional, the loading may be arbitrary and the dimensions in 3 axial direction X, Y, and Z are of the same order of magnitude.

The variables in solid elements are *displacements*, *strains* and *stresses*. Displacements are the basic variables in the nodes of solid elements. In the local element directions, the following displacements are present in the nodes: translation in x direction u_x, translation in y direction u_y and translation in z direction u_z.
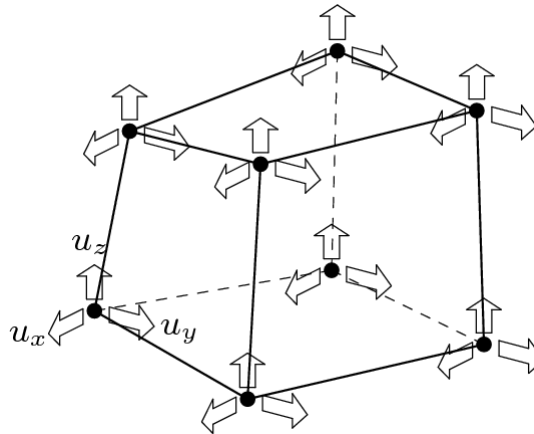
Figure 5.11: Displacements in the nodes of solid elements.

The displacements in the nodes give the deformations ($\mathrm{d}u_x$, $\mathrm{d}u_y$, $\mathrm{d}u_z$) of an infinitesimal part ($\mathrm{d}x$, $\mathrm{d}y$, $\mathrm{d}z$) of the element.
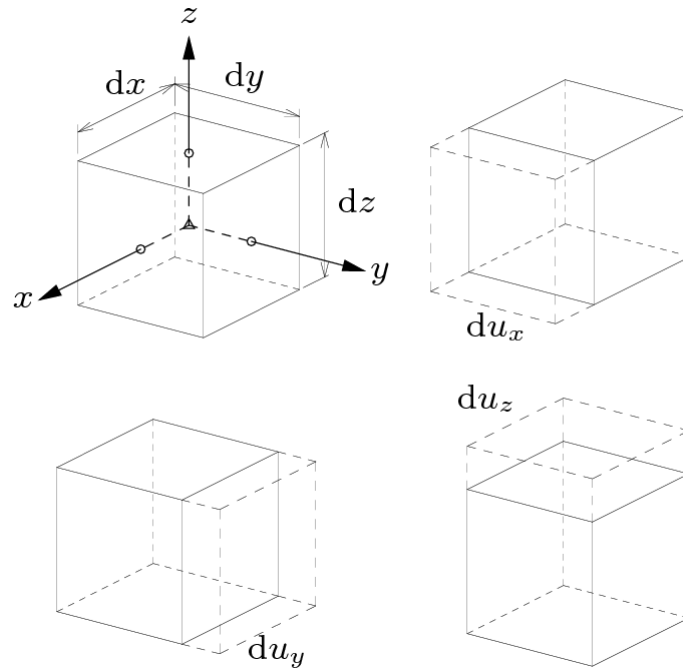
Figure 5.12: Deformations of a unit cube.

From these deformations, Diana derives the Green-Lagrange strains for all integration points of the element. And from the strains, the Cauchy stresses in the integration points are derived.
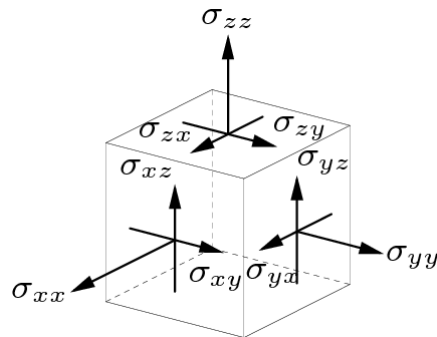

Figure 5.13: Cauchy stresses on a unit cube.

For the model of the concrete mock-up, TP18L and HX24L elements are used. These elements are regular solid elements. The basic variables for regular solid elements are the translations u_x, u_y and u_z where the derived variables are the Green-Lagrange strains and the Cauchy stresses.

TP18L is a six-node isoparametric solid wedge element. It is based on linear area interpolation in the triangular domain and a linear isoparametric interpolation in the ζ direction. By default Diana applies a 1-point integration scheme in the triangular domain and 2-point in the ζ direction. Schemes higher than 1 x 2 are not suitable.
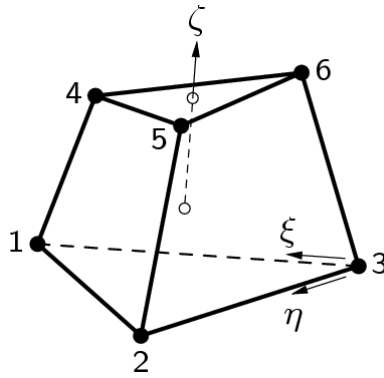
Figure 5.14: TP18L - 6-node isoparametric solid wedge element.

HX24L is an 8-node isoparametric solid brick element. It is based on linear interpolation and Gauss integration. The strain ϵ_{xx} and stress σ_{xx} are constant in x direction and vary linearly in y and z direction. The strain ϵ_{yy} and stress σ_{yy} are constant in y direction and vary linearly in x and z direction. The strain ϵ_{zz} and stress σ_{zz} are constant in z direction and vary linearly in x and y direction. By default DIANA applies a 2 x 2 x 2 integration scheme. Schemes higher than 2 x 2 x 2 are not suitable.
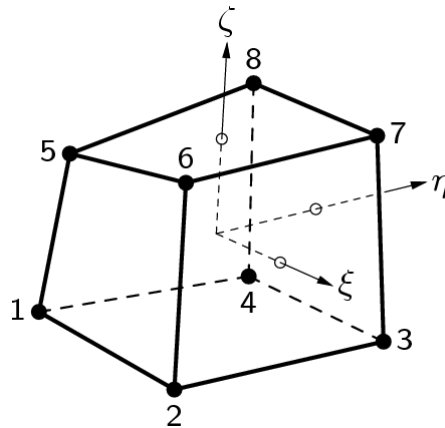
Figure 5.15: HX24L - 8-node isoparametric solid brick element.

5.1.2 Reinforcement

To model the reinforcement in the concrete structure, embedded reinforcement bars are used. The reinforcement in the mock-up looks as follows.
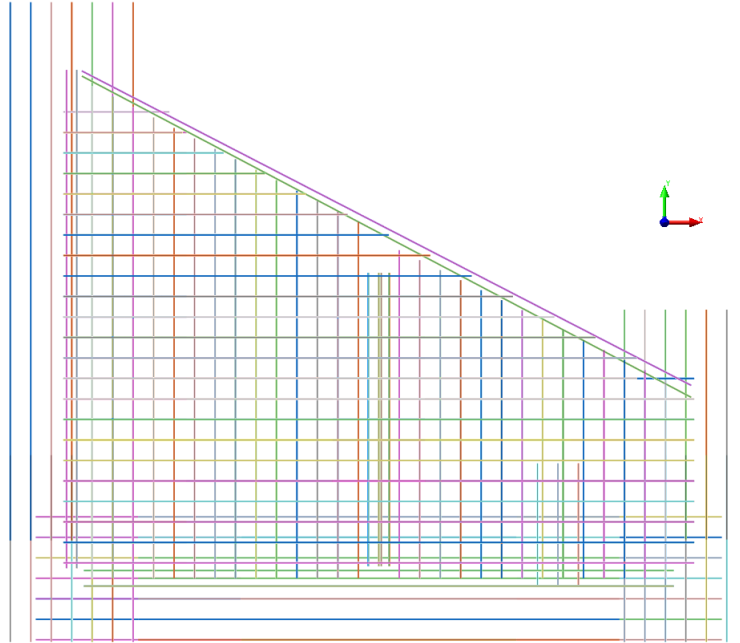

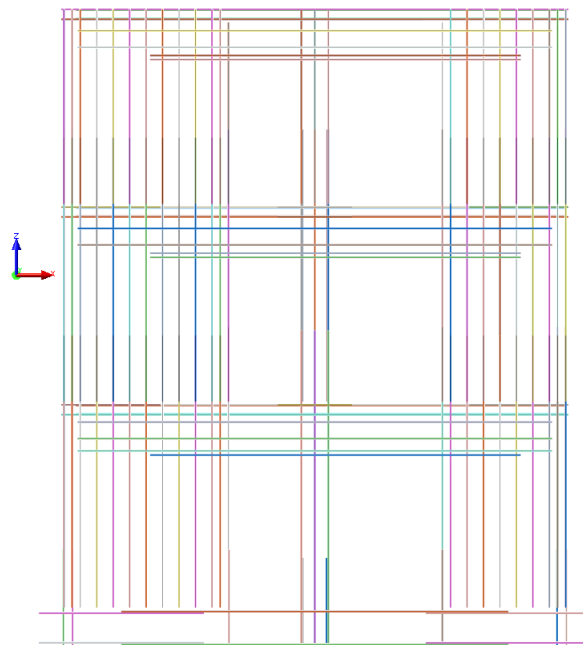Figure 5.16: Top view of embedded reinforcement bars.

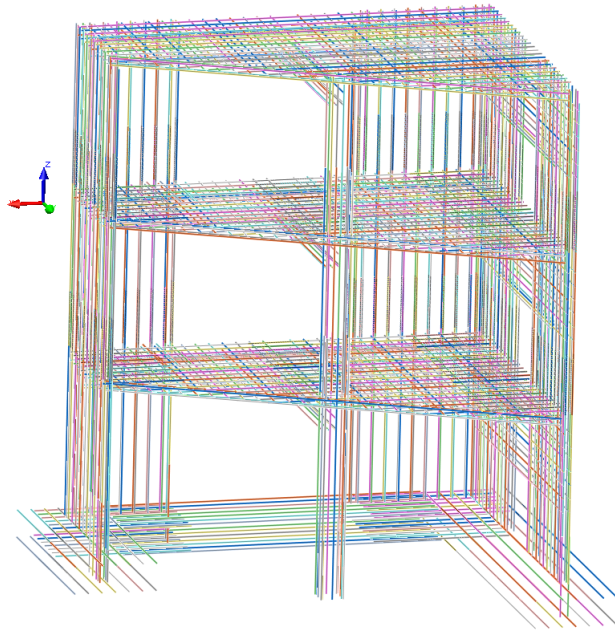Figure 5.17: Rear view of embedded reinforcement bars.

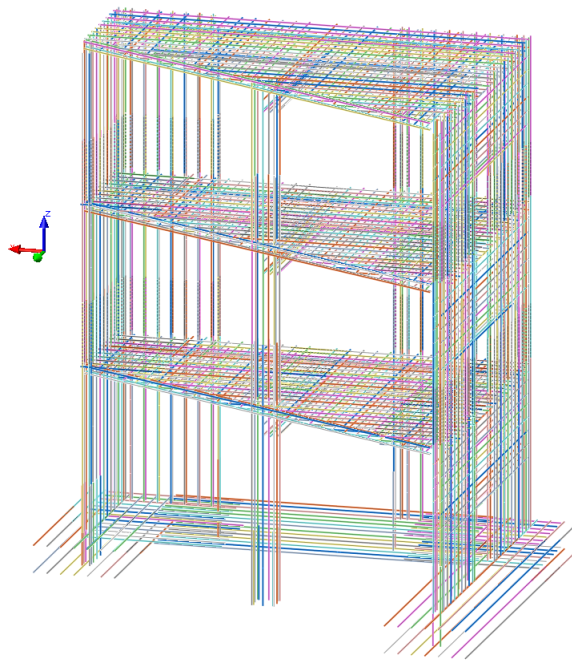Figure 5.18: Embedded reinforcement bars.

Figure 5.19: Embedded reinforcement bars.

In finite element analysis, reinforcements add only stiffness to the finite element model. They can be used to model steel reinforcements in concrete. By default, the reinforcements are embedded in the elements in which they are located and do not allow relative slip. This type of reinforcement is called *embedded reinforcement*. The main characteristics of embedded reinforcements are:

- reinforcements are embedded in structural elements, the so-called *mother elements*,
- embedded reinforcements do not have degrees of freedom of their own,
- in embedded reinforcements the strains in the reinforcements are computed from the displacement field of the mother elements. This implies perfect bond between the reinforcement and the surrounding material.

Reinforcement bars may be embedded in beams, plane stress (except three-dimensional membrane elements), curved shell and solid elements. In finite element models, with the just mentioned elements, reinforcement bars have the shape of a line. Bars may also be embedded in plane strain and axi-symmetric elements where they have the shape of a point.

The total length of the bar is considered to be divided in several *particles* where a particle must be completely inside a structural element.
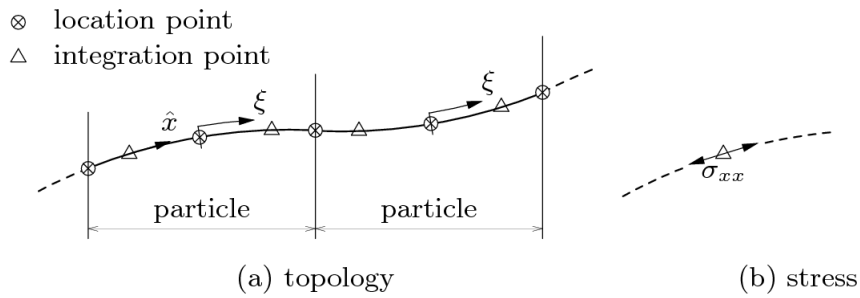

(a) topology   (b) stress

Figure 5.20: Embedded reinforcement bar.

The *location points* define the position of the particles in the finite element model. Some location points are the intersections of the bar with the element boundaries. Other location points are in-between these intersections, these points define the curvature of the bar. The location points are determined automatically by DIANA from input of *sections*, this process is called pre-processing of reinforcement location.

The variables for a reinforcement bar are the strains ϵ_{xx} and the stresses σ_{xx} oriented in the $\hat{x}$ axis. The strains and stresses are coupled to the degrees of freedom of the surrounding element.

As mentioned before, reinforcement bars can be embedded in solid elements.
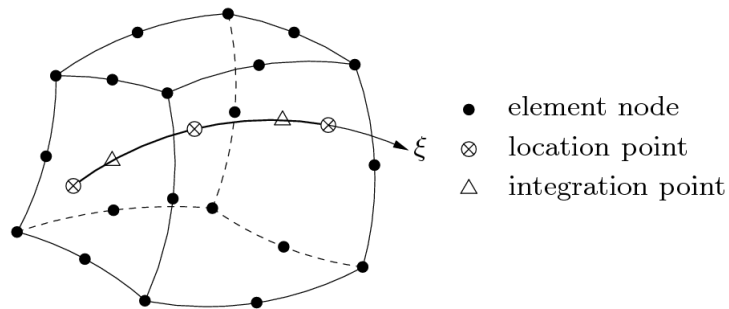

Figure 5.21: Bar particle in a solid element.

To embed reinforcement bars in solid elements, DIANA needs for each solid element the location points of the particle that is embedded in that element. These location points can be generated by pre-processing the input of sections.

5.1.3 Additional Masses

The additional masses on each floor are modeled with *boundary surface elements*. Boundary surface elements consist of line and surface elements. These elements can be used as *distributed translational mass* elements to add mass to a finite element model without influencing the stiffness of the model or to model the *free field medium* in a dynamic analysis.

Line boundary surface elements can be placed on the outer edge of a 2-dimensional model or on the upper face of a line interface element. Plane boundary surface elements can be placed on the outer surface of a 3-dimensional model or on the upper face of a plane interface element.

For the model of the additional masses, T9TM and Q12TM elements are used. T9TM is a 3-node isoparametric triangular element which acts as a surface boundary in the finite element model.
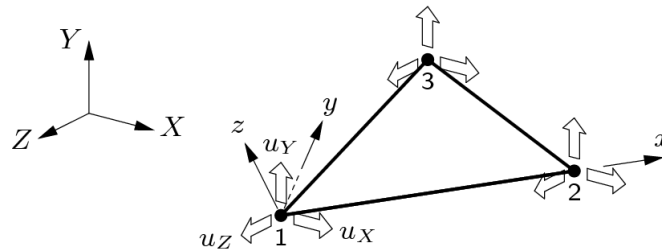
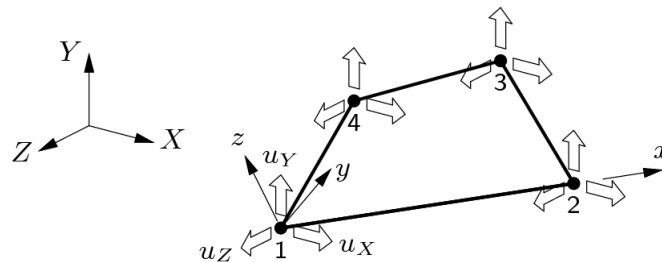

Figure 5.22: T9TM - 3-node isoparametric element.

This element is used to add distributed mass to the finite element model without influencing the stiffness of the model. The local element axes x and y are in the plane of the element and the local element z axis is normal to the plane of the element. The only variables of T9TM are the translations (u_X, u_Y, u_Z) in the global X, Y and Z directions.

Q12TM is 4-node isoparametric quadrilateral element which acts as a surface boundary in the finite element model.

Figure 5.23: Q12TM - 4-node isoparametric element.

This element is used to add distributed mass to the finite element model without influencing the stiffness of the model. The local element axes x and y are in the plane of the element and the local element z axis is normal to the plane of the element. The only variables of Q12TM are the translations (u_X, u_Y, u_Z) in the global X, Y and Z directions. Below some pictures are given to show how these translational masses are situated in the finite element model.
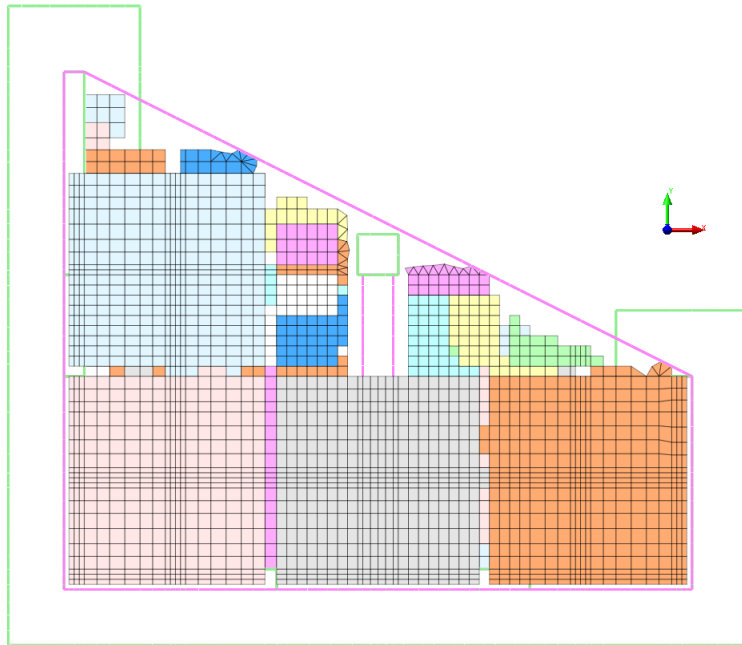
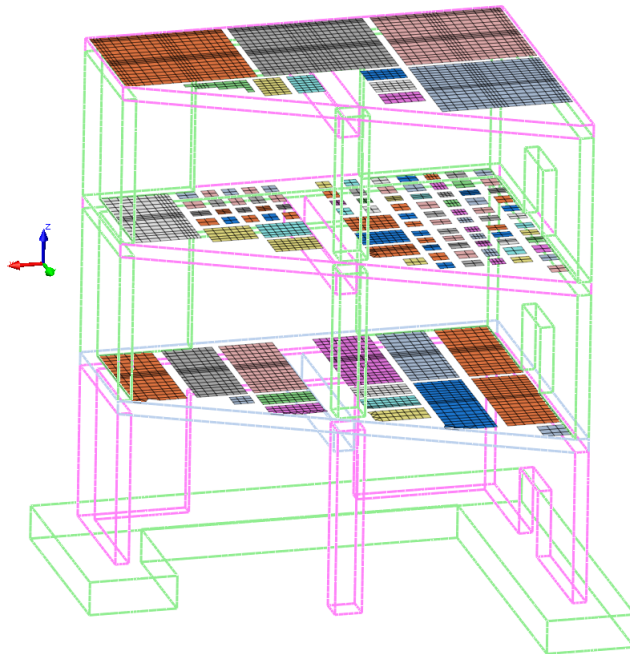Figure 5.24: Model of the additional masses.

Figure 5.25: Model of the additional masses.

5.1.4 Mesh of the Shaking Table

The shaking table is composed out of plates. It looks like it is one solid block, but it is not. The pictures below show how the shaking table is built up.
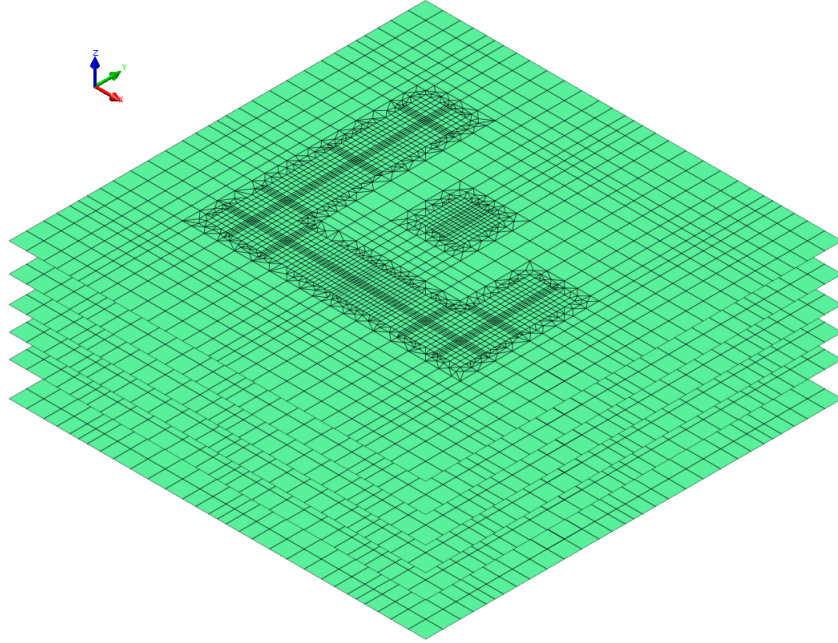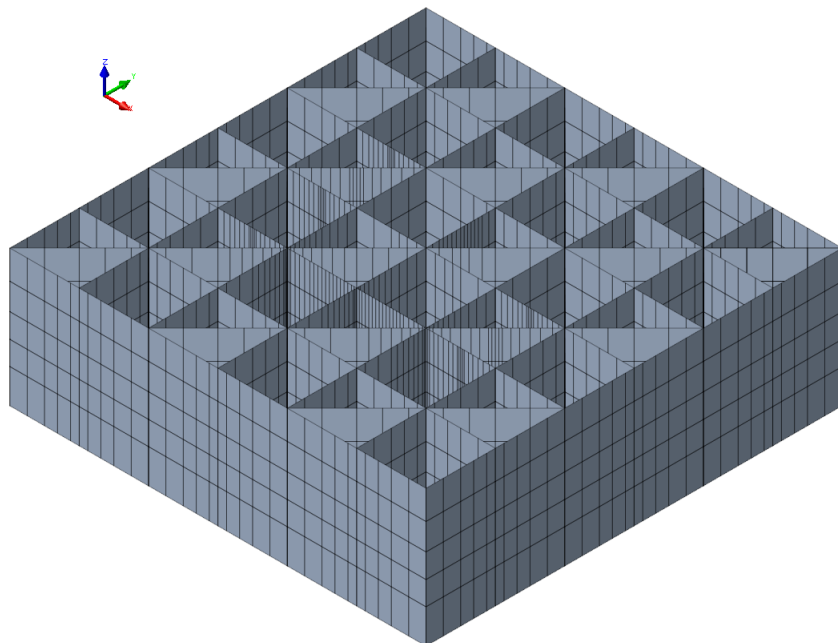

Figure 5.26: Horizontal plates model.
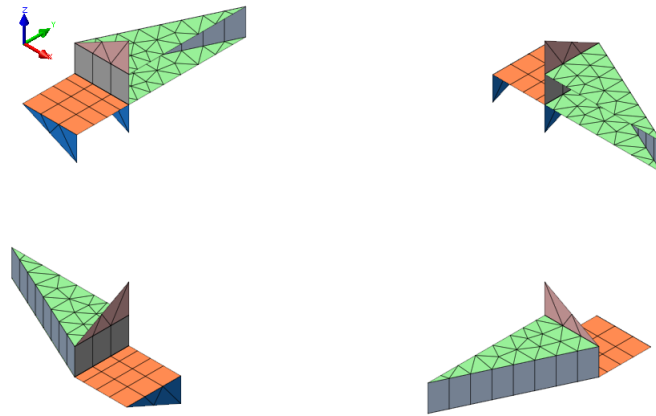

Figure 5.27: Lateral plates model.

Figure 5.28: Actuators model.

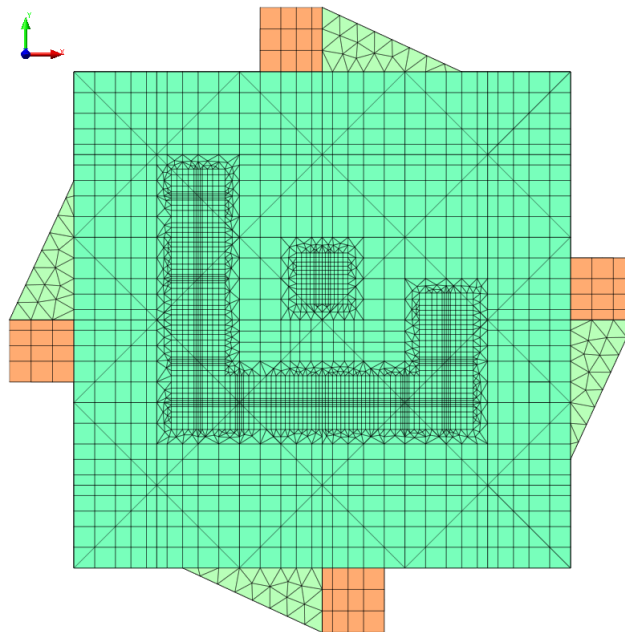Combining these parts, gives the shaking table.
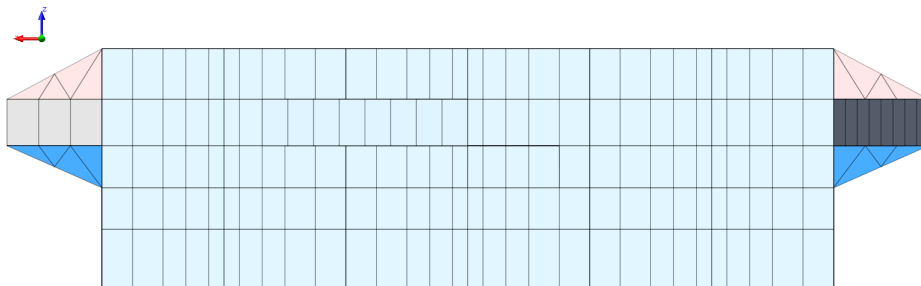

Figure 5.29: Top view shaking table model.

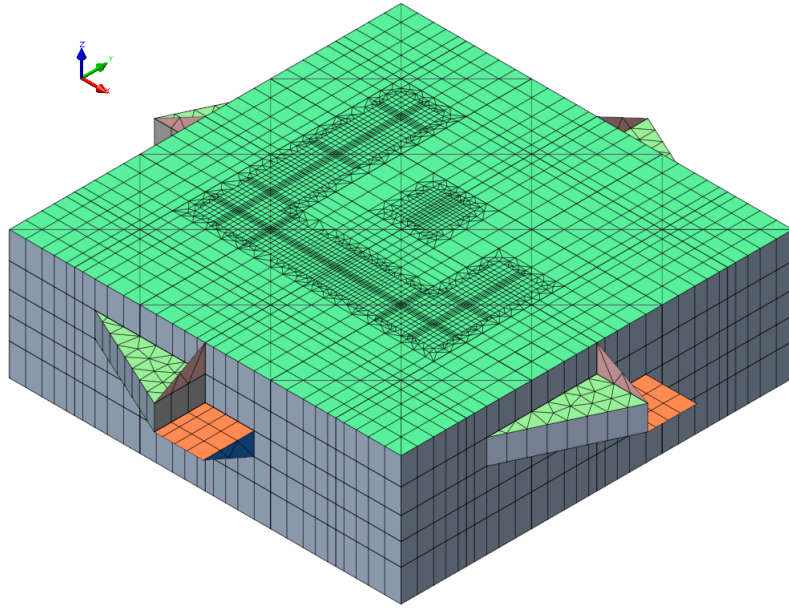Figure 5.30: Side view shaking table model.

Figure 5.31: Shaking table model.

The model of the shaking table consists of *curved shell elements*. Curved shell elements in DIANA are based on isoparametric degenerated-solid approach with the help of two shell hypotheses:

- *straight-normals*: assumes that normals remain straight, but not necessarily normal to the reference surface. Transverse shear deformation is included according to the Mindlin-Reissner theory.
- *zero-normal-stress*: assumes that the normal stress component in the normal direction of a lamina basis is forced to zero. The element tangent plane is spanned by a lamina basis which corresponds to a local Cartesian coordinate system (x_1, y_1) defined at each point of the shell with x_1 and y_1 tangent to the ξ, η plane and z_1 perpendicular to it.
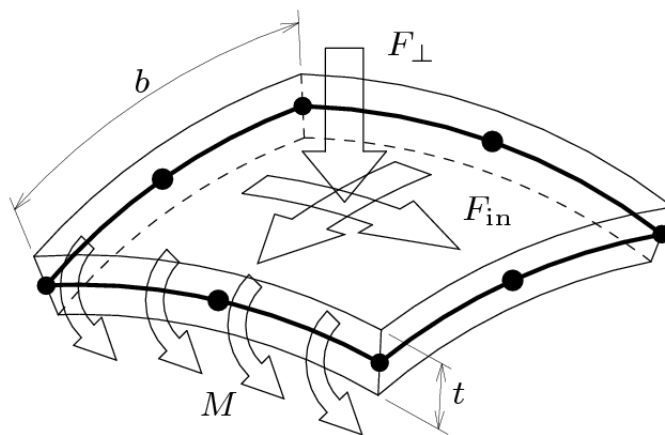

Figure 5.32: Characteristics of curved shell elements.

The in-plane lamina strains ϵ_{xx}, ϵ_{yy} and γ_{xy} vary linearly and the transverse shear strains γ_{xz} and γ_{yz} are forced to be constant in the thickness direction.

5 degrees of freedom are defined in every element node: 3 translations and 2 rotations. Further can be said that these elements have a small thickness t in comparison with the dimensions b. Forces F may act in any direction, between perpendicular to the surface and in the surface. Moments M should act around an axis which is in the element face.

The variables in curved shell elements are *displacements*, *strains* and *stresses*. The basic variables in the nodes of curved shell elements are translations u_X, u_Y, u_Z in the global X, Y and Z direction and the rotations ϕ_x, ϕ_y respectively around the local x axis and local y axis in the tangent plane.
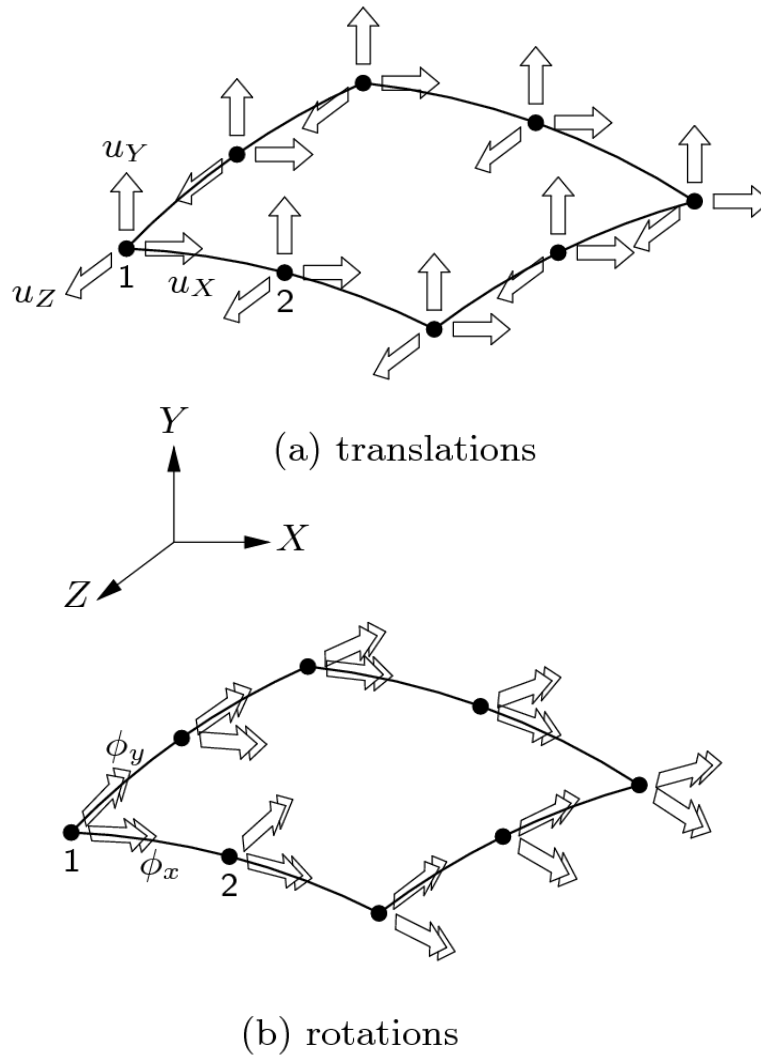

Figure 5.33: Displacements of curved shell elements.

The displacements in the nodes give the deformations $\mathrm{d}u_X$, $\mathrm{d}u_Y$ and $\mathrm{d}u_Z$ and $\mathrm{d}\phi_{\hat{x}}$, $\mathrm{d}\phi_{\hat{y}}$ of respectively an infinitesimal part $\mathrm{d}X$, $\mathrm{d}Y$ and $\mathrm{d}\hat{x}$, $\mathrm{d}\hat{y}$.
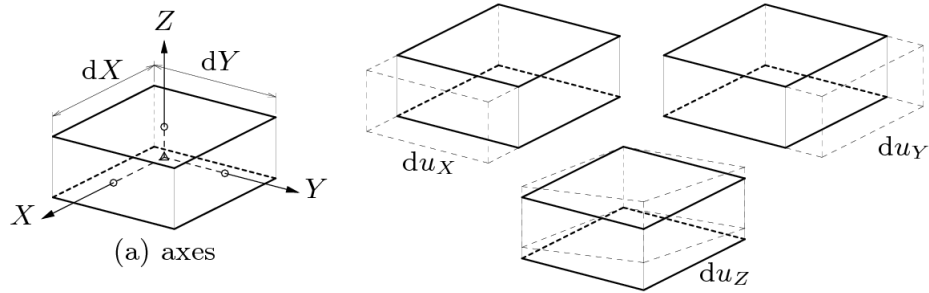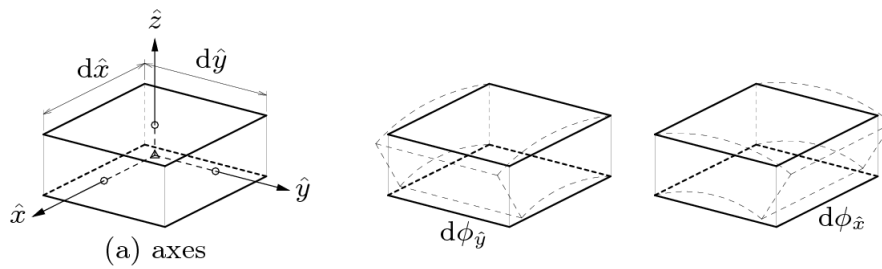
Figure 5.34: Translations of curved shell elements.

Figure 5.35: Rotations of curved shell elements.

From these deformations, the Green-Lagrange strains in the local axes $\hat{x}$, $\hat{y}$, $\hat{z}$ are derived for all integration points. From the strains, DIANA derives the Cauchy stresses in the integration points and from the stresses the generalized bending moments and forces can be derived.
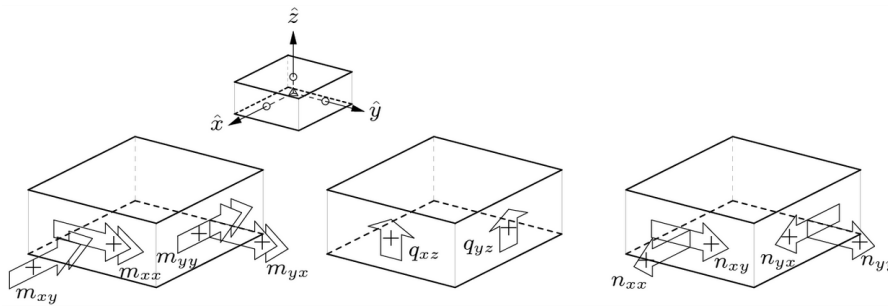

Figure 5.36: Generalized moments and forces.

For the model of the shaking table, T18SH and Q24SH elements are used. These are regular curved shell elements with drilling rotation. Regular element means that the basic variables are the translations u and rotations ϕ, where the derived variables are the strains, Cauchy stresses and the generalized moments and forces. In regular curved shell elements with drilling rotation, an additional rotation ϕ_z (drilling rotation) has been added to the basic variables of the regular curved shell elements. In applications where the elements are nearly co-planar in the nodes, the use of shell elements with drilling rotation is very attractive because they avoid an ill-condition of the assembled global stiffness matrix. The variables of regular curved shell elements with drilling rotation are the same as the variables of regular curved shell elements without drilling rotation.

T18SH is a 3-node triangular isoparametric curved shell element. It is based on linear

interpolation and area integration. The integration in ζ direction (thickness) may be Gauss or Simpson.
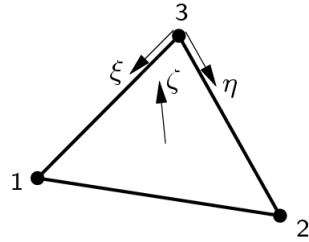

Figure 5.37: T18SH - 3-node isoparametric curved shell element.

The strain ϵ_{xx}, the curvature κ_{xx}, the moment m_{xx}, the membrane force n_{xx} and the shear force q_{xz} are constant in x direction and vary linearly in y direction. The strain ϵ_{yy}, the curvature κ_{yy}, the moment m_{yy}, the membrane force n_{yy} and the shear force q_{yz} are constant in y direction and vary linearly in x direction. The default integration scheme over the element area is a 3-point scheme. The default in ζ direction (thickness) is 3-point Simpson, 2-point Gauss is a suitable option. Schemes higher than 3-point in ζ direction are only useful in case of nonlinear analysis.

Q24SH is a 4-node quadrilateral isoparametric curved shell element. It is based on linear interpolation and Gauss integration over the ξ, η element area. The integration in ζ direction (thickness) may be Gauss or Simpson. To avoid shear locking, which results in a excessively stiff behavior, DIANA automatically modifies the transverse shear strain fields.
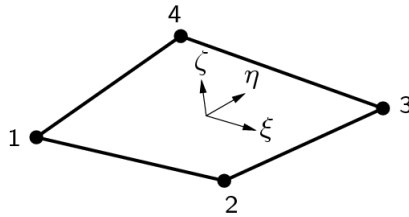

Figure 5.38: Q24SH - 4-node isoparametric curved shell element.

The strain ϵ_{xx}, the curvature κ_{xx}, the moment m_{xx}, the membrane force n_{xx} and the shear force q_{xz} are constant in x direction and vary linearly in y direction. The strain ϵ_{yy}, the curvature κ_{yy}, the moment m_{yy}, the membrane force n_{yy} and the shear force q_{yz} are constant in y direction and vary linearly in x direction. The only possible (and default) integration scheme over the element area is 2 x 2. The default in ζ direction (thickness) is 3-point Simpson, 2-point Gauss is a suitable option. Schemes higher than 3-point in ζ direction are only useful in case of nonlinear analysis.

5.1.5 Mesh of the Entire Model

The reinforced concrete mock-up and the shaking table combined look as follows.
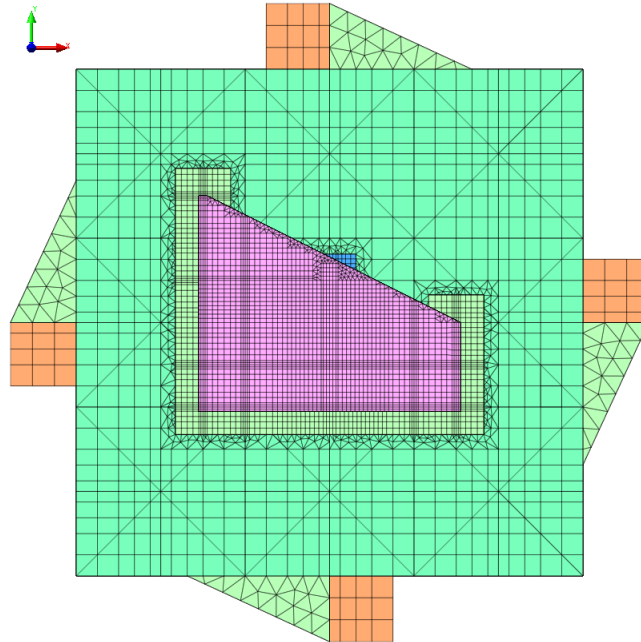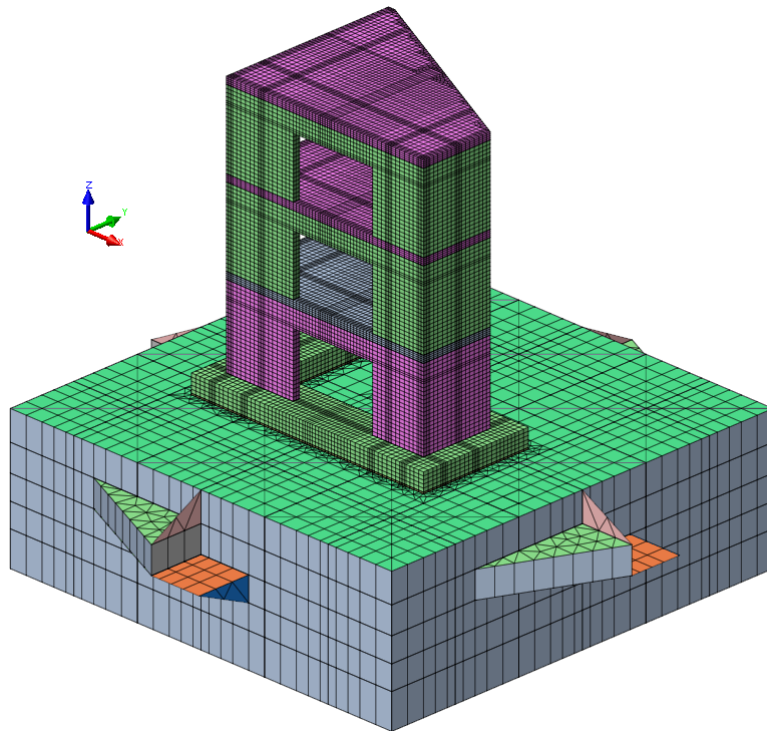

Figure 5.39: Top view.

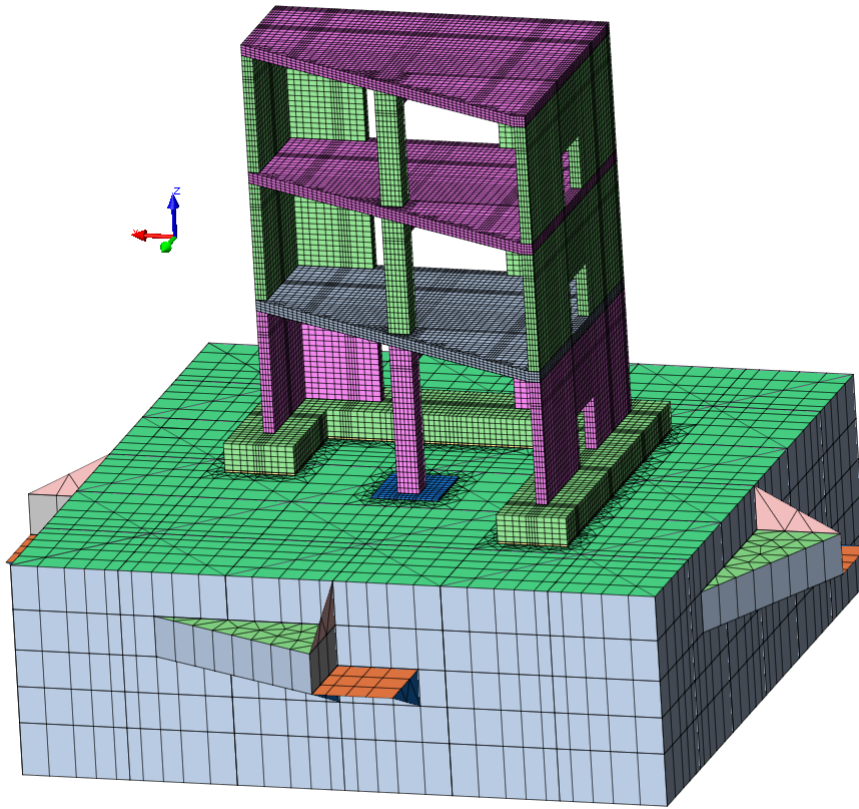Figure 5.40: Reinforced concrete mock-up and the shaking table.

Figure 5.41: Reinforced concrete mock-up and the shaking table.

5.1.6 Amount of Elements, Degrees of Freedom & Boundary Conditions

The finite element model of the concrete mock-up consists of 2784 TP18L and 68774 HX24L elements. In total there are 71558 solid elements with 89206 nodes.

The finite element model of the shaking table consists of 6358 T18SH and 19218 Q24SH elements. In total there are 25576 curved shell elements (with drilling rotation) with 18500 nodes.

The model of the additional masses consists of 48 T9TM and 3654 Q12TM elements. In total there are 3702 translational distributed mass elements with 4787 nodes.

By summing up the nodes from above, 112493 nodes will be obtained. It is important to realize that there will be an overlap between the nodes. Having that said, the finite element model consists of about 107682 nodes with 372774 degrees of freedom in total.

The finite element model is supported in 32 different points in the shaking table. The model is supported in 16 points at the 4 sides of the table in horizontal direction and at 16 points at the bottom of the table in vertical direction. The red arrows in the figures below are the supports of the model.
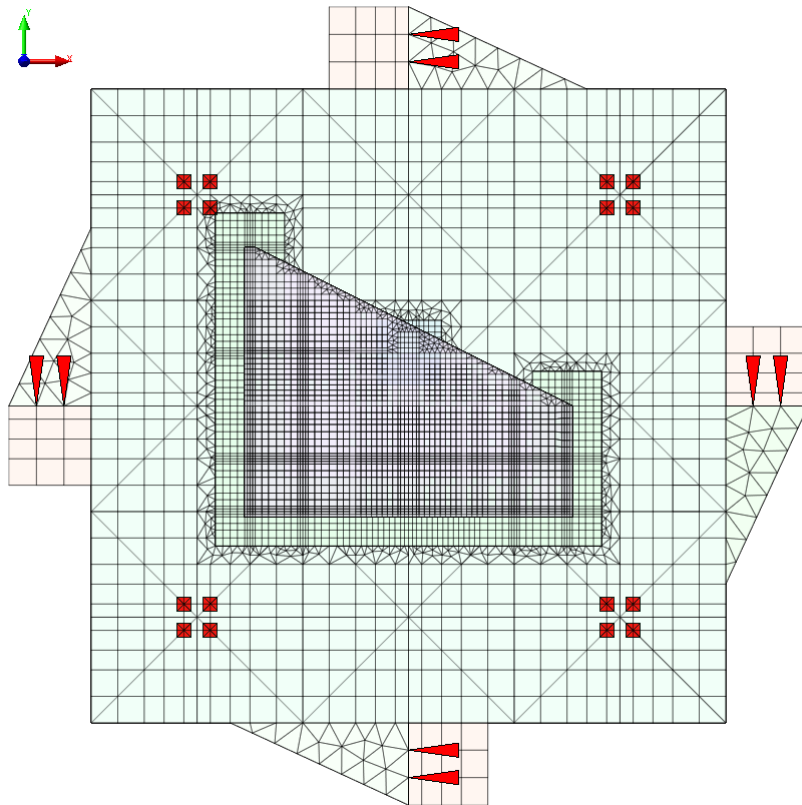

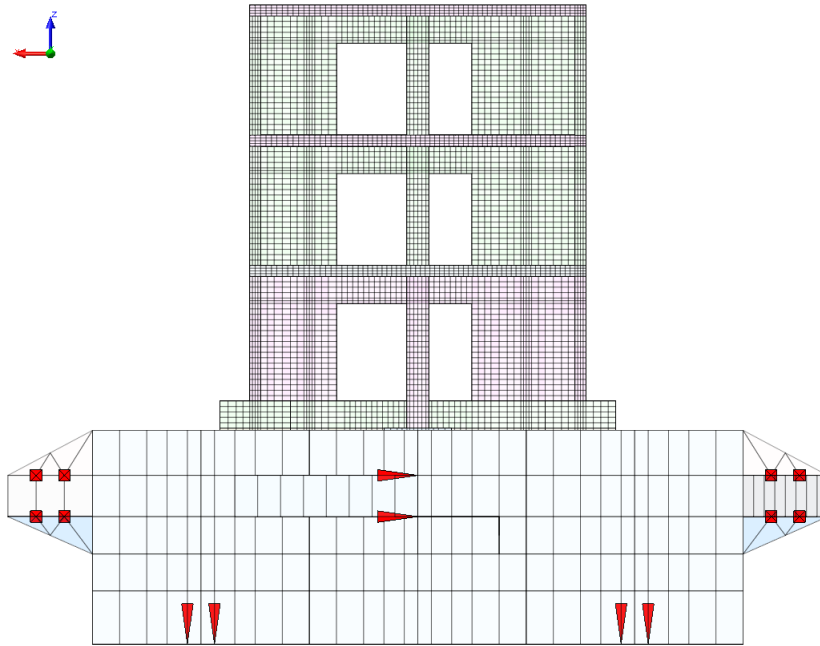Figure 5.42: Supports in horizontal and vertical direction.

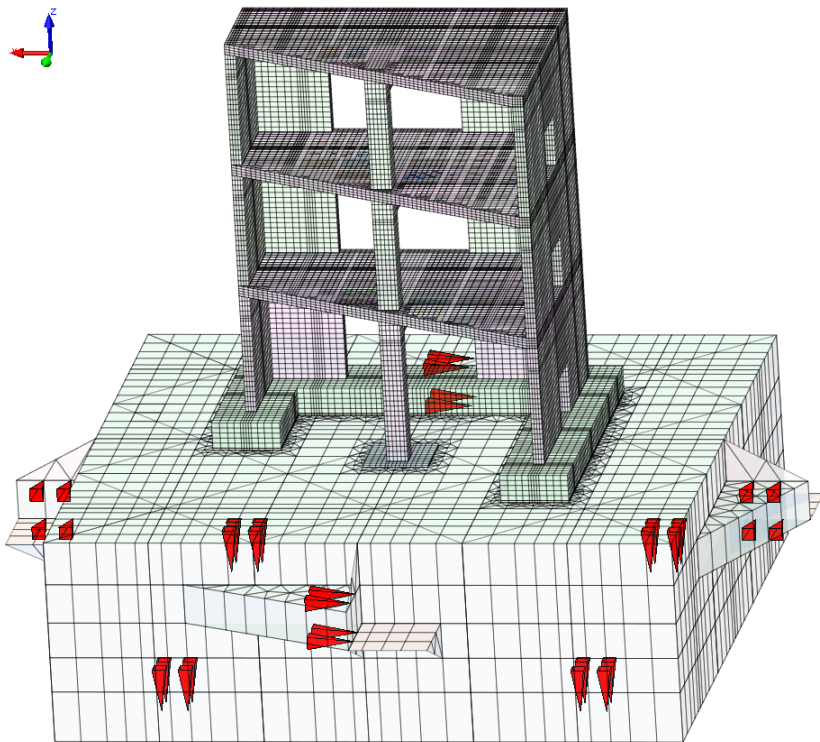Figure 5.43: Supports in horizontal and vertical direction.

Figure 5.44: Supports in horizontal and vertical direction.

5.2 Material Models

In this section a description is given about the material models that is chosen for concrete, reinforcement and shaking table steel. The concrete is modeled with the *total strain rotating crack* model, the reinforcement is modeled with the *Menegotto-Pinto* model and the shaking table steel is modeled with the *Von Mises plasticity* model. The information about the material models are coming from the *material library* of DIANA manual [5].

5.2.1 Total Strain Rotating Crack Model

To model structures made of brittle and quasi-brittle materials, like concrete structures, it is important to know that the constitutive behavior of these materials is characterized by tensile cracking and compressive crushing, and long-term effects like creep and shrinkage.

The cracking and crushing of concrete can be modeled with the following approaches:

- smeared cracking
- discrete cracking

The two models which make use of the smeared cracking approach are *multi-directional fixed* crack model and *total strain* crack model. In this project, the total strain crack model is chosen to model the behavior of concrete. To be more specific, the *total strain rotating* crack model is chosen.

A constitutive model based on total strain, describes the stress as a function of the strain. Within this concept, different approaches are possible. One commonly used approach is the *rotating crack model* in which the stress-strain relationships are evaluated in the principal directions of the strain vector. The crack directions in this coaxial stress-strain concept are continuously rotating with the principal directions of the strain vector. The rotating crack model has been applied for a long time to the constitutive modeling of reinforced concrete and has shown that this modeling approach is well suited for reinforced concrete structures. Another approach is the fixed stress-strain concept (*fixed crack model*) in which the stress-strain relationships are evaluated in a fixed coordinate system where the crack directions are fixed. The basic concept of the total strain crack models is that the stress is evaluated in the crack directions.

5.2.2 Lateral Influence

A specimen subjected to a uni-axial tensile or compressive loading will show lateral displacements because of the *Poisson effect* of the material.
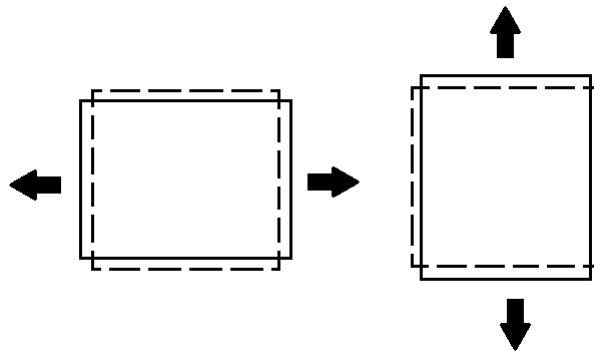

Figure 5.45: Poisson effect.

When these displacements are constrained, *lateral expansion effects* will occur due to the Poisson effect. These effects are considered important in a 3-dimensional modeling of reinforced concrete structures and has to be taken into account. The following lateral expansion effects can be distinguished: *lateral confinement*, *lateral cracking* and *Poisson's ratio reduction*.

The lateral confinement has been taken into account in the modeling by using a model which describes the increase in compressive strength due to this effect.

In the cracked state, the Poisson effect will cease to exist. This means that the Poisson's ratio will decrease with increasing damage of the material due to cracking. This has also been taken into account in the modeling. Lateral cracking has also been taken into account by using a functions which describes this.

5.2.3 Tensile Behavior

In the total strain crack model, the tensile behavior of reinforced concrete can be modeled by 9 different tension functions. From these 9 predefined tension functions, 3 are based on the fracture energy of the material. The tension functions based on fracture energy are:

- linear tension softening
- exponential tension softening
- nonlinear tension softening according to Hordijk et al.
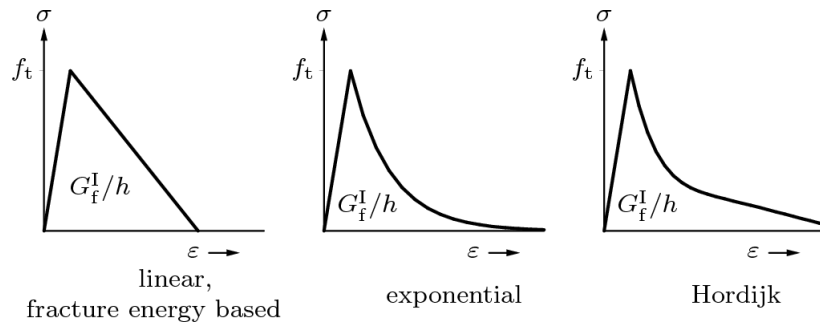
Figure 5.46: Tension softening functions - fracture energy based.

Tensile behavior which is not related to the fracture energy can also be modeled with the total strain concept. These softening functions are:

- elastic tension
- constant tension softening
- brittle tension softening
- linear tension softening
- multi-linear tension softening
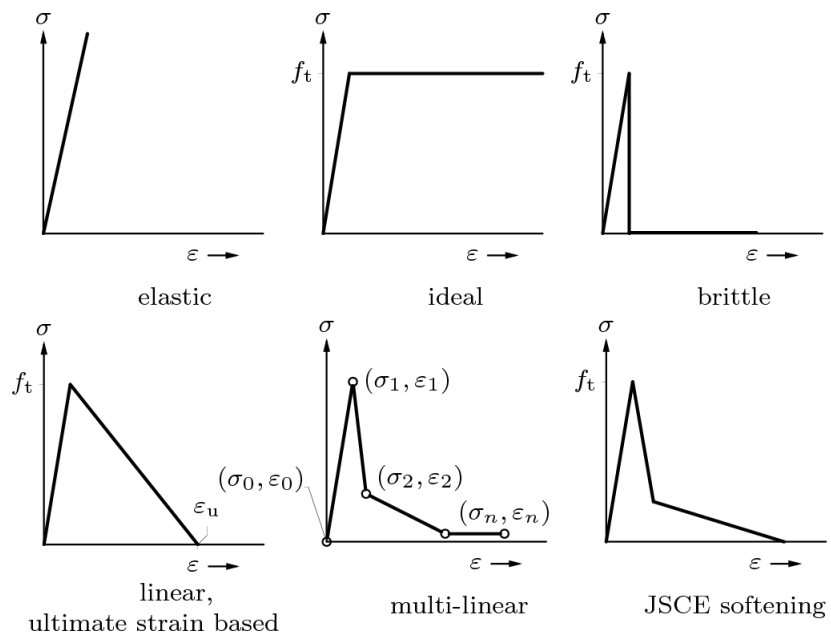- JSCE tension softening

Figure 5.47: Tension softening functions.

Al these softening functions are related to the crack bandwidth as is usual in smeared crack models. In this project, the softening function Hordijk is chosen to model the tensile behavior of concrete.

5.2.4 Compressive Behavior

The compressive behavior of reinforced concrete in the total strain crack model can be described by 9 different compression functions. These predefined compression functions describe the crushing behavior of concrete. The functions are:

- elastic compression
- constant compression
- Thorenfeldt compression
- linear compression
- multi-linear compression
- saturation compression
- parabolic compression
- EN 1992-1-2 compression
- Maekawa compression
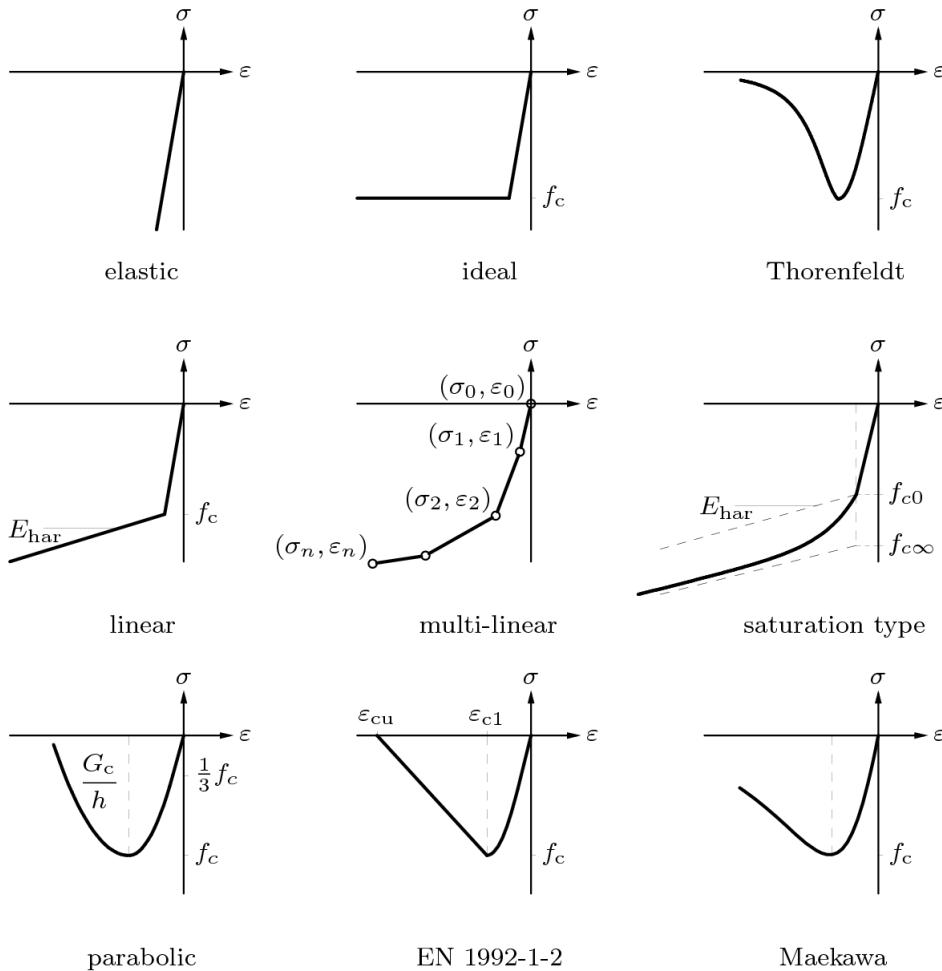
Figure 5.48: Compression functions.

The compression function Thorenfeldt is chosen to model the compressive behavior of concrete in this project. And as mentioned before, the tensile behavior of concrete is modeled with the tension function Hordijk. By combining these two functions, the following figure will be obtained.
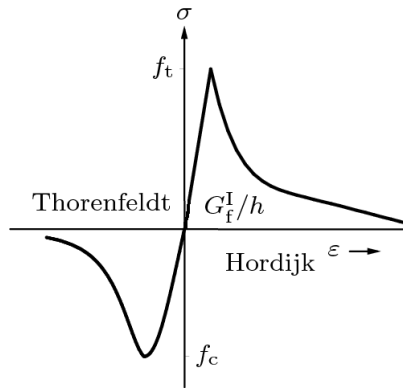
Figure 5.49: Material models for concrete.

It is important to mention that figure 5.49 is only meant for illustration because the size of the graphs are, relatively to each other, not correct. For concrete, the compressive strength is about 10 times higher then the tensile strength. So the graph for tension should be about 10 times smaller than the graph for compression, but the form of the graphs will be exactly the same as shown in figure 5.49.

5.2.5 Shear Behavior

The modeling of shear behavior is only necessary in the total strain fixed crack model where the shear stiffness is reduced after cracking according to

$$G^{cr} = \beta G \tag{1}$$

where β is the shear retention factor ($0 \leq \beta \leq 1$). For the total strain rotating crack model, β can be assumed to be 1.

5.2.6 Crack Bandwidth

For the total strain crack models, DIANA assumes a default value for the crack bandwidth h. The default value that DIANA assumes for solid elements is $\sqrt[3]{V}$ where V is the volume of the element.

5.2.7 Menegotto-Pinto Model

For embedded reinforcement DIANA offers 6 predefined material models:

- linear elasticity
- Von Mises plasticity for reinforcement yielding
- Menegotto-Pinto for cyclic loading
- Monti-Nuti for cyclic loading
- Dodd-Restreppo for cyclic loading
- Eurocode 2

For modeling the behavior of the reinforcement, the Menegotto-Pinto model is chosen. The Menegotto-Pinto is a special plasticity model for the cyclic behavior of steel and can be used for embedded reinforcement. The reason why this model is chosen is that Filippou et al. [SOURCE] has shown that this model works fine for modeling the hysteresis behavior of reinforcement in concrete.

5.2.8 Von Mises Plasticity Model

As mentioned before, the shaking table consists of plates. These plate are modeled with Von Mises plasticity model.

5.2.9 Secant Loading - Unloading

In DIANA the behavior of the material in loading and unloading is modeled with the secant approach. It is important to know that during cyclic loading the concrete is subjected to both tensile and compressive stresses which can results in cracking and crushing of the material. Figure 5.50 shows the secant loading-unloading of concrete.
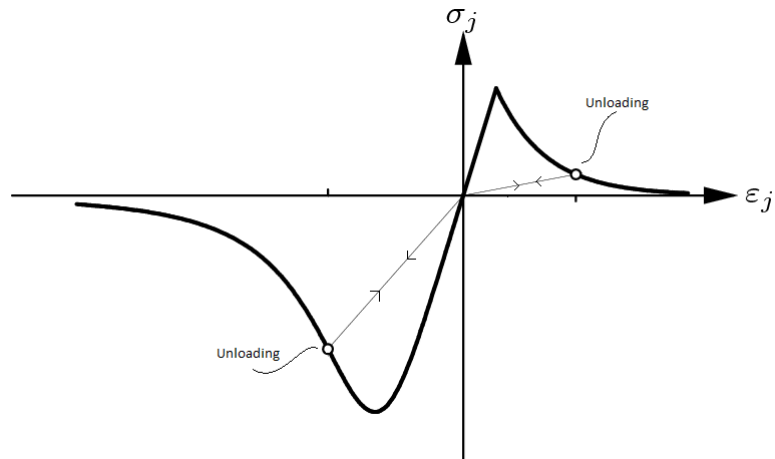
Figure 5.50: Secant loading-unloading.

5.3 Validation of the Material Models

The predictive power and the efficiency of a finite element model is mainly dependent on the accuracy of the material models. In the case of reinforced concrete structures, the material models which describe the behavior of concrete and reinforcement have to be checked in order to ensure reliability of the overall model. This can be done by performing some tests on a representative volume element (RVE). This RVE is a 3D 8-node cubic element with 1 m length in all sides (expect for the reinforced concrete element which has a different geometry). In the sections below, the tests will be described and the results will be given.

Table 5.1: Material tests.

Test	Material	Output Curves	Constitutive Behavior
C.1	Concrete	$\sigma - \epsilon$	Softening
C.2	Concrete	$\sigma - \epsilon$	Softening
C.3	Concrete	$\sigma - \epsilon$	Cyclic response
C.4	Concrete	Normalized σ - Normalized σ	Elastic domain
C.5	Concrete	Normalized σ - Normalized σ	Failure domain
S.1	Steel	$\sigma - \epsilon$ curve	Cyclic response
RC.1	Reinforced Concrete	$\sigma - \epsilon$	Cyclic response
RC.2	Reinforced Concrete	$\sigma - \epsilon$	Cyclic response
RC.3	Reinforced Concrete	M - ϕ	Cyclic response
RC.4	Reinforced Concrete	M - ϕ	Coupling response

The finite element model of the the cubic 8-node RVE looks as follows.
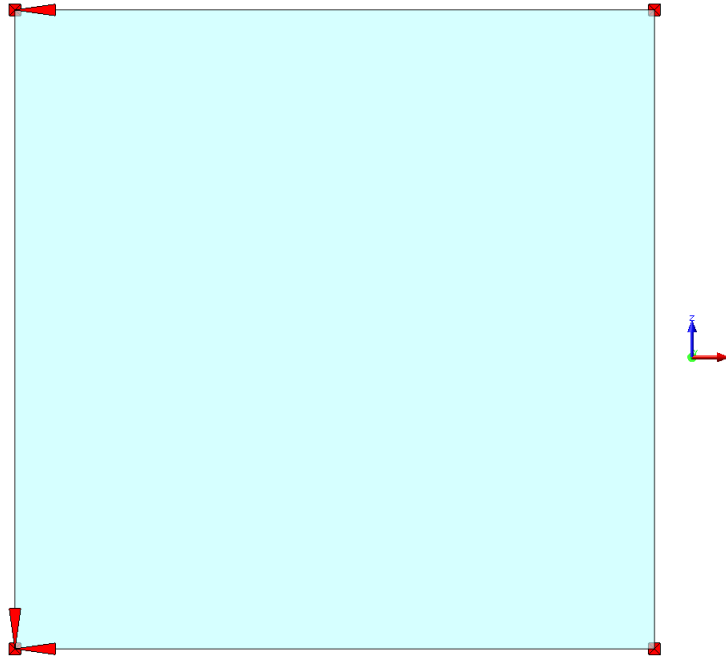
Figure 5.51: Front view.
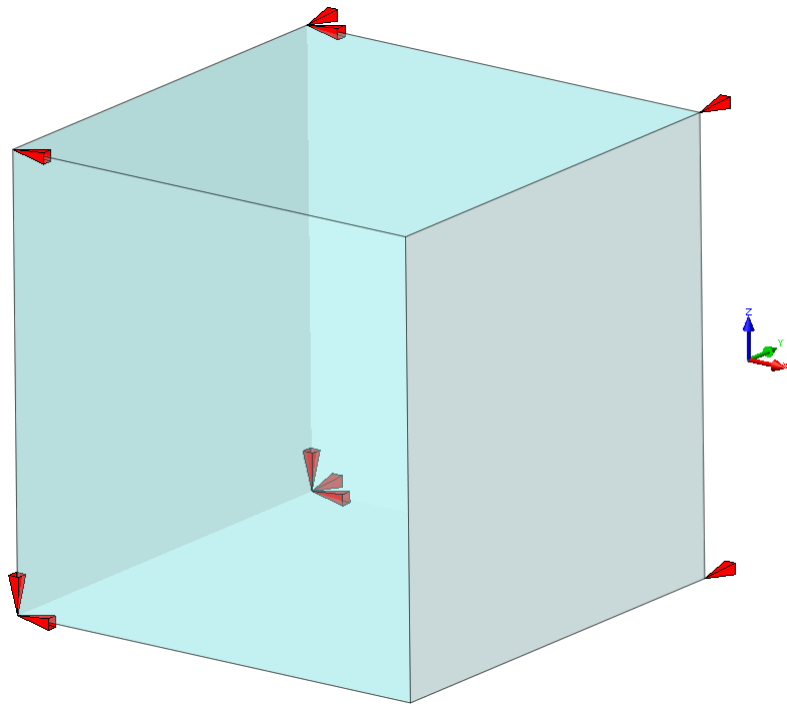
Figure 5.52: Cubic RVE.

The element from figure 5.52 is meant for tests C.1, C.2, C.3 and S.1. For tests RC.1, RC.2, RC.3 and RC.4 the following element is used.
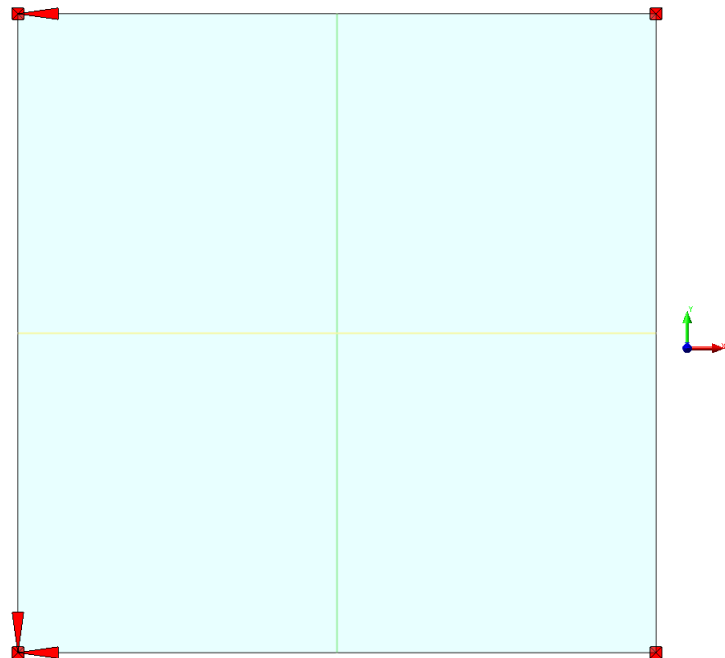
Figure 5.53: Front view.
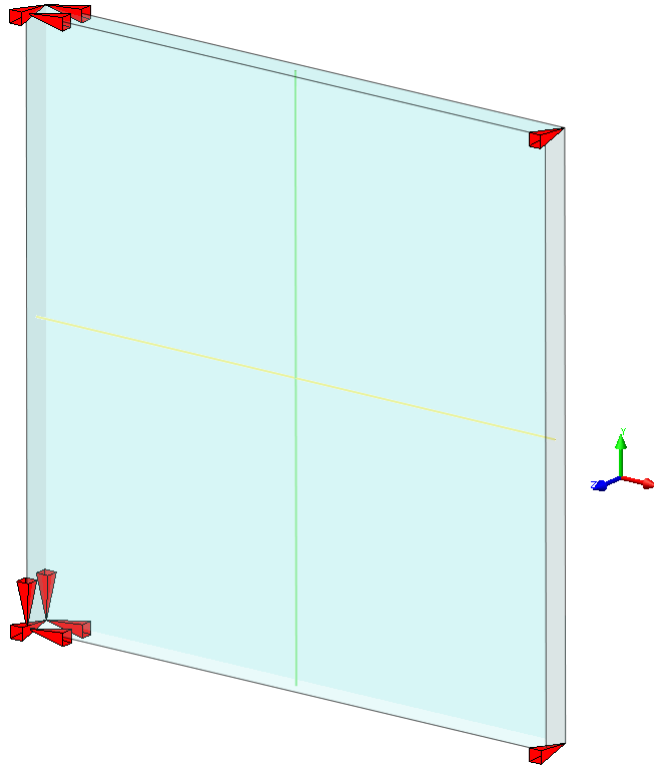
Figure 5.54: Reinforced concrete element.

The element from figure 5.54 has a height of 200 mm, a width of 200 mm and a thickness of 10 mm. Two reinforcement bars are used with a diameter of 8 mm, one in the horizontal direction and the other in the vertical direction.

The boundary conditions for the finite element models from figure 5.52 and 5.54 are chosen in such a way that the elements elongate/ shorten in x, y and z direction. This is done because of the Poisson effect.

The material parameters that is chosen for the finite element model of concrete are given in table 5.2.

Table 5.2: Material parameters for concrete.

Material	Concrete
Model	Total strain rotating crack
Young's modulus E [MPa]	32000
Tensile strength f_t [MPa]	2.4
Compressive strength f_c [MPa]	30
Fracture energy G_f^I [J/m^2]	270
Poisson's ratio [-]	0.2

The material parameters for the finite element models of reinforcement steel and the shaking table steel are given in tables 5.3 and 5.4.

Table 5.3: Material parameters for reinforcement steel.

Material	Reinforcement Steel
Model	Menegotto-Pinto
Young's modulus E [MPa]	210000
Yield stress f_y [MPa]	500
Poisson's ratio [-]	0.3

Table 5.4: Material parameters for the shaking table steel.

Material	Shaking table steel
Model	Von Mises plasticity
Young's modulus E [MPa]	210000
Yield stress f_y [MPa]	500
Poisson's ratio [-]	0.3

5.3.1 Test C.1 - Concrete

In test C.1 the concrete element is subjected to a uni-axial loading in tension. This tension load is applied on the cubic element by prescribing an incremental displacement with an increment of $0.001 \times 10^{-3} = 10^{-6}$ m, where 0.001 is the size of a load step. The prescribed displacement varies from 0 to 10^{-3} m. Figure 5.55 shows the set-up of test C.1.
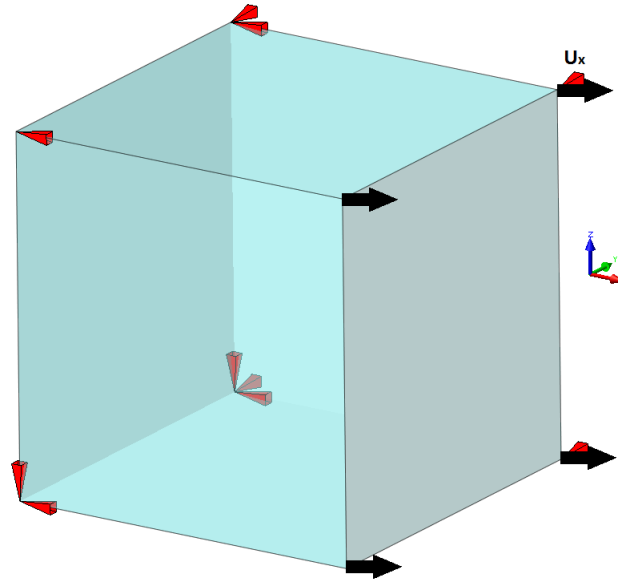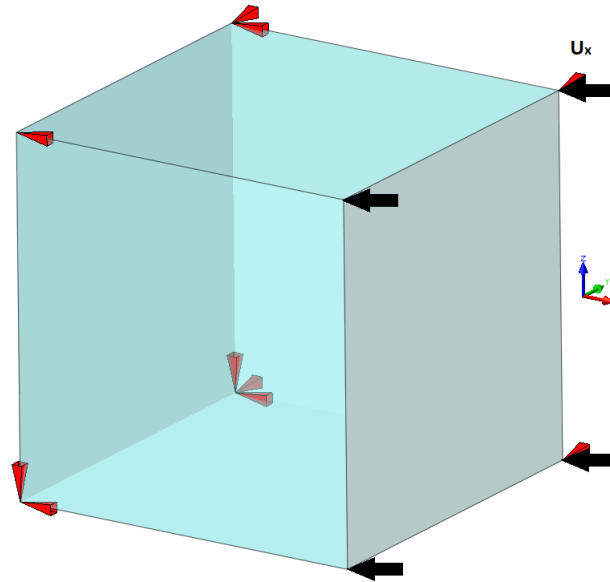

Figure 5.55: Test C.1.

The aim of this test is to investigate the tensile behavior of the RVE where the element elongates in x direction and contracts in z direction. A free displacement of the element is allowed in y direction.

Figure 5.56 shows the obtained stress - strain diagram for test C.1.
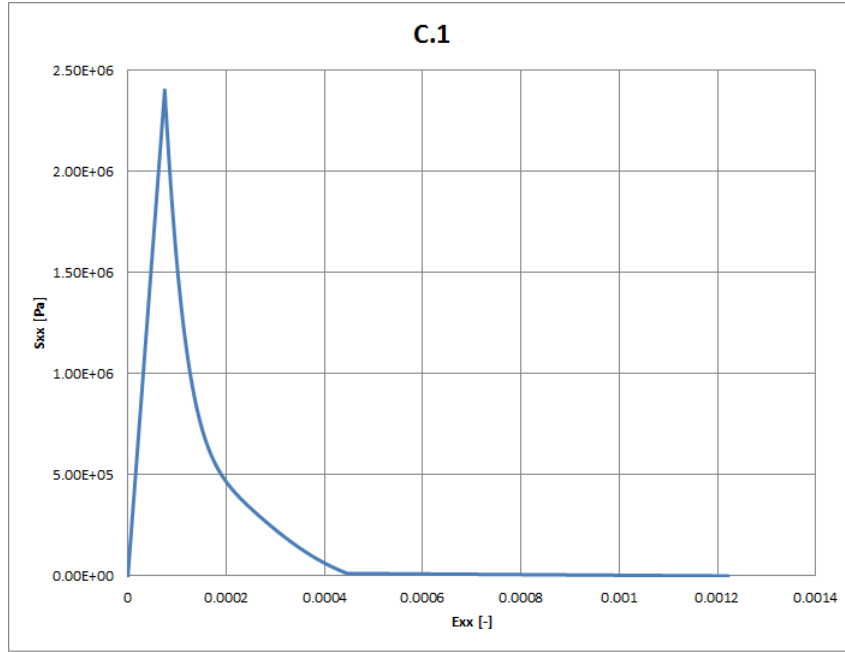
Figure 5.56: Stress-strain diagram test C.1.

Figure 5.56 shows that the maximum tensile stress of the concrete element is $2.4 \cdot 10^6$ Pa where the corresponding strain is $7.5 \cdot 10^{-5}$. This maximum stress of $2.4 \cdot 10^6$ Pa is the tensile strength f_t of concrete. The first part of the curve, with a stress range of $0 - 2.4 \cdot 10^6$ Pa, is linear. After the linear part, the concrete element begins to crack and then softens according to Hordijk which is not linear. This tension softening occurs when the tensile strength f_t of concrete is reached.

The Young's modulus E of concrete from table 5.2 can be checked from the graph by using the following equation.

$$E = \frac{\sigma}{\epsilon} = \frac{2.4 \cdot 10^6}{7.5 \cdot 10^{-5}} = 3.2 \cdot 10^{10} \text{ Pa} \tag{2}$$

The Young's modulus E calculated from the graph of figure 5.56 is $3.2 \cdot 10^{10}$ Pa, which corresponds exactly to the value of E from table 5.2. For fracture energy, a value of 270 J/m^2 was assigned to the concrete element. This value can be obtained by calculating the area A under the graph of figure 5.56 and then multiplying this value A with the crack bandwidth h according to the following equation:

$$G_f^I = h \times A = \sqrt[3]{V} \times A \tag{3}$$

The area under the graph of figure 5.56 has been calculated in Excel by using the Trapezoidal rule. The calculated area under the graph is approximately 275 Pa. The volume of the concrete element is 1 m^3. Multiplying 275 Pa with $\sqrt[3]{1}$ m gives 275 J/m^2, which is almost the same as the assigned value of 270 J/m^2 from table 5.2. The difference between the assigned value of 270 J/m^2 and the numerically obtained value of 275 J/m^2 is approximately 1.85 %.

It is also important to know how the concrete element is deformed, figure 5.57 shows this.

[UNIT] N , m
[DATA] Structural Nonlinear , EXX Nodes , Load Step 75(0.075)
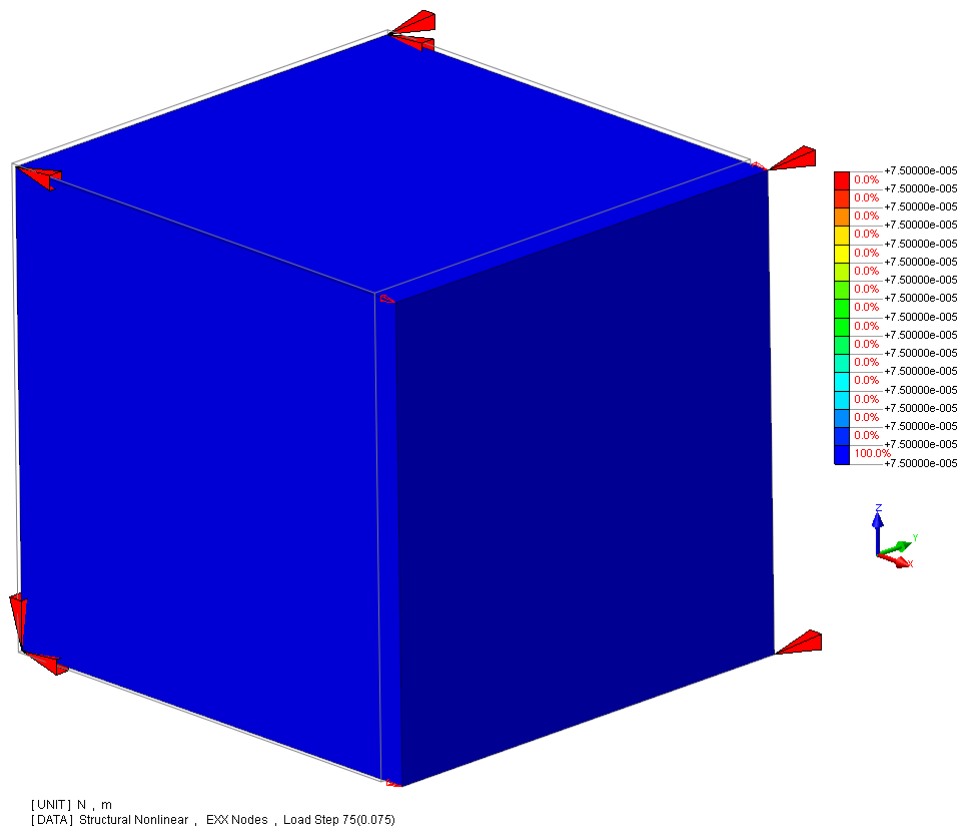
Figure 5.57: Strains in x direction.

In figure 5.57, the wire frame is the undeformed element and the blue contour plot is the deformed element. Figure 5.57 shows that the strains in the element are everywhere equal to $7.5 \cdot 10^{-5}$. The reason why the strains are the same everywhere in the element is that this cubic element is loaded uni-axially in x direction where the element is not damaged yet. Also the Poisson effect can be observed very nicely from figure 5.57.

5.3.2 Test C.2 - Concrete

In test C.2 the concrete element is subjected to a uni-axial loading in compression. This compression load is applied on the cubic element by prescribing an incremental displacement with an increment of $0.001 \times 10^{-3} = 10^{-6}$ m, where 0.001 is the size of a load step. The prescribed displacement varies from 0 to 10^{-3} m. Figure 5.58 shows the set-up of test C.2.

Figure 5.58: Test C.2.

The aim of this test is to investigate the compression behavior of this RVE where the element contracts in x direction and elongates in z direction. A free displacement of the element is allowed in y direction.

The found stress-strain diagram looks as follows.
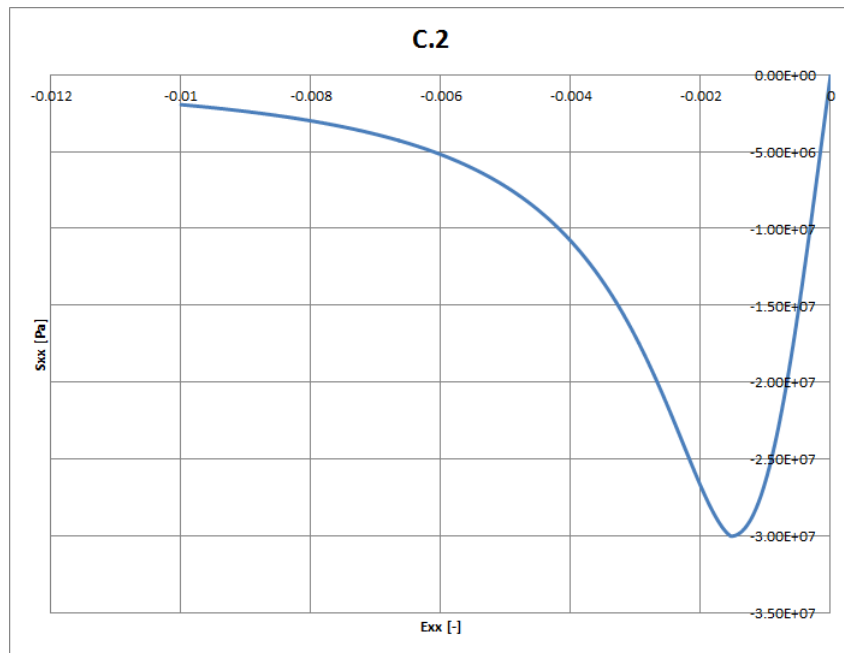
Figure 5.59: Stress-strain diagram C.2.

Figure 5.59 shows that the maximum compressive stress of concrete is $30 \cdot 10^6$ N/m^2 where the corresponding strain is 0.001525. This maximum stress is the compressive strength f_c of concrete.

The first part of the graph, with a stress range of 0 - $30 \cdot 10^7$ N/m^2, is not completely linear. It is linear until a certain point. From that point to the peak, where the compressive strength f_c will be reached, is not linear. After the compressive strength f_c of concrete has been reached, the concrete begins to crush and the curve decreases. This crushing phenomena is modeled with Thorenfeldt.

The strain distribution from figure 5.60 shows how the concrete is deformed when the element is loaded uni-axially in compression.

[UNIT] N , m
[DATA] Structural Nonlinear , EXX Nodes , Load Step 153(0.153)
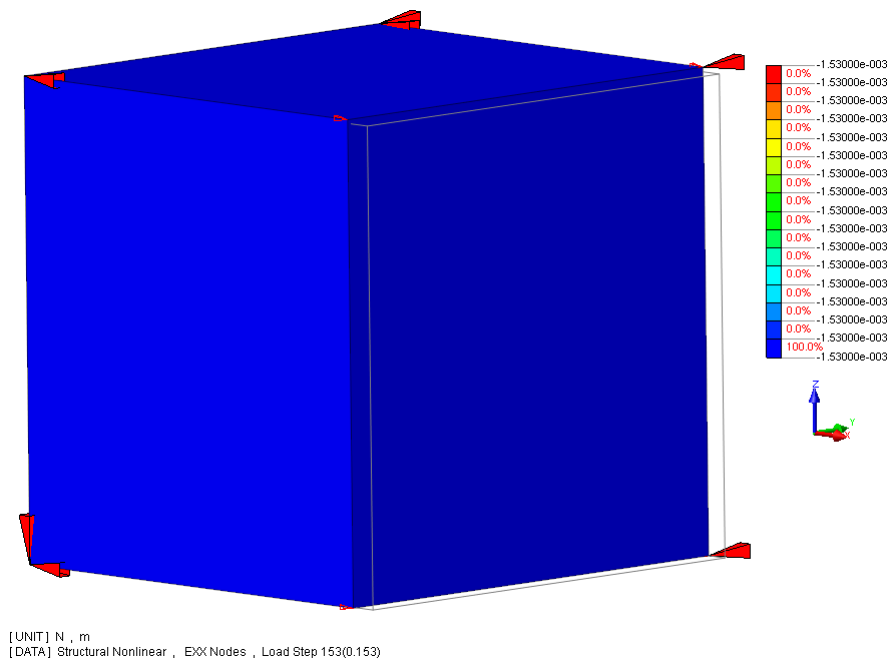
Figure 5.60: Strains in x direction.

Figure 5.60 shows that the strains in the concrete element are everywhere the same. The reason for this is that the cubic element is loaded uni-axially in compression where the element is not damaged yet.

Also the Poisson effect can be seen where the element contracts in x direction and elongates in z direction with a free movement in y direction.

5.3.3 Test C.3 - Concrete

In test C.3, the RVE is subjected to a uni-axial cyclic loading. The imposed displacements varies from 0 to $5 \cdot 10^{-4}$ m, from $5 \cdot 10^{-4}$ to 0 m, from 0 to $6 \cdot 10^{-4}$ m, from $6 \cdot 10^{-4}$ to $-8 \cdot 10^{-3}$ m and from $-8 \cdot 10^{-3}$ to 10^{-3} m. The concrete element is first loaded in tension and then in compression, this set-up is repeated according to the imposed displacements mentioned in the previous sentence. The set-up of the test is shown in figure 5.61.
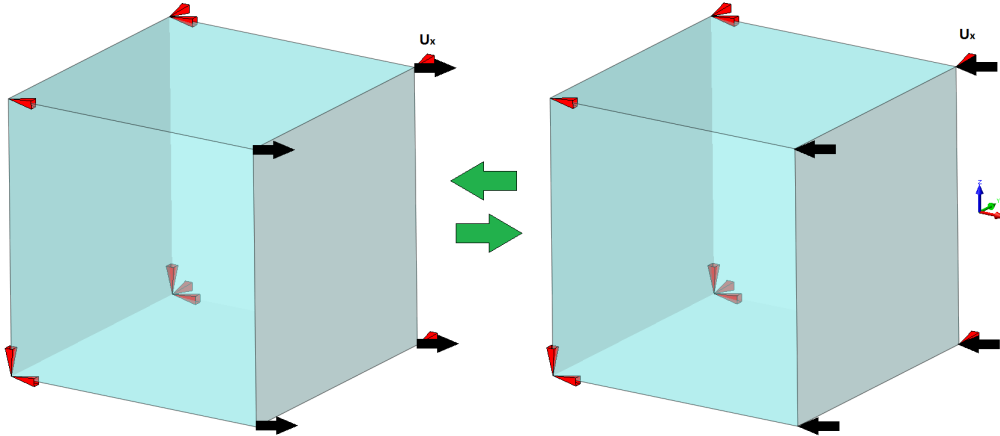
Figure 5.61: Test C.3.

The aim of this test is to investigate the tensile and compressive behavior of the concrete element under cyclic loading. Here the element first elongates in x direction and contracts in z direction and then the element contracts in x direction and elongates in z direction which is repeated a couple of times. A free displacement of the element is allowed in y direction.

The deformations of the RVE in this test is a combination of the deformations from test C.1 and test C.2. The found stress-strain diagram is as follows.
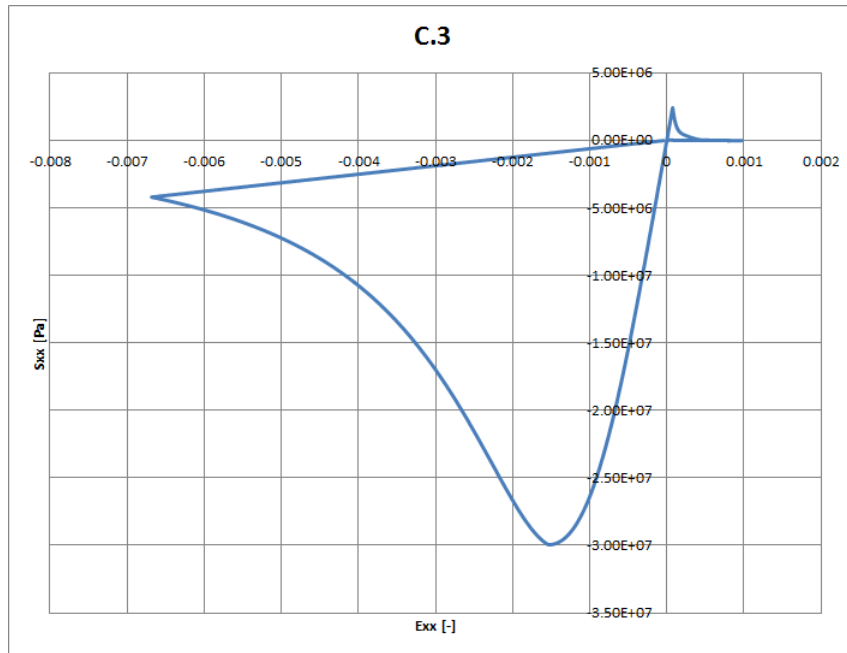
Figure 5.62: Stress-strain diagram C.3.

Figure 5.62 shows the Hordijk tension softening and Thorenfeldt compression crushing of the concrete element very well. Figure 5.62 also shows that the transition from the tension zone to the compression zone takes place via the secant loading-unloading approach. Further can be seen that the concrete has a tensile strength f_t of $2.4 \cdot 10^6$ N/m^2 and a compressive strength f_c of $3.0 \cdot 10^7$ N/m^2. Here can also be seen that the compressive strength f_c of concrete is about 10 times higher than the tensile strength f_t.

Lets zoom in at the origin of the graph of figure 5.61 to see what exactly happens there.
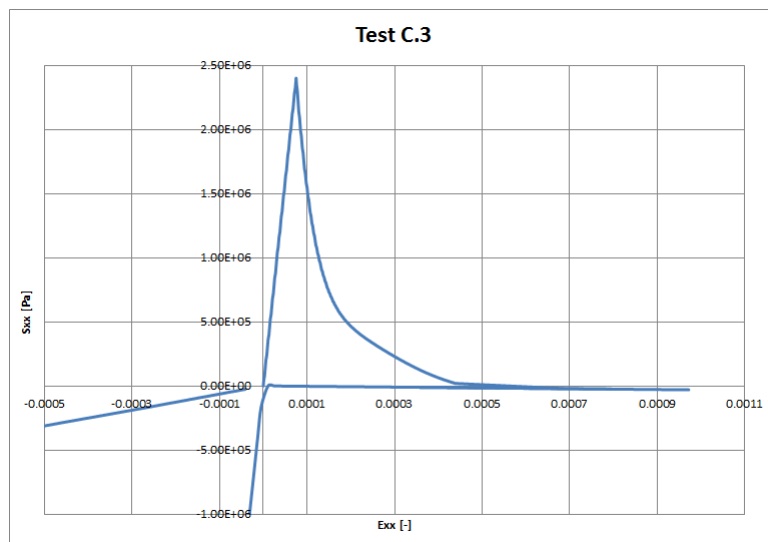
Figure 5.63: Stress-strain diagram C.3.
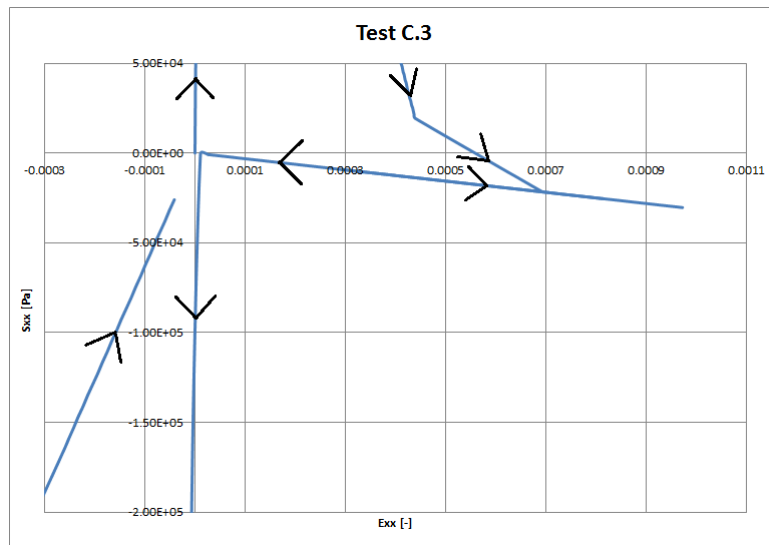
Figure 5.64: Stress-strain diagram C.3 with directions.
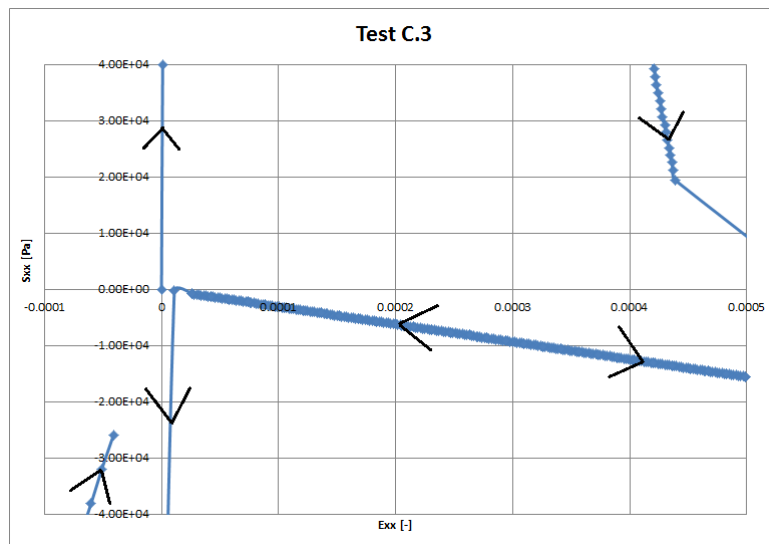
Figure 5.65: Stress-strain diagram C.3 with directions.

Figure 5.64 shows the direction of how the graph proceeds and figure 5.65 gives another representation of the graph to see clearly how the graph proceeds by showing all points where the graph consists of.

Figures 5.63, 5.64 and 5.65 show that the secant approach in not completely respected because the transition from the tension zone to the compression zone doesn't start from the origin of the graph (zero) and the graph does not end at the origin of the graph (zero) from the compression zone. A possible reason for this is that this graph has been calculated numerically and numerical procedures have a certain accuracy. This accuracy is related to the *convergence criteria* that is used in DIANA. By making the convergence criteria more strict the loading and unloading will go more towards the origin. But the overall cyclic behavior is calculated nicely that is shown in figure 5.62.

5.3.4 Test C.4 & C.5 - Concrete

In test C.4 the elastic capacity of concrete will be investigated. Here, the elasticity surface will be given in terms of normalized stresses with respect to the compressive strength.

In test C.5 the plastic capacity of concrete will be investigated. Here, the failure surface will be given in terms of normalized stresses with respect to the compressive strength.

The elasticity surface and failure surface with respect to the compressive strength look as follows.
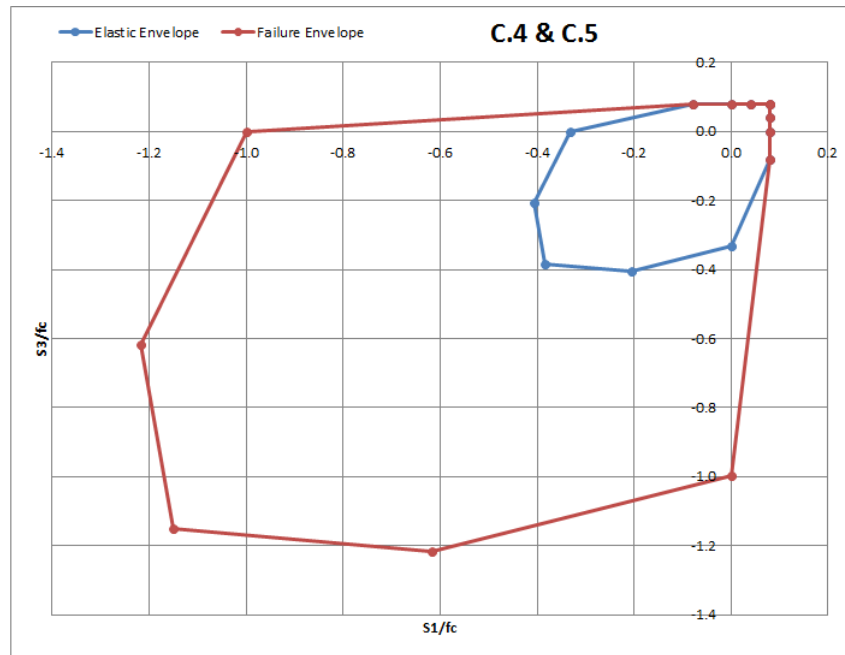
Figure 5.66: Elasticity and failure surface.

5.3.5 Test S.1 - Steel

In this test, the cubic element made of steel is subjected to a cyclic loading. The imposed displacements vary from 0 to 10^{-2} m, from 10^{-2} to -10^{-2} m and from -10^{-2} to 0 m. The set-up of test S.1 is shown in figure 5.67.
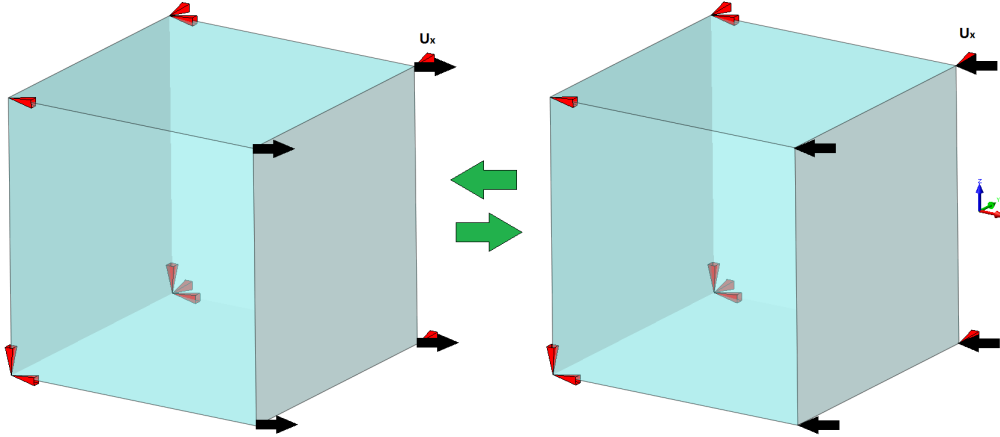
Figure 5.67: Test S.1.

As mentioned before, the Von Mises plasticity model has been chosen to model the behavior of the plates of the shaking table. The same RVE as in test C.1 and C.2 has been used to investigate the behavior of the Von Mises plasticity material model when the material model is subjected to cyclic loading.

The found stress-strain diagram for Von Mises plasticity is.
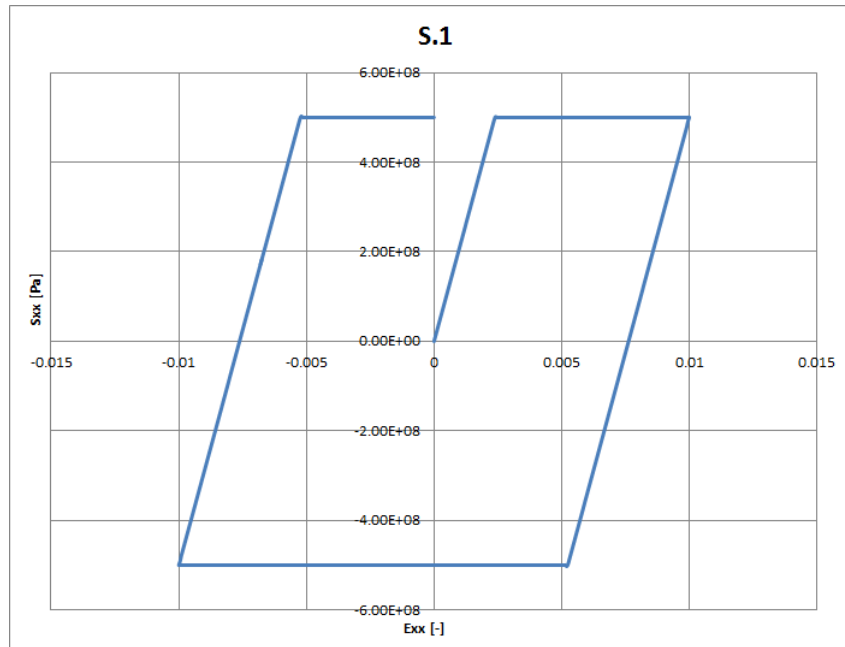
Figure 5.68: Stress-strain diagram.

Figure 5.68 shows the strain hardening of steel where the element is subjected to cyclic

loading. The yield stress of the steel element is 500 MPa.

5.3.6 Test RC.1 - Reinforced Concrete

In this test, the reinforced concrete element is loaded to a cyclic loading. The imposed displacements vary from 0 to $1.5 \cdot 10^{-3}$ m, from $1.5 \cdot 10^{-3}$ to $-4 \cdot 10^{-3}$ m and from $-4 \cdot 10^{-3}$ to 0 m. The figure below shows the set-up of test RC.1.
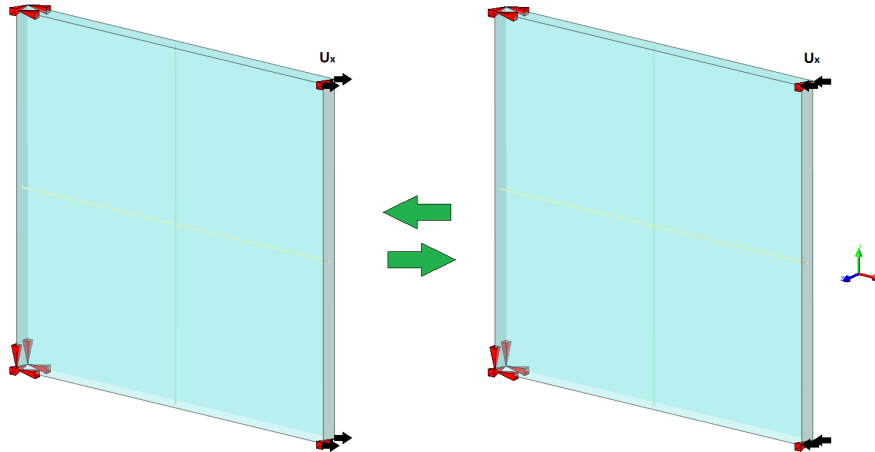
Figure 5.69: Test RC.1.

The found stress-strain diagram for concrete is.
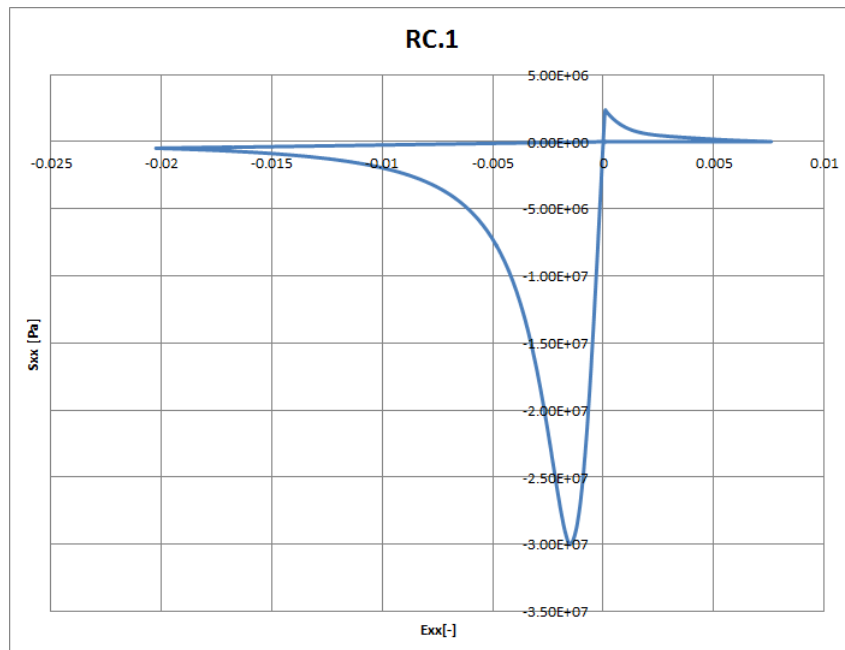
Figure 5.70: Stress-strain diagram RC.1.

In the stress-strain can be seen that the reinforced concrete element is loaded in tension first, then unloaded to zero. After that, loaded in compression and again unloaded until the strains are zero.

Also the behavior of embedded reinforcement when subjected to cyclic loading has been

analyzed here. In order to analyze the behavior of the Menegotto-Pinto model, it is important to know that this model can only be analyzed when there is a mother element around the embedded reinforcement.

The found stress-strain diagram for the embedded reinforcement subjected to cyclic loading looks as follows.
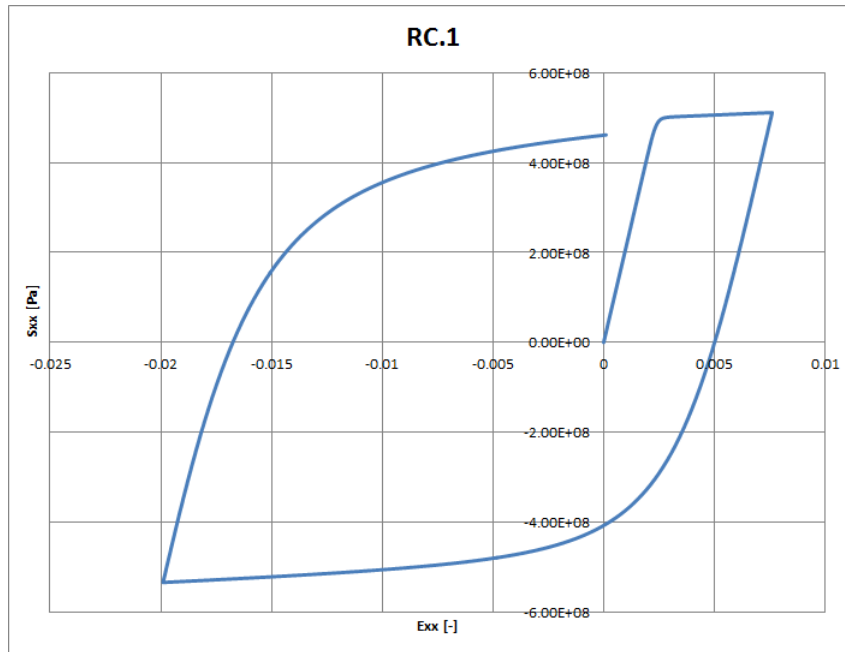
Figure 5.71: Stress-strain diagram.

In figure 5.71, the Bauschinger effect can be seen clearly. The Bauschinger effect is the effect where a plastic deformation in one direction affects the subsequent plastic response in the other direction. For example, a material which is loaded in tension first and then in compression will show a reduction in compressive strength and vice versa. In figure 5.71 can be seen that the yield stress is equal to 500 MPa.

5.3.7 Test RC.2 - Reinforced Concrete

In this test, the element is loaded cyclically with shear forces. The shear forces vary from 0 to $6 \cdot 10^3$ N, from $6 \cdot 10^3$ to $-6 \cdot 10^3$ N and from $-6 \cdot 10^3$ to 0 N. These shear forces has been applied as pressure loads on the element. To get the pressure load in N/m^2, the shear forces has been divided by the area of the element where the shear forces are applied. The pressure load is calculated as follows:

$$\frac{6 \cdot 10^3}{0.01 \cdot 0.2} = 30 \cdot 10^6 \tag{4}$$

Figure 5.72 shows the reinforced concrete element loaded by shear pressure.
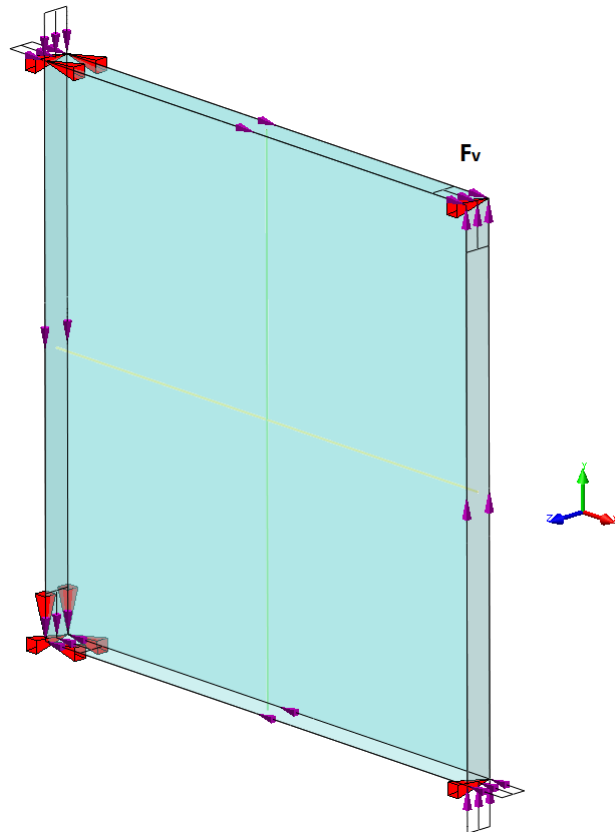
Figure 5.72: Test RC.2.

The found shear stress- shear strain diagram looks as follows.
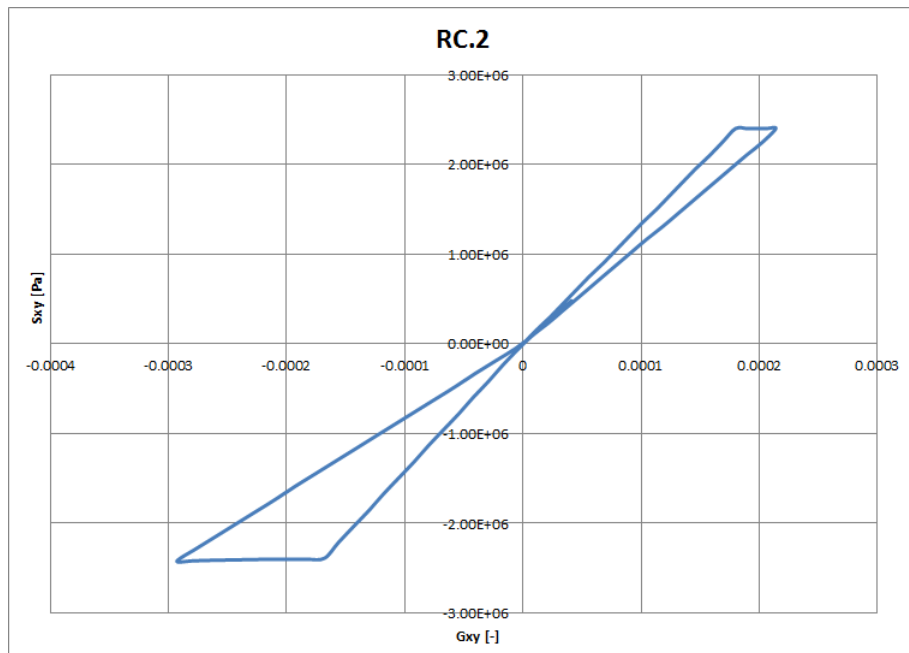
Figure 5.73: Stress-strain diagram RC.2.

5.3.8 Test RC.3 - Reinforced Concrete

In this test, the element is uni-axially loaded in bending. The imposed rotation varies from 0 to $1.5 \cdot 10^{-3}$ rad, from $1.5 \cdot 10^{-3}$ to $-1.5 \cdot 10^{-3}$ rad and from $-1.5 \cdot 10^{-3}$ to 0 rad. For this test, the rotation is applied in terms of displacements in the nodes of the element. The maximum displacement in m in x direction has been calculated using the provided maximum rotation as follows:

$$\frac{0.01 \cdot 0.0015}{2} = 7.5 \cdot 10^{-6} \tag{5}$$

Figure 5.74 shows how the element is loaded in bending.
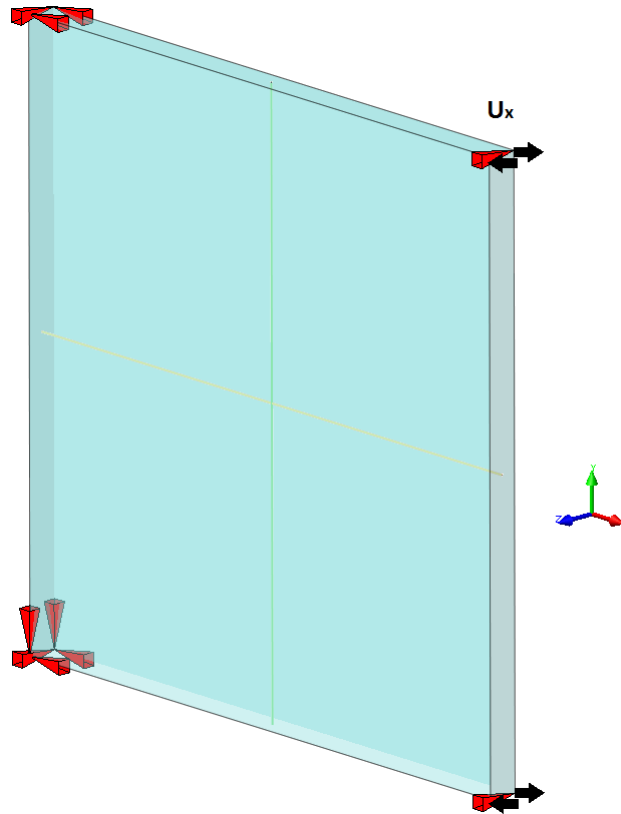
Figure 5.74: Test RC.3.

The aim of this test is to analyze the behavior of the element that is subjected to bending. The found moment-rotation curve looks as follows.
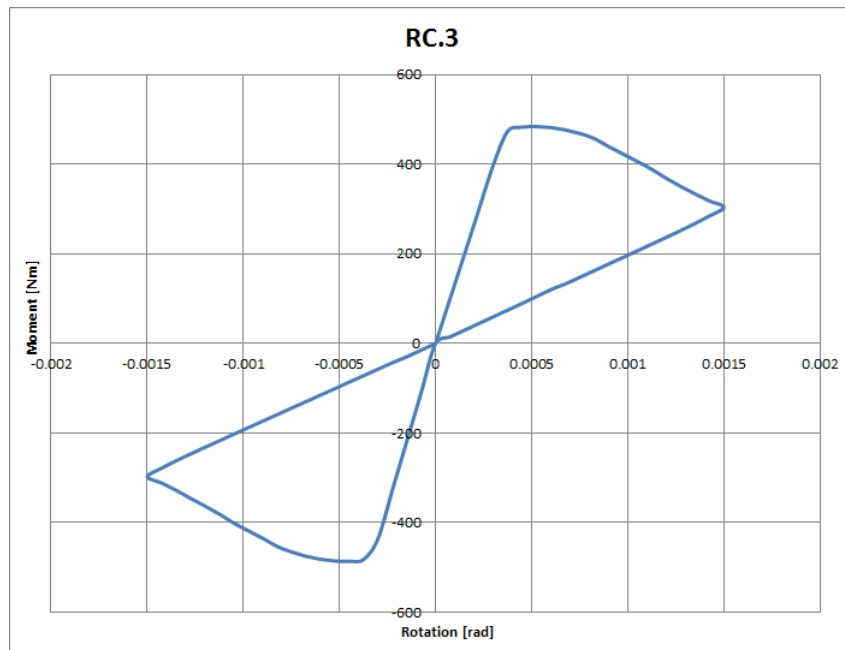
Figure 5.75: Moment-rotation curve RC.3.

5.3.9 Test RC.4 - Reinforced Concrete

In this test, the element is first loaded in tension and then loaded cyclically in bending. The maximum displacement is 10^{-4} m where the maximum rotation is $1.5 \cdot 10^{-3}$ rad. The rotation is applied as displacements on the node of the element. Figure 5.76 shows that the element is loaded in tension first and then in bending.
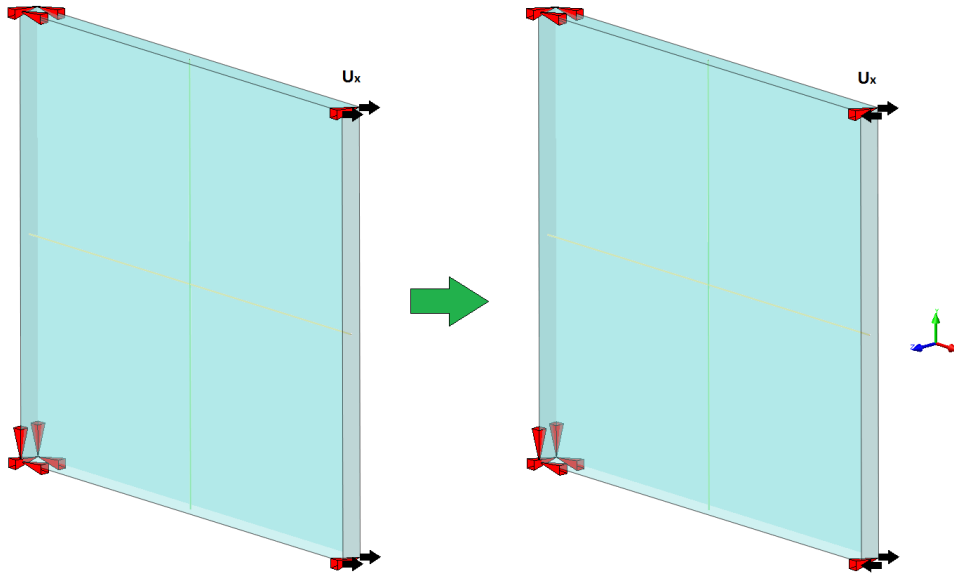
Figure 5.76: Test RC.4.

The aim of this test is to show that the bending moment capacity of the element from this test is smaller than the bending moment capacity of the element from test RC.3 because the element in test RC.4 is elongated before it is loaded to cyclic bending.
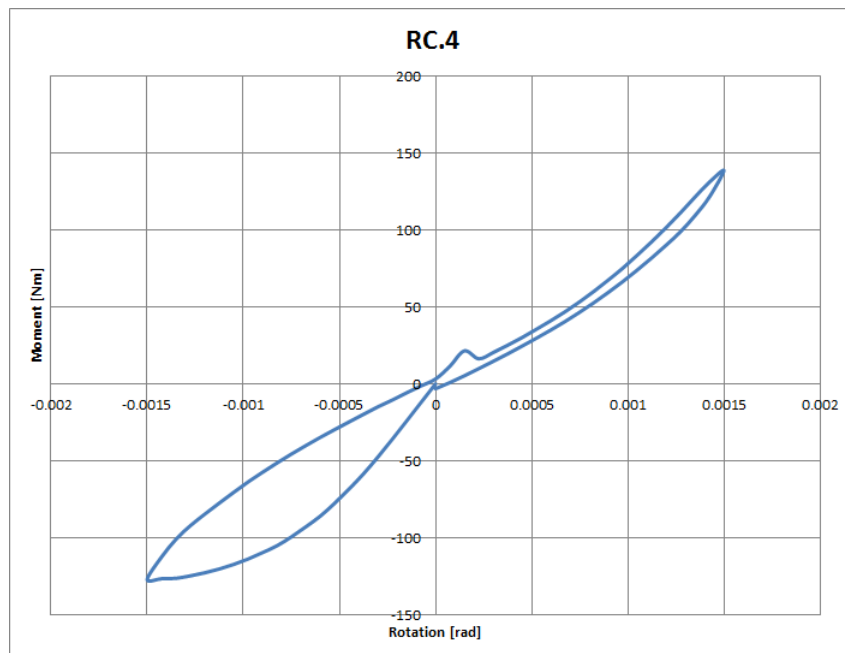
Figure 5.77: Moment-rotation curve RC.4.

Figure 5.77 shows that the bending moment capacity of the element from this test is smaller in comparison with the bending capacity from the element of test RC.3. The reason for this is that the bending moment capacity is reduced due to the initial elongation of the element before the element was loaded in bending.

5.4   Summary Stage 1

In stage 1 of this thesis the finite element model is developed. This finite element model consists of the model of concrete, reinforcement, additional masses and the shaking table.

The concrete is modeled with solid elements. The reason why concrete is modeled with solid elements is because it is chosen to mimic the real concrete mock-up from the laboratory as good as possible. In order to mimic the dynamic behavior of the real concrete mock-up as good as possible, accurate results from the finite element analyses are necessary and with solid elements it is possible to get accurate results from the finite element analyses.

The reinforcement is modeled with embedded reinforcement. In the real mock-up reinforcement bars are used and to mimic the reality as good as possible it is chosen to model the reinforcement with embedded reinforcement. It is also interesting to know that in finite element analysis embedded reinforcement add only stiffness to the finite element model. These embedded reinforcement are embedded in the elements in which they are located and do not allow relative slip

Distributed translational mass elements are used to model the additional masses on each floor. These elements add mass to the finite element model without influencing the stiffness of the model. These elements are only active when performing a dynamic analysis.

The shaking table in the laboratory consists of plates and these plates are modeled with curved shell elements. It is chosen to model this shaking table in order to simulate the real mock-up + shaking table system as good as possible. In stage 2 it will be shown that it is important to model the shaking when performing eigenvalue analyses to calibrate the finite element model.

After developing the finite element model, material models are assigned to concrete, reinforcement and the shaking table plates. These material models describe the behavior of these materials. The total strain rotating crack model, with Hordijk softening and Thorenfeldt crushing, is chosen to model the behavior of concrete. The Menegotto-Pinto model describes the cyclic behavior of the reinforcement and the Von Mises plasticity model describes the behavior of the shaking table plates. In the past, the just mentioned material models have shown that they are suitable to model the nonlinear behavior of concrete and steel when subjected to cyclic loading like earthquakes.

After choosing the material models, one-element tests are performed in order to validate these material models. The results of these validations look good and can be found at the end of this stage.

The first two research questions of this thesis are hereby answered. These research questions are treated more in detail in the previous sections of this stage.

6 Stage 2 - Linear Response of the Model

Stage 2 of this master thesis is focused on the calibration of the finite element model based on linear structural behavior of the mock-up. The calibration of the finite element model is very important because in order to make reliable predictions about the dynamic behavior of the mock-up it is essential to calibrate the finite element model with the mock-up. For the calibration of the finite element model, *eigenvalue analyses* are performed. The numerical results of the eigenvalue analyses are compared with the provided experimental results of the eigenvalue analyses by the SMART 2013 benchmark committee. For a sufficient calibration of the finite element model it is important that the numerical results are as close as possible to the experimental results.

After the eigenvalue analyses, *linear transient analyses* are performed to see how the dynamic behavior of the model is and how good the predictions of the finite element model are for the dynamic behavior of the mock-up. Besides eigenvalue analyses and linear transient analyses, *response spectrum analyses* are performed.

6.1 Seismic Analysis

Earthquakes typically produce broadband random ground motion in three dimensions. The motions are characterized by simultaneous but statistically independent horizontal and vertical components. The strong motion portion of severe earthquakes may be from 10 to 15 seconds duration and the total duration considerably longer. Earthquake motion has potentially damaging effects over a wide range of frequencies.

The response of a structure depends on the nature of the ground motion and the dynamic characteristics of the structure. The ground motion may be amplified or attenuated. The alternation (amplification or attenuation) depends on the natural frequency and damping of the system. The broadband characteristics of response spectra that describe earthquake ground motion imply that multi-frequency excitation is likely to occur.

For equipment mounted on building structures, the ground motion will be filtered by the intervening structure resulting in amplified or attenuated narrowband motion at the location the equipment is mounted. The accelerations experienced by the equipment will be the result of further amplification or attenuation of the in-structure motion. Whether the in-structure motion is amplified or attenuated will depend on the natural frequencies and damping of the equipment. The narrowband motion, due to filtering within building structures, implies single frequency excitation of the equipment may dominate the equipment response.

The seismic response of structures will also depend on the nature of the foundation system, the foundation soils contributing to the stiffness and damping of the structural system.

All the above effects should be considered when planning, executing and reporting a finite element seismic analysis.

6.1.1 Seismic Input

The reinforced concrete mock-up is subjected to several seismic excitation's. These seismic excitation's are provided in terms of prescribed displacements and prescribed accelerations. In this thesis, the prescribe displacements are used to perform the linear and non-linear transient analyses. The seismic excitation's are called RUNs and they are given in table 6.1. This table contains the PGA of each RUN for x-, y- and z-direction.

Table 6.1: Input ground motions - seismic sequences.

RUN	PGA x [g]	PGA y [g]	PGA z [g]	Type
6	0.09	0.10	0.05	White noise (synthetic)
7	0.15	0.20	0.09	Design signal (scaled)
9	0.25	0.35	0.18	Design signal (real)
11	0.22	0.18	0.09	Northridge earthquake (scaled)
13	0.42	0.32	0.24	Northridge earthquake (scaled)
17	0.63	0.44	0.41	Northridge earthquake (scaled)
19	1.11	1.03	0.49	Northridge earthquake (real)
21	0.15	0.20	0.09	Northridge after shock (scaled)
23	0.65	0.46	0.25	Northridge after shock (real)

From these 9 RUNs, the first 2 RUNs are used for the linear transient analysis. The remaining 7 RUNs are used for the non-linear transient analysis. It is also interesting to see how the RUNs look like. Appendix A shows the graphs of each RUN.

Please note that the graphs of the RUNs are prescribed displacements and table 6.1 shows the PGA of each RUN in g (1 g = 9.81 m/s^2).

6.1.2 Instrumentation Plan

During the SMART 2013 experimental campaign the response (displacements and accelerations) of the mock-up, due to seismic excitation's, is measured in several points. These points are shown in figure 6.1.
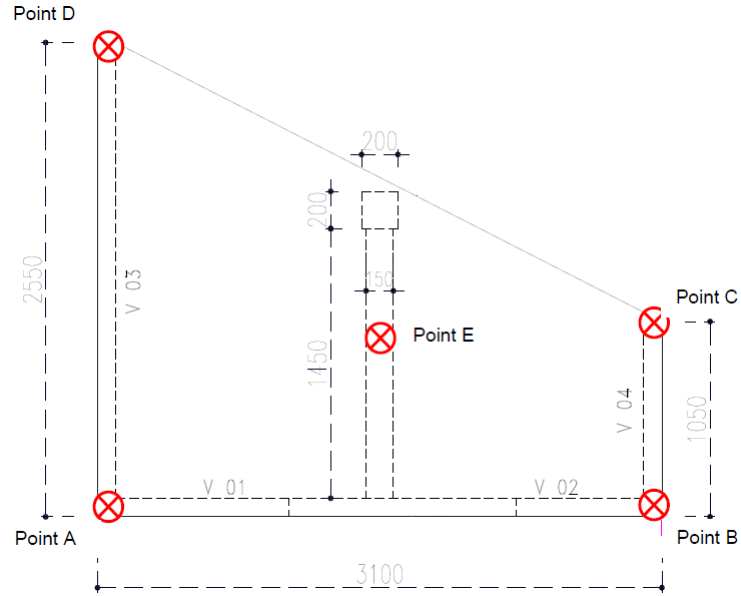
Figure 6.1: Positions of the points for an arbitrary floor - dimensions in mm.

The coordinates of these points with respect to the defined coordinate system are given in table 6.2.

Table 6.2: Coordinates of the points related to the mock-up - (x,y) plane.

Point	x [m]	y [m]
A	0	0
B	3	0
C	3	1
D	0	2.5
E	1.5	0.73

Four different levels are defined according to the vertical position of the points. These levels are given in table 6.3

Table 6.3: Altitude of each floor.

Floor	z [m]
0	0
1	1.2
2	2.4
3	3.6

It is important to mention that these points are located at the top of each floor and floor 0 is the top of the foundation. Also the response of the finite element model will be calculated in points A, B, C, D and E.

6.2 Eigenvalue Analysis

In this section the numerical and the provided experimental results of the eigenvalue analysis of respectively the model and the mock-up are presented. The eigenvalue analysis is performed in order to see what the *natural frequencies* and the corresponding *mode shapes* of the finite element model are. After obtaining the numerical natural frequencies and the corresponding mode shapes, these results are compared with the provided experimental results of the eigenvalue analysis for the calibration of the finite element model. The eigenvalue analysis is performed for the following three cases:

1. the mock-up is fixed at the lower face of the foundation and is not loaded with additional masses,
2. the mock-up is fixed at the lower face of the foundation and is loaded with additional masses,
3. the mock-up is linked to the shaking table and is loaded with additional masses.

It is important to mention that only the first three modes are considered. The reason why only the first three modes are considered, is that these modes are *global modes* which describe the global behavior of the model. The higher modes will be *local modes* which are not interesting in this case.

6.2.1 Case 1

The first mode shape of the model for case 1 looks as follows.
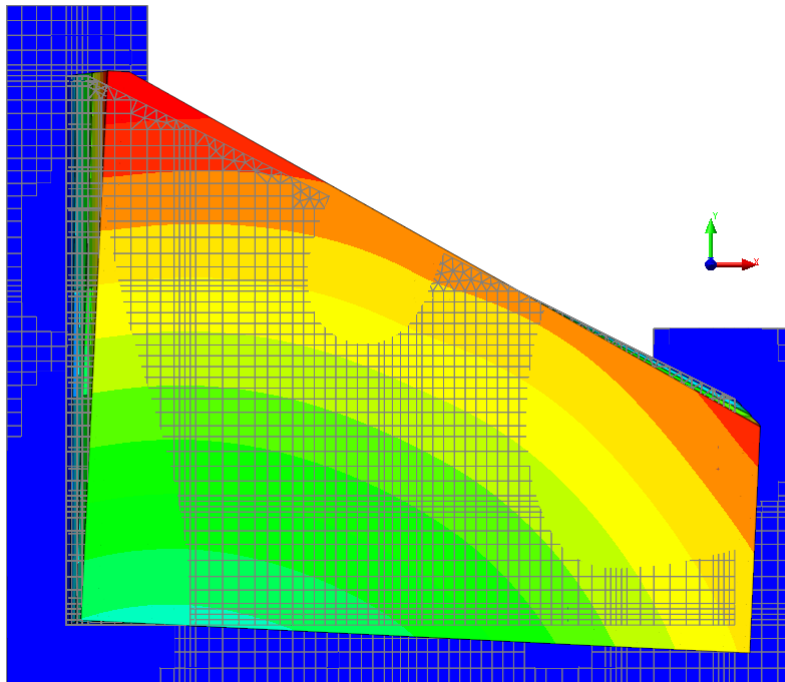
Figure 6.2: Mode shape 1 - top view.
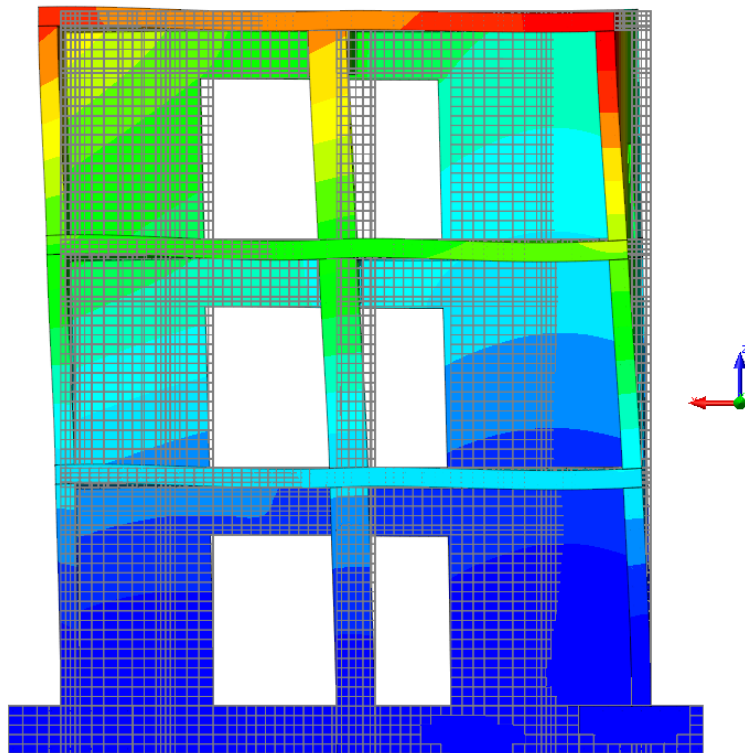
Figure 6.3: Mode shape 1 - front view.
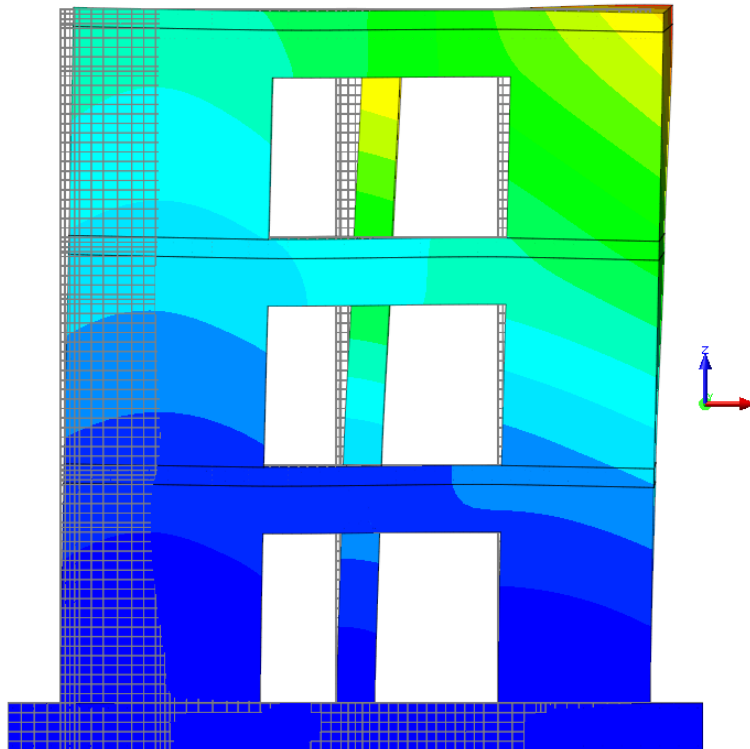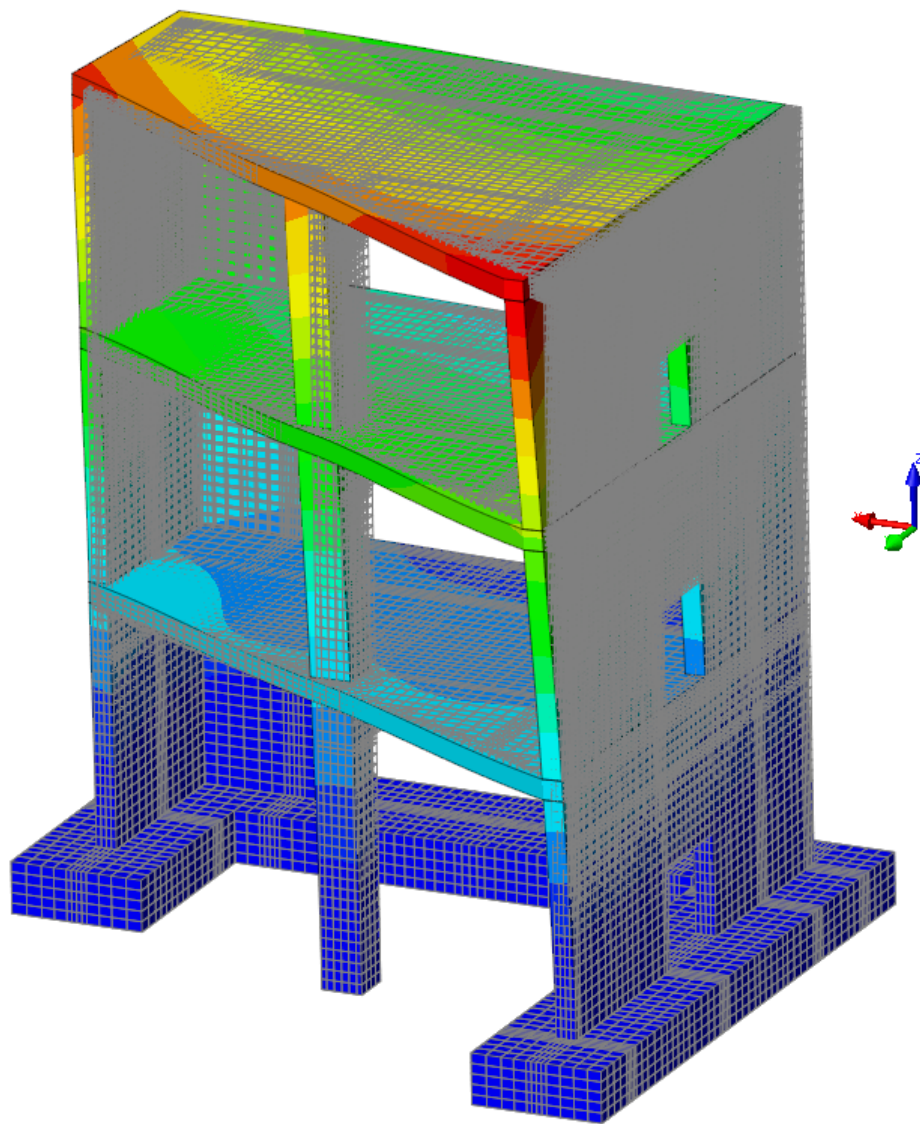

Figure 6.4: Mode shape 1 - rear view.

79
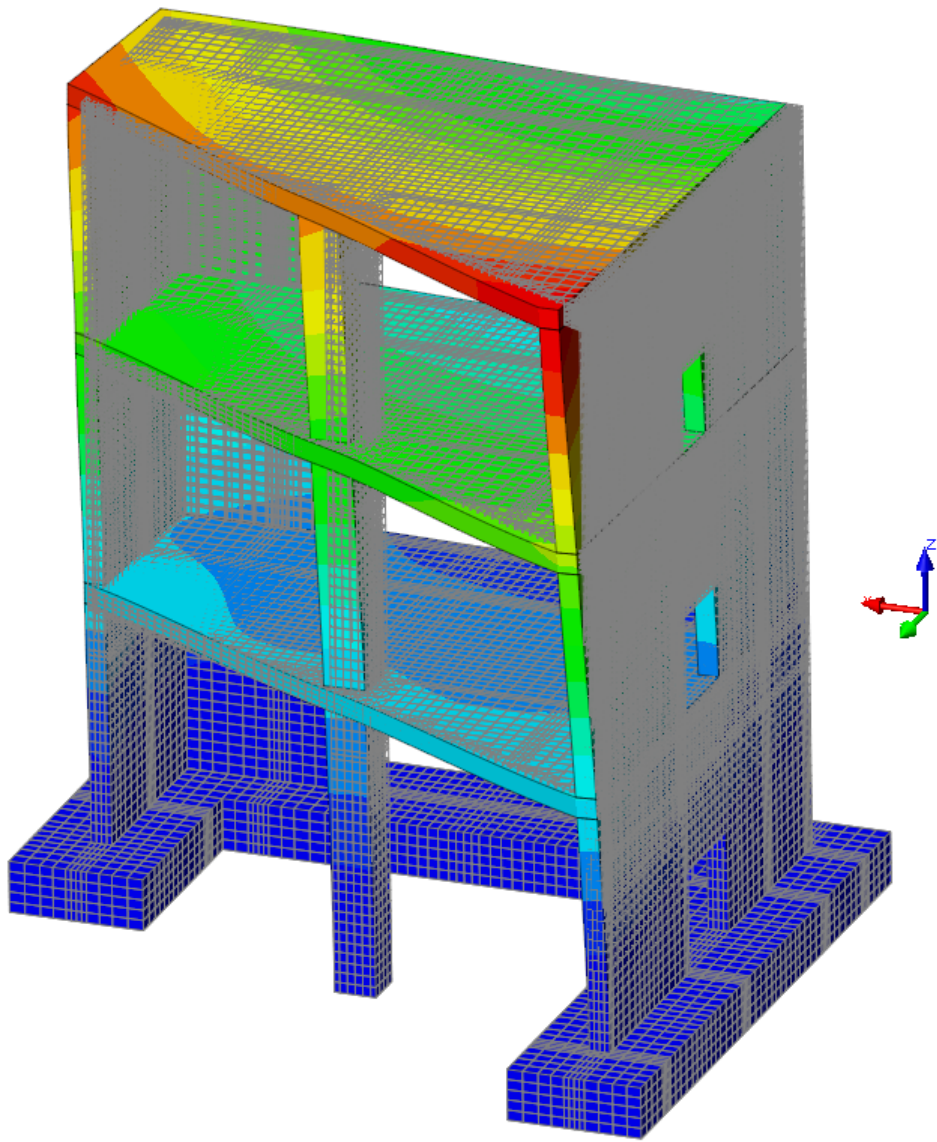
Figure 6.5: Mode shape 1.

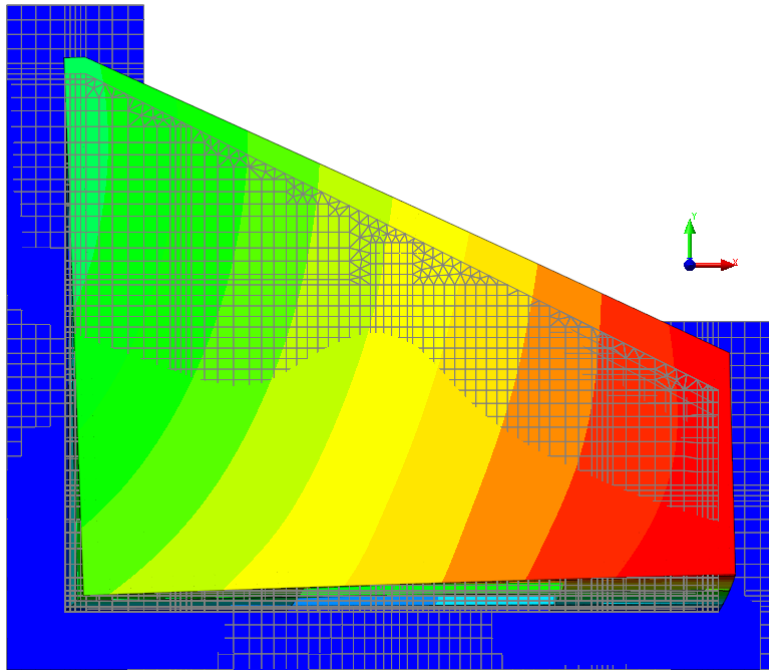The second mode shape of the model for case 1 looks as follows.
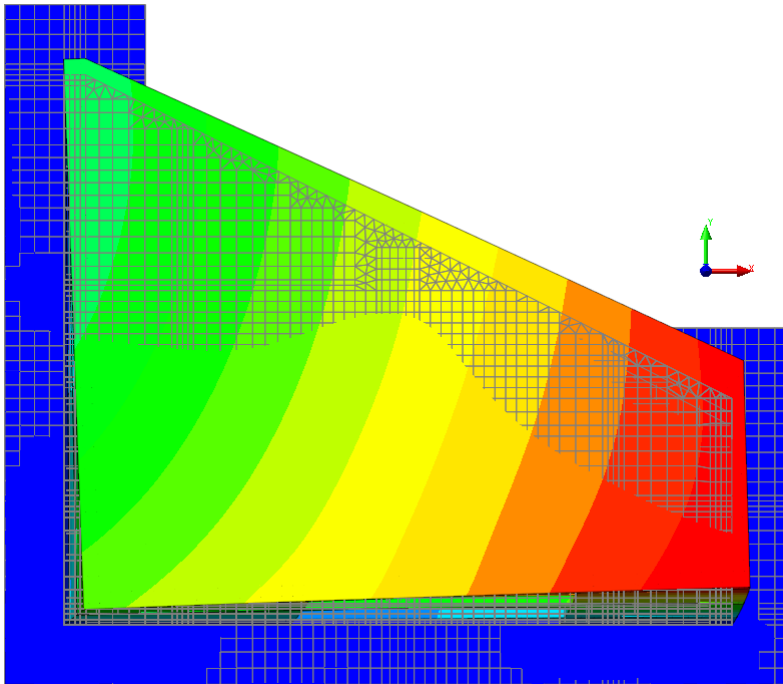
Figure 6.6: Mode shape 2 - top view.
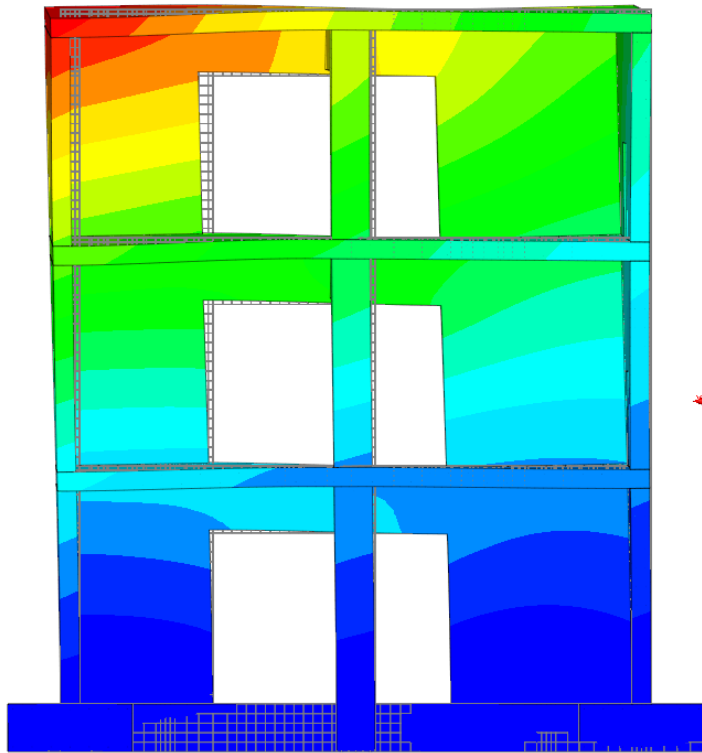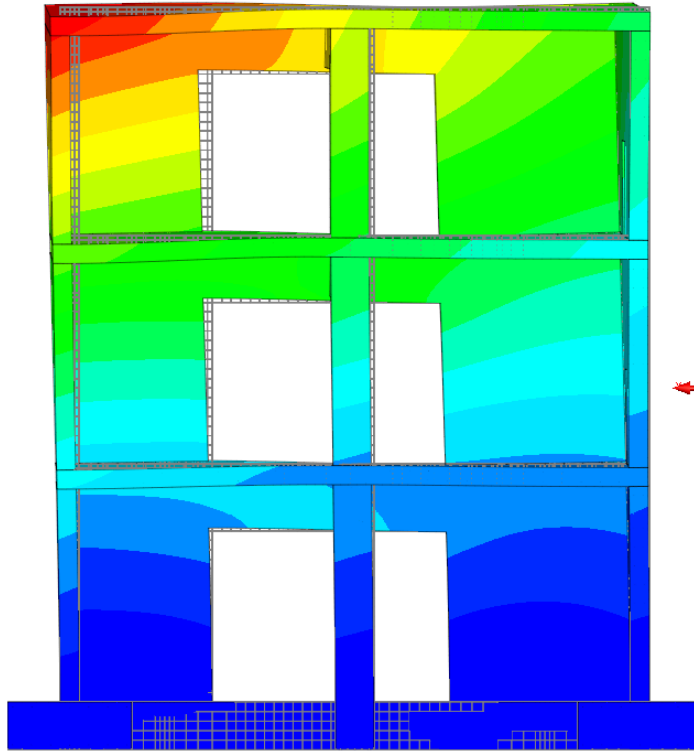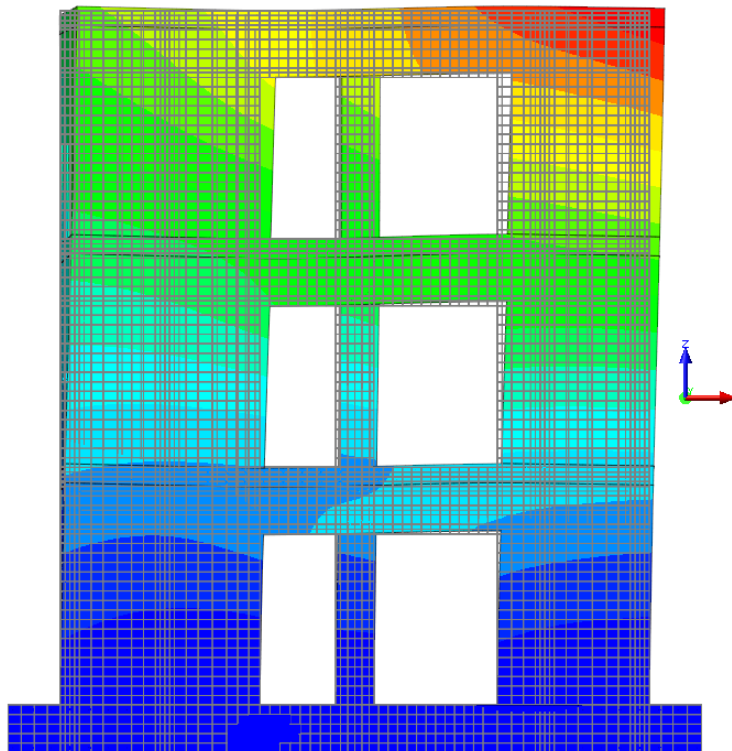
Figure 6.7: Mode shape 2 - front view.
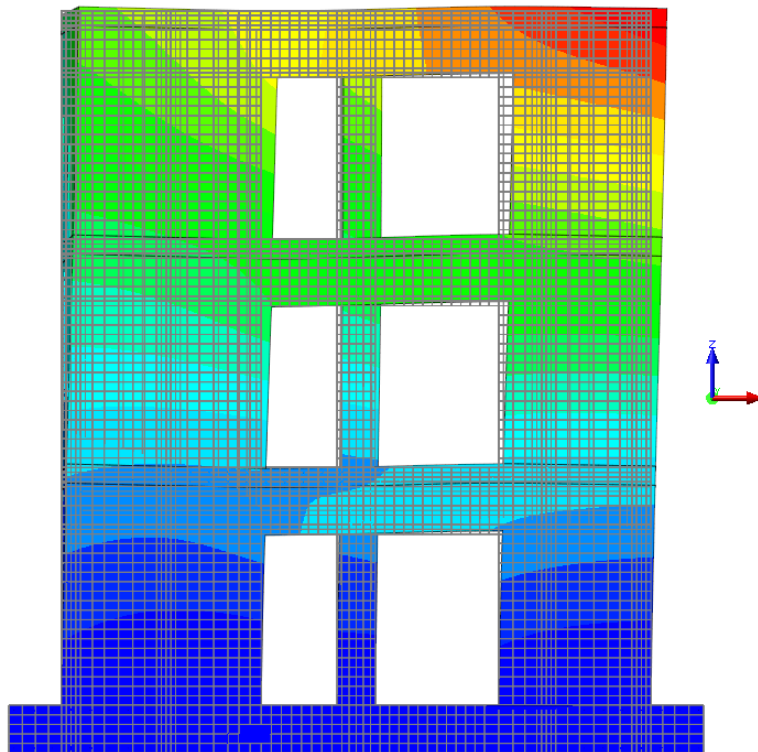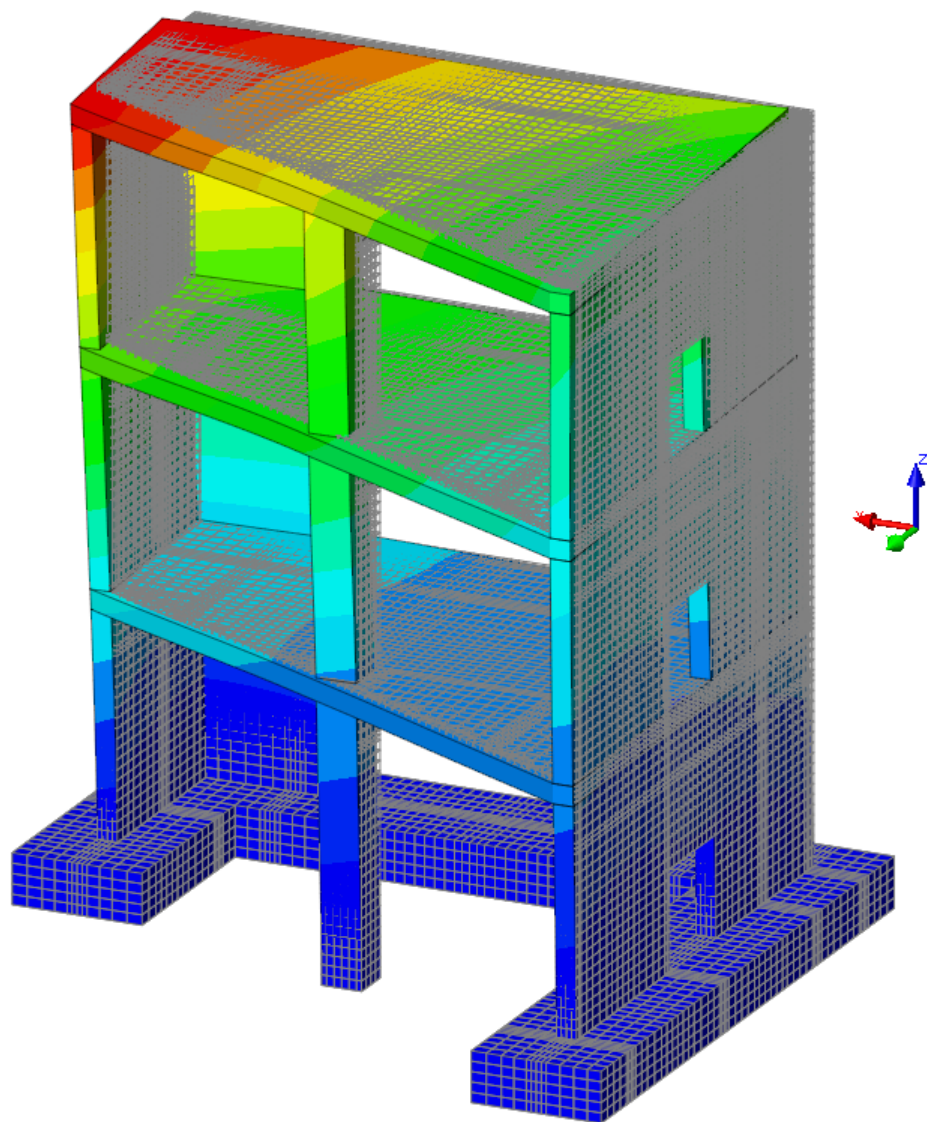

Figure 6.8: Mode shape 2 - rear view.
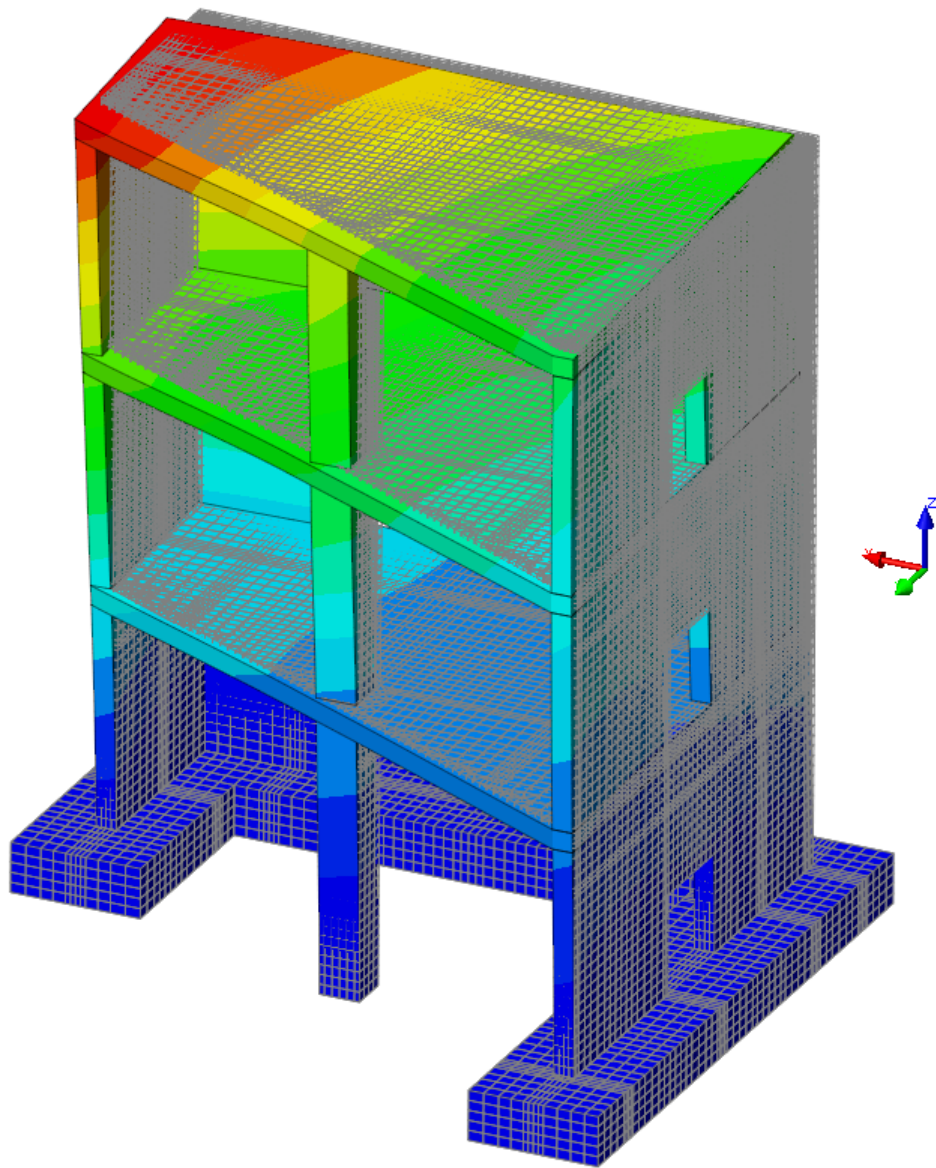
Figure 6.9: Mode shape 2.

The third mode shape of the model for case 1 looks as follows.
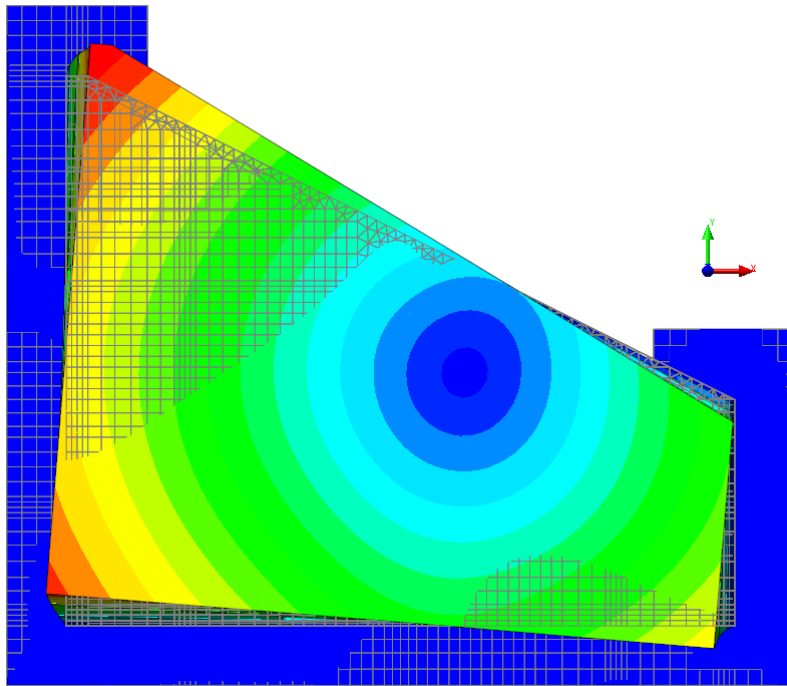

Figure 6.10: Mode shape 3 - top view.
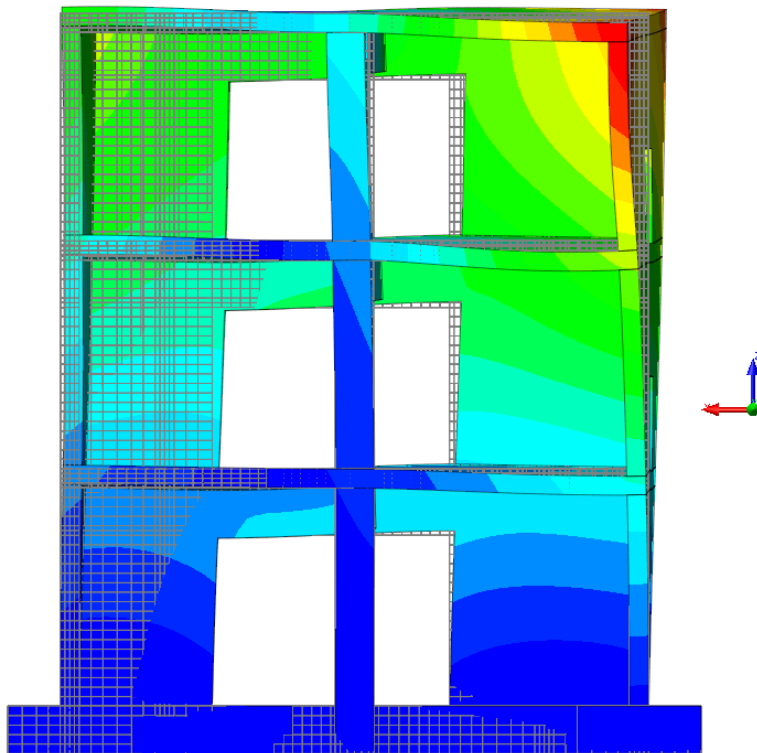
Figure 6.11: Mode shape 3 - front view.
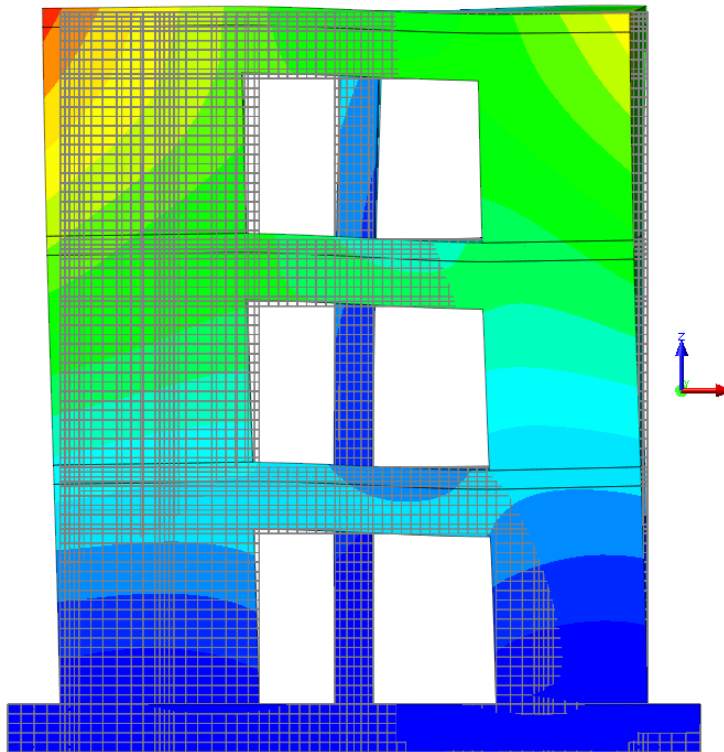
Figure 6.12: Mode shape 3 - rear view.
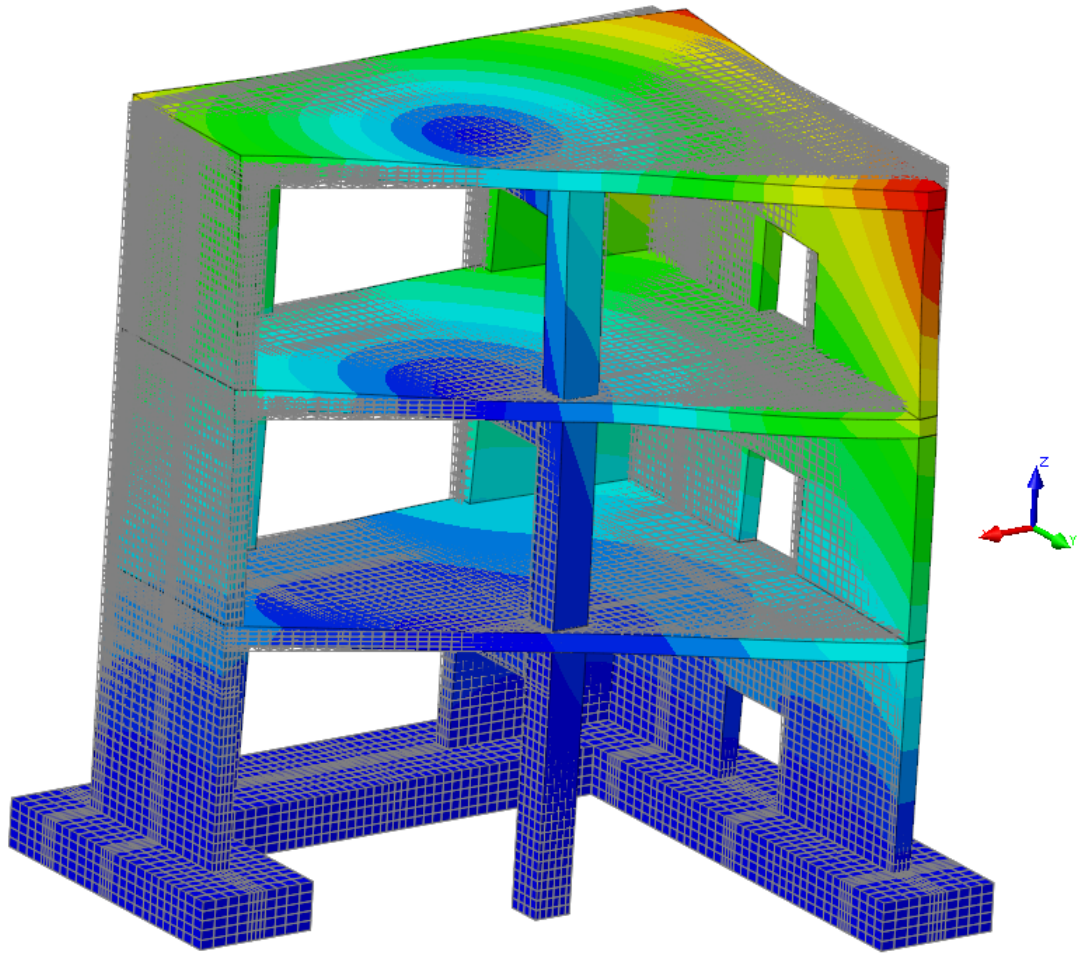
Figure 6.13: Mode shape 3.

The figures from above show that mode 1 is a sway mode in x-direction, mode 2 is a sway mode in y-direction and mode 3 is a torsion mode in z-direction. The tables below will validate the statement from the previous sentence by giving the effective masses of the finite element model for each mode in every direction. Note that the total mass of the model, in this case, is 11.3 ton.

Table 6.4: Effective mass in x-direction.

Mode	Effective mass [kg]	Percentage [%]	Cum. percentage [%]
1	4484	39.57	39.57
2	1433	12.65	52.22
3	754	6.66	58.88

Table 6.5: Effective mass in y-direction.

Mode	Effective mass [kg]	Percentage [%]	Cum. percentage [%]
1	573	5.06	5.06
2	4401	38.84	43.9
3	1389	12.26	56.16

Table 6.6: Effective mass in z-direction.

Mode	Effective mass [kg]	Percentage [%]	Cum. percentage [%]
1	0.74	0.0066	0.0066
2	0.31	0.0027	0.0093
3	1.12	0.0099	0.0192

Table 6.4 shows that the effective mass in x-direction is the biggest for mode 1. This means that most of the mass of the model (39.57 %) moves in x-direction. This implies that mode 1 is a sway mode in x-direction.

Table 6.5 shows that mode 2 is a sway mode in y-direction because most of the mass of the model (38.84 %) moves in y-direction. Tables 6.4 and 6.5 show that the effective mass percentages in x- and y-direction for mode 3 are 6.66 % and 12.26 %, which is not high in comparison with mode 1 and mode 2. This doesn't mean that the structure is moving less, for mode 3, in the x- and y-direction. If this structure was a symmetric structure, then the effective mass percentages for mode 3 in x- and y-direction would be zero. Because of the anti-symmetric geometry of this structure, the effective mass percentages for mode 3 in x- and y-direction are not zero. This implies that mode 3 is a torsion mode in z-direction.

Table 6.6 shows that the effective mass percentages for all three modes in z-direction are very small (in comparison with x- and y-direction), which means that the none of the mode shapes are modes dominant in z-direction.

The natural frequencies of the first three modes for case 1 are shown in the table below.

Table 6.7: Natural frequencies for case 1.

Mode	Natural frequency [Hz]
1	20.96
2	35.84
3	64.61

6.2.2 Case 2

Now lets consider case 2. The total mass of the model for case 2 is 45.3 ton. The first mode shape of the model for case 2 looks as follows.
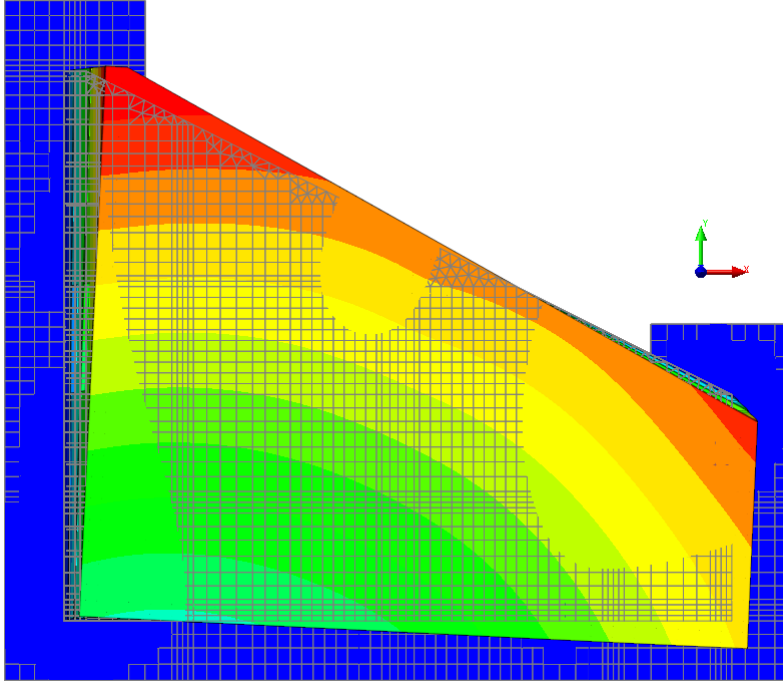
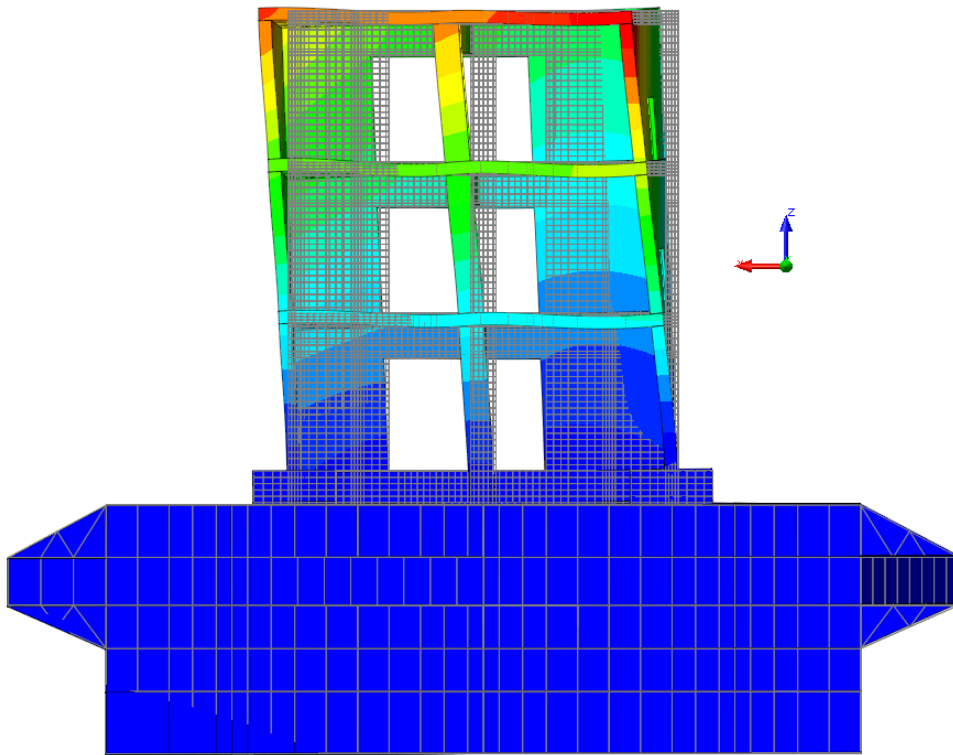Figure 6.14: Mode shape 1 - top view.
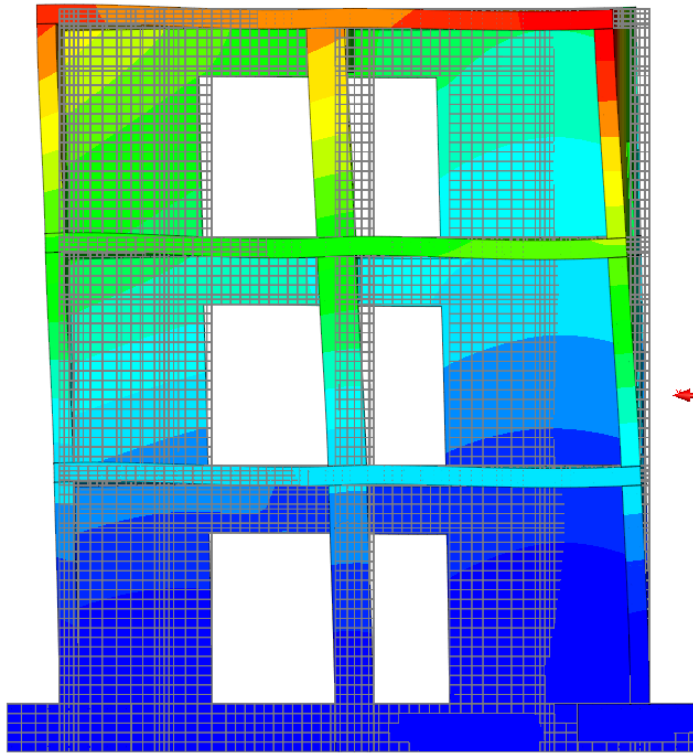
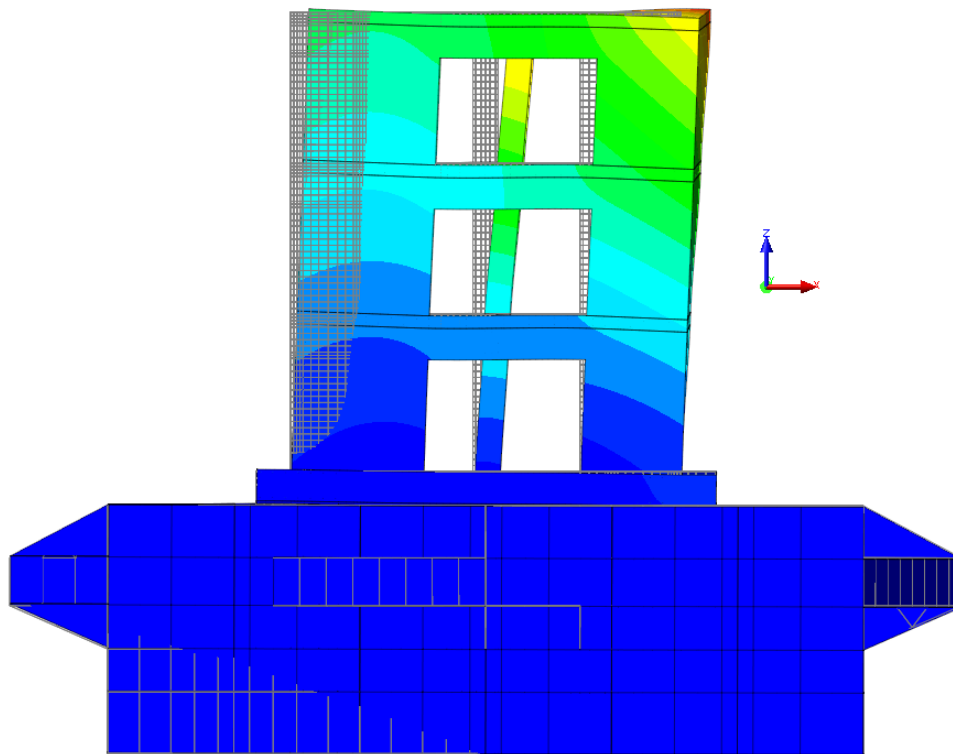Figure 6.15: Mode shape 1 - front view.
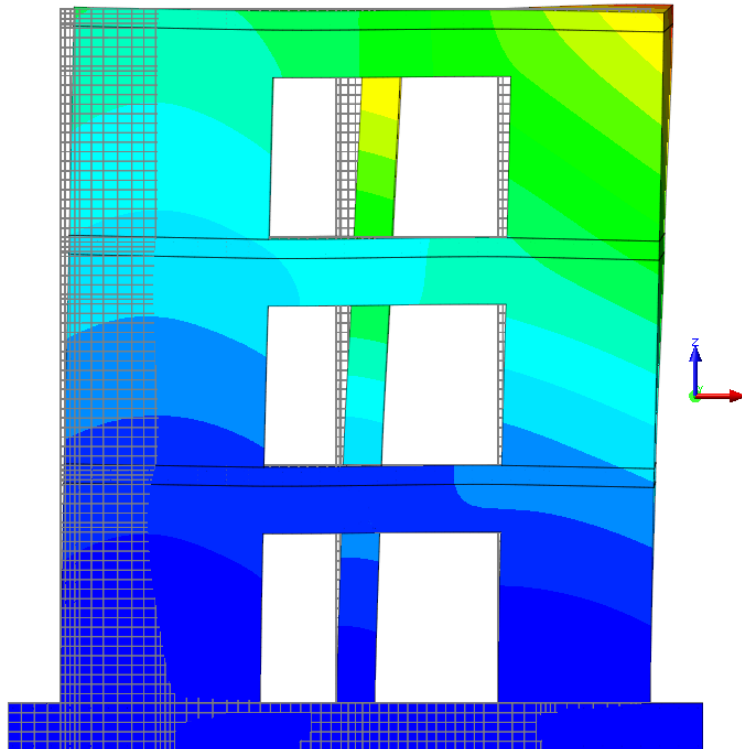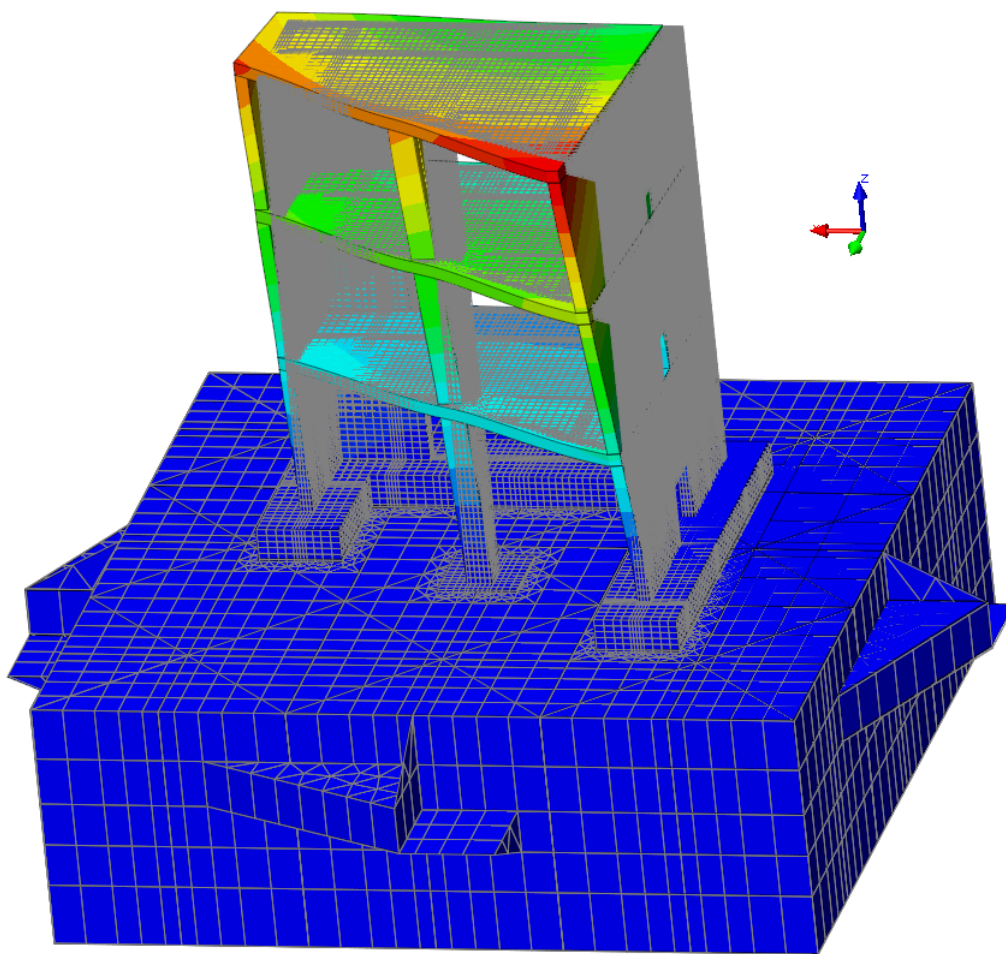

Figure 6.16: Mode shape 1 - rear view.

Figure 6.17: Mode shape 1.

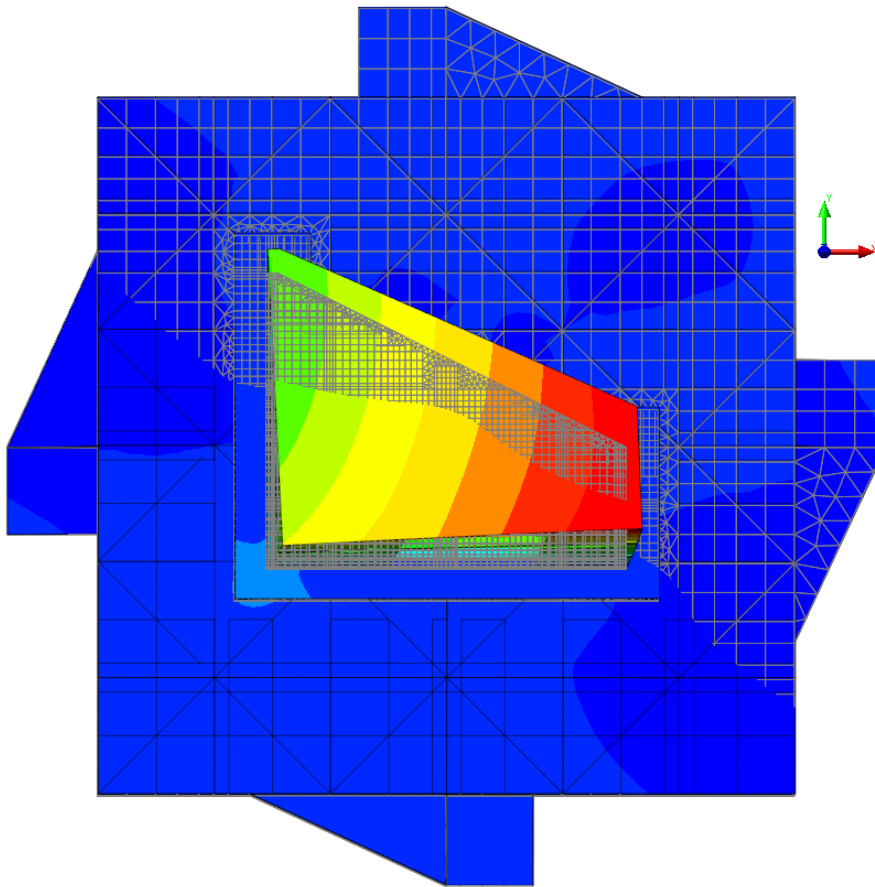The second mode shape of the model for case 2 looks as follows.

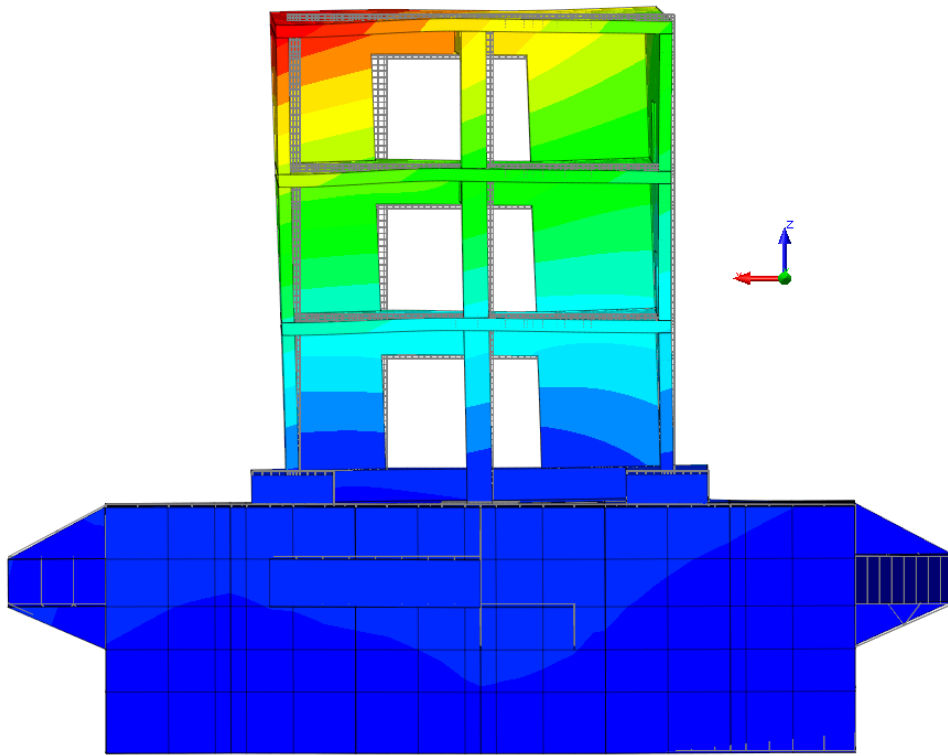Figure 6.18: Mode shape 2 - top view.
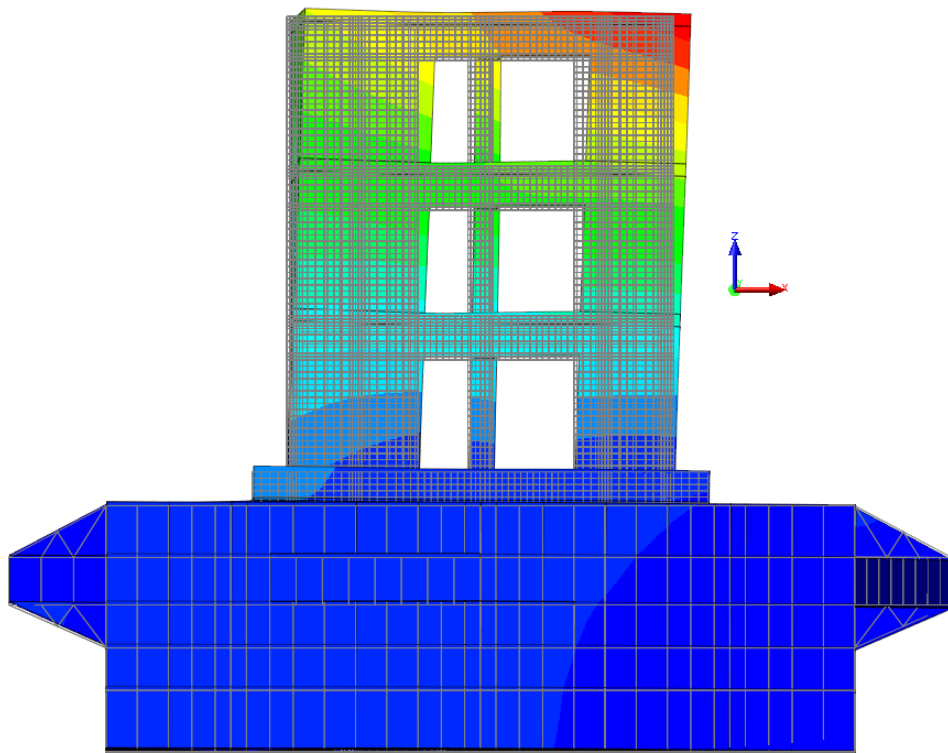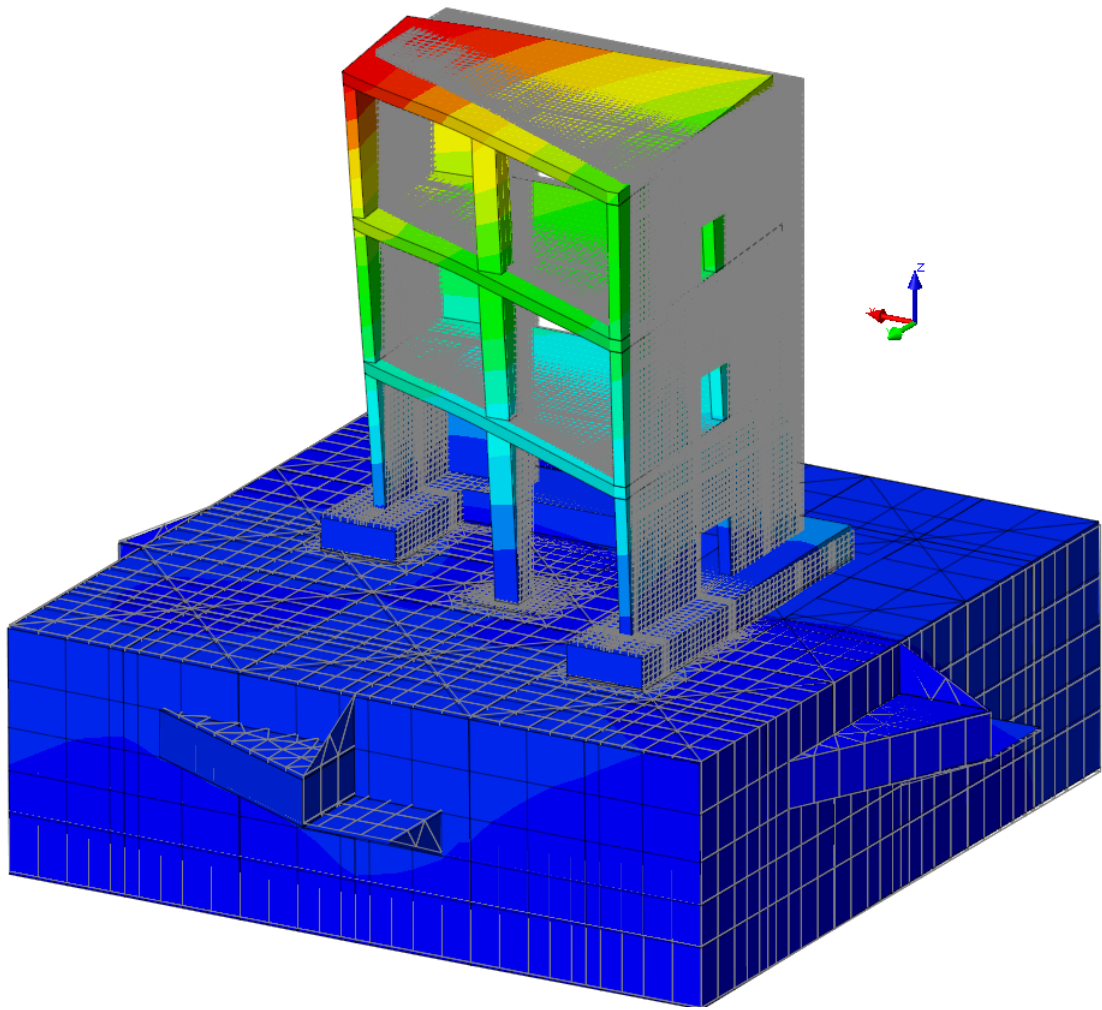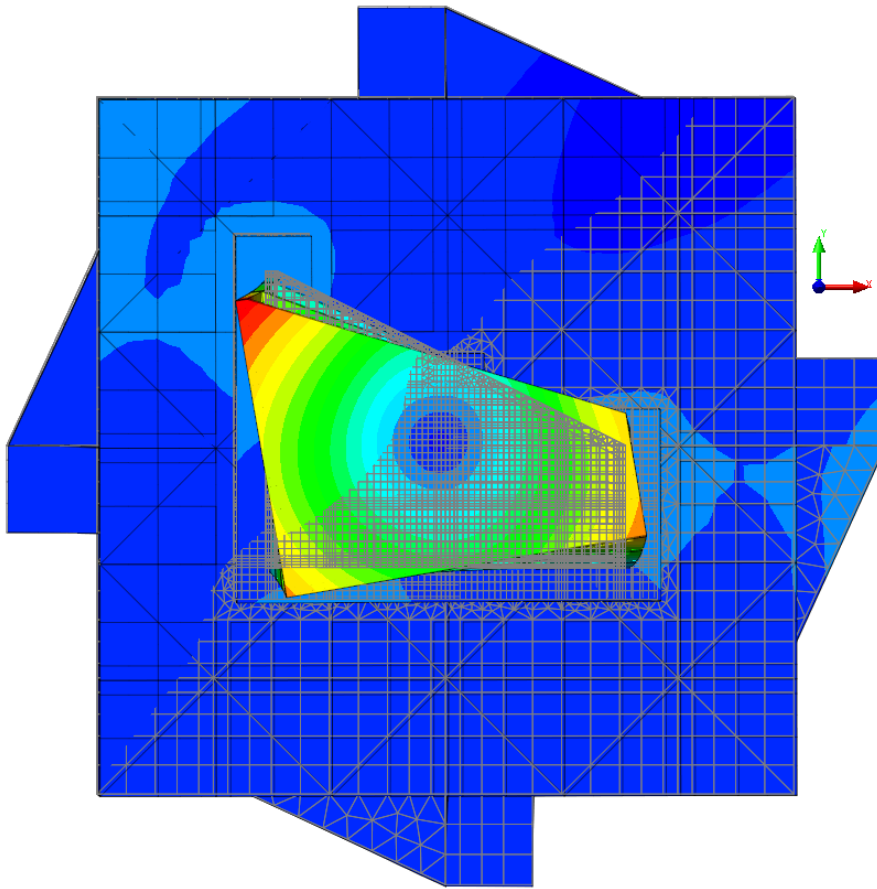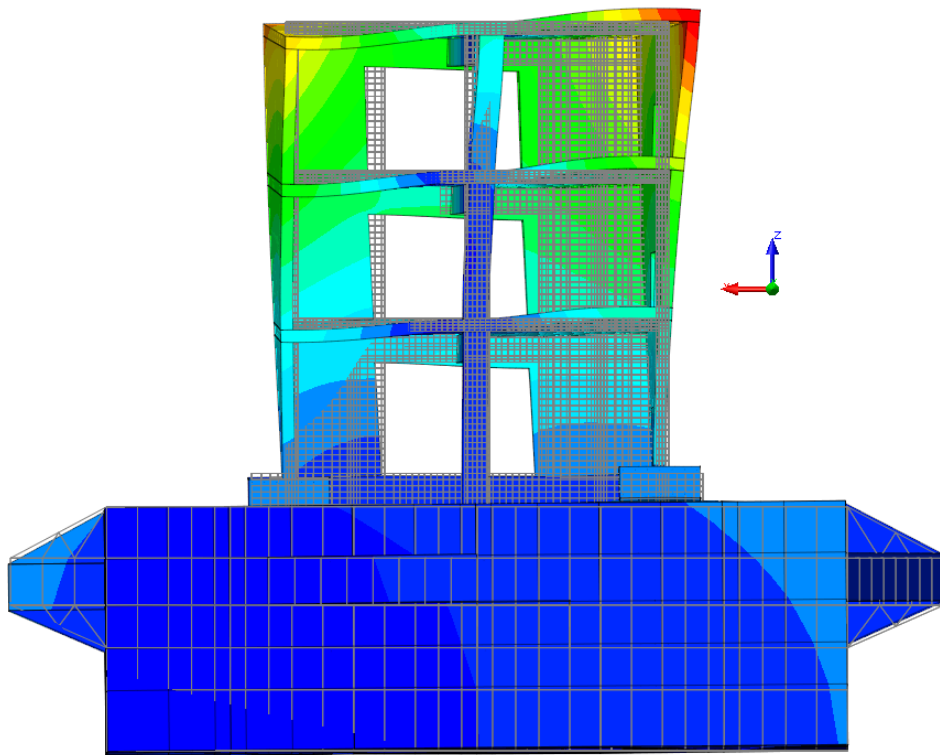
Figure 6.19: Mode shape 2 - front view.

Figure 6.20: Mode shape 2 - rear view.

Figure 6.21: Mode shape 2.

The third mode shape of the model for case 2 looks as follows.
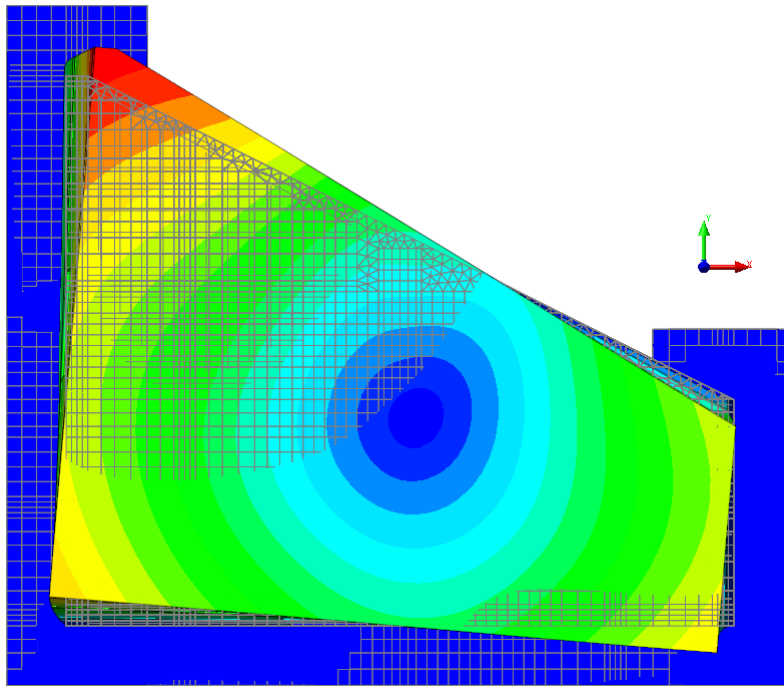
Figure 6.22: Mode shape 3 - top view.
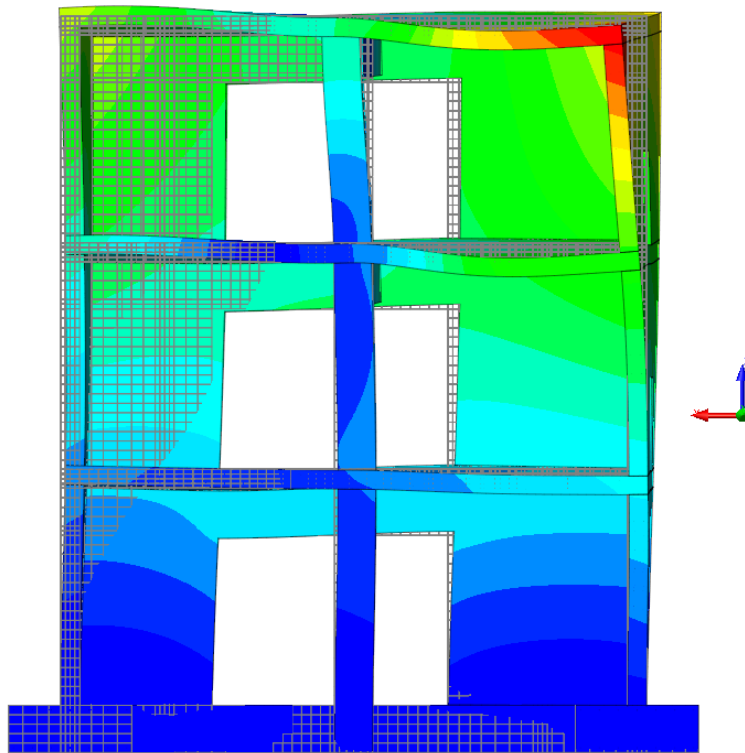
Figure 6.23: Mode shape 3 - front view.
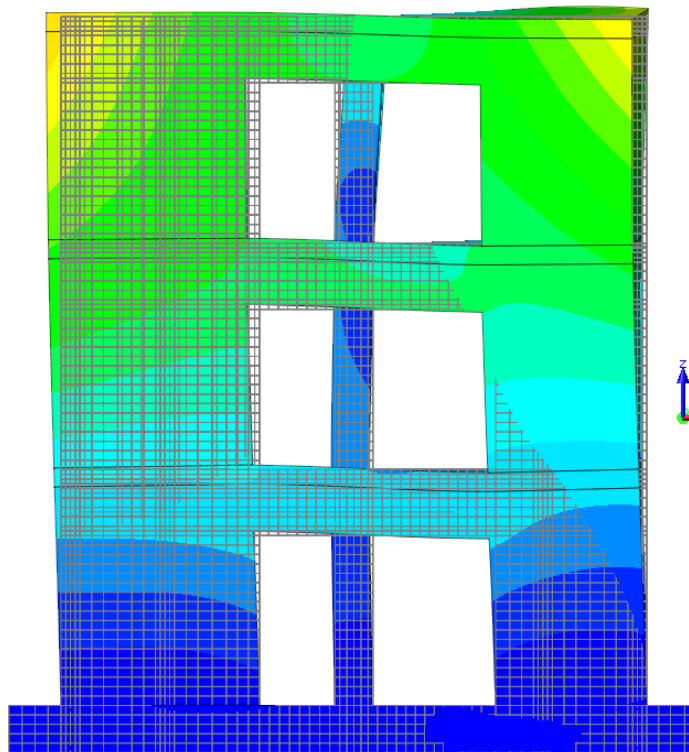
Figure 6.24: Mode shape 3 - rear view.
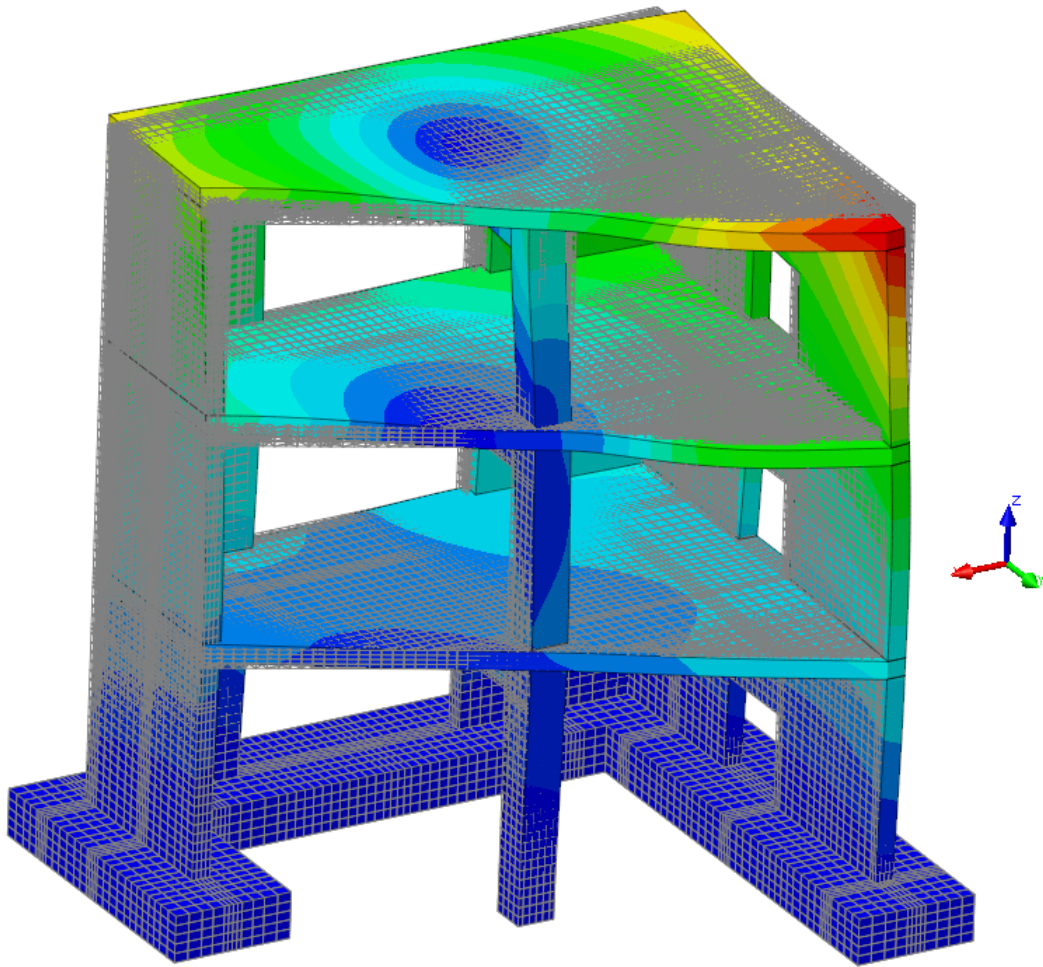
Figure 6.25: Mode shape 3.

Like in the first case, mode 1 is a sway mode in x-direction. Mode 2 is a sway mode y-direction and mode 3 is a torsion mode in z-direction. The tables below show this by giving the effective masses for each mode for each direction.

Table 6.8: Effective mass in x-direction.

Mode	Effective mass [kg]	Percentage [%]	Cum. Percentage [%]
1	25018	55.29	55.29
2	6654	14.71	70
3	4465	9.87	79.87

Table 6.9: Effective mass in y-direction.

Mode	Effective mass [kg]	Percentage [%]	Cum. Percentage [%]
1	3271	7.23	7.23
2	24566	54.29	61.52
3	5879	12.99	74.51

Table 6.10: Effective mass in z-direction.

Mode	Effective mass [kg]	Percentage [%]	Cum. Percentage [%]
1	7.19	0.016	0.016
2	14.85	0.033	0.049
3	98.89	0.22	0.269

The natural frequencies of the first three modes for case 2 are shown in the table below.

Table 6.11: Natural frequencies for case 2.

Mode	Natural frequency [Hz]
1	9.00
2	15.08
3	30.00

6.2.3   Case 3

Lets consider the mode shapes for case 3. The total mass of the model is 69.4 ton. The first mode shape of the model for case 3 looks as follows.
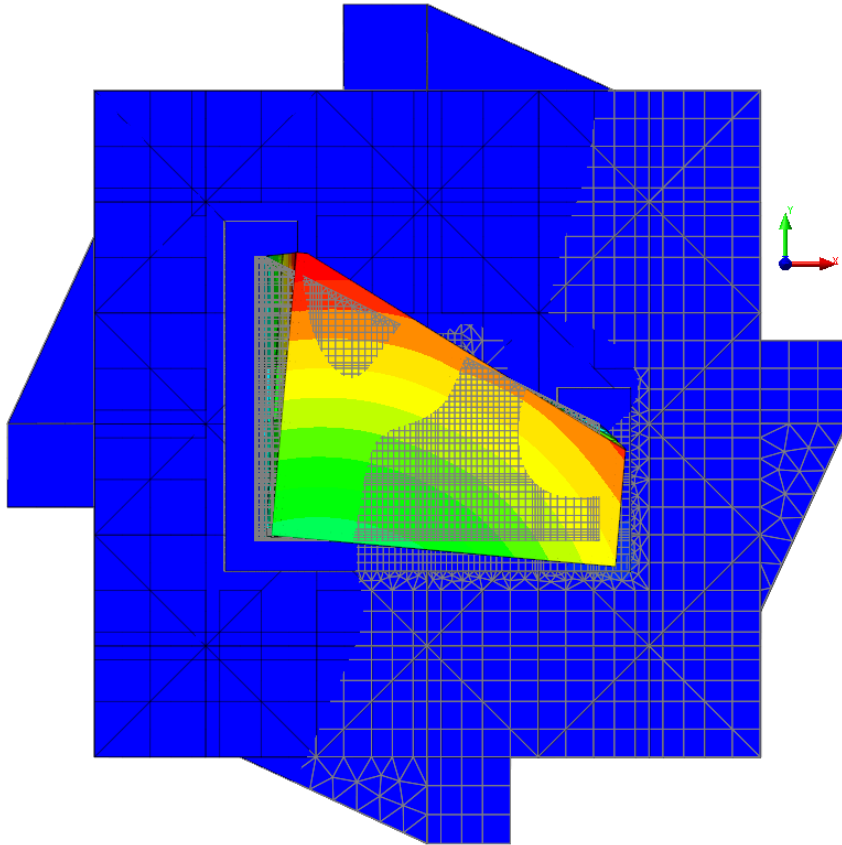
Figure 6.26: Mode shape 1 - top view.

Figure 6.27: Mode shape 1 - front view.

Figure 6.28: Mode shape 1 - rear view.

Figure 6.29: Mode shape 1.

The second mode shape of the model for case 3 looks as follows.

Figure 6.30: Mode shape 2 - top view.

Figure 6.31: Mode shape 2 - front view.

Figure 6.32: Mode shape 2 - rear view.

Figure 6.33: Mode shape 2.

The third mode shape of the model for case 3 looks as follows.

Figure 6.34: Mode shape 3 - top view.

Figure 6.35: Mode shape 3 - front view.
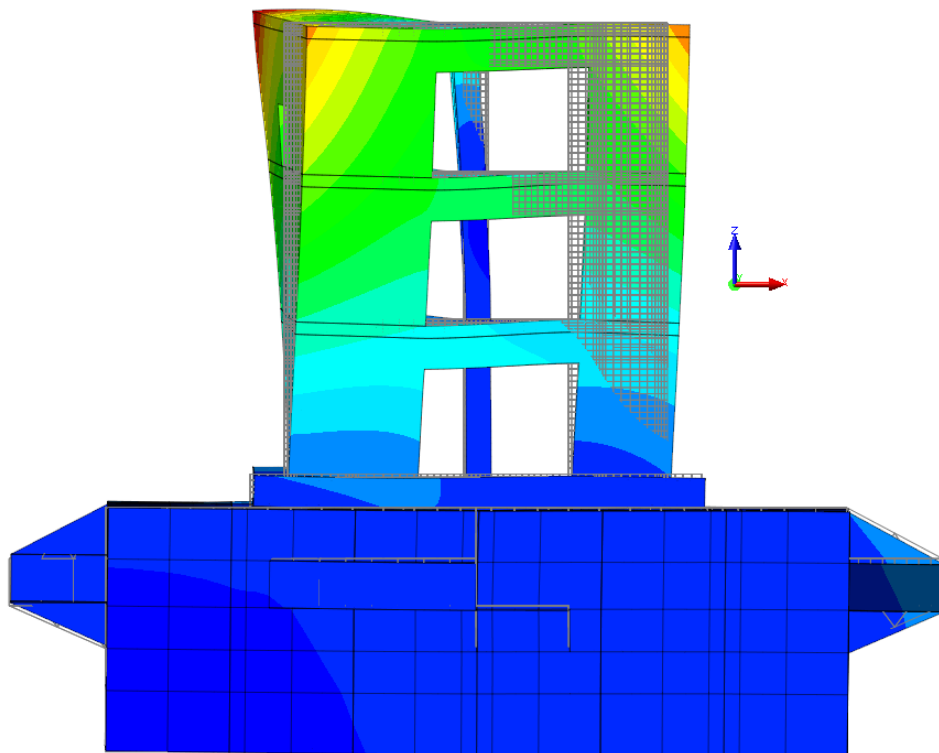
Figure 6.36: Mode shapes 3 - rear view.
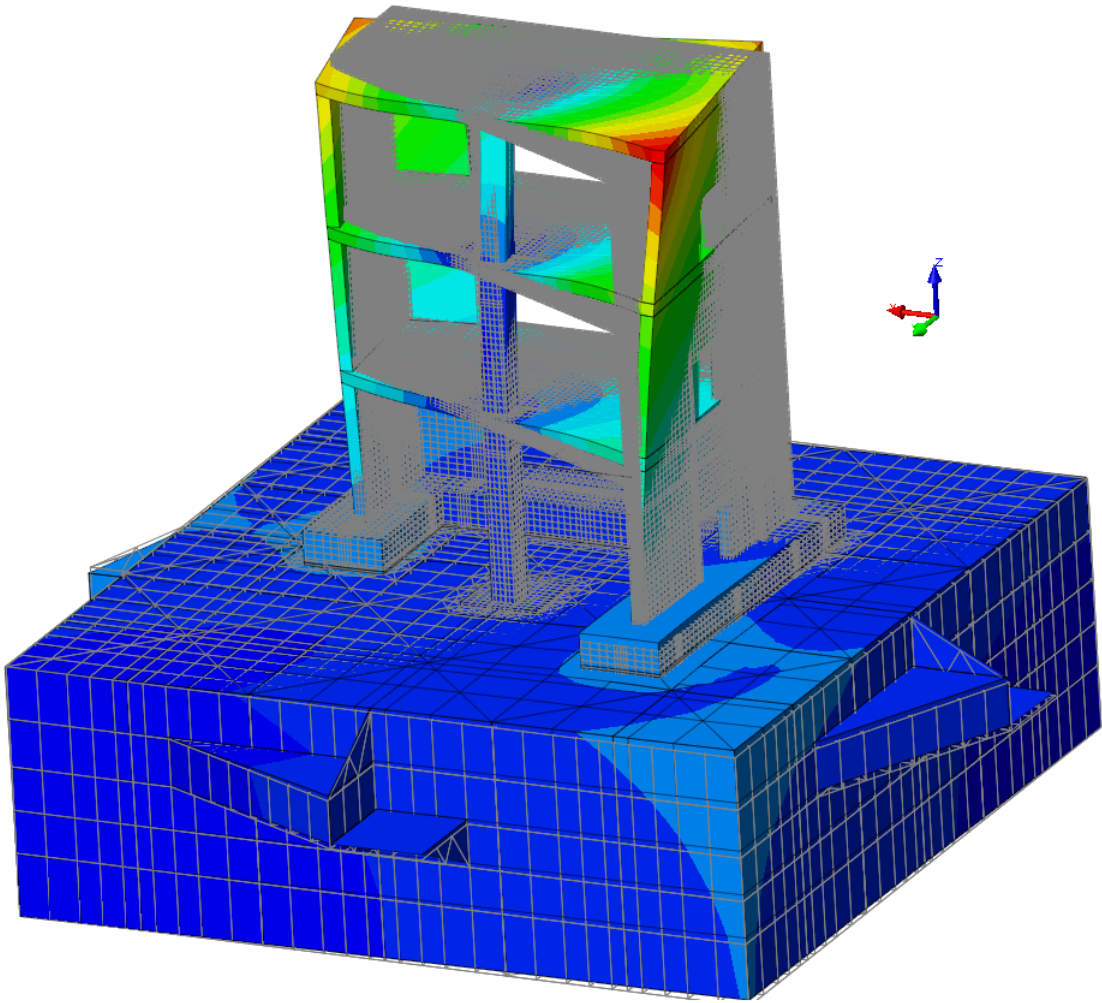
Figure 6.37: Mode shape 3.

Like the previous two cases, mode 1 is a sway in x-direction. Mode 2 is a sway mode in y-direction and mode 3 is a torsion in z-direction. The table below shows that by giving the effective masses for each mode in each direction.

Table 6.12: Effective mass in x-direction.

Mode	Effective mass [kg]	Percentage [%]	Cum. Percentage [%]
1	29645	42.71	42.71
2	5205	7.5	50.21
3	5688	8.2	58.41

Table 6.13: Effective mass in y-direction.

Mode	Effective mass [kg]	Percentage [%]	Cum. Percentage [%]
1	2894	4.17	4.17
2	33103	47.69	51.86
3	4397	6.34	58.2

Table 6.14: Effective mass in z-direction.

Mode	Effective mass [kg]	Percentage [%]	Cum. Percentage [%]
1	0.092	0.00013	0.00013
2	9.15	0.0132	0.013
3	421	0.61	0.62

The natural frequencies of the first three modes for case 3 are given in the table below.

Table 6.15: Natural frequencies for case 3.

Mode	Natural frequency [Hz]
1	7.02
2	10.06
3	20.59

The figures from above show that the mode shapes for each case are the same but the natural frequencies are not, which is quite logical. The table below gives an overview of the natural frequencies for each case.

Table 6.16: Numerical natural frequencies.

Case	Mode	Natural frequency [Hz]
1	1	20.96
	2	35.84
	3	64.61
2	1	9.00
	2	15.08
	3	30.00
3	1	7.02
	2	10.06
	3	20.59

It is important to know that the natural frequency of a system depends on the mass and the stiffness of that system. For a linear one-degree of freedom system without damping, the natural frequency is given by the following equation:

$$\omega = \sqrt{\frac{k}{m}} \tag{6}$$

Where k is the stiffness of the system and m is the mass of the system. The same dependency holds also for linear multi-degree of freedom systems. When the mass of a system with a constant stiffness gets higher, the natural frequency of that system gets lower and table 6.16 shows this. The natural frequencies of case 2 are lower then the natural frequencies of case 1 because the model in case 2 has a higher mass then the model in case 1 where both systems have the same stiffness. The natural frequencies of the model in case 3 are lower then the natural frequencies of the model in case 2 because it has a higher mass. The decrease of the natural frequencies of the model in case 3 in comparison with the model in case 2 is less then the decrease of the natural frequencies of the model in case 2 in comparison with the model in case 1, because also the stiffness of the model, together with the mass, in case 3 increases.

The SMART 2013 committee provided their numerical results of the eigenvalue analysis for the specimen+table system using MATLAB. The first three mode shapes with the corresponding natural frequencies are provided. The following three figures show the mode shapes of the MATLAB model. Note that only the specimen is shown, but the mode shapes do respond to the specimen+table system.
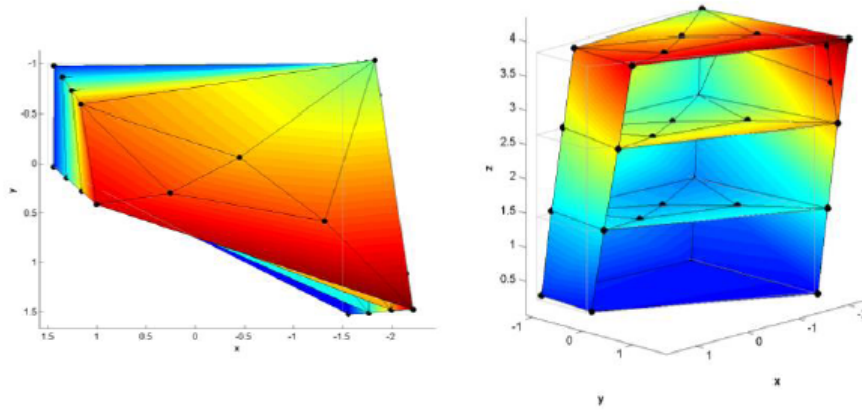
Figure 6.38: SMART 2013 mode shape 1.
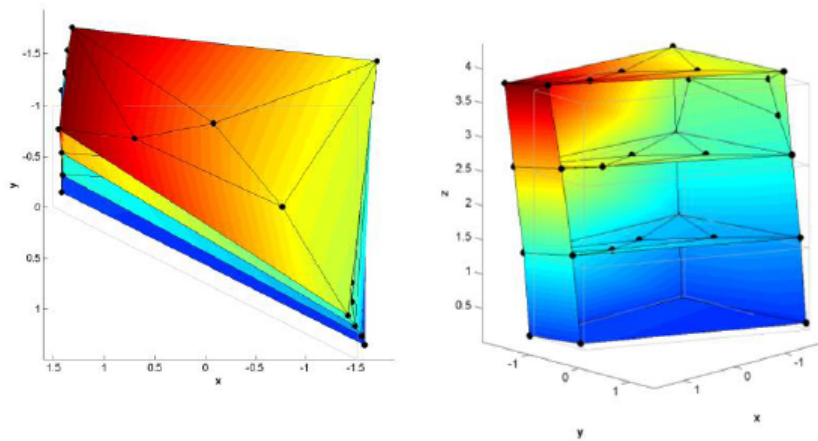
Figure 6.39: SMART 2013 mode shape 2.
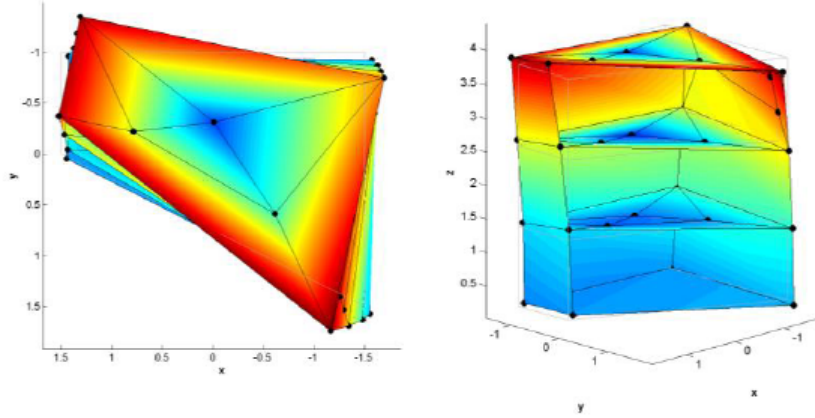
Figure 6.40: SMART 2013 mode shape 3.

The SMART 2013 numerical natural frequencies are shown in the table below.

Table 6.17: SMART 2013 numerical natural frequencies.

Mode	Natural frequency [Hz]
1	6.28
2	7.86
3	16.5

Now lets compare the numerical results of the eigenvalue analysis obtained with DIANA with the SMART 2013 numerical results. From here on, the numerical results from case 3 will be considered. The mode shapes obtained from DIANA are almost the same as the SMART 2013 MATLAB mode shapes but the numerically obtained natural frequencies from DIANA are not the same as the SMART 2013 numerical natural frequencies. Table 6.20 shows this.

Table 6.18: Numerical natural frequencies.

Mode	Smart 2013 [Hz]	Numerical [Hz]	Difference [%]
1	6.28	7.02	12
2	7.86	10.06	28
3	16.5	20.59	25

Table 6.20 shows that the numerical natural frequencies from DIANA are higher then the SMART 2013 numerical natural frequencies. It is possible to get close to the SMART 2013 numerical natural frequencies by changing the mass or the stiffness of the numerical model. In this case only the stiffness of the finite element model has to be changed to get close to the SMART 2013 numerical natural frequencies because the total mass (specimen+table) of the finite element model (69.4 ton) is almost the same as the total mass of the real mock-up (70 ton). According to Model Code 2010 85% the E-modulus of the model should be used when performing an elastic linear analysis in order to account for initial plastic strain, causing some irreversible deformations. When taking 85% of the E-modulus, the following numerical frequencies from DIANA are obtained.

Table 6.19: Numerical natural frequencies - 85% E-modulus.

Mode	Natural frequency [Hz]
1	6.66
2	9.68
3	19.72

Lets compare the newly obtained numerical natural frequencies from DIANA with SMART 2013 numerical natural frequencies.

Table 6.20: Numerical natural frequencies.

Mode	Smart 2013 [Hz]	Numerical [Hz]	Difference [%]
1	6.28	6.66	6
2	7.86	9.68	23
3	16.5	19.72	20

It is important to mention that it is not possible to get exactly the same natural frequencies as the provided ones. The reason for that is that the finite element model used in this thesis is not the same as the model which is used by the SMART 2013 committee. As can be seen in figure 6.40, the model of the SMART 2013 committee is made of 2D plate elements while the model for this thesis is made of 3D solid elements. Further it is not known which material properties the SMART 2013 committee has used for their 2D model when performing the eigenvalue analysis in MATLAB. In general can be said that if the model is not the same, then it is not possible to get the same natural frequencies.

A better way for comparing the numerical natural frequencies with the real experimental natural frequencies is to analyze the discrete Fourier transformation (DFT) of RUN7 and the DFT of experimental response of the mock-up to RUN7. From the DFT's it is possible to see what the natural frequencies of the mock-up in the laboratory are. The figures below give the DFT's of RUN7 in x- and y-direction together with the DFT's of the response of the mock-up to RUN7 in x- and y-direction.
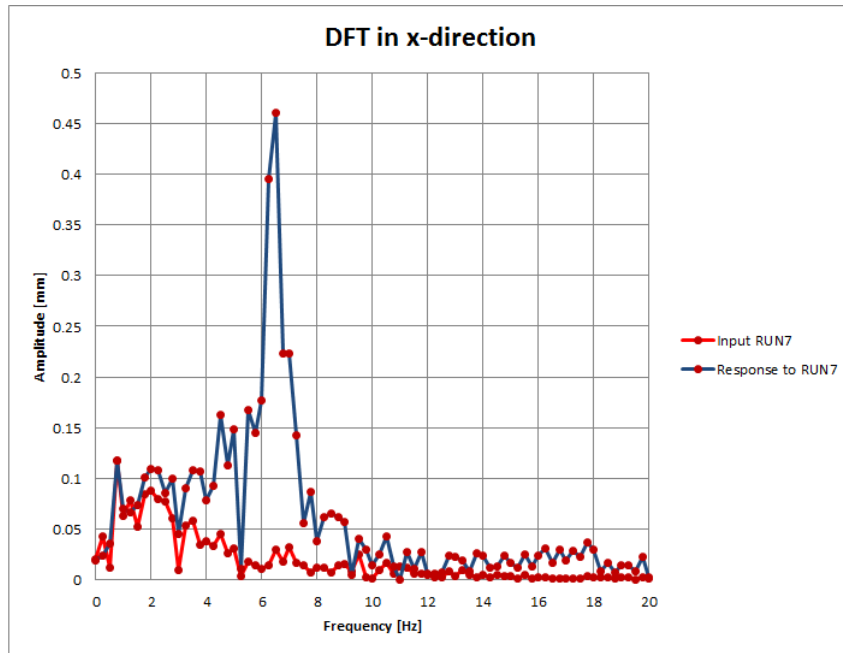
Figure 6.41: DFT of RUN7 and DFT of the response to RUN7.
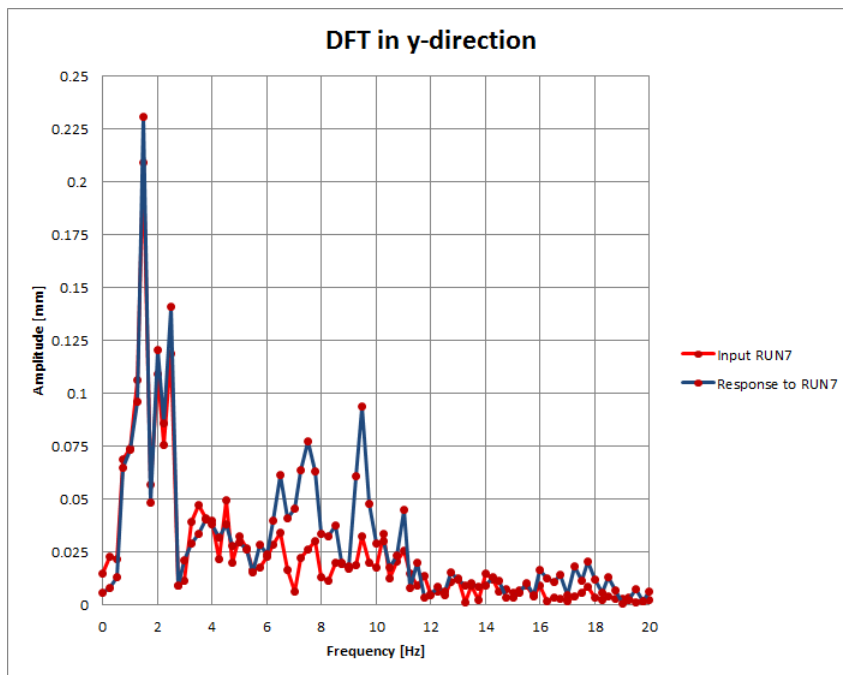
Figure 6.42: DFT of RUN7 and DFT of the response to RUN7.

In figure 6.41, the red line is the DFT of RUN7 in x-direction where the blue line is the DFT of the experimental response of the mock-up to RUN7 in x-direction. The red line shows what the governing frequencies of RUN7 in x-direction are. The blue line shows what could be the natural frequencies of the mock-up in x-direction. By plotting the DFT of RUN7 and the DFT of the response to RUN7 it is possible to determine the natural frequencies of

the mock-up. Figure 6.41 shows that in the beginning the mock-up follows the load quite well. But after 3 Hz, the mock-up goes its own way and at 6.5 Hz it shows a very high peak. And after 6.5 Hz, again the mock-up follows more or less the excitation. By looking at this phenomena it can be concluded that 6.5 Hz is a natural frequency of the mock-up in x-direction. This 6.5 Hz is the natural frequency of mode 1 because it has been determined before that mode 1 is a sway mode in x-direction.

Figure 6.42 shows also the same phenomena as in figure 6.41 but then in y-direction. In the beginning the mock-up follows the load very well and after 6 Hz the blue line shows 3 peaks at 6.5 Hz, 7.5 Hz and 9.5 Hz. From these 3 peaks, the peak at 9.5 Hz is the highest. Because the peak at 9.5 Hz is the highest, it can be concluded that 9.5 Hz is also a natural frequency of the mock-up. This 9.5 Hz is probably the second natural frequency because the numerical eigenvalue analysis showed that mode 2 is a sway mode in y-direction.

The natural frequency for mode 3 can not be determined from the DFT's of figures 6.41 and 6.42 because these figures don't show convincing peaks after 10 Hz.

The experimental natural frequencies, obtained with the help of DFT, and the numerical natural frequencies are given in the tables below. The first table shows the numerical natural frequencies where the E-modulus of the model is not reduced. The second table shows the numerical natural frequencies where the E-modulus of the model is reduced with 15%.

Table 6.21: Natural frequencies - total E-modulus.

Mode	Experimental [Hz]	Numerical [Hz]	Difference [%]
1	6.5	7.02	8
2	9.5	10.06	6
3	-	20.59	-

Table 6.22: Natural frequencies - 85% E-modulus.

Mode	Experimental [Hz]	Numerical [Hz]	Difference [%]
1	6.5	6.66	3
2	9.5	9.68	2
3	-	19.72	-

Table 6.22, where 85% E-modulus of the model is taken into account, shows that the numerical natural frequencies are very close to the experimental natural frequencies. It is important to mention that it is difficult to get exactly the same natural frequencies as the experimental ones because to get that, the finite element model must have exactly the same properties like mass and stiffness as the real mock-up. Here it is tried to mimic the real mock-up as good as possible but the finite element model does not have exactly the same properties as the real mock-up. That is why it is sufficient that the numerical natural frequencies are this close to the experimental natural frequencies. It can be concluded that the calibration of the finite element model, in terms of natural frequencies and corresponding mode shapes, is very good.

6.3   Rayleigh Damping

In the transient dynamic analysis it is necessary to apply Rayleigh damping. There are different Rayleigh damping matrices. First, the constant Rayleigh damping matrix is considered. This damping matrix can be calculated as follows:

$$C = aM + bK \tag{7}$$

Where a and b are constant scalar coefficients. M is the mass matrix and K is the stiffness matrix. A second method lies in considering the tangent stiffness matrix instead of the initial stiffness one. This leads to:

$$C = aM + bK^t \tag{8}$$

Where K^t is the tangent stiffness matrix. Last, assuming the values of the coefficients a and b can be updated according to the following equation:

$$C = a(t)M + b(t)K^t \tag{9}$$

Where t is an updating parameter that can be chosen as the frequency or time. In the first approach, the damping is clearly overestimated over the structure since the effects of cracking on the stiffness matrix are not taken into account. In the second and third approaches, the fact that the tangent stiffness is considered leads to high damping in lower modes (low frequencies) and to low damping in higher modes (high frequencies). Furthermore, considering the tangent stiffness may lead to negative terms in the damping matrix, especially in the case of materials exhibiting a negative hardening.

In this thesis, the second approach is chosen where the tangent stiffness matrix is considered. In the formulation of the Rayleigh damping matrix can be seen that Rayleigh damping is characterized by the coefficients a and b. These coefficients can be determined as follows:

$$a = 2\omega_1\omega_2\beta \qquad\qquad b = 2\beta \tag{10}$$

Where

$$\alpha = \frac{\omega_1}{\omega_2} \qquad\qquad \beta = \frac{(1-\alpha)\xi}{\omega_2 - \alpha\omega_1} \tag{11}$$

This gives:

$$a = \frac{2\omega_1\omega_2(\xi_1\omega_2 - \xi_2\omega_1)}{\omega_2^2 - \omega_1^2} \qquad\qquad b = \frac{2(\xi_2\omega_2 - \xi_1\omega_1)}{\omega_2^2 - \omega_1^2} \tag{12}$$

ξ is the damping coefficient and ω_1 and ω_2 are the frequencies of interest. A convenient way for choosing ω_1 and ω_2 is to consider the first two natural frequencies of the structure. By considering the first two natural frequencies of the structure, it is possible to make sure that the these frequencies are damped with ξ. Also performing a discrete Fourier transformation (DFT) on RUN6 and RUN7, to see what the governing frequencies of these RUNs are, can be helpful for determining the ω_1 and ω_2.

The DFT of RUN6 shows that the governing frequency of RUN6 is 1.0 Hz in x-direction, 0.5 Hz in y-direction and 0.5 Hz in z-direction. The DFT of RUN7 shows that the governing frequency of RUN7 is 0.75 Hz in x-direction, 1.5 Hz in y-direction and 9.5 Hz in z-direction. and the governing frequency of RUN7 is 1.5 Hz. The first two natural frequencies of the model is 7.02 Hz and 10.06 Hz, as will be shown in the next sections.

By taking the first two natural frequencies of the model and the results of the DFT on RUN6 and RUN7 in account, the following two frequencies are chosen.

$$f_1 = 0.5\,\text{Hz} \rightarrow \omega_1 = 3.14\,\text{rad/s} \qquad f_2 = 15\,\text{Hz} \rightarrow \omega_2 = 125.66\,\text{rad/s} \qquad (13)$$

With a damping coefficient of 5% (usually for concrete) the following values for the constants of Rayleigh damping are calculated:

$$a = 0.304 \qquad b = 0.001 \qquad (14)$$

Figure 6.43 shows with which damping ratio the model will be damped when the model vibrates at a certain frequency. For the example, if the model vibrates with 0.5 Hz or 15 Hz, then the model will be damped with 5% damping ratio.
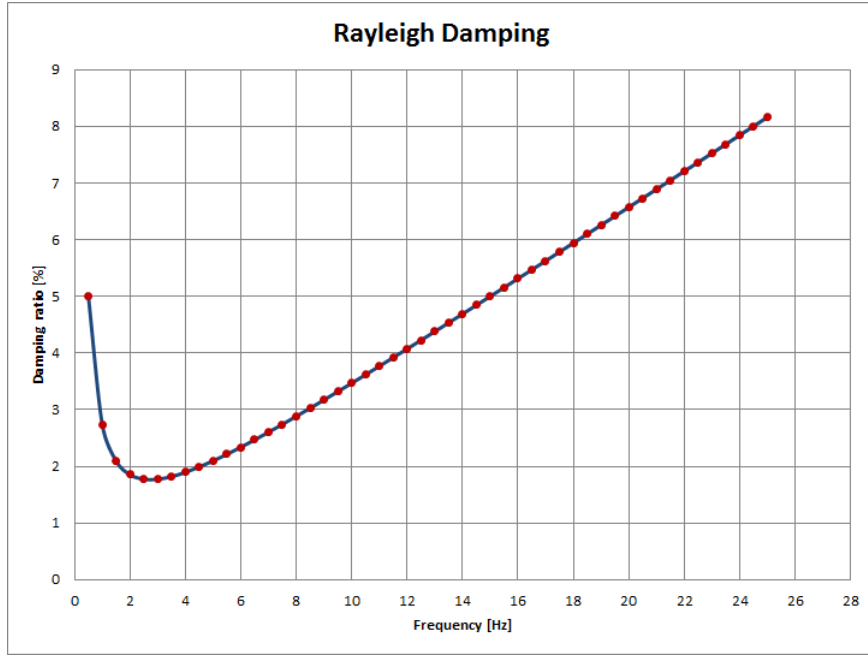
Figure 6.43: Rayleigh damping.

This graph can be obtained by using the following equations in Excel:

$$a = \frac{2\omega_1\omega_2(\xi_1\omega_2 - \xi_2\omega_1)}{\omega_2^2 - \omega_1^2} \qquad b = \frac{2(\xi_2\omega_2 - \xi_1\omega_1)}{\omega_2^2 - \omega_1^2} \qquad (15)$$

With

$$\xi_i = \frac{a + b\omega_i^2}{2\omega_i} \qquad \omega_i = 2\pi f_i \qquad (16)$$

Where f is the frequency in Hz.

114

6.4   Linear Transient Analysis

The seismic inputs which are used for the linear transient analysis are RUN6 and RUN7. These seismic excitations are imposed on the model at the actuators in the shaking table.

Figures 6.44 and 6.45 show where the actuators are. The big fully colored red arrows show the places of the actuators where the model is supported. The seismic excitations are applied at these supports. The small red arrows represent the seismic loads.
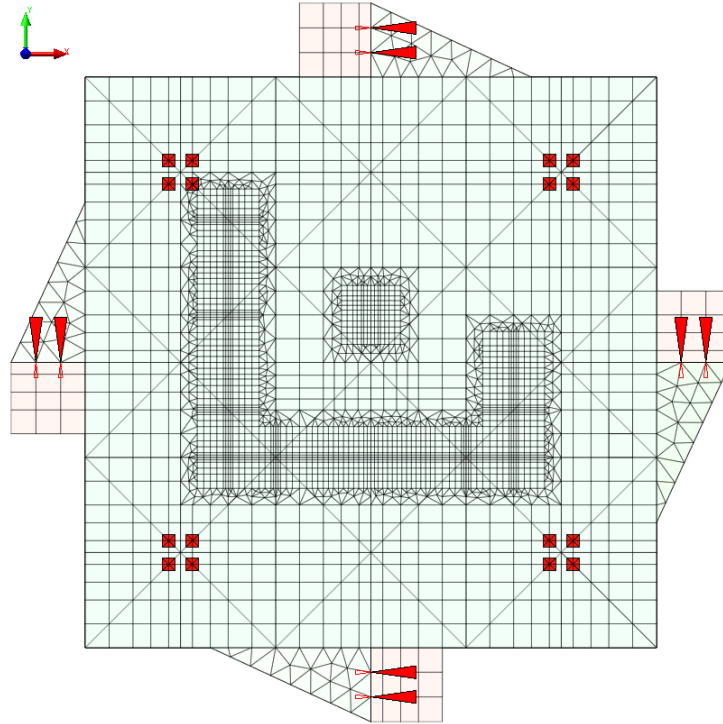
Figure 6.44: Application points of all RUNs.
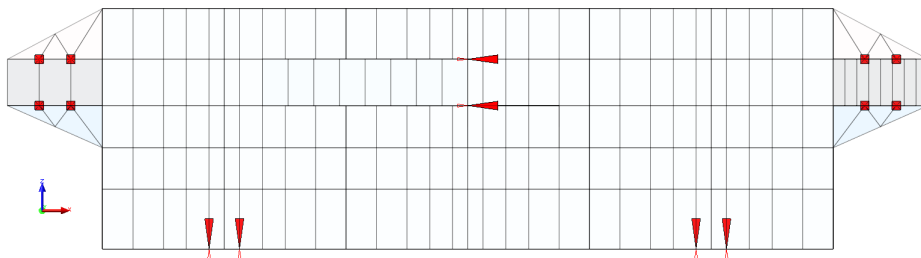
Figure 6.45: Application points of all RUNs.

The idea here is to compare the response of the finite element model with the response of the real mock-up with respect to RUN6 and RUN7 to see how good the finite element model predicts the response of the mock-up with respect to these two RUNs. With this comparison it is possible to asses how reliable the predictions of the finite element model are. If the match between the numerical and experimental responses are close to each other then the finite element model did reliable predictions for the dynamic behavior of the mock-up.

6.4.1 Linear Response with Respect to RUN6

In this section the responses of the finite element model, in terms of displacements and accelerations, are compared with the responses of the real mock-up with respect to RUN6. Only the responses on floor 3 in point D are compared. The reason why the results on floor 3 in point D are considered, is that this point gives the biggest displacements and accelerations. The responses in other points on other floors are not given in this report to make sure that the size of this report doesn't become too large. On request, the responses of other floors can be provided in an Excel file.

The blue graphs are the numerical results and the red graphs are the experimental ones. The first graphs from each page show the total response and the second graphs show a piece of the total response to show in detail how the matches between the numerical and experimental responses are.
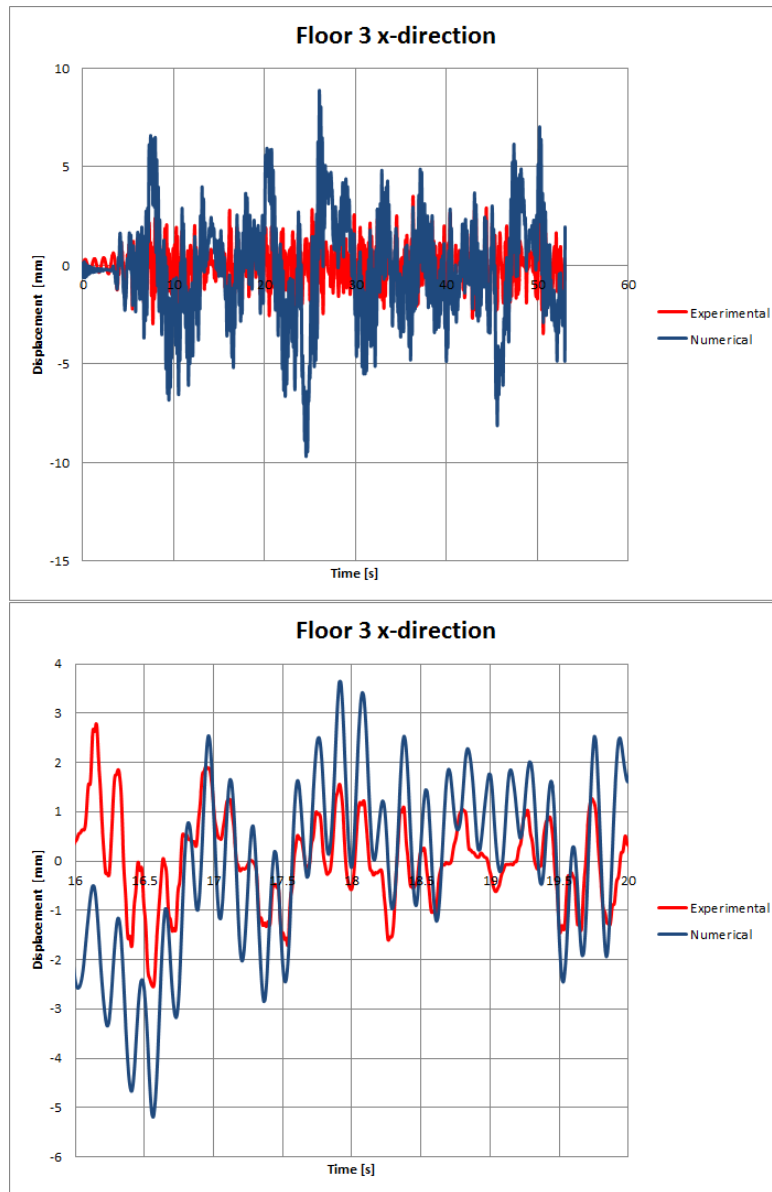
Figure 6.46: Experimental vs numerical displacement - RUN6.
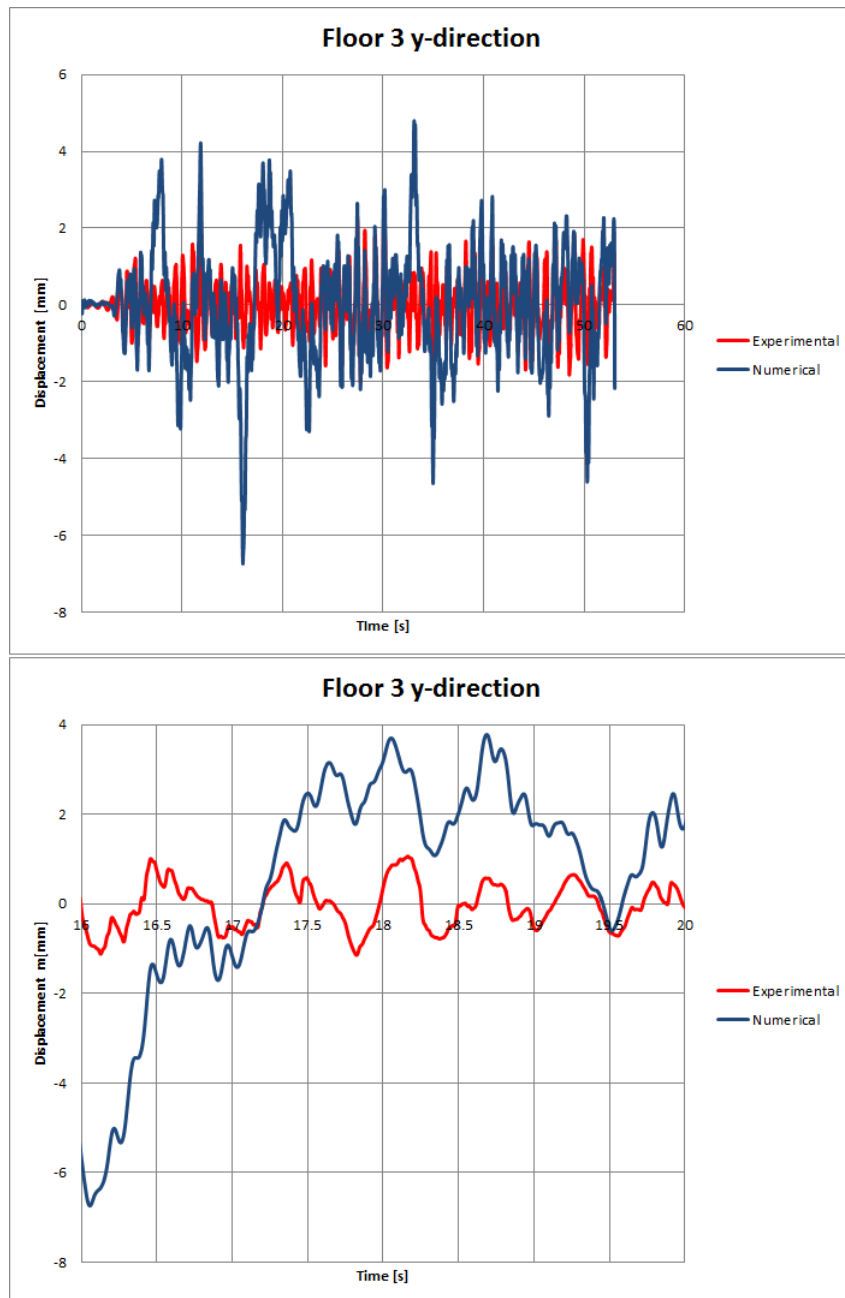
Figure 6.47: Experimental vs numerical displacement - RUN6.

The numerically obtained displacements doesn't match the experimentally provided displacements, but there is something interesting to see in the graphs. That is that the form of both graphs are almost the same, with almost the same period, but the amplitudes are not the same. A reason could be that the provided displacements are not absolute displacements, but relative displacements to the shaking table. The statement from the previous sentence can be verified by making the provided relative displacements, absolute displacements by adding up the seismic input from RUN6 in x- and y-direction with the provided relative displacements in point D on floor 3. The figures below show the corrected results.
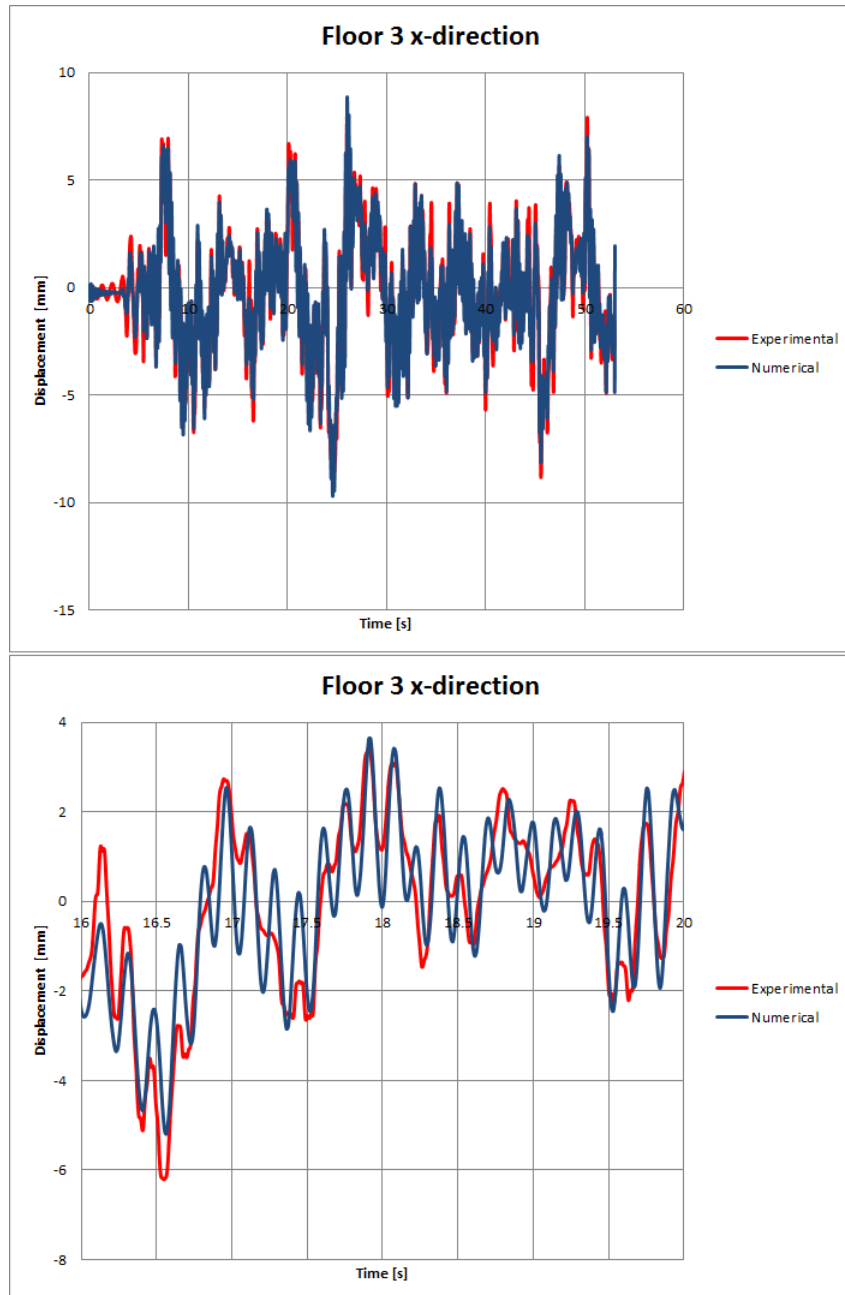
Figure 6.48: Corrected experimental vs numerical displacement - RUN6.
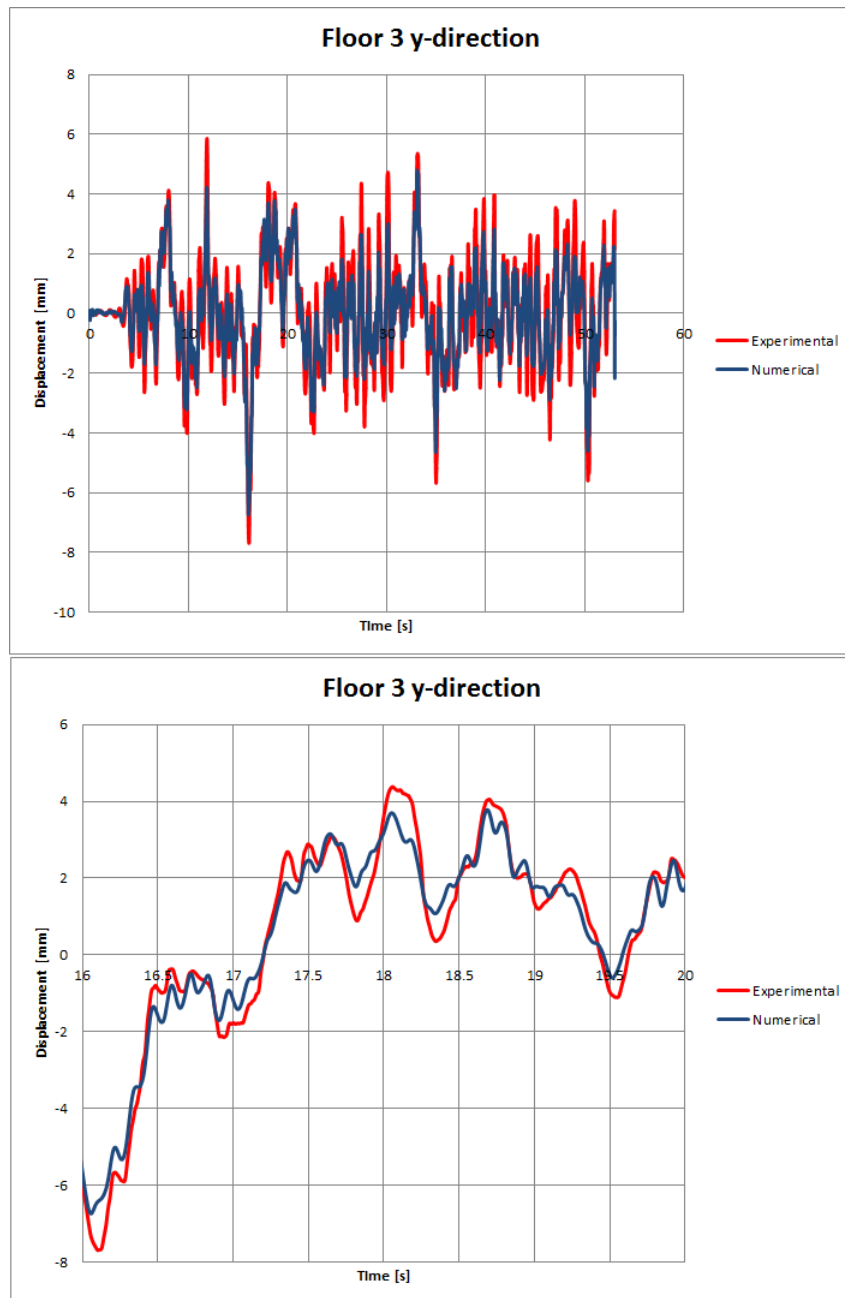
Figure 6.49: Corrected experimental vs numerical displacement - RUN6.

The provided displacements were indeed relative to the shaking table. Now the graphs show that the numerically obtained displacements are almost the same as the experimentally provided displacements. There are little differences between the numerical and experimental graphs. The amplitudes differ a bit and sometimes the graphs are a bit out-of-phase. But the overall match is very good. This shows that the finite element model made reliable predictions for the dynamic response of the mock-up with respect to RUN6 in point D on floor 3.

6.4.2 Linear Response with Respect to RUN7

Finally the responses with respect to RUN7 are compared. The match between the numerical response and the experimental response with respect to RUN7 are also good. Again, they are little differences in terms of amplitudes and phases. The figures below show that.
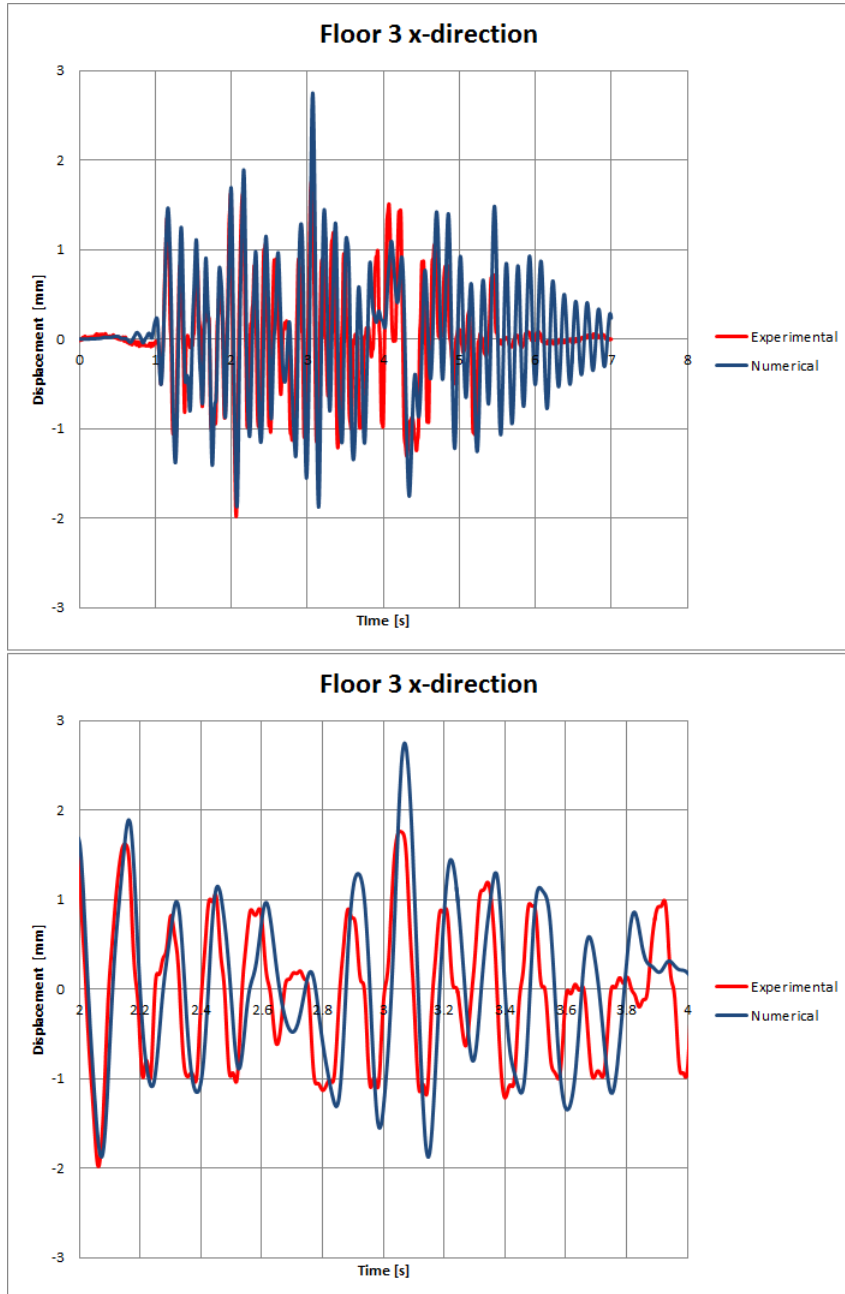
Figure 6.50: Experimental vs numerical displacement - RUN7.
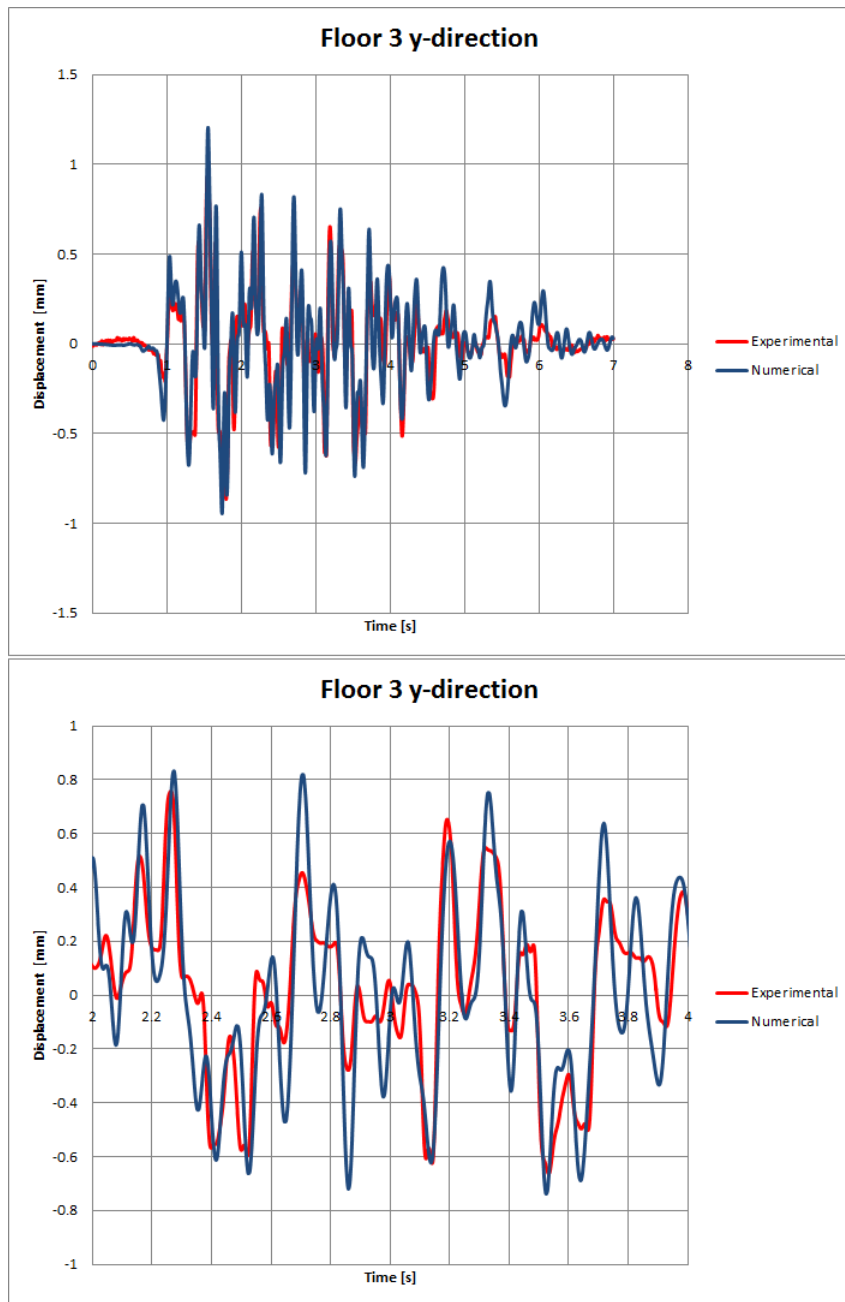
Figure 6.51: Experimental vs numerical displacement - RUN7.

6.4.3 RUN6 & RUN7

The graphs from above show that the numerical responses are close to the experimental responses with respect to RUN6 and RUN7. Some of the graphs show that the finite element model has higher natural frequencies in comparison with the natural frequencies of the mock-up in the laboratory (which was confirmed in the previous section), where the finite element model shows high-frequency responses in some points. Because of the higher natural frequencies of the model the model has a shorter natural period and that is why the numerical and experimental responses are a bit out-of-phase in some points. Also some of the graphs show a bit difference in the magnitude of the amplitudes which is because of the different E-moduli of the model and the mock-up. These mismatches between the experimental response of the mock-up and the numerical response of the model are small and hence acceptable.

Once again, the graphs from above show the responses in point D on floor 3. By looking at all these graphs it can be concluded that the numerically obtained responses are close to the experimentally provided responses, hence it can be said that the finite element model makes reliable predictions of the dynamic response of the mock-up in point D on floor 3. The responses in other points on other floors are also investigated but they are not given in this thesis because of the big size of this thesis. On request, the responses in other points on other floors can be provided in an Excel file.

6.5 Response Spectrum Analysis

Response spectrum analysis (RSA) is a linear dynamic statistical analysis method which measures the contribution from each natural mode of vibration to indicate the likely maximum response of an essentially elastic structure. Response spectrum analysis provides insight into dynamic behavior by measuring pseudo spectral acceleration, velocity or displacement as a function of structural period for a given history and level of damping. It is practical to response spectra such that a smooth curve represents the peak response for each realization of structural period [1].

Response-spectrum analysis is useful for design decision-making because it relates structural type-selection to dynamic performance. Structures of shorter period experience greater acceleration, whereas those of longer period experience greater displacement. Structural performance objectives should be taken into account during preliminary design and response-spectrum analysis [1].

In this section, response spectrum analyses are performed for each RUN where the response spectra of each RUN are used as input. Response spectrum analyses are performed to calculate the tensile stresses in the model. These calculated tensile stresses show how big the stresses in the model are. With this information it is possible to see where the concrete model will crack, if the concrete cracks, and where the reinforcement will yield, if the reinforcement yields, when nonlinear transient analyses are performed for each RUN in stage 3.

In the upcoming sections, contour plots of the tensile stresses of the concrete model and the reinforcement are shown. The contour plots of the concrete model, from a certain RUN, show where in the model the tensile stresses are higher then the tensile strength (2.4 MPa) of concrete. So when performing nonlinear transient analysis for a certain RUN, then the concrete will probably crack in these high tensile stress areas. The contour plots of the stress distribution of the reinforcement, for a certain RUN, show where the reinforcement yields, if the reinforcement yields, when performing nonlinear transient analysis for that RUN.

In advance it can be said that the contour plots from each RUN which give the tensile stresses in the concrete model show the same stress pattern. Dependent of the intensity of each RUN the stresses differ in magnitude in terms of areas which they cover but the stress patterns are the same. For the low intensity RUNs, the contour plots will show that the lower front part of wall V04 and the lower part of wall V02 are loaded very heavily. The stresses in these parts are higher then 2.4 MPa.. Also the lower parts of walls V01 and V03 show high tensile stresses. Other interesting observations will be that all edges of the openings and the connections between the columns and floors show high stress concentrations. The connection between the foundation and the walls are also loaded heavily. When the intensity of the RUNs increase the stresses will develop from the same areas as the low intensity RUNs and expand itself to the other parts of the model. Further can be said that none of the RUNs show yielding of the reinforcement but it will show where in the model the reinforcement is loaded relatively heavy.

In summary it can be said that the results of the RSA from this section give an indication where the model might reach its capacity when performing nonlinear transient analyses.

6.5.1 Linear Response with Respect to RUN9 Response Spectrum

The contour plots which are shown below are calculated using the response spectrum of RUN9 as input. When performing nonlinear transient analysis in stage 3 using RUN9, the model will probably crack in the areas where the tensile stresses are (much) higher then the tensile strength of concrete.
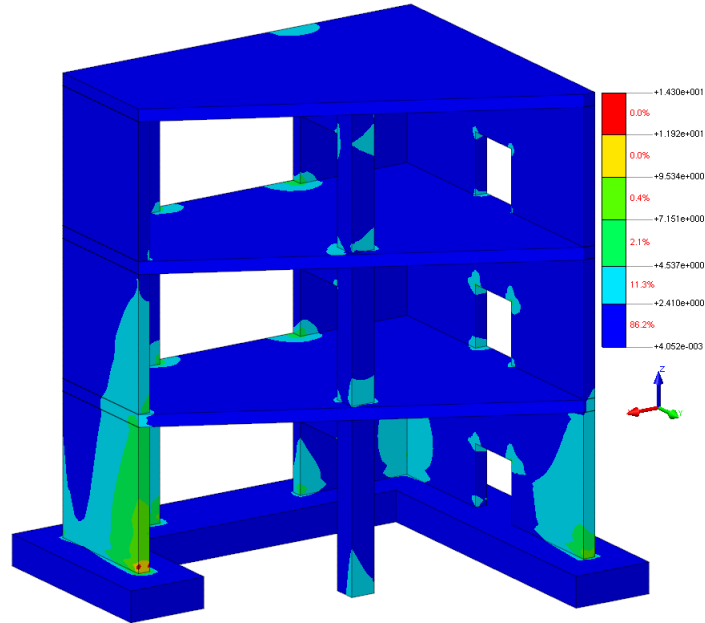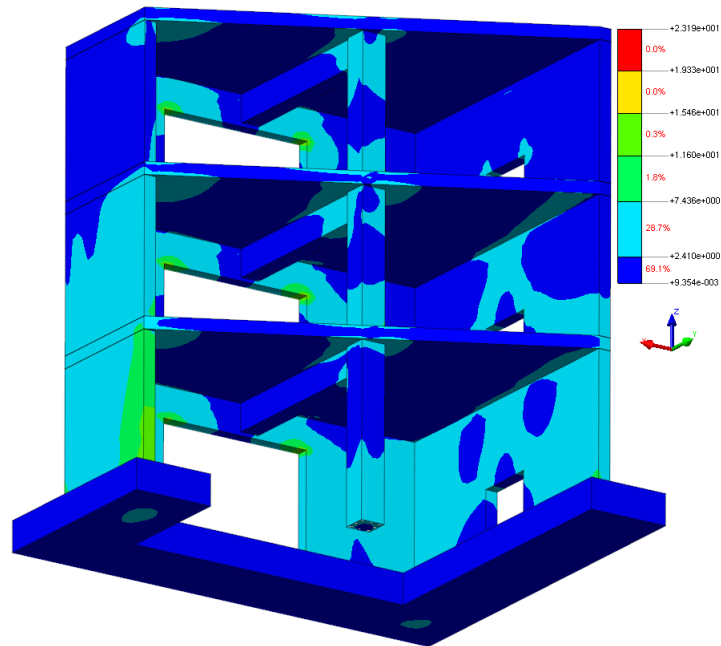

Figure 6.52: Principle stresses in S1 in N/mm^2.
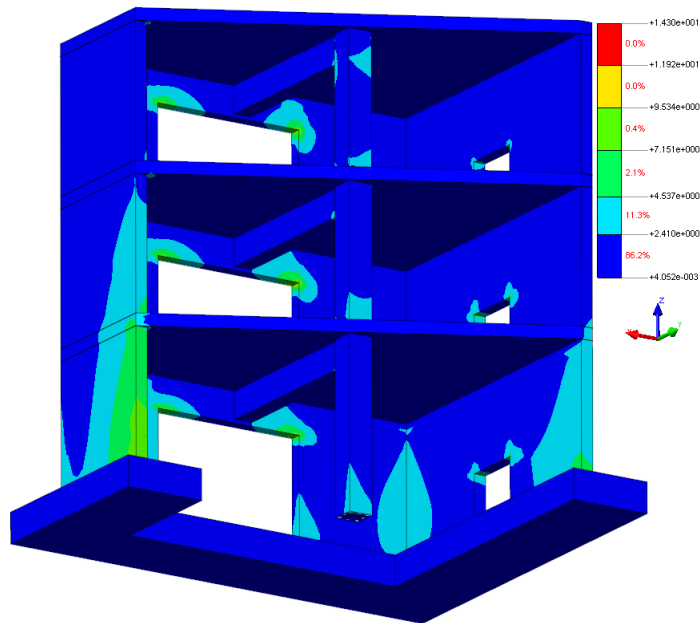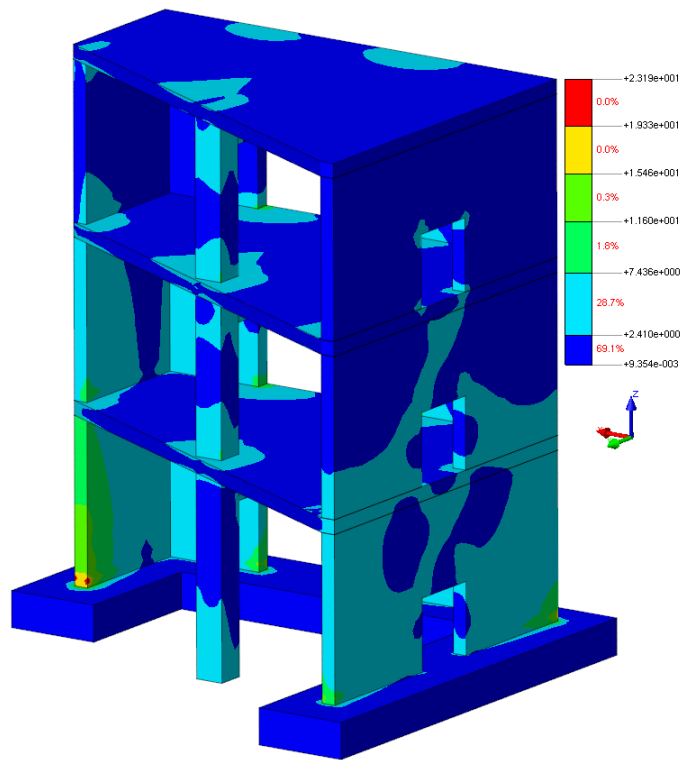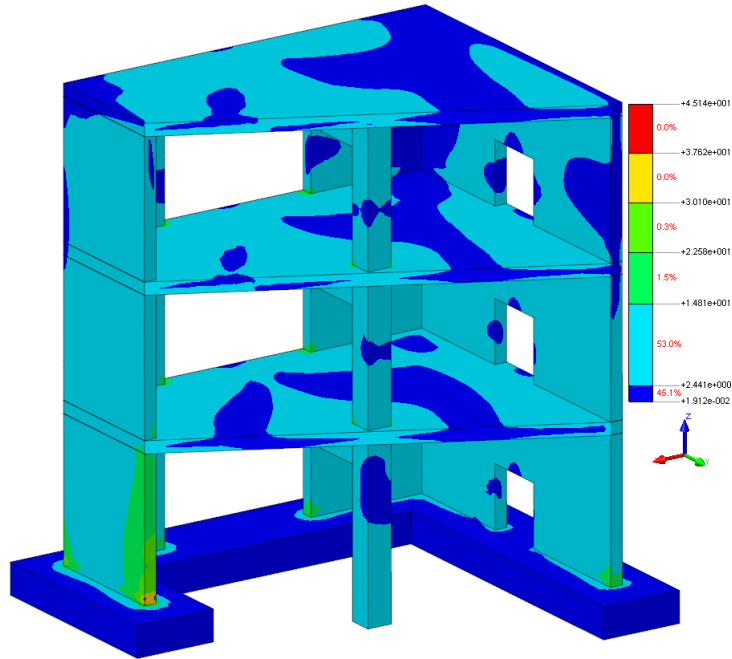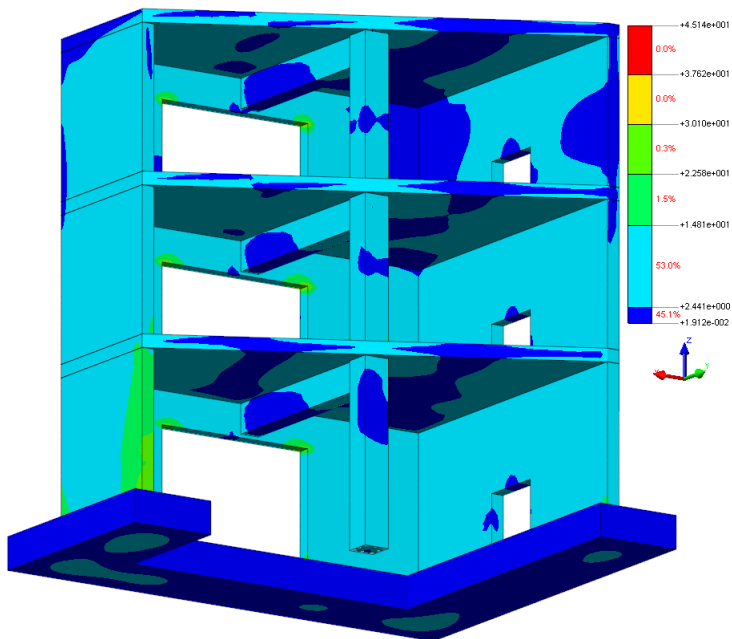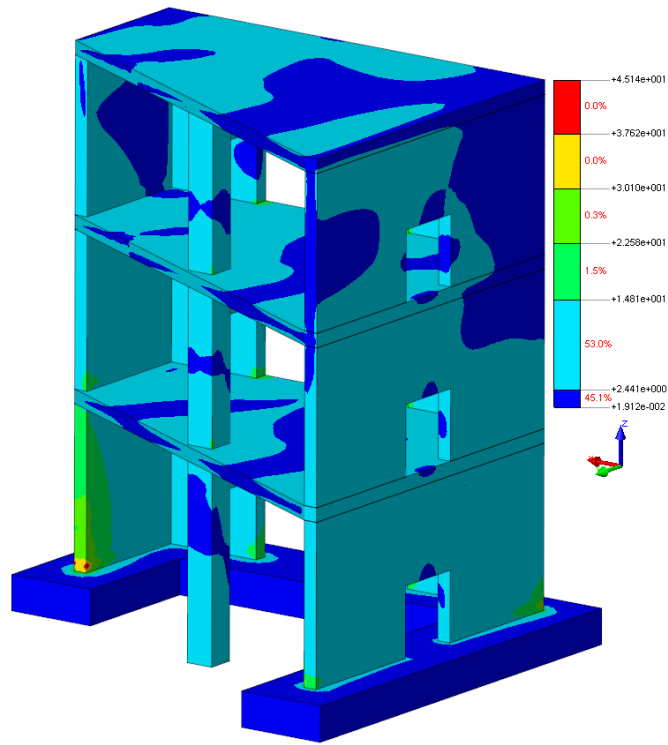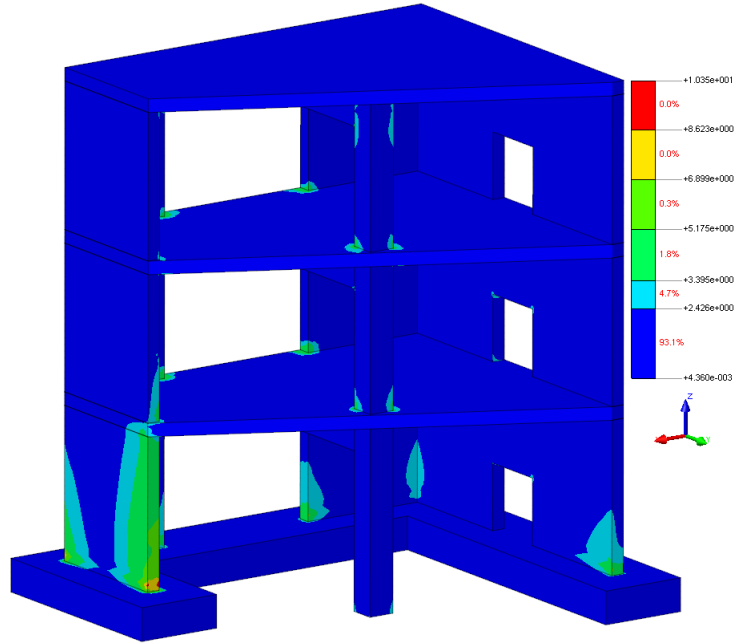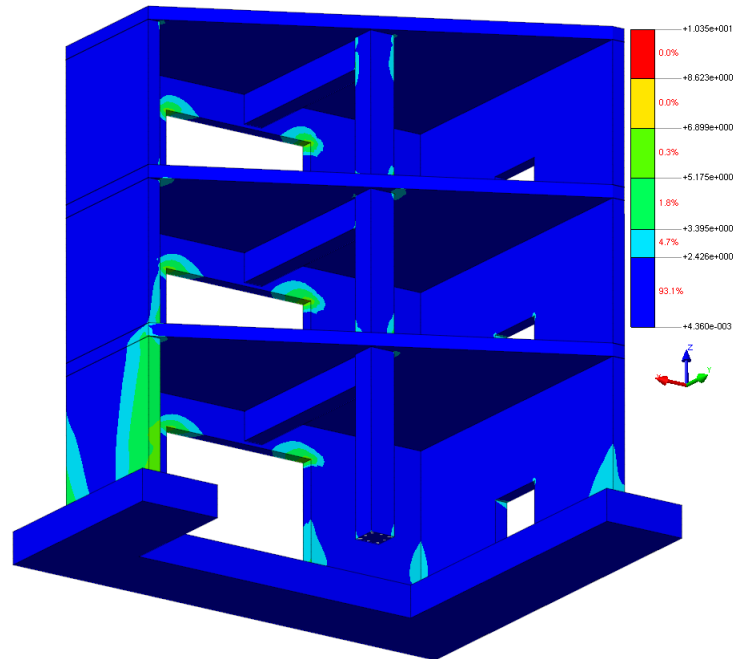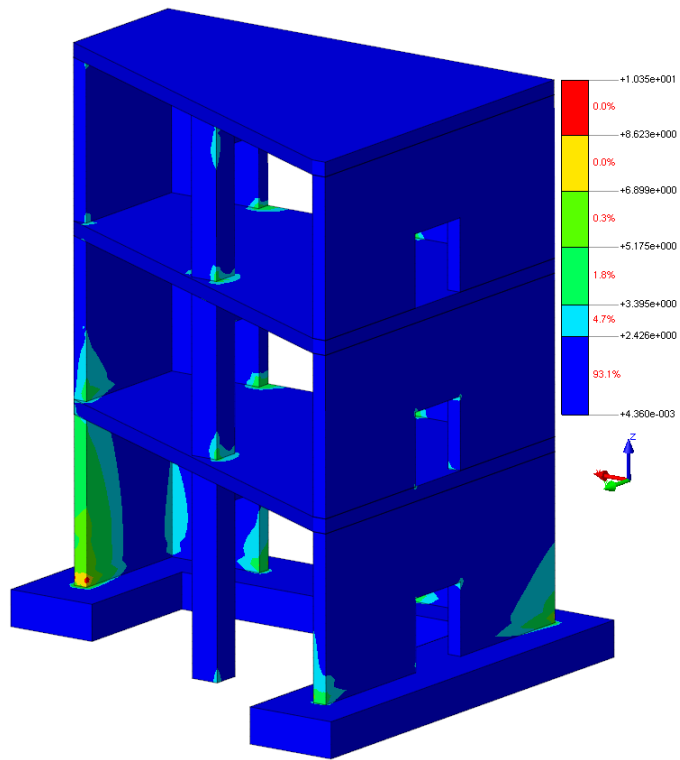

Figure 6.53: Principle stresses in S1 in N/mm^2.
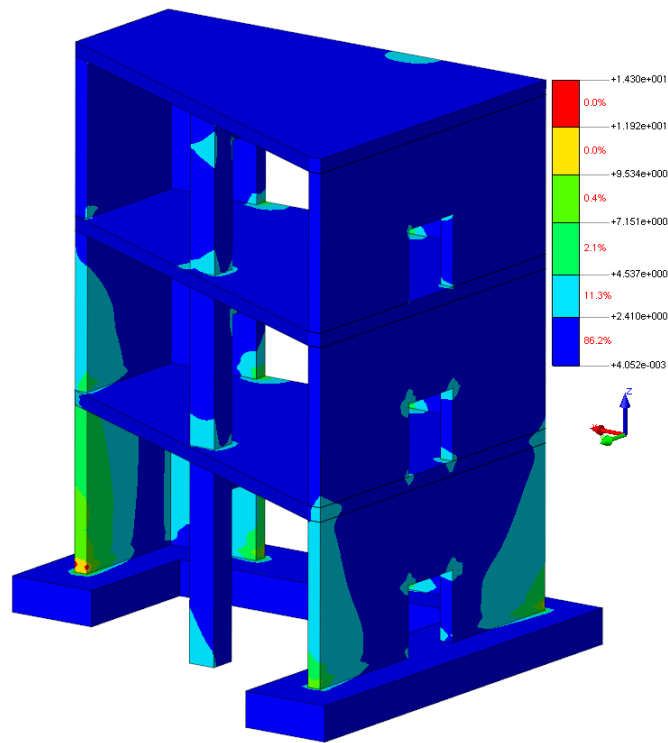
Figure 6.54: Principle stresses in S1 in N/mm^2.
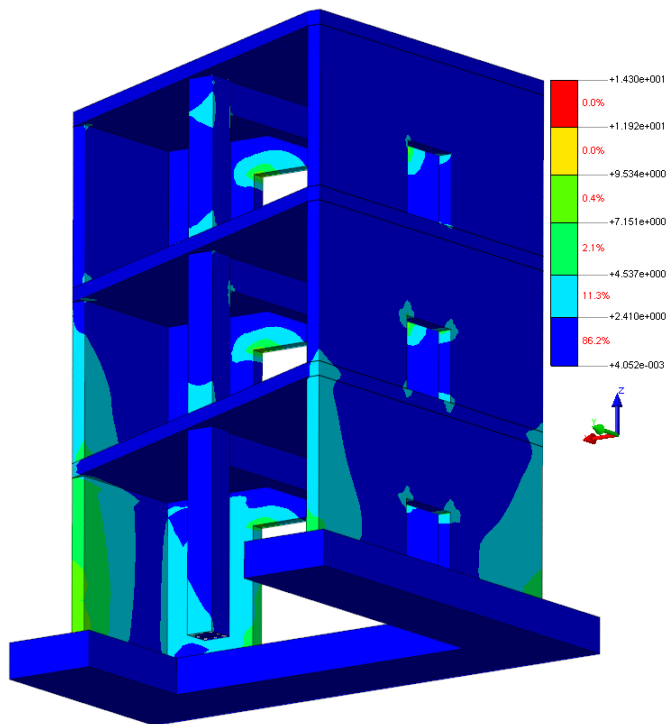
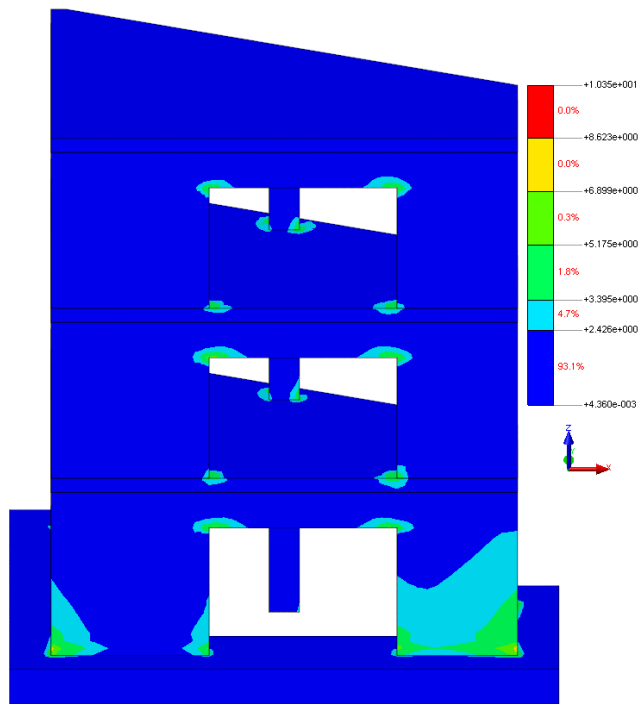Figure 6.55: Principle stresses in S1 in N/mm^2.
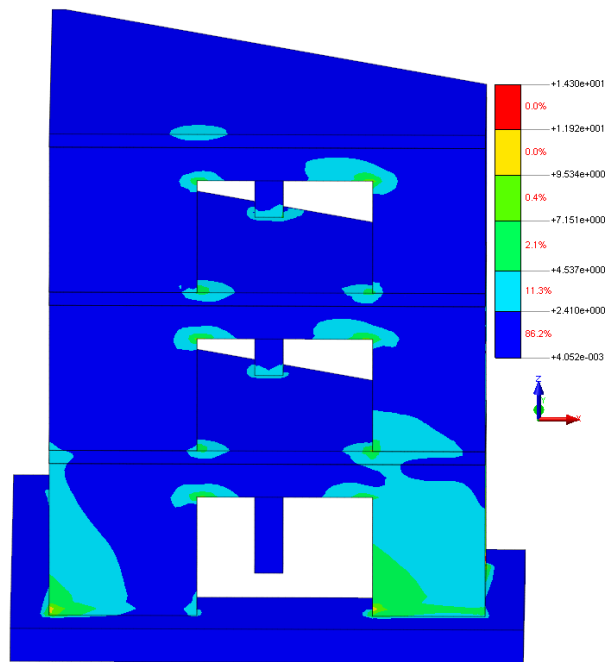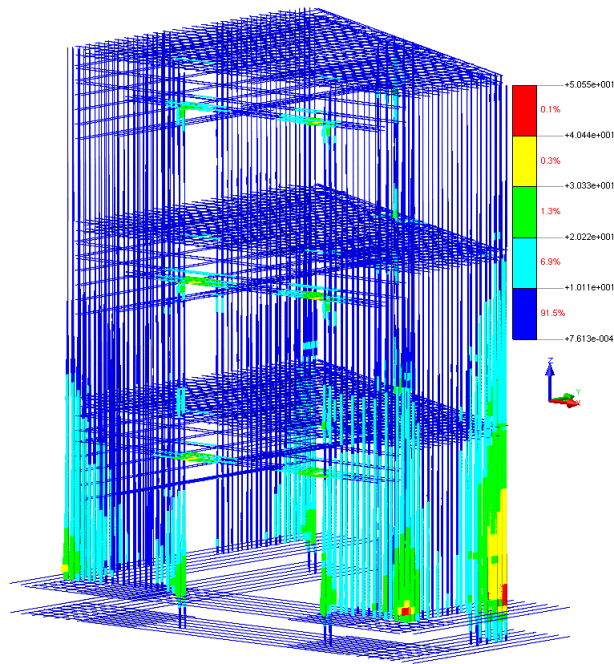
Figure 6.56: Principle stresses in S1 in N/mm^2.
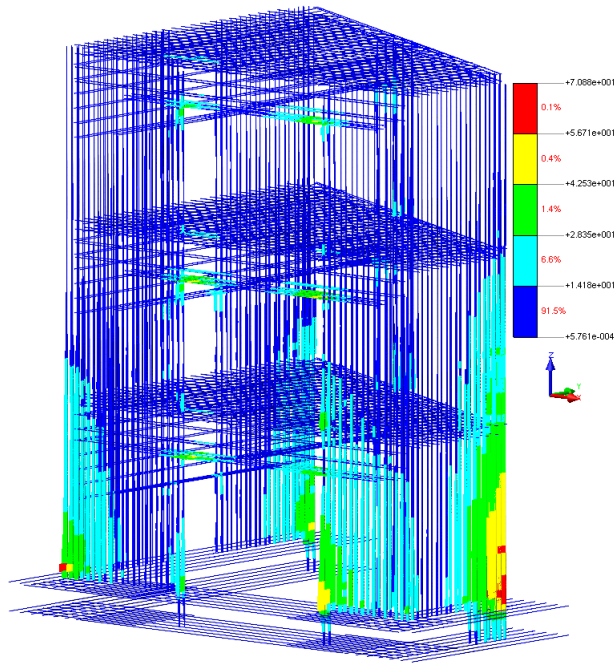
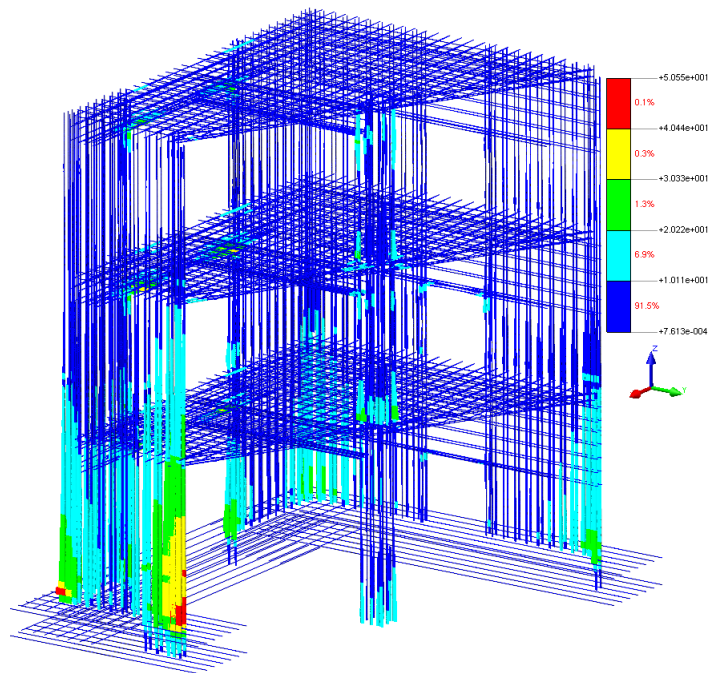Figure 6.57: Stresses in reinforcement in N/mm^2.
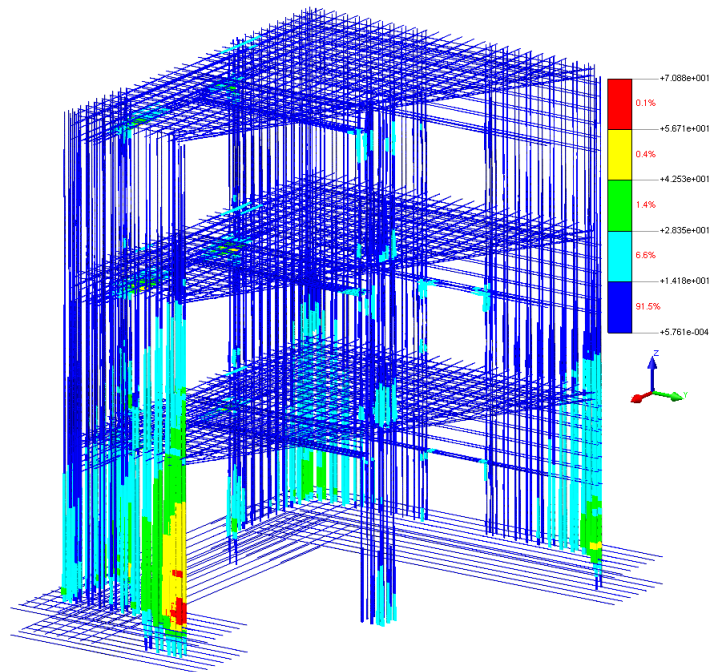
Figure 6.58: Stresses in reinforcement in N/mm^2.

6.5.2   Linear Response with Respect to RUN11 Response Spectrum

The contour plots which are shown below are calculated using the response spectrum of RUN11 as input. When performing nonlinear transient analysis in stage 3 using RUN11, the model will probably crack in the areas where the tensile stresses are (much) higher then the tensile strength of concrete.
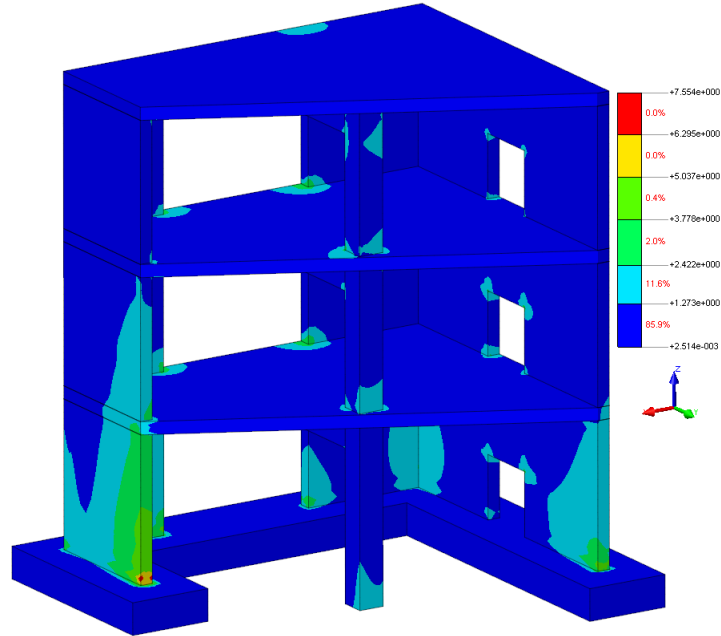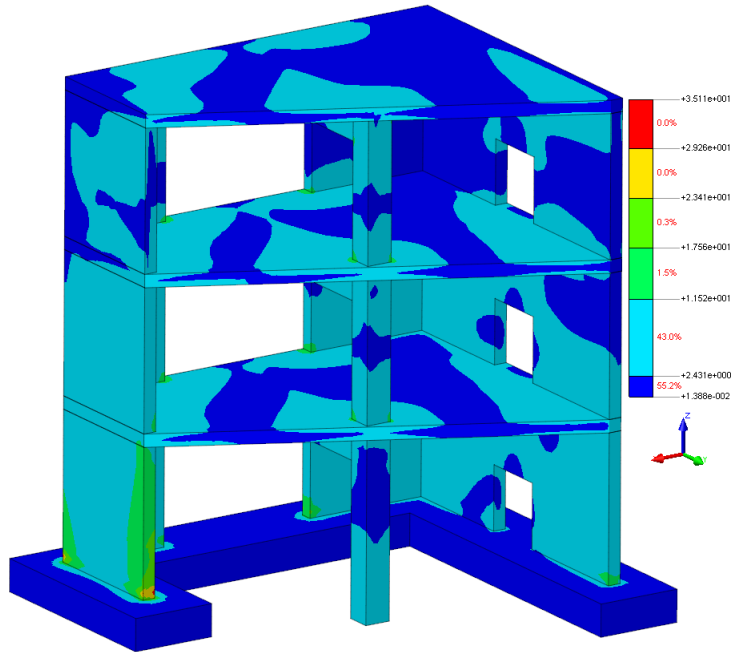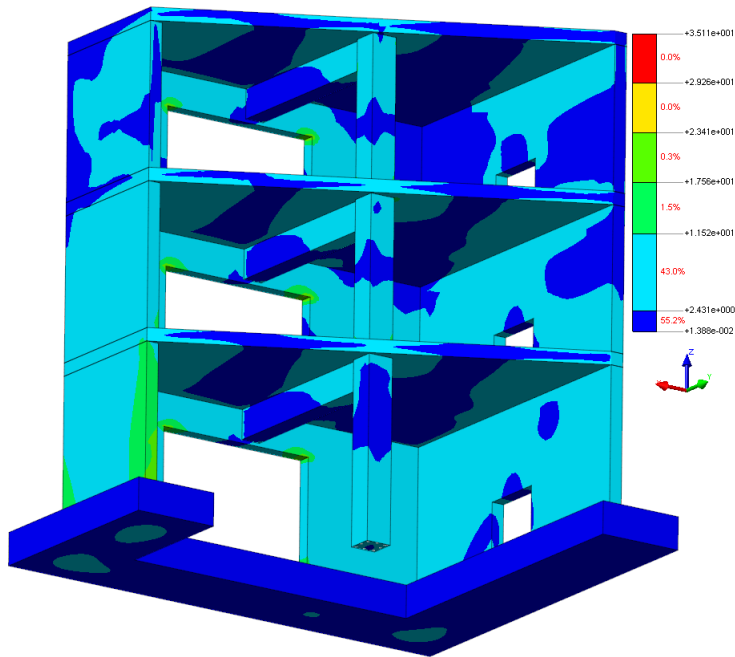

Figure 6.59: Principle stresses in S1 in N/mm^2.
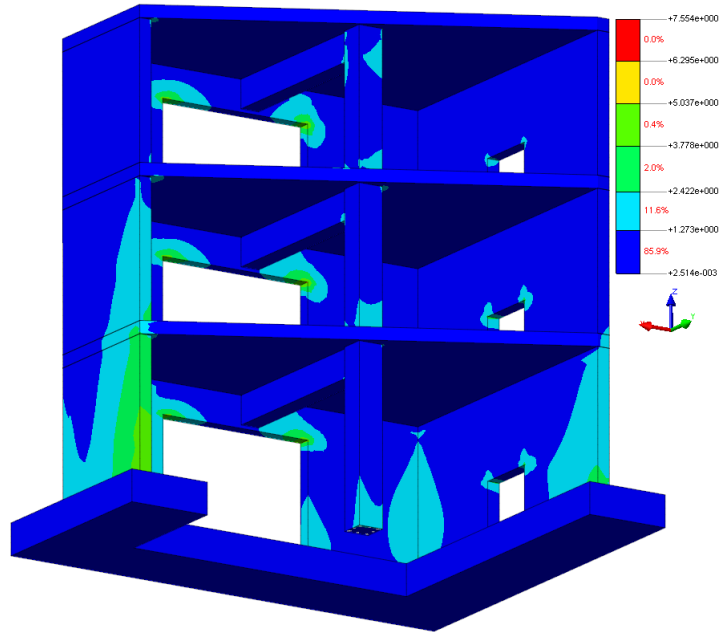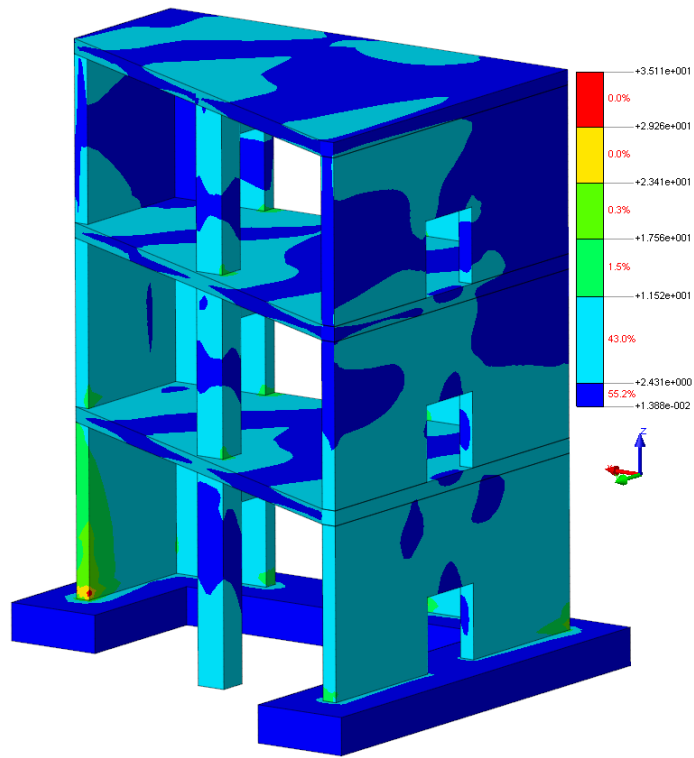

Figure 6.60: Principle stresses in S1 in N/mm^2.
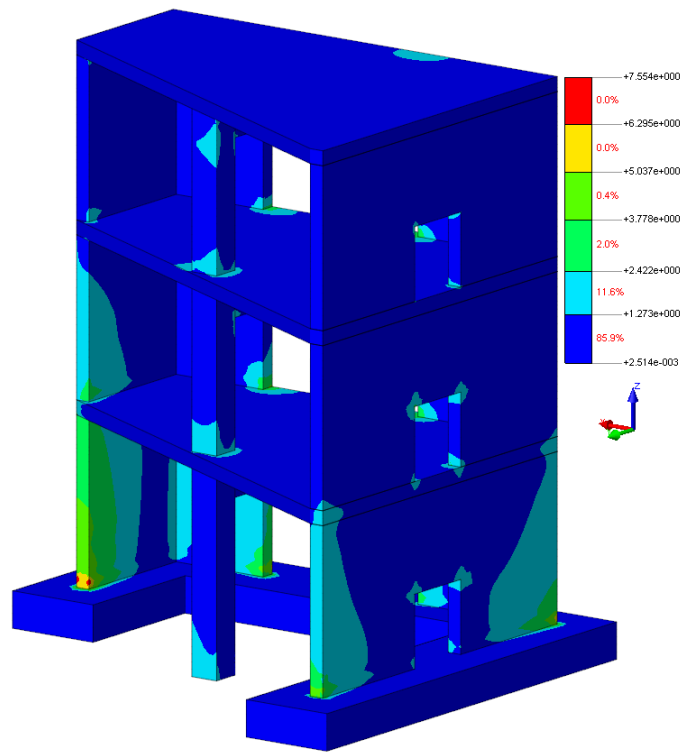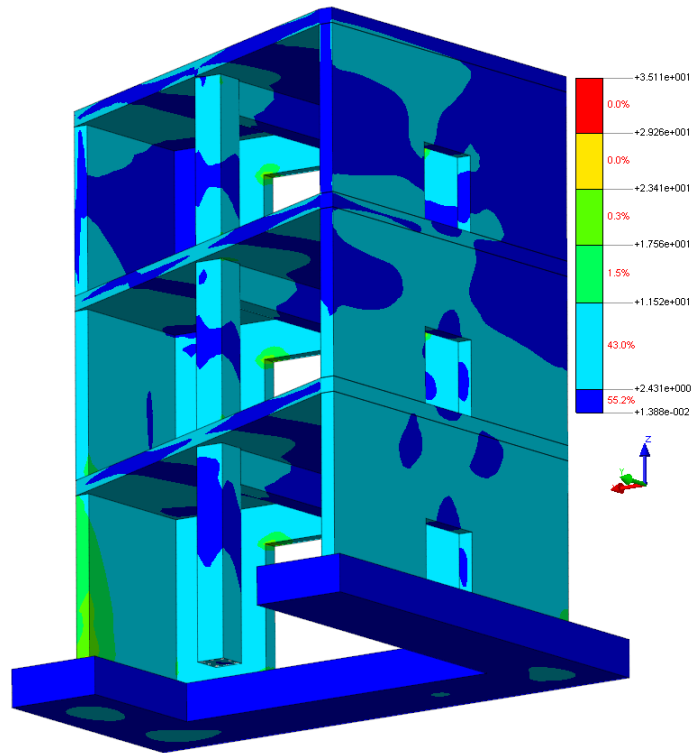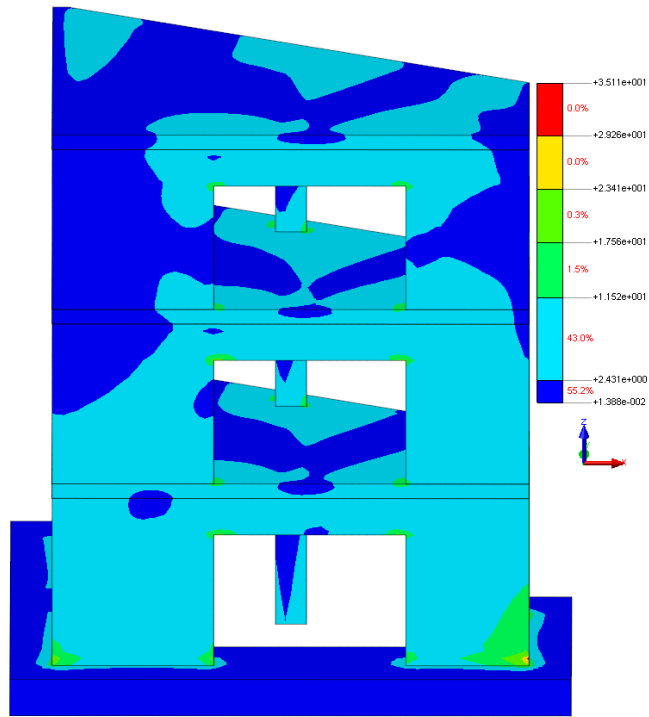
Figure 6.61: Principle stresses in S1 in N/mm^2.
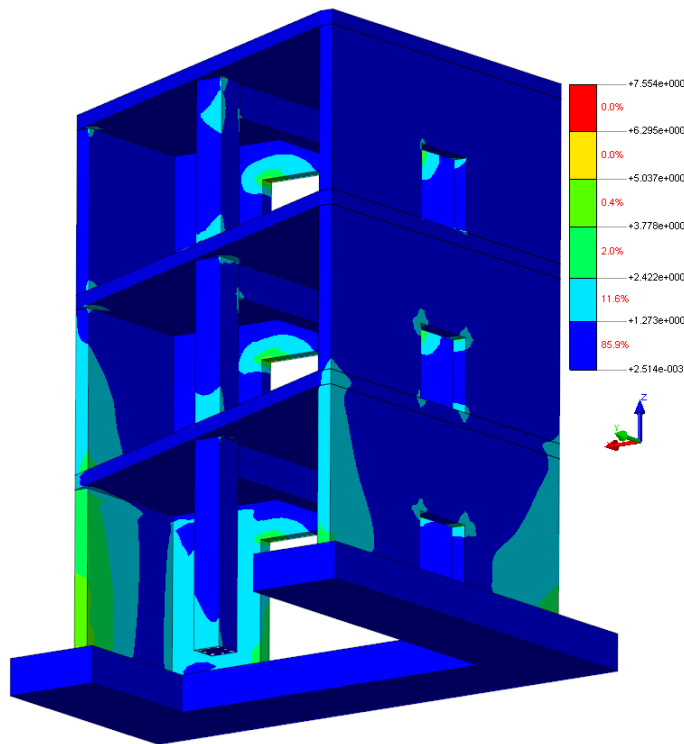
Figure 6.62: Principle stresses in S1 in N/mm^2.
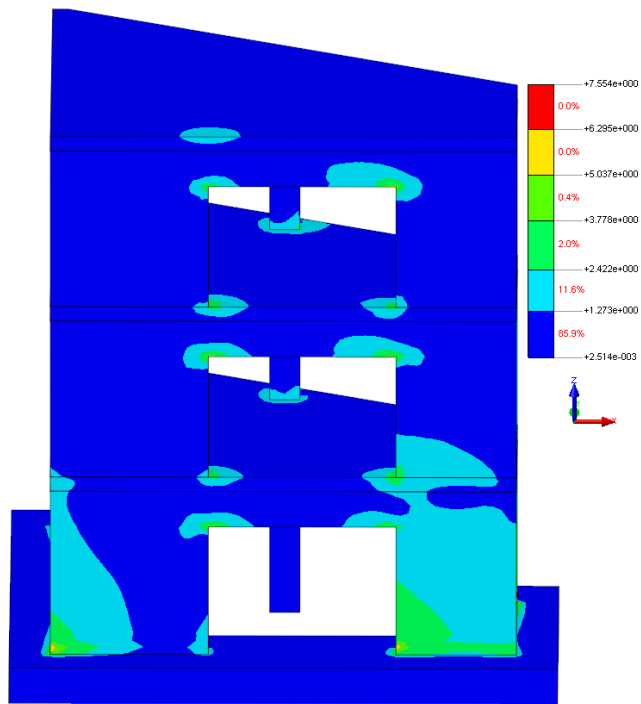
Figure 6.63: Principle stresses in S1 in N/mm^2.
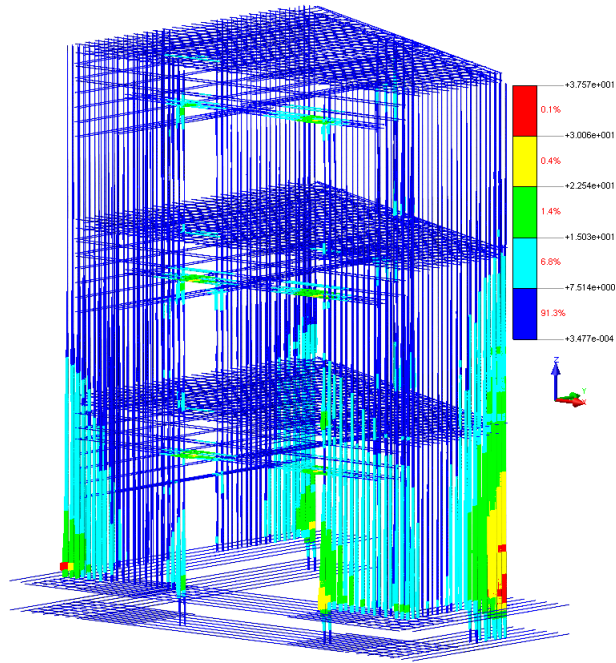
Figure 6.64: Stresses in reinforcement in N/mm^2.
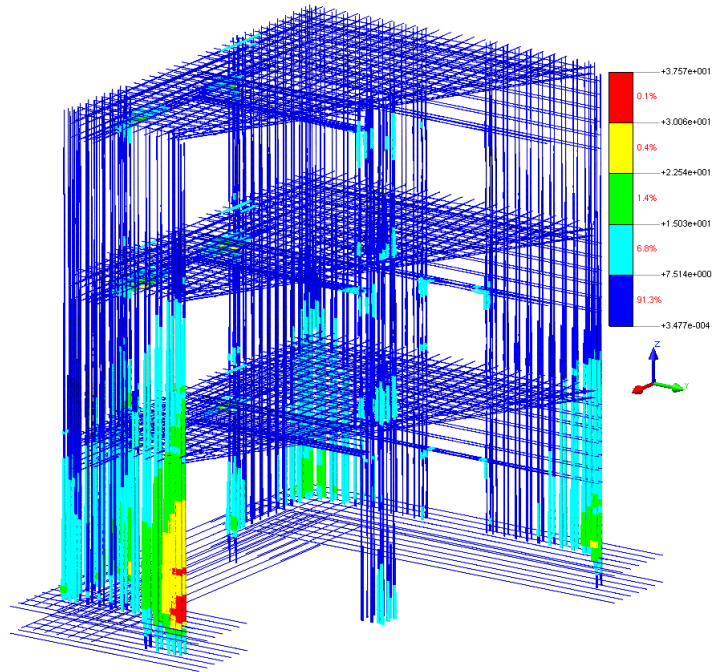
Figure 6.65: Stresses in reinforcement in N/mm^2.

6.5.3 Linear Response with Respect to RUN13 Response Spectrum

The contour plots which are shown below are calculated using the response spectrum of RUN13 as input. When performing nonlinear transient analysis in stage 3 using RUN13, the model will probably crack in the areas where the tensile stresses are (much) higher then the tensile strength of concrete.
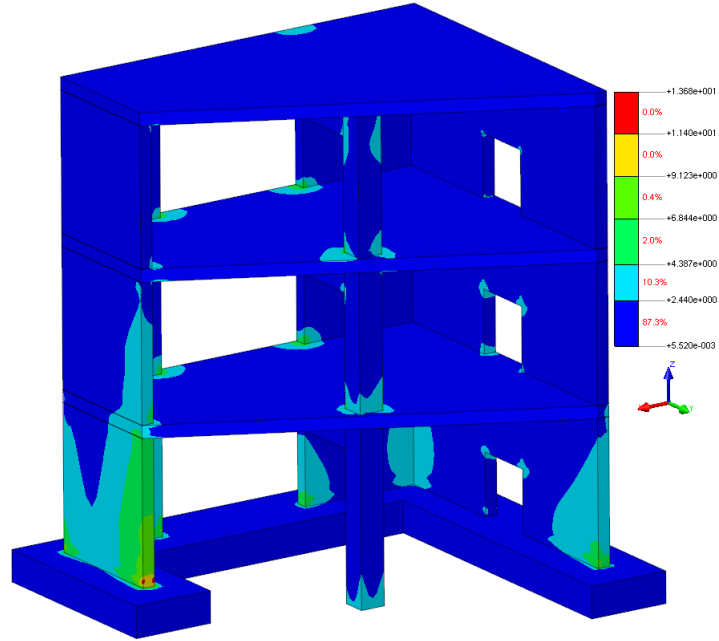
Figure 6.66: Principle stresses in S1 in N/mm^2.
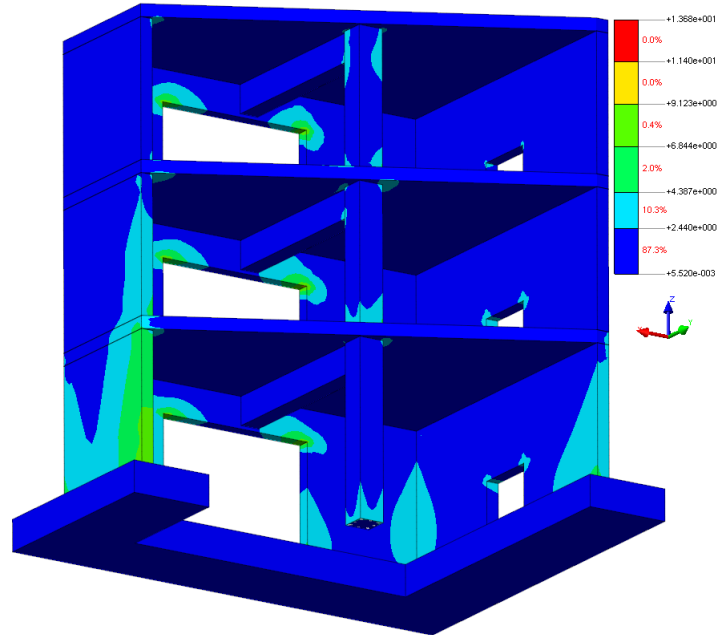
Figure 6.67: Principle stresses in S1 in N/mm^2.
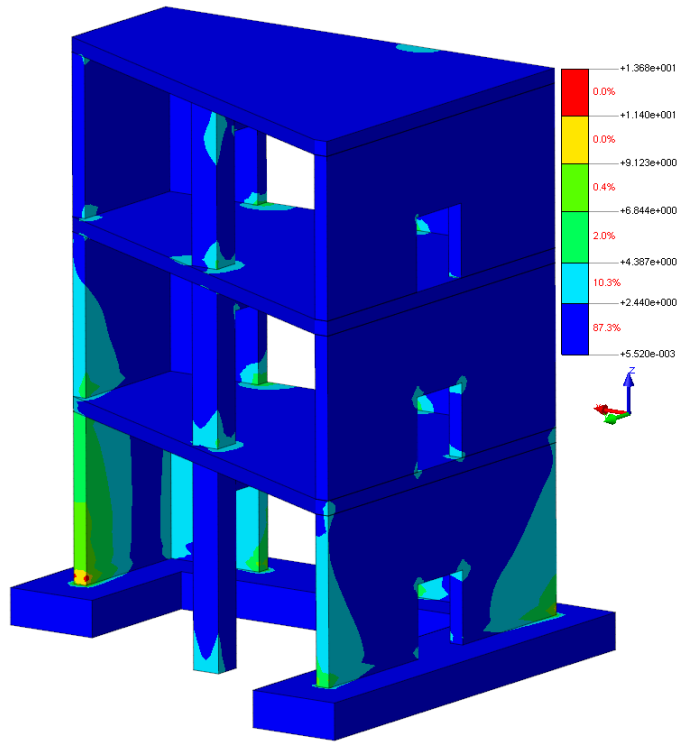
Figure 6.68: Principle stresses in S1 in N/mm^2.
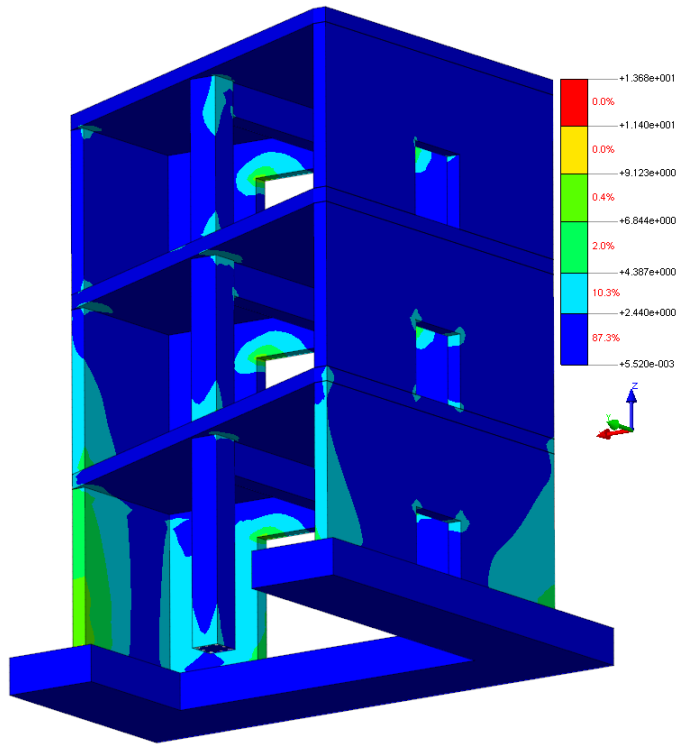
Figure 6.69: Principle stresses in S1 in N/mm^2.
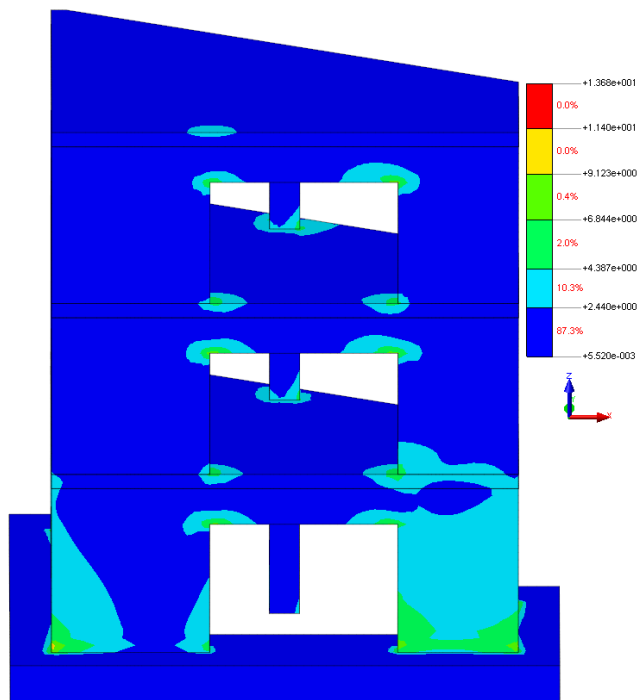
Figure 6.70: Principle stresses in S1 in N/mm^2.
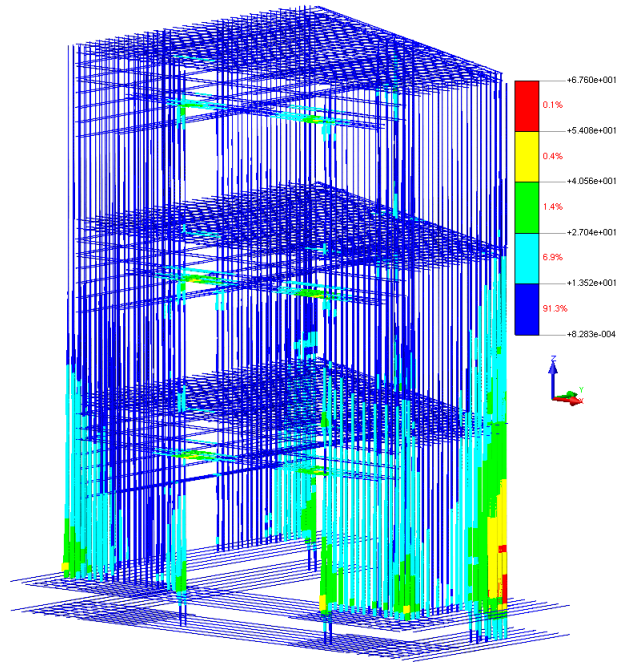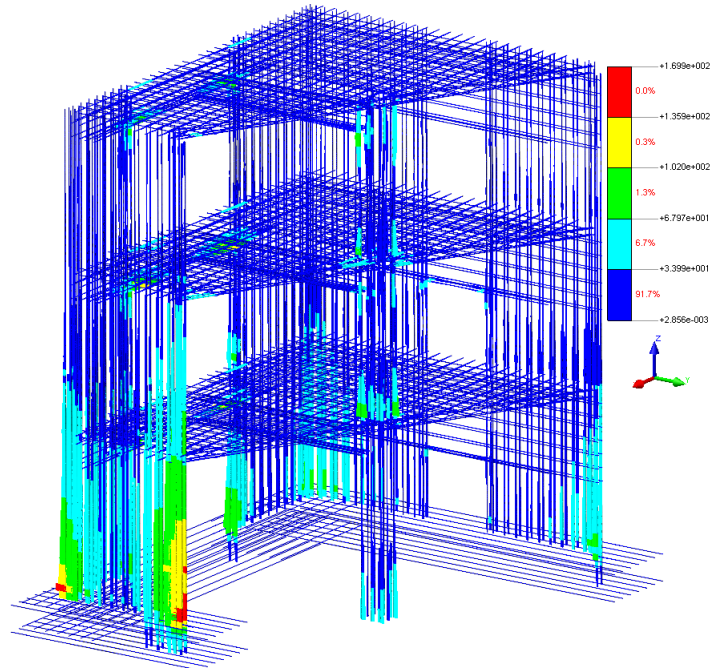
Figure 6.71: Stresses in reinforcement in N/mm^2.
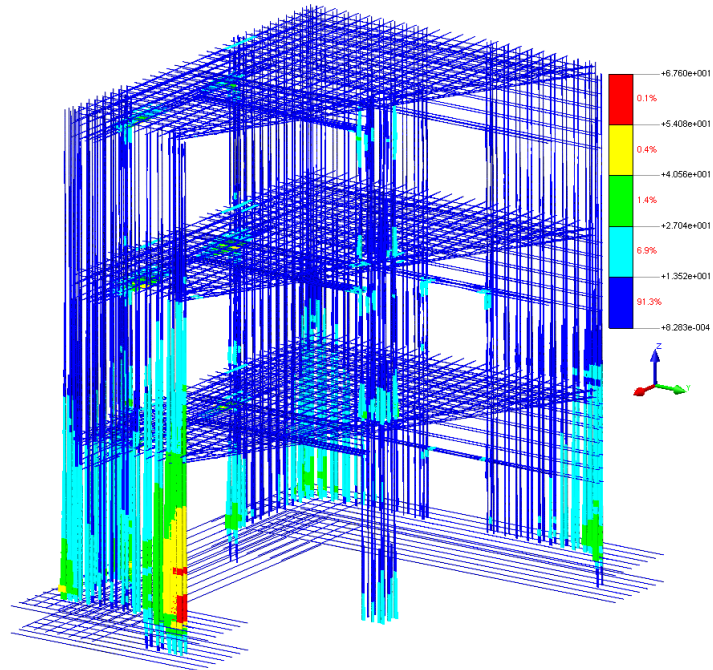
Figure 6.72: Stresses in reinforcement in N/mm^2.

6.5.4 Linear Response with Respect to RUN17 Response Spectrum

The contour plots which are shown below are calculated using the response spectrum of RUN17 as input. When performing nonlinear transient analysis in stage 3 using RUN17, the model will probably crack in the areas where the tensile stresses are (much) higher then the tensile strength of concrete.
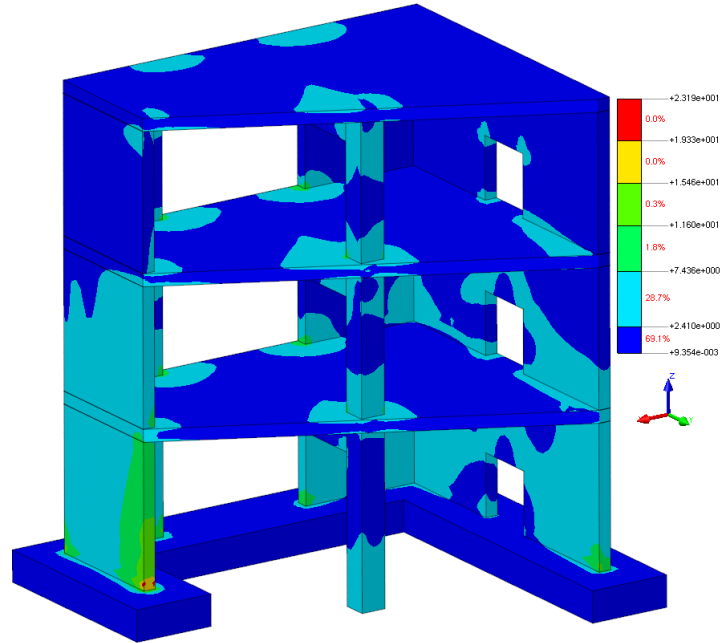
Figure 6.73: Principle stresses in S1 in N/mm^2.

Figure 6.74: Principle stresses in S1 in N/mm^2.

Figure 6.75: Principle stresses in S1 in N/mm^2.
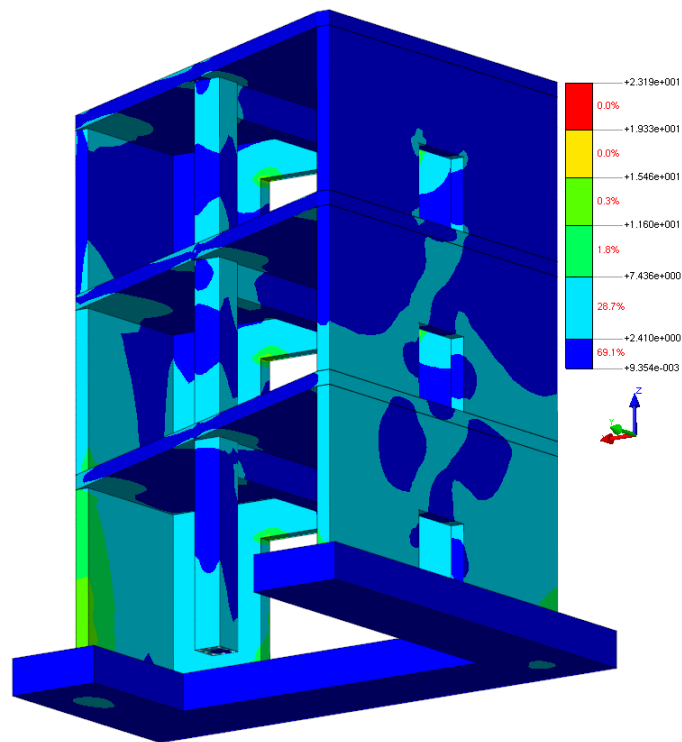
Figure 6.76: Principle stresses in S1 in N/mm^2.
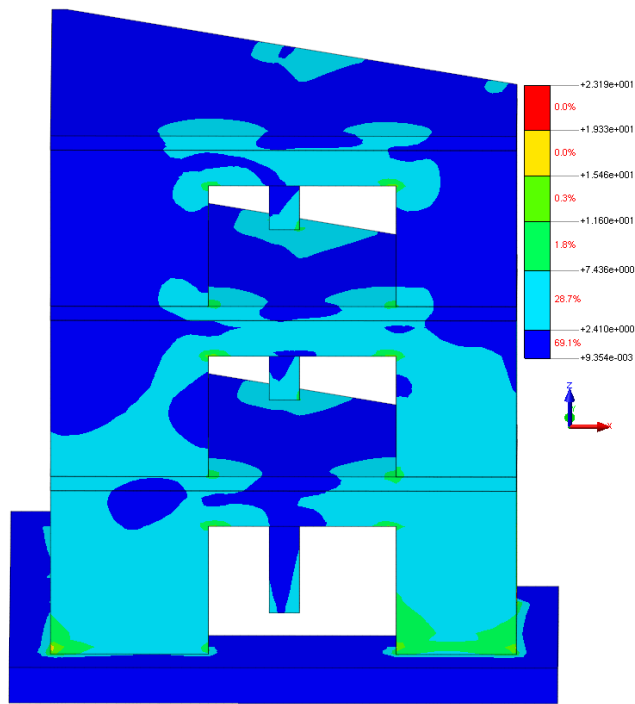
Figure 6.77: Principle stresses in S1 in N/mm^2.
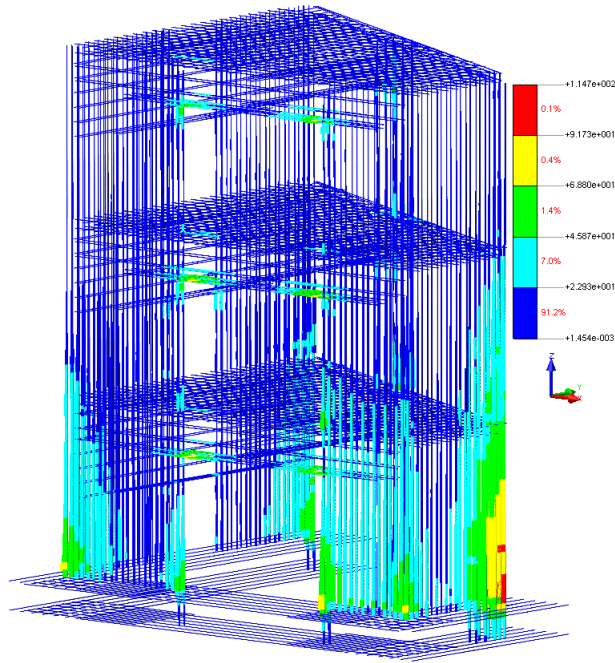
Figure 6.78: Stresses in reinforcement in N/mm^2.
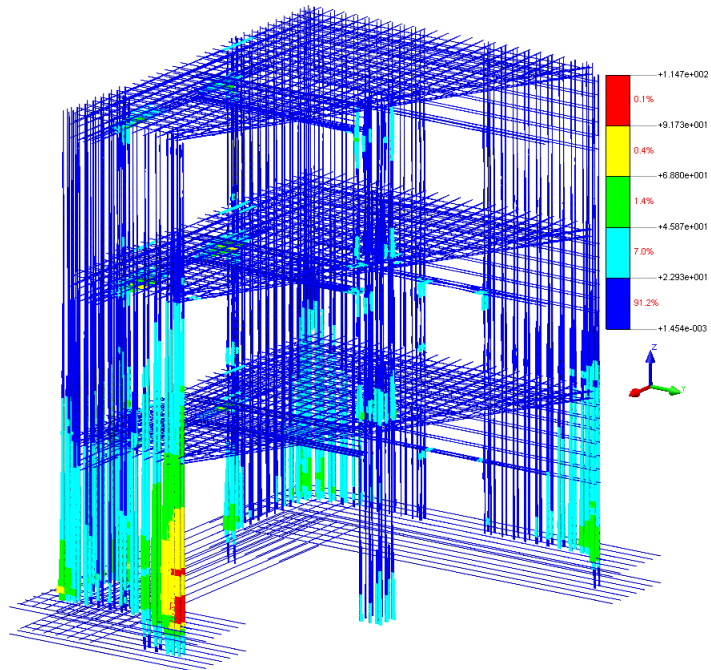
Figure 6.79: Stresses in reinforcement in N/mm^2.

6.5.5 Linear Response with Respect to RUN19 Response Spectrum

The contour plots which are shown below are calculated using the response spectrum of RUN19 as input. When performing nonlinear transient analysis in stage 3 using RUN19, the model will probably crack in the areas where the tensile stresses are (much) higher then the tensile strength of concrete.

Figure 6.80: Principle stresses in S1 in N/mm^2.

Figure 6.81: Principle stresses in S1 in N/mm^2.

Figure 6.82: Principle stresses in S1 in N/mm^2.
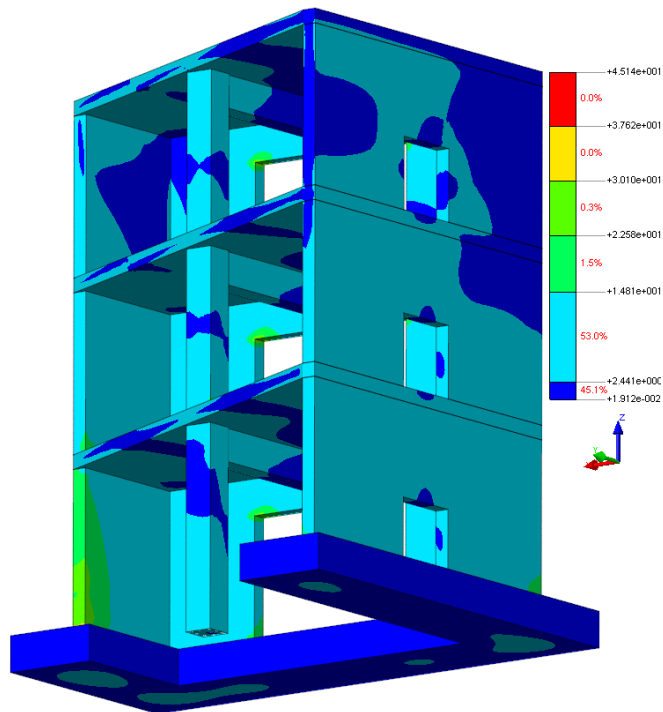
Figure 6.83: Principle stresses in S1 in N/mm^2.
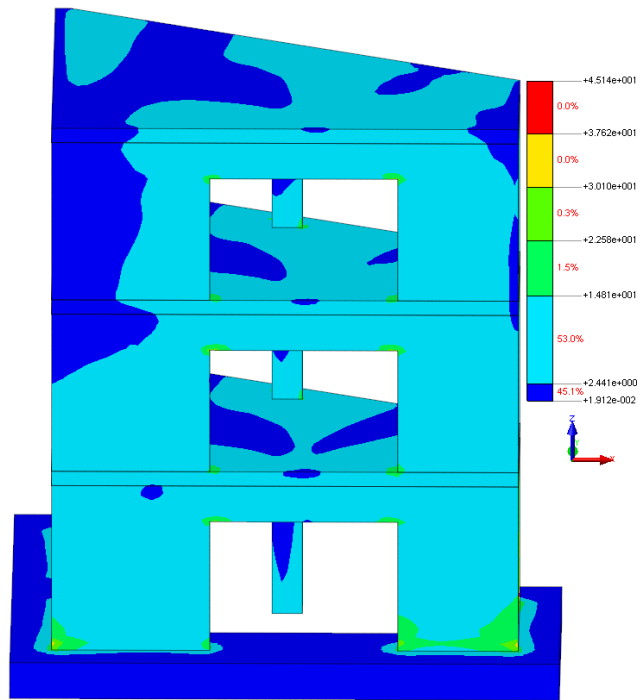
Figure 6.84: Principle stresses in S1 in N/mm^2.
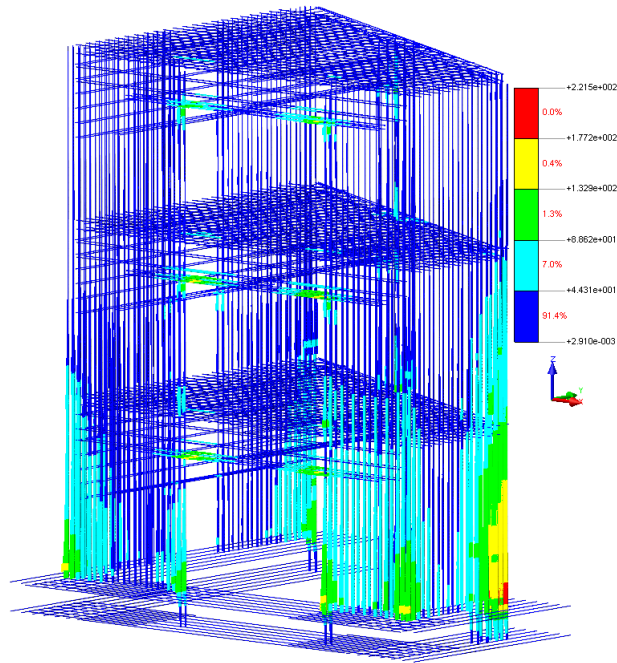
Figure 6.85: Stresses in reinforcement in N/mm^2.
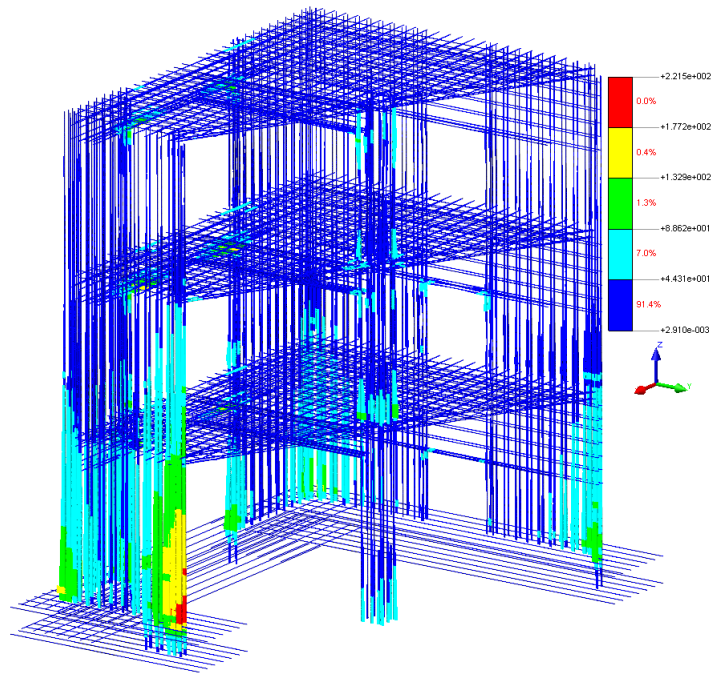
Figure 6.86: Stresses in reinforcement in N/mm^2.

6.5.6 Linear Response with Respect to RUN21 Response Spectrum

The contour plots which are shown below are calculated using the response spectrum of RUN21 as input. When performing nonlinear transient analysis in stage 3 using RUN21, the model will probably crack in the areas where the tensile stresses are (much) higher then the tensile strength of concrete.

Figure 6.87: Principle stresses in S1 in N/mm^2.

Figure 6.88: Principle stresses in S1 in N/mm^2.

Figure 6.89: Principle stresses in S1 in N/mm^2.
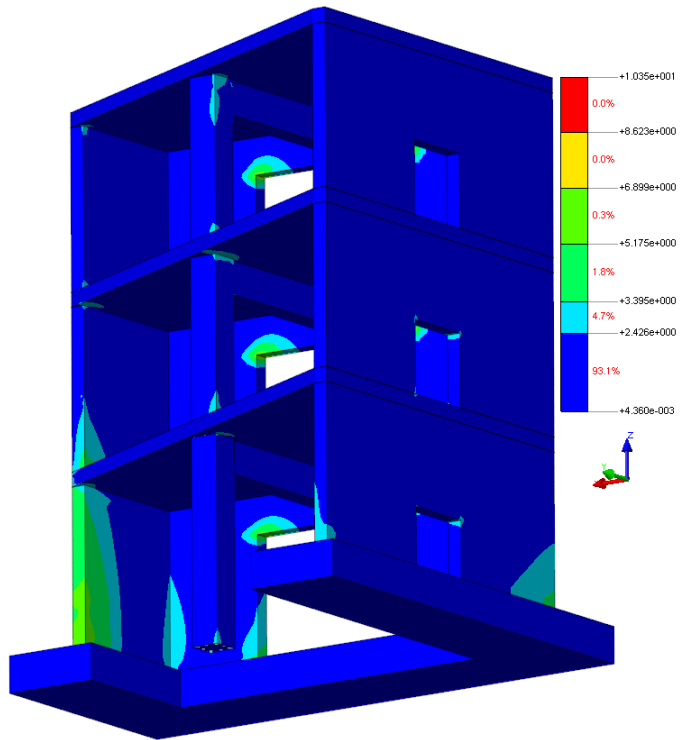
Figure 6.90: Principle stresses in S1 in N/mm^2.

Figure 6.91: Principle stresses in S1 in N/mm^2.

Figure 6.92: Stresses in reinforcement in N/mm^2.

Figure 6.93: Stresses in reinforcement in N/mm^2.

6.5.7 Linear Response with Respect to RUN23 Response Spectrum

The contour plots which are shown below are calculated using the response spectrum of RUN23 as input. When performing nonlinear transient analysis in stage 3 using RUN23, the model will probably crack in the areas where the tensile stresses are (much) higher then the tensile strength of concrete.

Figure 6.94: Principle stresses in S1 in N/mm^2.

Figure 6.95: Principle stresses in S1 in N/mm^2.

Figure 6.96: Principle stresses in S1 in N/mm^2.

Figure 6.97: Principle stresses in S1 in N/mm^2.

149

Figure 6.98: Principle stresses in S1 in N/mm^2.
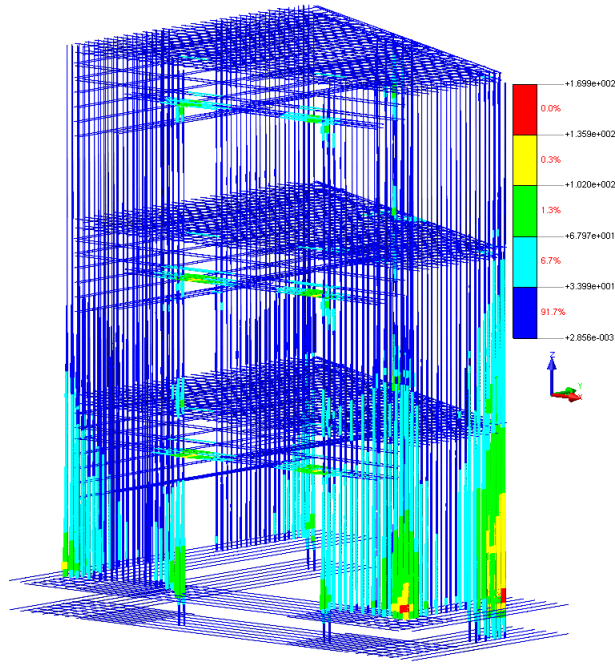
Figure 6.99: Stresses in reinforcement in N/mm^2.

Figure 6.100: Stresses in reinforcement in N/mm^2.

6.6 Summary Stage 2

To calibrate the finite element model with the reinforced concrete mock-up, eigenvalue analyses are performed. In the eigenvalue analyses, the numerical natural frequencies of the model together with the corresponding mode shapes for the first three modes are compared with the provided experimental natural frequencies of the mock-up together with the corresponding mode shapes for case 3. Lets look at the natural frequencies.

Table 6.23: Natural frequencies - total E-modulus.

Mode	Experimental [Hz]	Numerical [Hz]	Difference [%]
1	6.5	7.02	8
2	9.5	10.06	6
3	-	20.59	-

This table shows that the differences of 8% and 6% between the first two numerical and experimental natural frequencies arr so big. This difference can be further reduced by using a reduced E-modulus of the model. According to Model Code 2010, 85% the E-modulus of the model should be used when performing an elastic linear analysis in order to account for initial plastic strain, causing some irreversible deformations. The natural refquencies of the model with reduced E-modulus are given below.

Table 6.24: Natural frequencies - 85% E-modulus.

Mode	Experimental [Hz]	Numerical [Hz]	Difference [%]
1	6.5	6.66	3
2	9.5	9.68	2
3	-	19.72	-

These experimental natural frequencies are obtained by performing a DFT on RUN7 and the response of the mock-up to RUN7 on floor 3 in point D. Lets consider table 8.2. The first and second natural frequencies are obtained but the third one couldn't be obtained. But looking at the first and second natural frequencies, it can be seen that the difference between the first numerical and experimental natural frequencies is 3% and the difference between the second numerical natural frequency and experimental natural frequency is 2%. The differences are not big and acceptable. It is also interesting to see how the mode shapes of the model looks like. The following figures show this. Please note that the mode shapes from below correspond to the model of the mock-up + shaking table but the shaking table is not shown.

Figure 6.101: Mode shape 1.
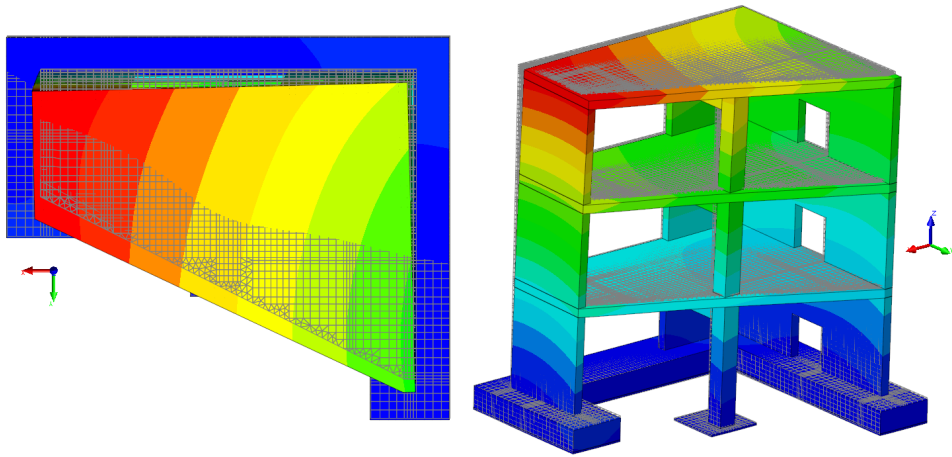
Figure 6.102: Mode shape 2.
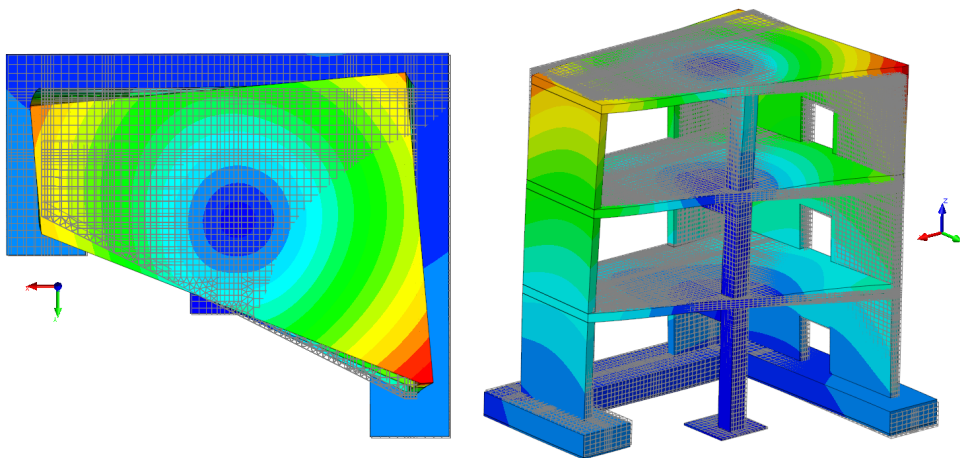
Figure 6.103: Mode shape 3.

For the linear transient analysis, comparisons are made between the numerical responses (in terms of displacements and accelerations) of the model to RUN6 and RUN7 with the experimental responses of the mock-up to RUN6 and RUN7 on floor 3 in point D. The match between the numerical responses and the experimental responses was good as shown in the previous sections of this stage.

It appears that it is important to calibrate the finite element model as good as possible with the real mock-up in order to make reliable predictions of the dynamic behavior of the mock-up. The match between the numerical responses and the experimental responses to RUN6 and RUN7 showed that the match was good. This nice match was only possible because of the calibration of the finite element model using the results of the eigenvalue analyses.

At last, response spectrum analyses are performed to calculate the tensile stresses in the model. These calculated tensile stresses show how big the tensile stresses in the model are. With this information it is possible to see where the concrete model will crack (when the concrete cracks) and where the reinforcement will yield (when the reinforcement yields) when nonlinear transient analyses for each RUN are performed. So this information obtained from RSA is very useful.

Hereby are research questions 3, 4, 5 and 6 answered. Research question 7 is partially answered here as the real usefulness and the power of RSA remains to be seen in stage 3 when analyzing the results of the nonlinear transient analyses. Also research question 8 is answered here.

7 Stage 3 - Nonlinear Response of the Model

This stage aims at evaluating the nonlinear response of the model under high intensity seismic loading. RUN9, RUN11, RUN13, RUN17, RUN19, RUN21 and RUN23 are used for the nonlinear transient analysis. The graphs of these RUNs are shown in appendix A.

All these RUNs were combined into one RUN with an interval of 1 second between these RUNs and then performed the nonlinear transient analysis as one analysis. The is done to take the *damage history* of the model into account. During the analysis, when the model was excited with RUN17 (after the excitation with RUN9, RUN11 and RUN13), the analysis diverged. Then the analyses with RUN19, RUN21 and RUN23 were performed separately. From these separate analyses only RUN21 converged, the others diverged. In order to let the analyses with RUN17, RUN19 and RUN23 converge, different things has been tried out. The following measures were taken but none of them helped the analyses converge:

- The model was given a higher Rayleigh damping in order to damp the excitation with higher damping ratios so the concrete will show lower responses.
- The concrete was given residual strength of 5% - 10% of its total strength. Giving concrete residual strength means that the concrete will keep this strength the whole time.
- The time steps were reduced twice the original time steps.
- The shaking table was set linear. After that the thickness of the shaking table was set 10 times higher.
- The embedded reinforcement was set linear.

The last measure which was taken was to use *bond-slip-reinforcement* instead of embedded reinforcement in order to take the shear forces. And this measure helped. This made sure that the nonlinear transient analysis with RUN17, RUN19 and RUN23 converged.

So RUN9, RUN11 and RUN13 are combined into one RUN, with 1 second interval between the RUNs, and performed as one analysis. The reason why this is done is to take the *damage history* of the model into account. RUN17, RUN19, RUN21 and RUN23 are performed separately. This is done because RUN17, RUN19 and RUN23 diverged in the beginning.

In the following sections the contour plots of the crackwidth are given in order to show where the model has cracked and how big these cracks (in mm) are. Together with the contour plots of the crackwidth for each RUN, the contour plots of the tensile stresses from the response spectrum analyses are given to show how good the response spectrum analysis is with describing the dynamic response of the model. The contour plots of the crackwidth are taken at the end of each RUN to show how the model has responded to the entire RUN and where the model has cracked.

Before showing the contour plots, the experimental response of the mock-up and the numerical response of the model are compared in terms of displacements to see how good the finite element model predicts the nonlinear response of the mock-up.

Also pushover analyses are performed in this section to estimate the seismic capacity of the model. Maybe the results of the pushover analyses can give insight in why RUN17, RUN19 and RUN23 diverged. So first the results of the pushover analyses are presented and then the results of the nonlinear transient analyses.

7.1 Pushover Analysis

In this section a pushover analysis is performed in order to estimate the seismic safety of the model. The idea here is to estimate the capacity of the model. For the pushover analysis it is important to know how and in which direction the model has to be loaded. That is why DIANA offers the following mode shape dependent load:

$$f_{push} = \sum_j a\mathbf{M}\Phi_i x_j \tag{17}$$

Where a is the specified acceleration, $\mathbf{M}$ is the mass matrix, Φ_i is the ith eigenmode (normalized with respect to the mass matrix) and x_j is the direction of the loading. This provides a load distribution over all elements that have a mass matrix. In this case, f_{push} will be a volume-load because the finite element model of the mock-up consists of 3D solid elements.

Before using f_{push}, an eigenvalue analysis has to be performed to determine the mode shapes and after that a nonlinear static analysis will be done. The pushover analysis will be a force-controlled analysis as f_{push} will be incrementally increased until the finite element model has reached its capacity.

Why using the mode shapes of the model to perform the pushover analysis? The reason for that is that the mode shapes are one of the natural characteristics of the model and when the model is loaded to seismic excitation's, the model will definitely vibrate at its natural frequencies and its corresponding mode shapes. In order to make a reasonable estimation of the seismic safety of the model, the mode shapes of the model are chosen at which the model will be loaded to its capacity.

Three pushover analyses (without the shaking table) are performed where the model is loaded to its capacity according to the first three mode shapes. For each mode shape, the governing direction is considered. The results of the pushover analyses are force-displacement diagrams in point D on floor 3. The forces are horizontal reaction forces and the displacements are the horizontal displacements in point D on floor 3. In these force-displacement diagrams, the maximum horizontal reaction forces are important which are used to calculate the Peak Horizontal Floor Acceleration (PHFA) of the model. These calculated PHFA are used to estimate the Peak Ground Acceleration (PGA). These estimated PGAs give an indication of what the capacity of the model will be when the model is loaded with earthquakes. Therefore, the following equation is used to estimate the PGA:

$$\text{PHFA} = \Omega_i \text{PGA} \tag{18}$$

Where Ω_i is the amplification factor of floor acceleration. This factor is given by:

$$\Omega_i = 1 + (\alpha - 1)\frac{h_i}{h_n} \tag{19}$$

Where h_i is the height of the considered floor, h_n is the height of the uppermost level of the structure both measured form the base and α is a period-dependent factor for the model. It is given by:

$$
\begin{aligned}
T < 0.5 \qquad & \alpha = 3 \\
T > 1 \qquad & \alpha = \frac{2.5}{T^{3/4}} \\
0.5 \le T \le 1 \qquad & \alpha = \frac{2.5}{T^{1/4}}
\end{aligned}
\tag{20}
$$

Where T is the fundamental period of the model. The fundamental period is the inverse of the natural frequency of the model.

It is important to mention that the equations from above are determined by performing a non-linear time history dynamic analysis on full scale steel moment-resisting frame buildings [2]. In this thesis, the reinforced concrete model is scaled and the relation from equation 19 may not completely hold for the model. That is why, the amplification factor which describes the relation between PHFA and PGA in equation 19 will be tested by using the response of the model with respect to all RUNs in section 7.9.

As mentioned before, for the pushover analysis the maximum horizontal reaction forces are interesting to calculate. It is known that the finite element model is a 3D model, this means that the model will give reaction forces in x-, y- and z-direction. For the pushover analysis, only the reaction forces in x- and y-direction are interesting. For all three pushover analyses, reaction forces in x- and y-direction are calculated and only the highest reaction forces are taken for each pushover analysis to calculate the PHFA and then the PGA. For example, for the first pushover analysis the reaction force in x-direction is higher than the reaction force in y-direction, then the reaction force in x-direction is taken to calculate the PHFA and after that the PGA. The force-displacement diagrams presented below, contain the maximum reaction forces in a certain direction. For the first pushover analysis, the reaction force in x-direction is the highest. In the second and third pushover analyses, the reaction forces in y-direction are the highest.

It is also interesting to know where the concrete in the model cracks when it cracks and what the corresponding stress distribution is and where in the model the reinforcement become plastic. These quantities are presented after the estimation of the capacity of the model for each pushover analysis.

7.1.1 Mode Shape 1

The force-displacement diagram for the first pushover analysis looks as follows:
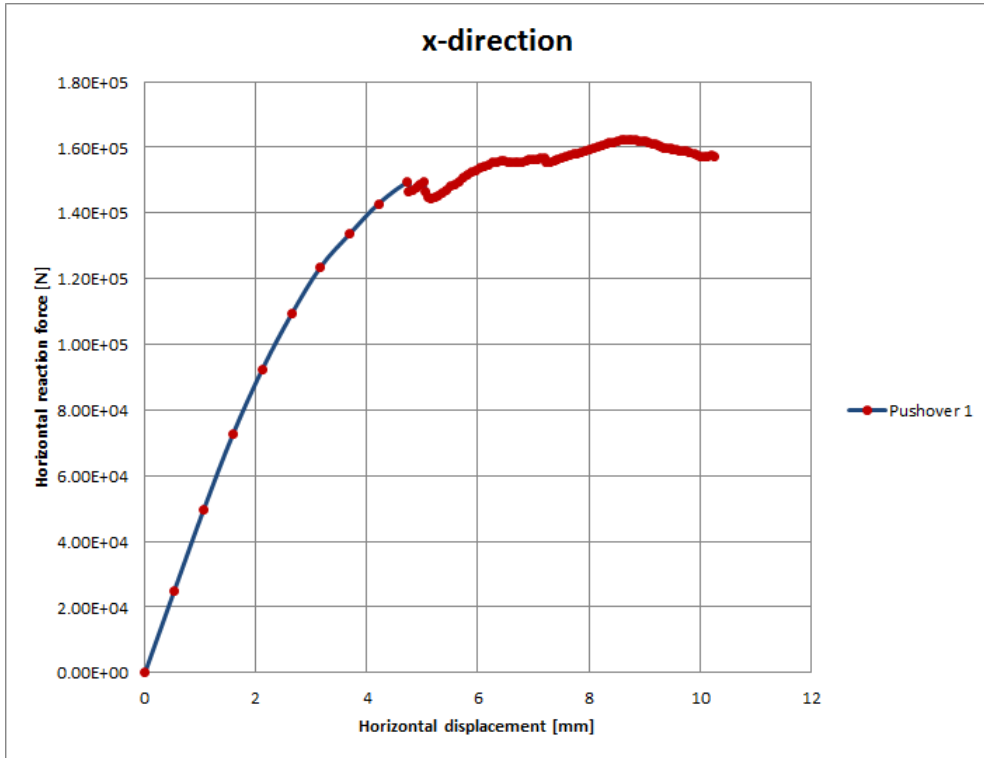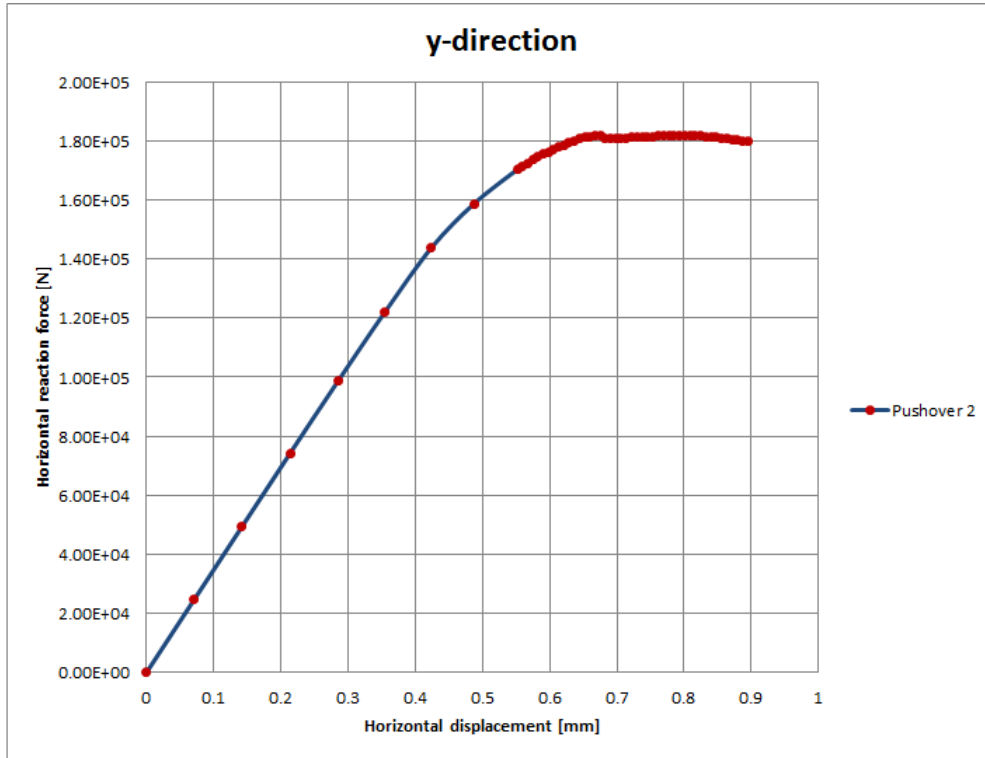

Figure 7.1: Force-displacement diagram in floor 3.

Figure 7.1 is obtained after performing many pushover analyses with different load steps. The very first pushover analysis was performed with load steps 5000(10) and after that different load steps has been used and finally the results with load steps 5000(9) 500(100) is chosen which gives figure 7.1. The reason why the analysis with load steps 5000(9) 500(100) is chosen is because these load steps give the most interesting results. The figures below show the diagrams which were obtained by performing the pushover analyses with different load steps.
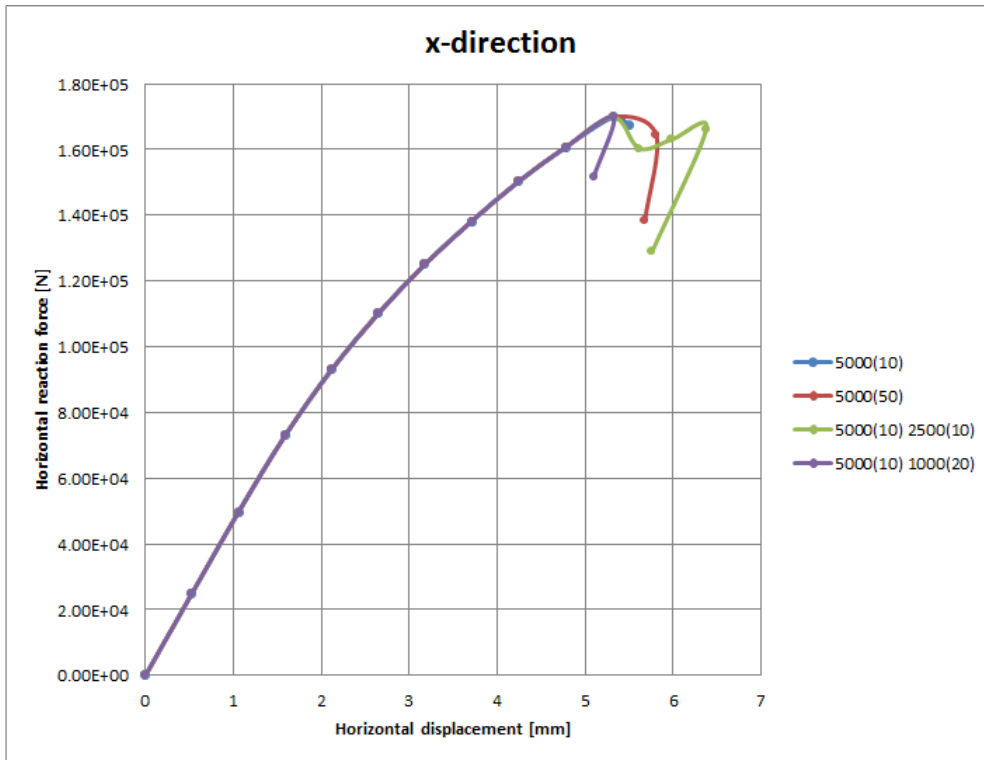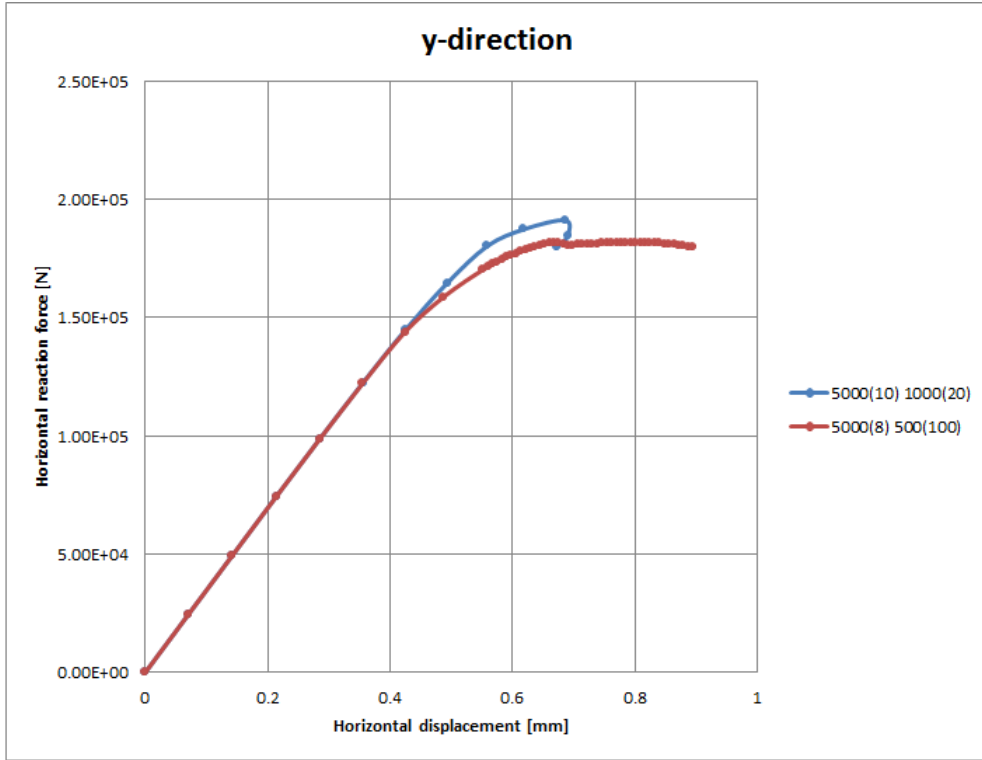
Figure 7.2: Force-displacement diagram in floor 3.
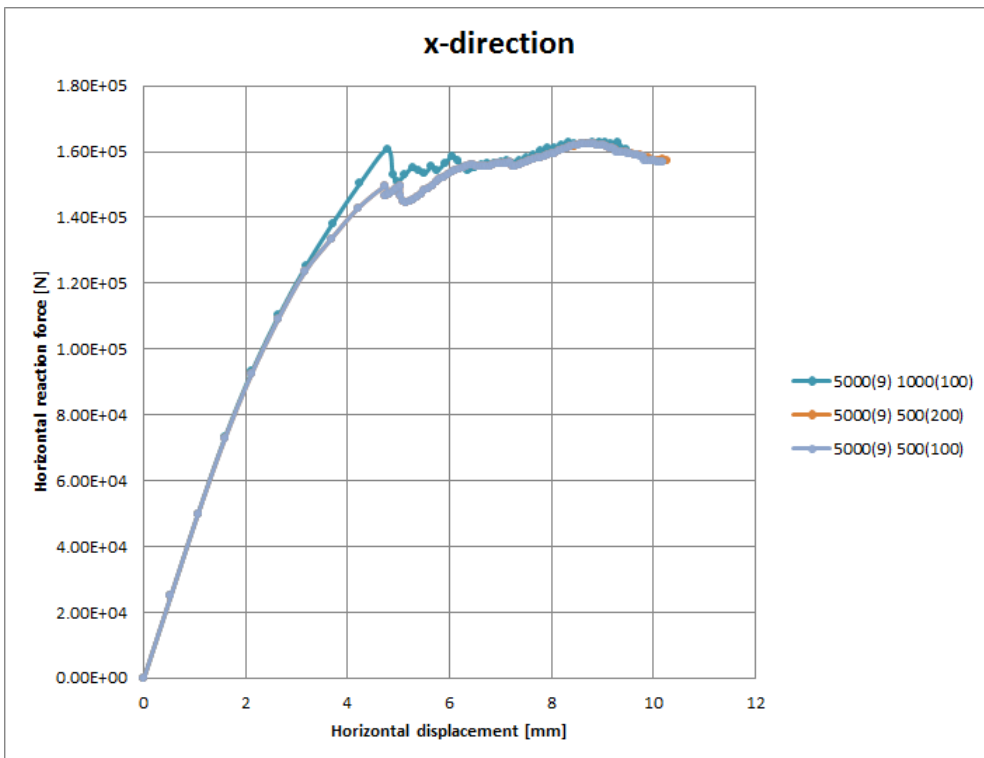
Figure 7.3: Force-displacement diagram in floor 3.

159

The PHFA on floor 3 from the first pushover analysis, based on the total mass of the model, is given in the table below.

Table 7.1: PHFA based on the total mass of the model.

Total mass [kg]	Maximum force [N]	Acceleration [m/s^2]	PHFA [g]
45300	162410	3.59	0.37

The PHFA on floor 3 from the first pushover analysis, based on the effective mass of the model, is given in the table below.

Table 7.2: PHFA based on the effective mass of the model.

Effective mass [kg]	Maximum force [N]	Acceleration [m/s^2]	PHFA [g]
25018	162410	6.49	0.66

By taking the total mass of the mock-up into account, the PGA will be as follows:

$$PGA = \frac{PHFA}{\Omega} = \frac{0.37}{3} = 0.12 \text{ g} \tag{21}$$

By taking the effective mass of the mock-up into account, the PGA will be as follows:

$$PGA = \frac{PHFA}{\Omega} = \frac{0.66}{3} = 0.22 \text{ g} \tag{22}$$

It is mentioned before that the model in the first pushover analysis will be loaded according to its first mode shape. The deformation of the first mode is given in the figures below. These figures show the deformed and undeformed states of the model where the undeformed state of the model is given by the grey mesh.
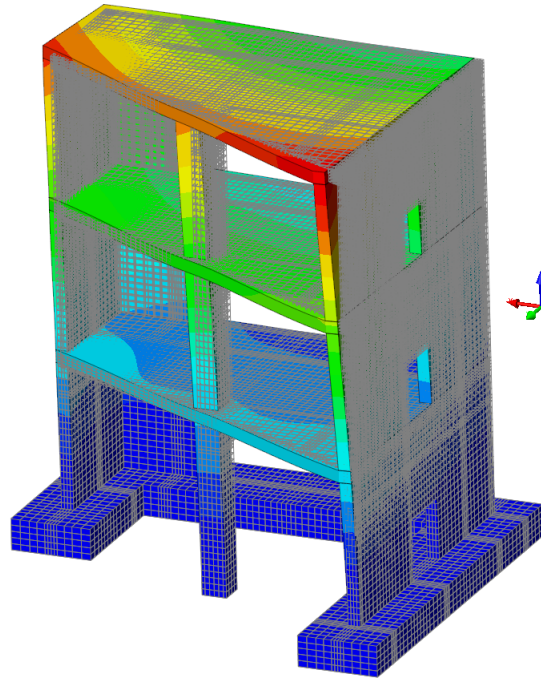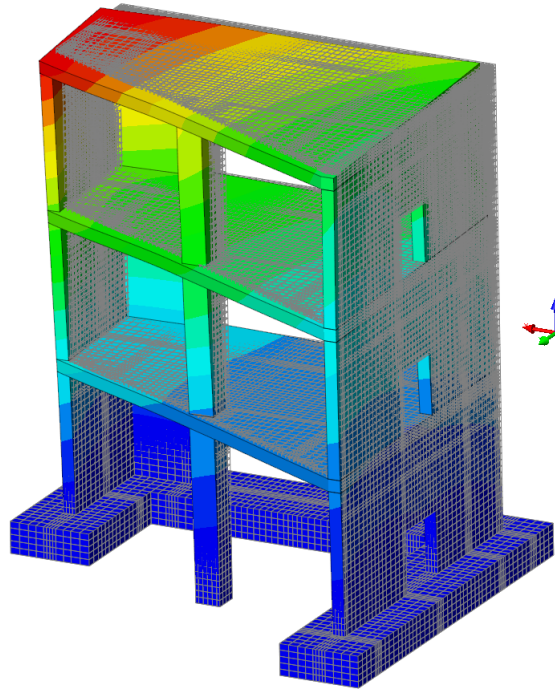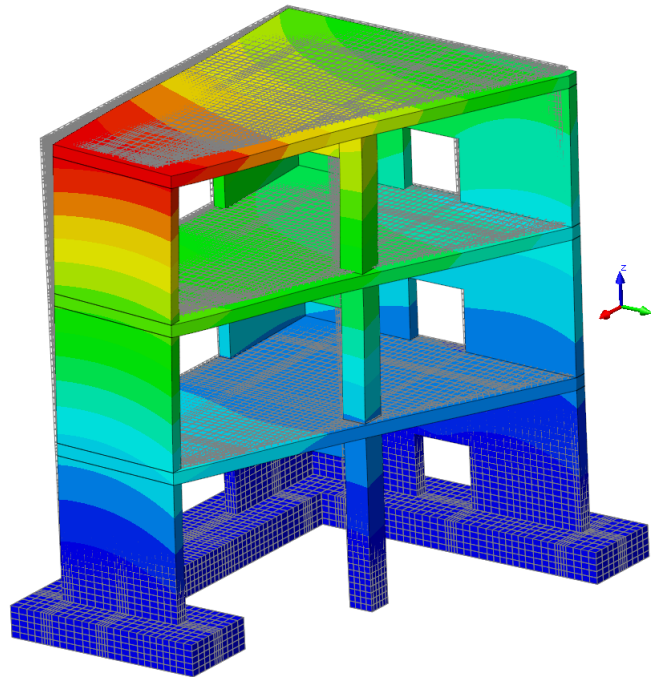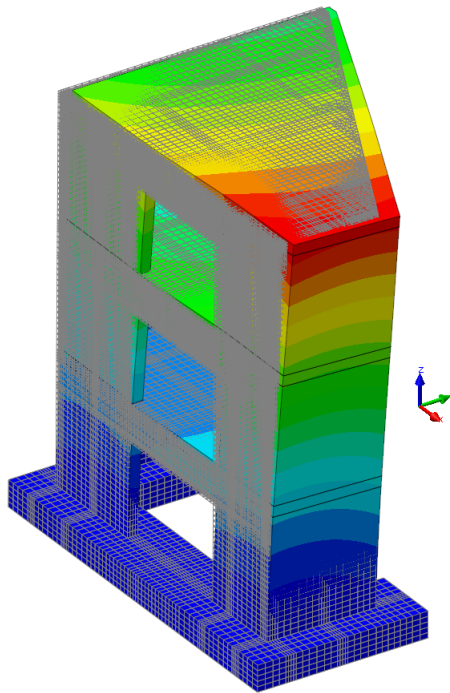

Figure 7.4: Mode shape 1.
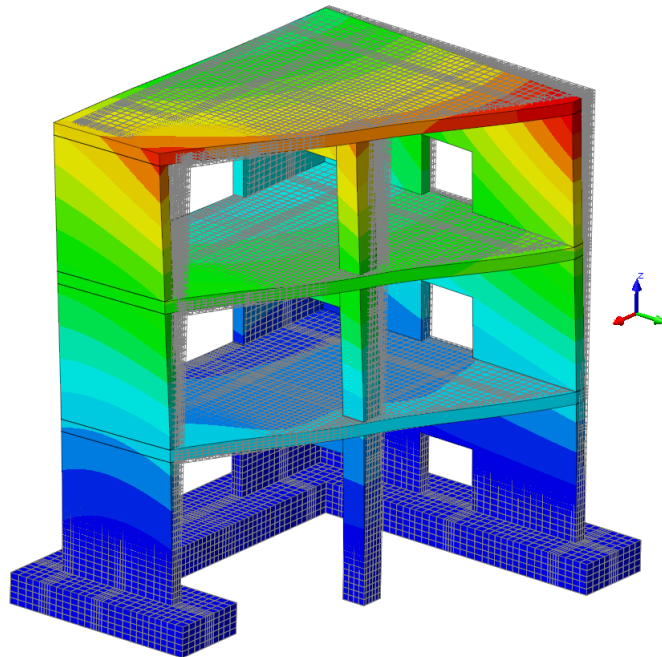
Figure 7.5: Mode shape 1.
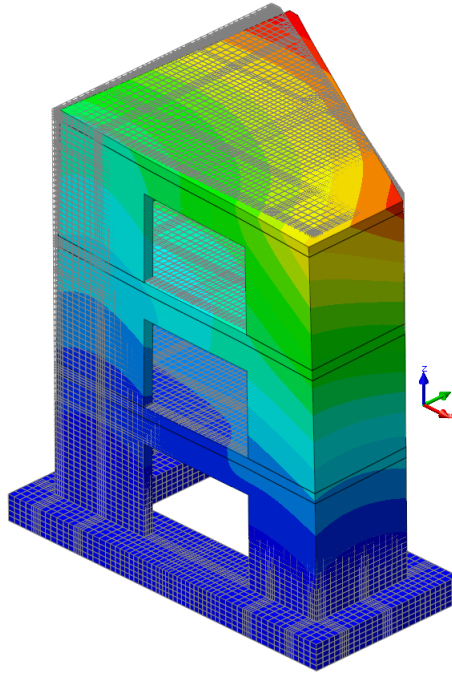
Figure 7.6: Mode shape 1.

These figures show that the model is translating in x- and y-direction where the translation in x-direction is bigger. The figures also show that the upper part of the model translates more then the lower parts of the model where the model near the foundation doesn't translate and reacts very stiff. Because of the geometry of the model, the model shows also a little torsion where wall V04 is loaded heavily near the foundation. Also the points where walls V01 and V03 come together near the foundation are loaded heavily. The columns and the beams in the model translate mainly in x-direction and some parts of the floors deform also in z-direction.

Lets look at the crack patterns, the corresponding stress distributions and the plasticity of the reinforcement of the model. The contour plots that show these quantities are taken at the moment when the maximum horizontal reaction forces in the model occur. First, a crack pattern is shown then the corresponding stress distribution for different views of the model. The stresses that are shown are the principles stresses in S1 which give the tensile stresses in the model. Next to each contour plot, a legend is given. This legend shows the value for each quantity. For example, the legends for the crack patterns show how big the strains (ϵ_{knn}) in the cracks are. And the legends of the contour plots for the principal stresses in S1 give the values of the tensile stresses in the model. Please note that in some local places in the model the tensile stresses that are shown, are higher then the tensile strength of the model. This is because these tensile stresses are extrapolated from the integration points (where the stresses are calculated) to the nodes. The contour plots are given below.
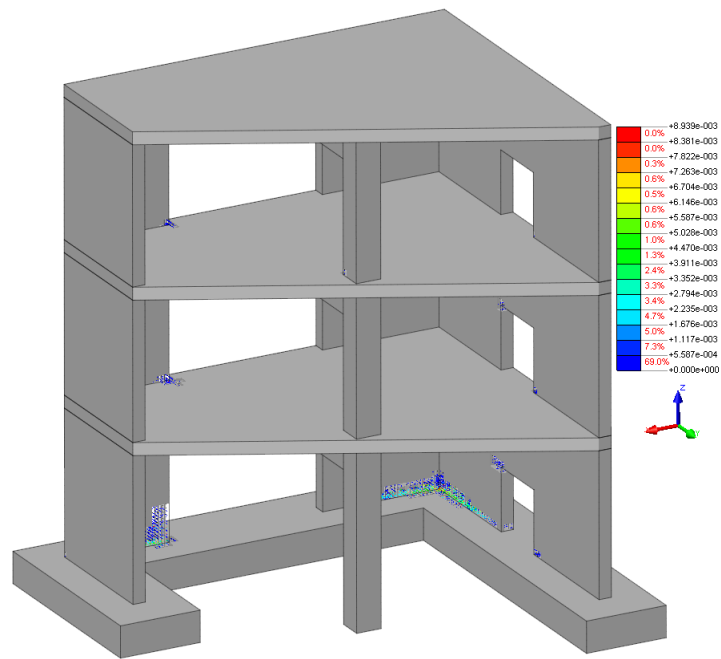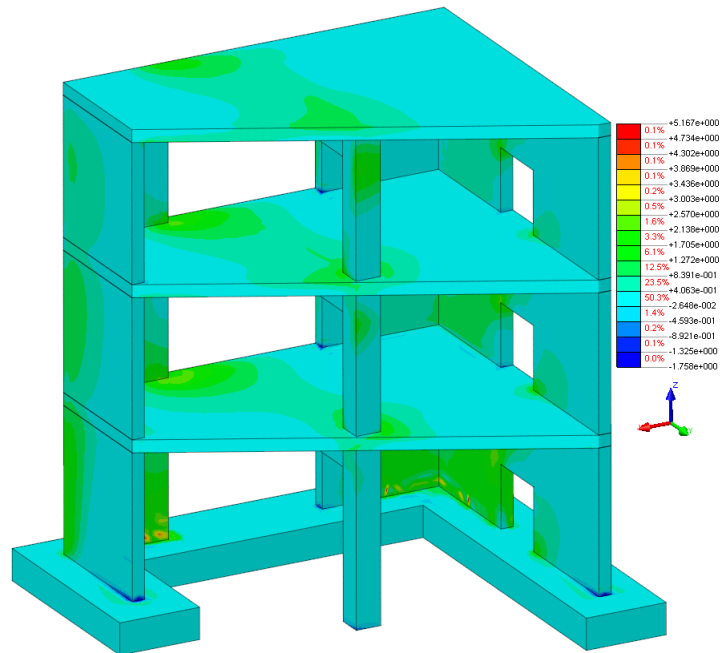
Figure 7.7: Crack pattern.
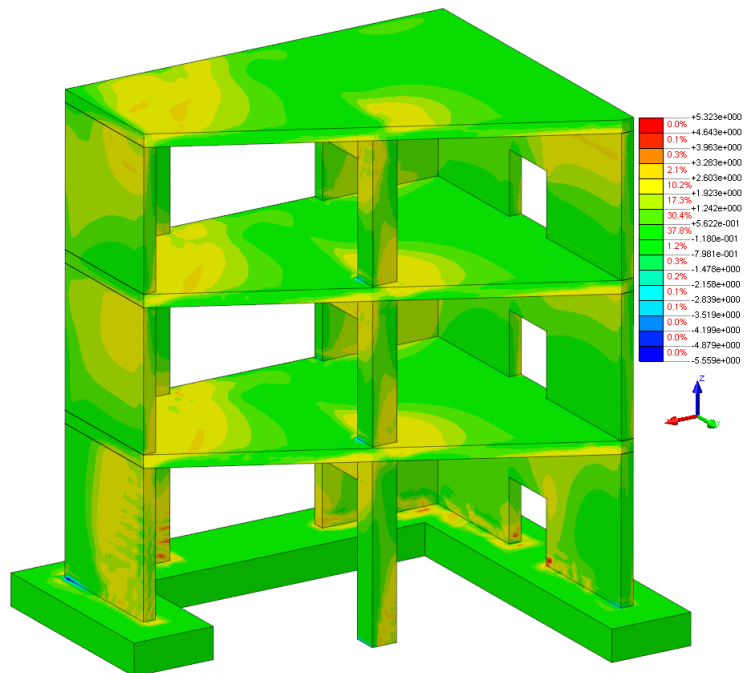
Figure 7.8: Tensile stresses in principle direction 1 in N/mm^2.

The two figures from above show that where the tensile stresses in the model are high (and higher then the tensile strength of the model) the cracks occur in those places. This relation between the contour plots of the crack patterns and the stress distribution are shown further below for different views of the model.
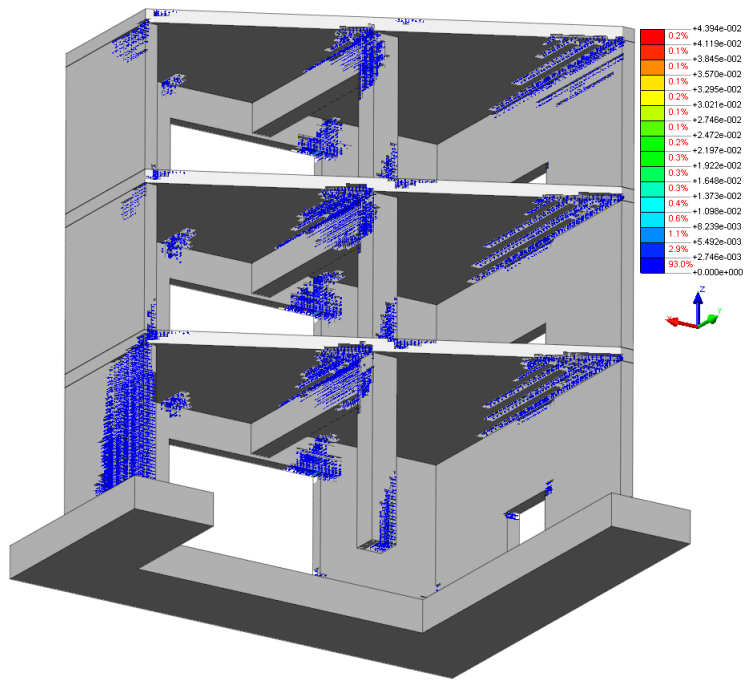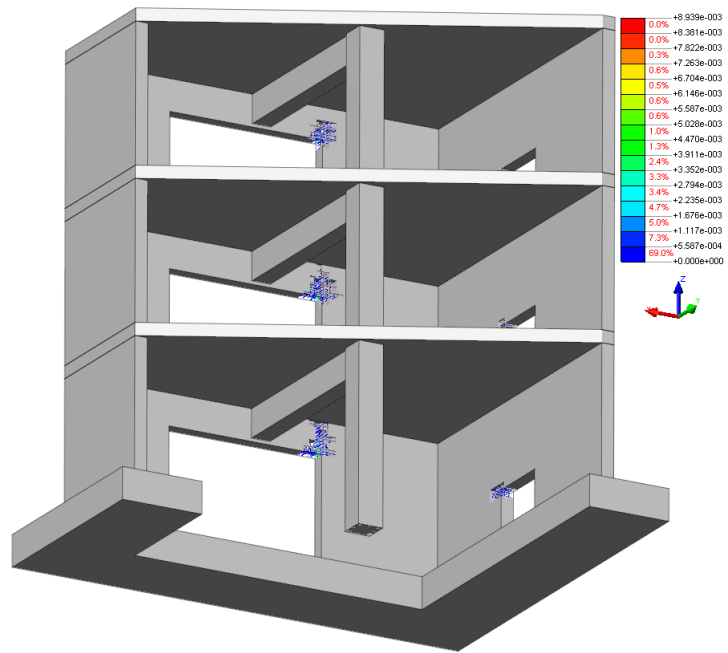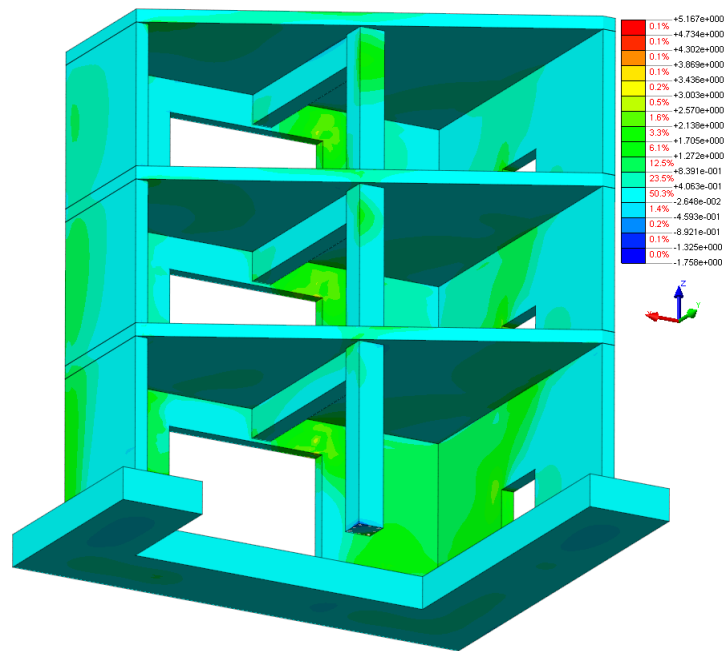
Figure 7.9: Crack pattern.
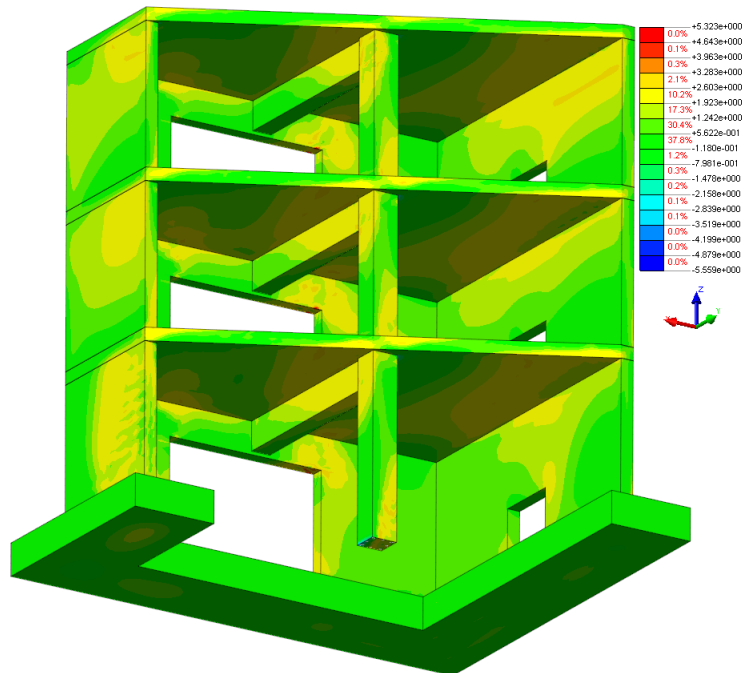
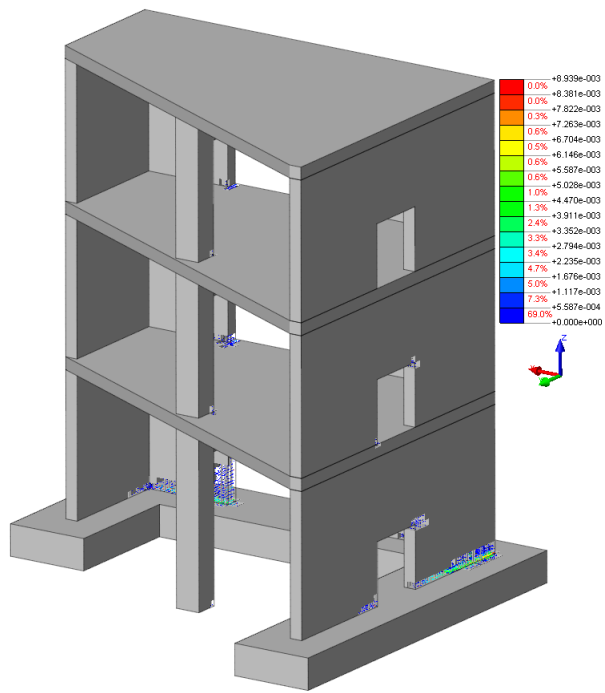Figure 7.10: Tensile stresses in principle direction 1 in N/mm^2.
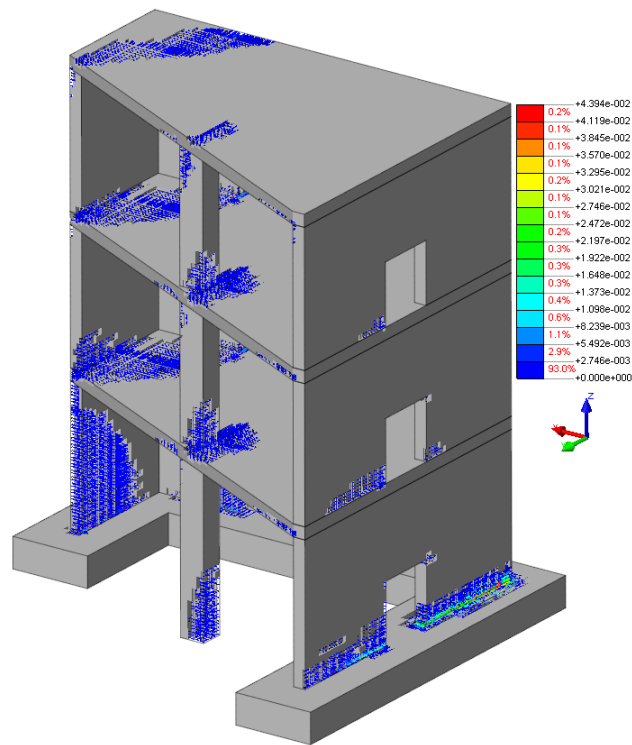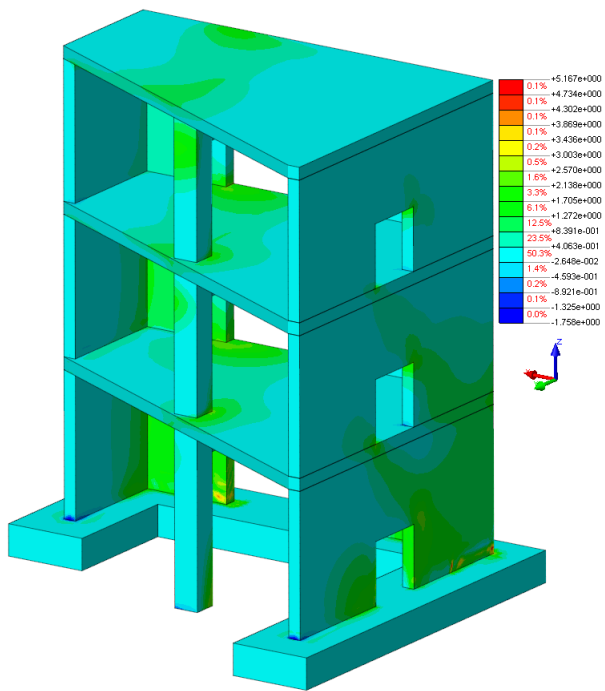
Figure 7.11: Crack pattern.
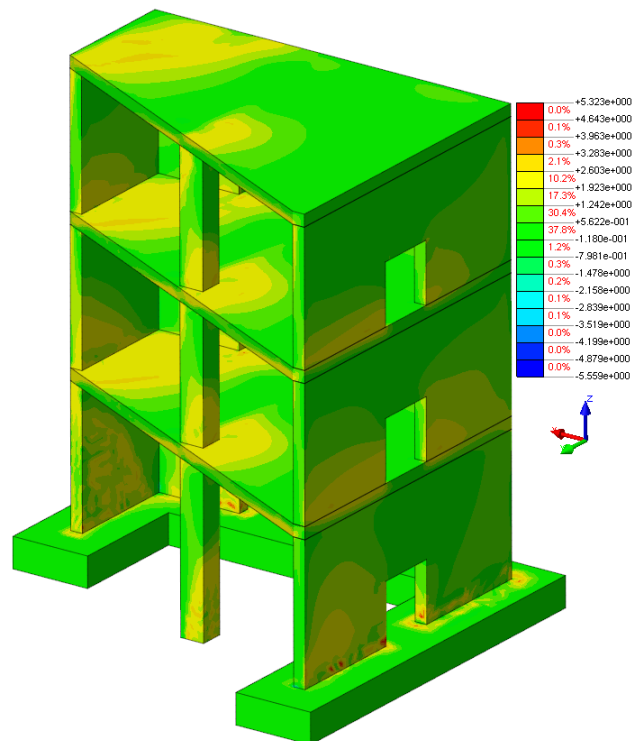
Figure 7.12: Tensile stresses in principle direction 1 in N/mm^2.
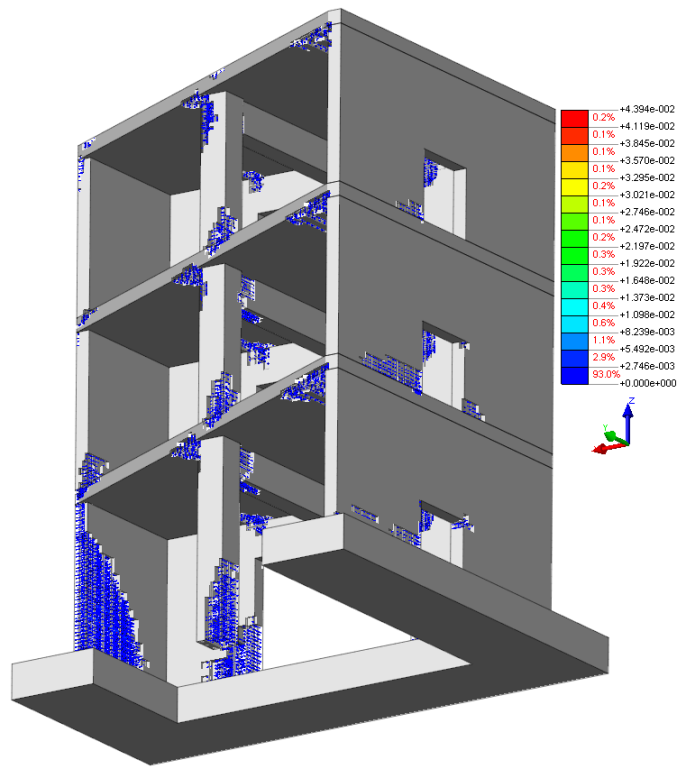
Figure 7.13: Crack pattern.
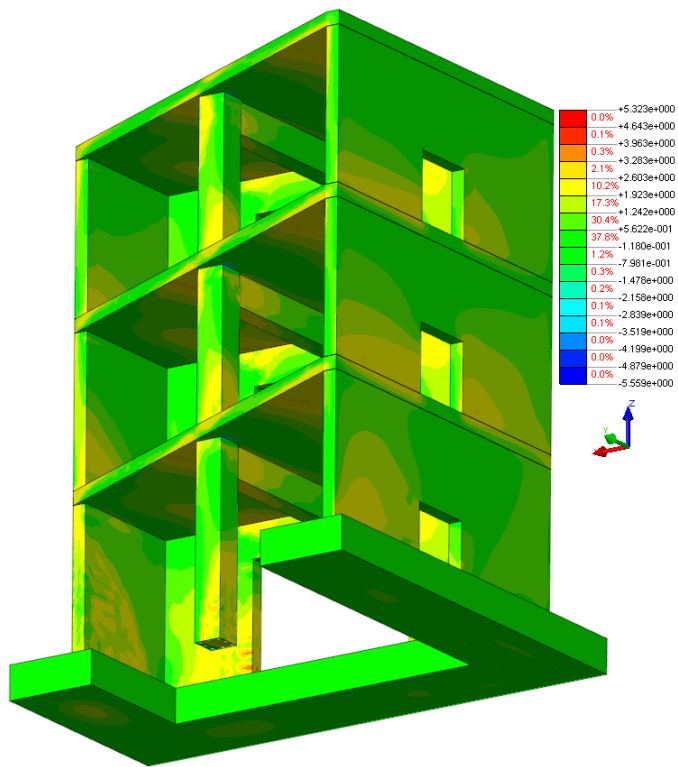
Figure 7.14: Tensile stresses in principle direction 1 in N/mm^2.
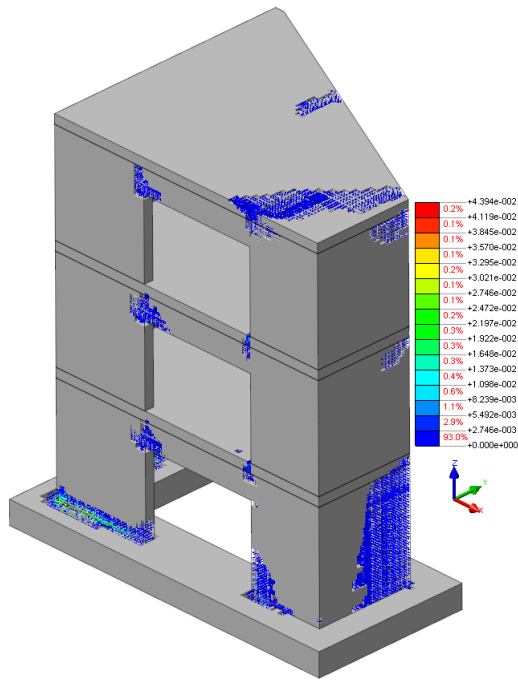
Figure 7.15: Crack pattern.
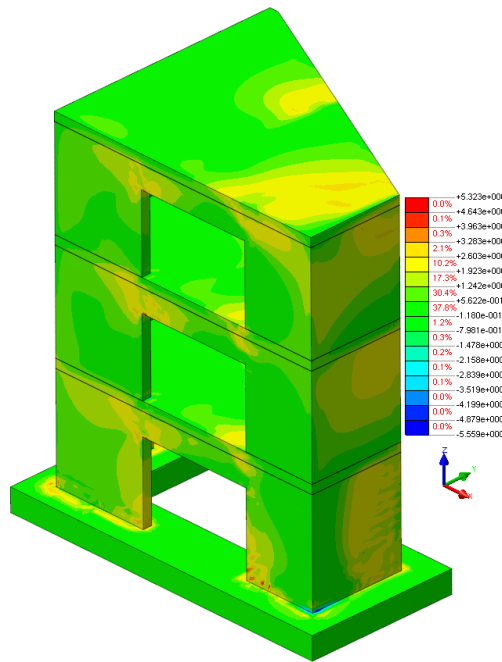
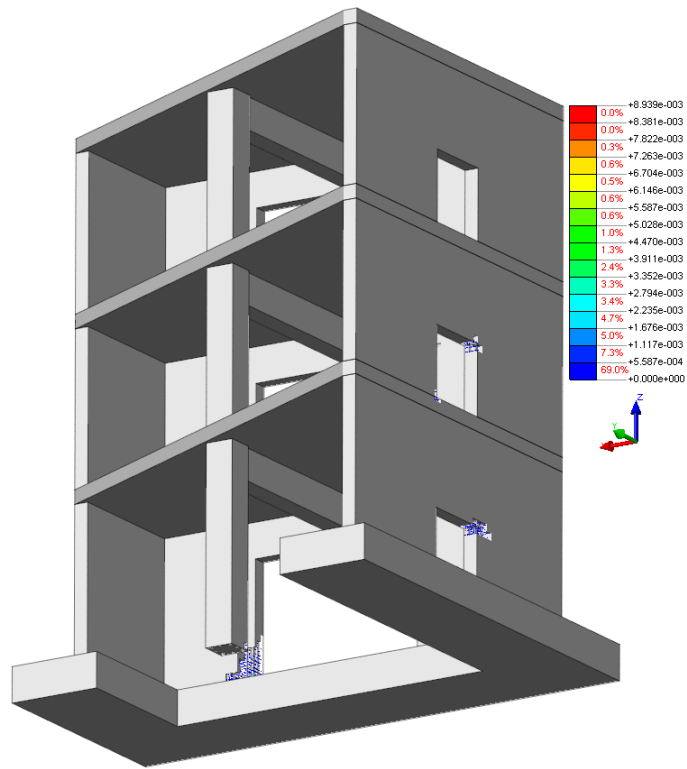Figure 7.16: Tensile stresses in principle direction 1 in N/mm^2.

The figures from above show that the cracks that occur in the model are mainly in the major lower front part of wall V04 and the connection between the foundation and walls V01 V02 and V03. Also the edges of all openings show cracks together with the connection between the columns and the floors. All three floors near walls V03 and V04 and near the beams show cracks.

167

The contour plots below show what the stresses (S_{xx}) in the reinforcements are and where in the model the reinforcements are plastic (ϵ_{pxx}). The reinforcement in wall V03 near the foundation next to the opening yields.
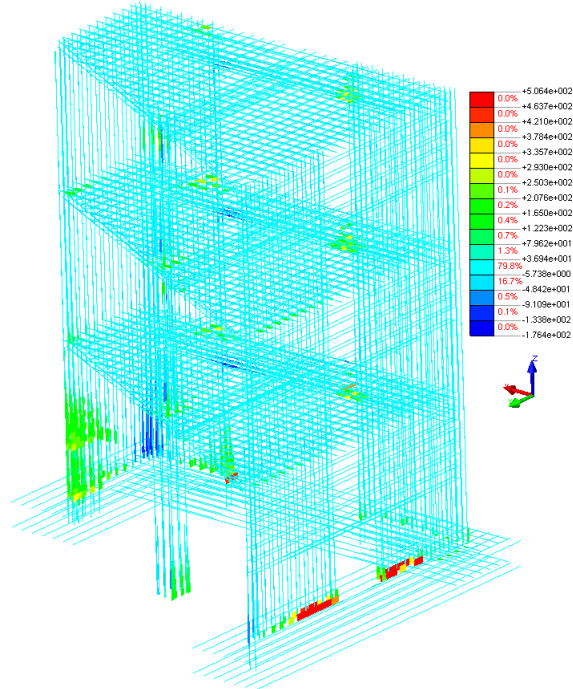
Figure 7.17: Stresses in the reinforcement.
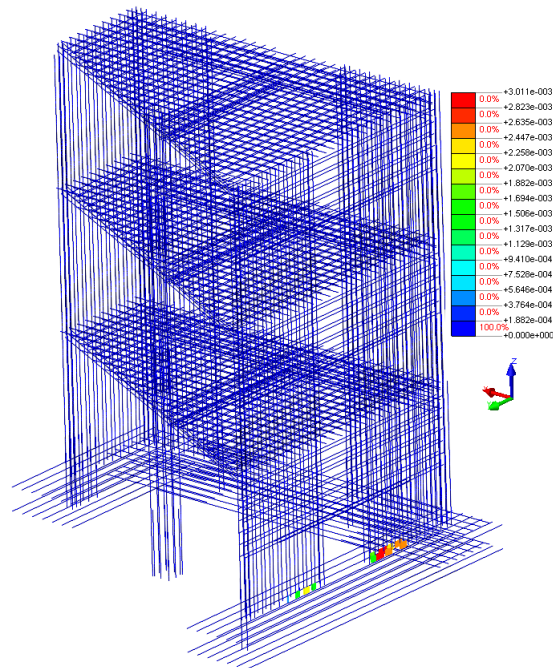
Figure 7.18: Plastic strains in the reinforcement.

7.1.2 Mode Shape 2

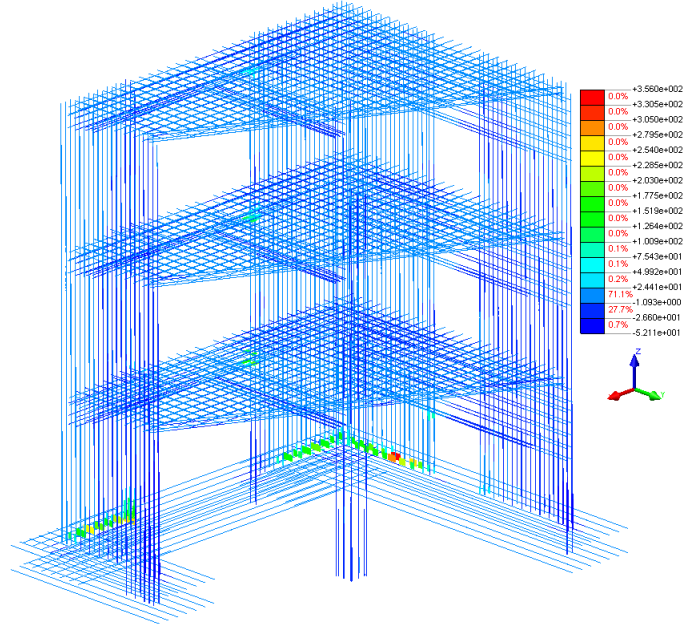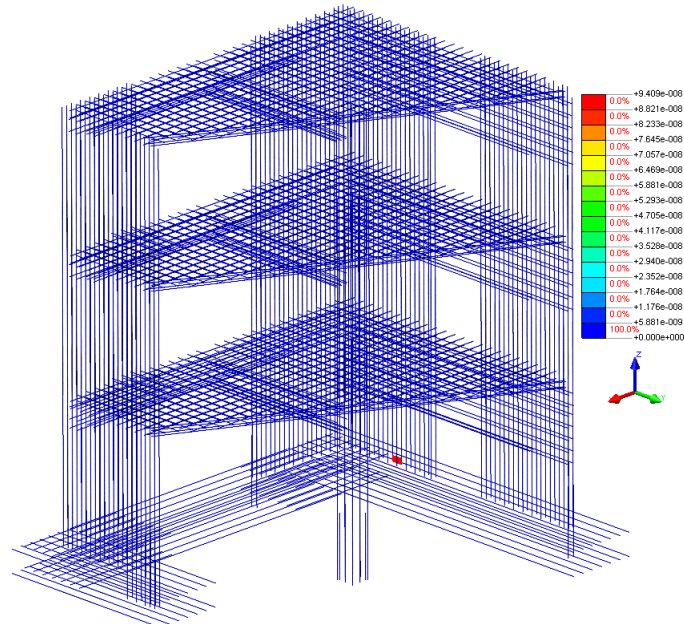The force-displacement diagram for the second pushover analysis looks as follows:

Figure 7.19: Force-displacement diagram in floor 3.

Figure 7.19 is obtained after performing two pushover analyses with different load steps. The first pushover analysis was performed with load steps 5000(10) 1000(20) and after that with load steps 5000(8) 500(100). The analysis with load steps 5000(8) 500(100) is chosen which gives figure 7.19. The reason why the analysis with load steps 5000(8) 500(100) is chosen is because these load steps give the most interesting results. The figure below shows the two graphs which were obtained by performing the pushover analyses with two different load steps.

Figure 7.20: Force-displacement diagram in floor 3.

The PHFA on floor 3 from the second pushover analysis, based on the total mass of the model, is given in the table below.

Table 7.3: PHFA based on the total mass of the model.

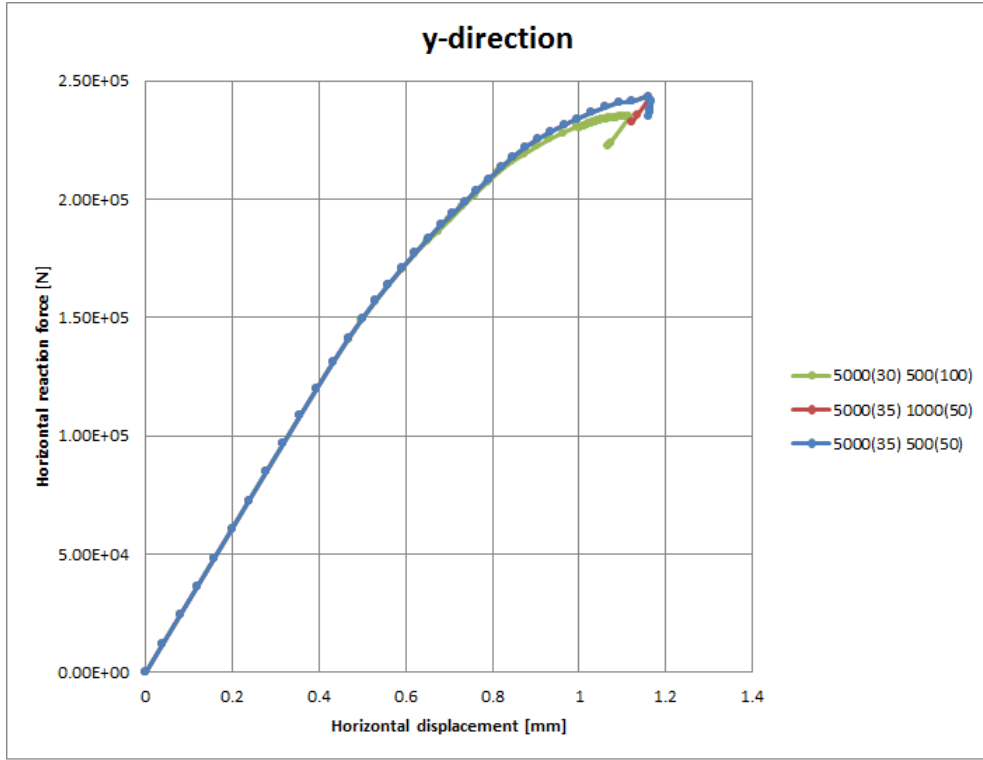| Total mass [kg]	Maximum force [N]	Acceleration [m/s^2]	PHFA [g]
45300	181770	4.01	0.41

The PHFA on floor 3 from the second pushover analysis, based on the effective mass of the model, is given in the table below.

Table 7.4: PHFA based on the effective mass of the model.

Effective mass [kg]	Maximum force [N]	Acceleration [m/s^2]	PHFA [g]
24566	181770	7.39	0.75

By taking the total mass of the mock-up into account, the PGA will be as follows:

$$PGA = \frac{PHFA}{\Omega} = \frac{0.41}{3} = 0.14 \text{ g} \tag{23}$$

By taking the effective mass of the mock-up into account, the PGA will be as follows:

$$PGA = \frac{PHFA}{\Omega} = \frac{0.75}{3} = 0.25 \text{ g} \tag{24}$$

It is mentioned before that the model in the second pushover analysis will be loaded according to its second mode shape. The deformation of the second mode is given in the figures below. These figures show the deformed and undeformed states of the model where the undeformed state of the model is given by the grey mesh.
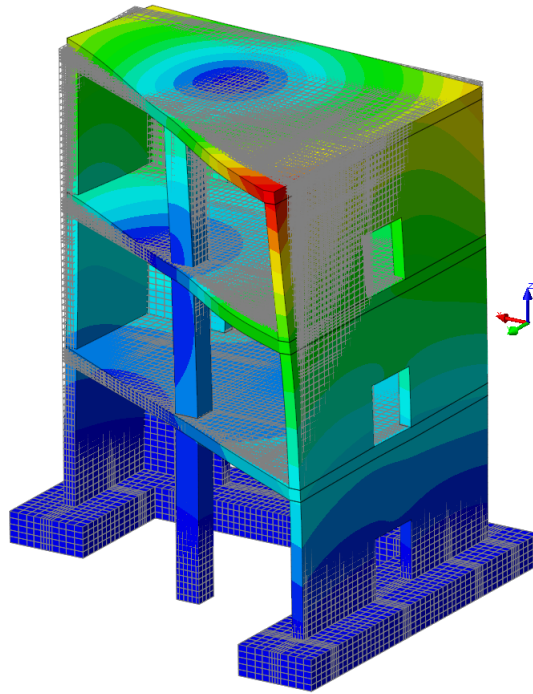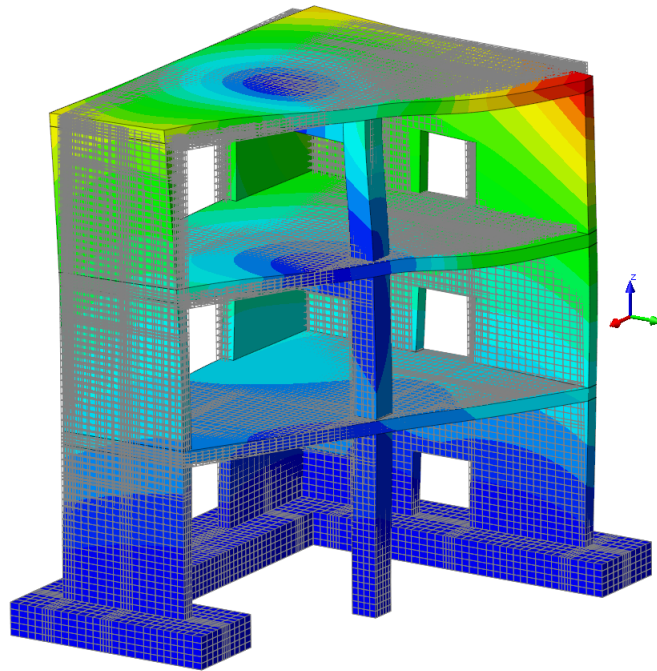

Figure 7.21: Mode shape 2.
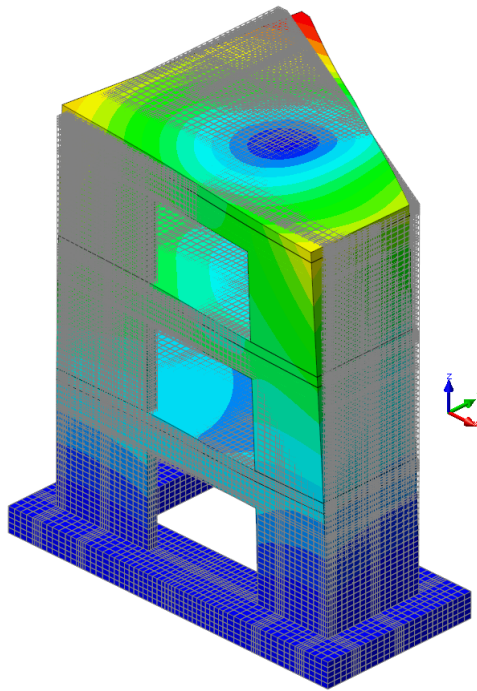

Figure 7.22: Mode shape 2.

Figure 7.23: Mode shape 2.

These figures show that the model is moving in x- and y-direction where the translation in y-direction is bigger. The figures also show that the upper part of the model translates more then the lower parts of the model where the model near the foundation doesn't translate and reacts very stiff. Because of the the big translation of the model in y-direction, the walls V01 and V02 are loaded heavily. Also the points where walls V01 and V03 come together near the foundation are loaded heavily. The columns and the beams in the model translate in x- and y-direction, but mainly in y-direction. Some parts of the floors deform also in z-direction.

Lets look at the crack patterns, the corresponding stress distributions and the plasticity of the reinforcement of the model. The contour plots that show these quantities are taken at the moment when the maximum horizontal reaction forces of the model occur. First, a crack pattern will be shown then the corresponding stress distribution for different views of the model. The stresses that will be shown are the principles stresses in S1 which give the tensile stresses in the model. Next to each contour plot, a legend is given. This legend shows the value for each quantity. For example, the legends for the crack patterns show how big the strains (ϵ_{knn}) in the cracks are. And the legends of the contour plots for the principal stresses in S1 give the values of the tensile stresses in the model. Please note that in some local places in the model the tensile stresses that are shown, are higher then the tensile strength of the model. This is because these tensile stresses are extrapolated from the integration points (where the stresses are calculated) to the nodes. The contour plots are given below.

Figure 7.24: Crack pattern.
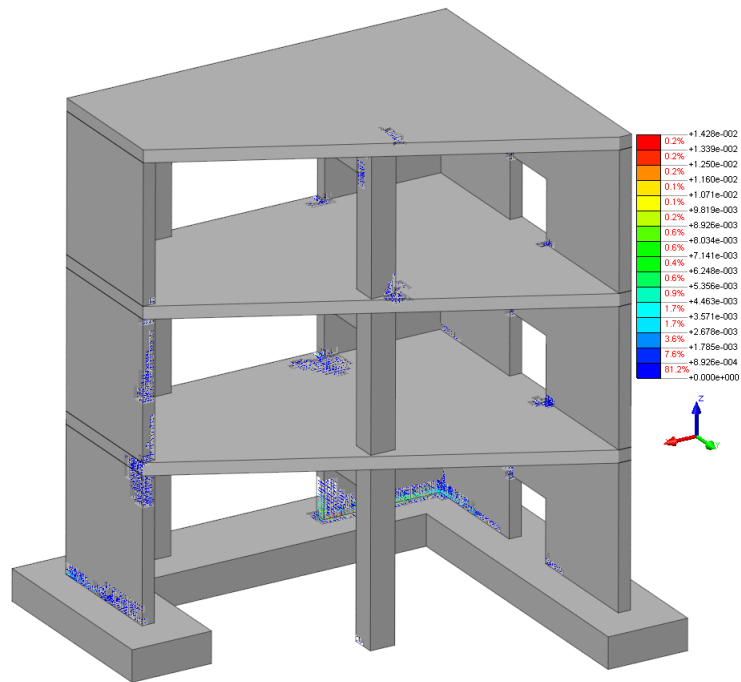

Figure 7.25: Tensile stresses in principle direction 1 in N/mm^2.

The two figures from above show that where the tensile stresses in the model are high (and higher then the tensile strength of the model) the cracks occur in those places. This relation between the contour plots of the crack patterns and the stress distribution are shown further below for different views of the model.

Figure 7.26: Crack pattern.

Figure 7.27: Tensile stresses in principle direction 1 in N/mm^2.

Figure 7.28: Crack pattern.

Figure 7.29: Tensile stresses in principle direction 1 in N/mm^2.
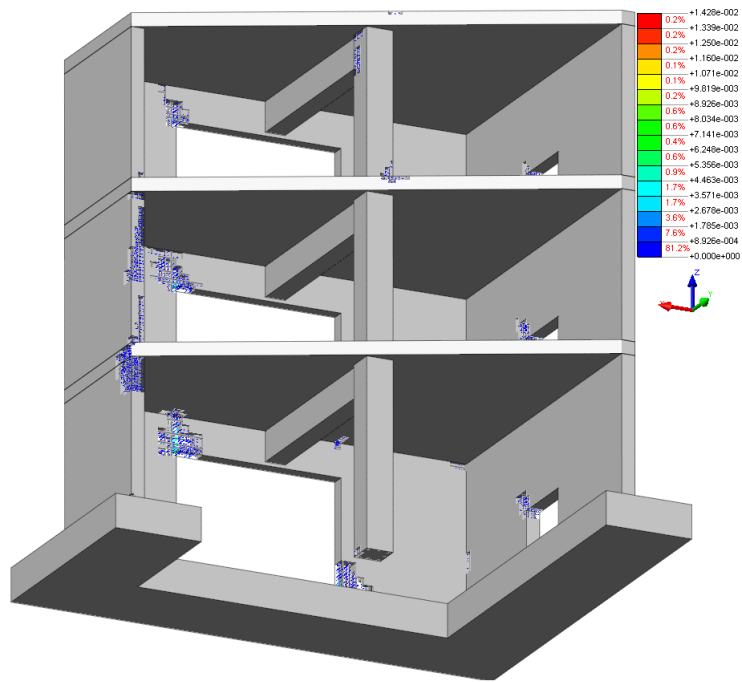
Figure 7.30: Crack pattern.
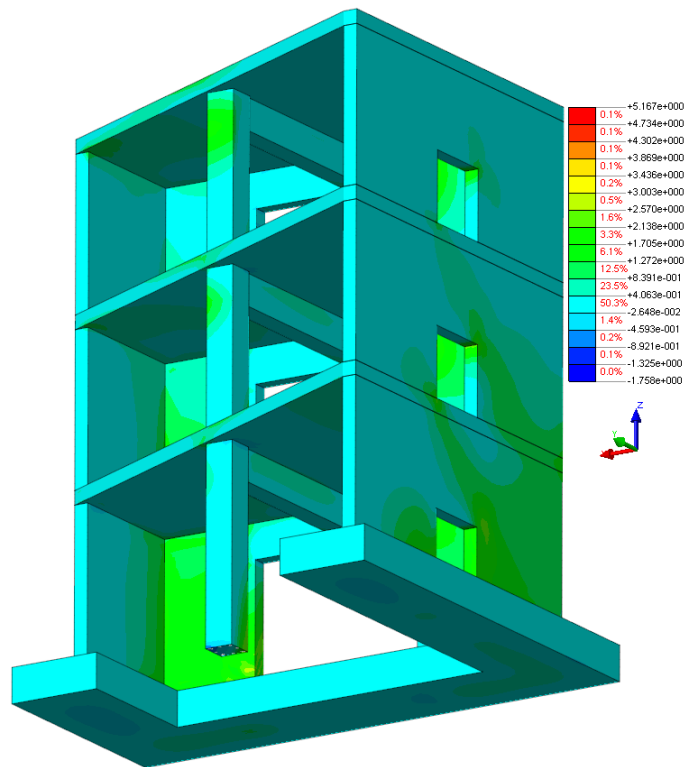
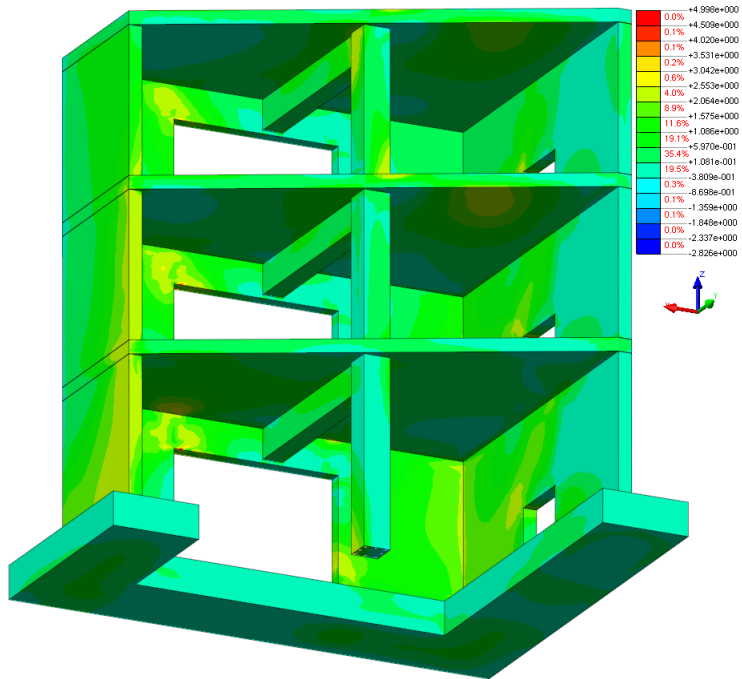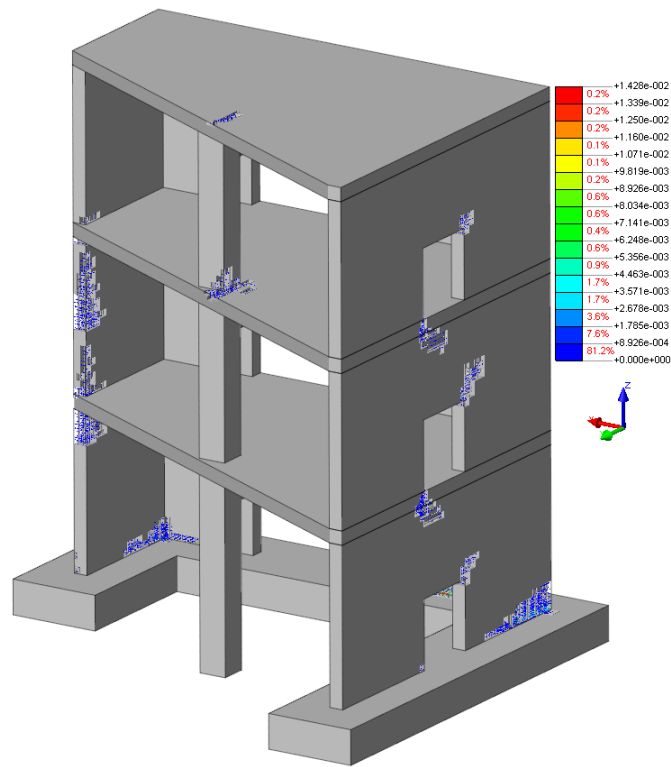Figure 7.31: Tensile stresses in principle direction 1 in N/mm^2.

176
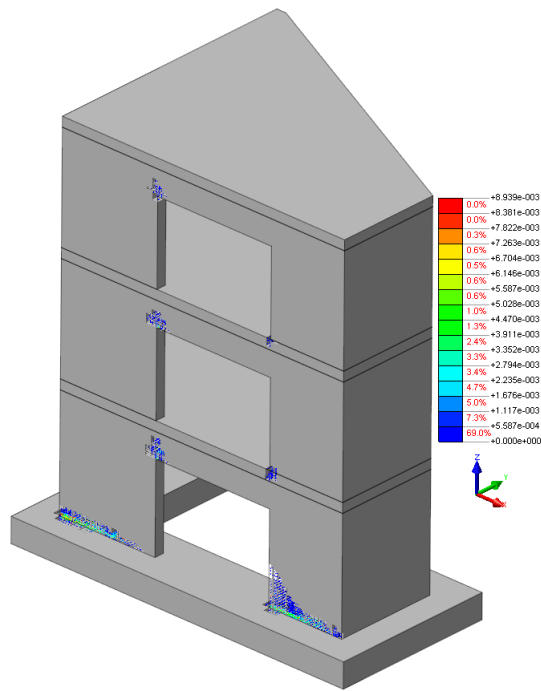
Figure 7.32: Crack pattern.
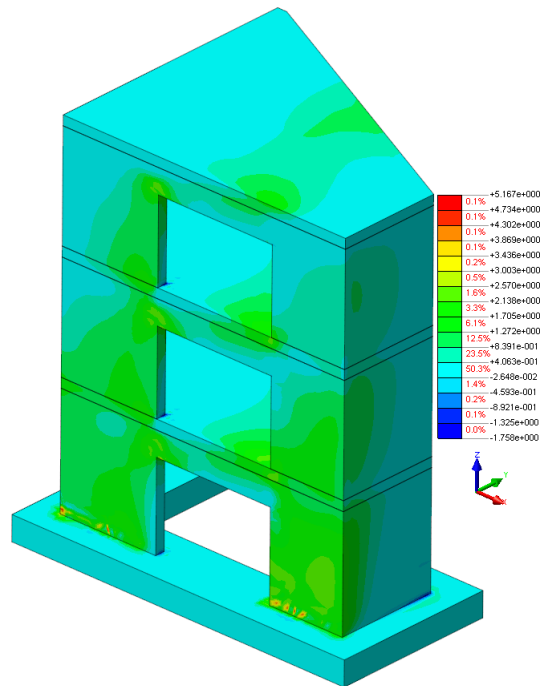
Figure 7.33: Tensile stresses in principle direction 1 in N/mm^2.

The crack patterns here show that the floors are not cracked, the columns and the beams are intact. The cracks here are mainly at the edges of the openings and at the connection between the foundation and walls V01 and V02.

The contour plots below shows what the stresses (S_{xx}) in the reinforcements are and where in the model the reinforcements are plastic (ϵ_{pxx}). The reinforcement in wall V03 near the foundation next to the opening yields.

Figure 7.34: Stresses in the reinforcement.

Figure 7.35: Plastic strains in the reinforcement.

7.1.3 Mode Shape 3

The force-displacement diagram of the third pushover analysis looks as follows:
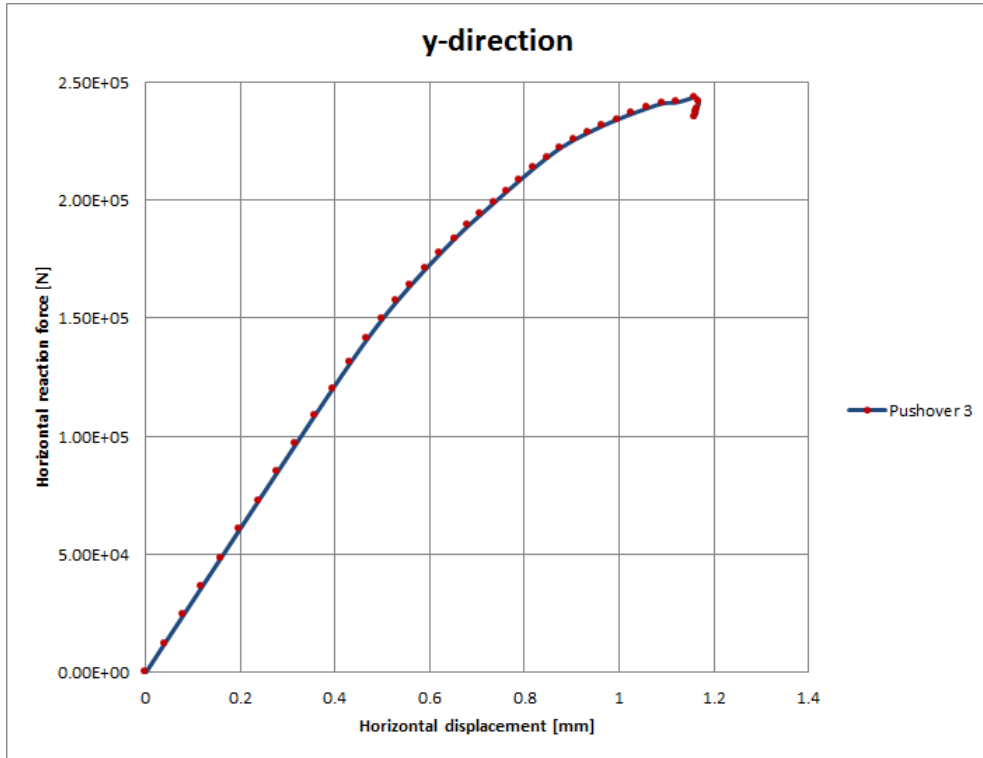
Figure 7.36: Force-displacement diagram in floor 3.

Figure 7.36 is obtained after performing three pushover analyses with different load steps. The first pushover analysis was performed with load steps 5000(30) 500(100) and after that with load steps 5000(35) 1000(50) and 5000(35) 500(50). The analysis with load steps 5000(35) 500(50) is chosen which gives figure 7.36. The reason why the analysis with load steps 5000(30) 500(50) is chosen is because these load steps give the most interesting results. The figure below shows the two diagrams which were obtained by performing the pushover analyses with three different load steps.

Figure 7.37: Force-displacement diagram in floor 3.

The PHFA on floor 3 from the third pushover analysis, based on the total mass of the model, is given in the table below.

Table 7.5: PHFA based on the total mass of the model.

Total mass [kg]	Maximum force [N]	Acceleration [m/s²]	PHFA [g]
45300	243360	5.37	0.55

The PHFA on floor 3 from the third pushover analysis, based on the effective mass of the model, is given in the table below.

Table 7.6: PHFA based on the effective mass of the model.

Effective mass [kg]	Maximum force [N]	Acceleration [m/s²]	PHFA [g]
5879	243360	41.39	4.22

By taking the total mass of the mock-up into account, the PGA will be as follows:

$$PGA = \frac{PHFA}{\Omega} = \frac{0.55}{3} = 0.18 \text{ g} \tag{25}$$

By taking the effective mass of the mock-up into account, the PGA will be as follows:

$$PGA = \frac{PHFA}{\Omega} = \frac{4.22}{3} = 1.41 \text{ g} \tag{26}$$

180

It is mentioned before that the model in the third pushover analysis will be loaded according to its third mode shape. The deformation of the second mode is given in the figures below. These figures show the deformed and undeformed states of the model where the undeformed state of the model is given by the grey mesh.

Figure 7.38: Mode shape 3.

Figure 7.39: Mode shape 3.

Figure 7.40: Mode shape 3.

These figures show that the model is twisting in z-direction. Like the first and second mode, the upper part of the model is twisting more then the lower parts of the model where the model near the foundation doesn't twist and reacts very stiff. Because of the the big translation of the model in y-direction, walls V01 and V02 are loaded heavily. Also the points where walls V01 and V03 come together near the foundation are loaded heavily. The columns and the beams in the model translate in x- and y-direction. Some parts of the floors deform also in z-direction.

Lets look at the crack patterns, the corresponding stress distributions and the plasticity of the reinforcement of the model. The contour plots that show these quantities are taken at the moment when the maximum horizontal reaction forces of the model occur. First, a crack pattern will be shown then the corresponding stress distribution for different views of the model. The stresses that will be shown are the principles stresses in S1 which give the tensile stresses in the model. Next to each contour plot, a legend is given. This legend shows the value for each quantity. For example, the legends for the crack patterns show how big the strains (ϵ_{knn}) in the cracks are. And the legends of the contour plots for the principal stresses in S1 give the values of the tensile stresses in the model. Please note that in some local places in the model the tensile stresses that are shown, are higher then the tensile strength of the model. This is because these tensile stresses are extrapolated from the integration points (where the stresses are calculated) to the nodes. The contour plots are given below.

Figure 7.41: Crack pattern.
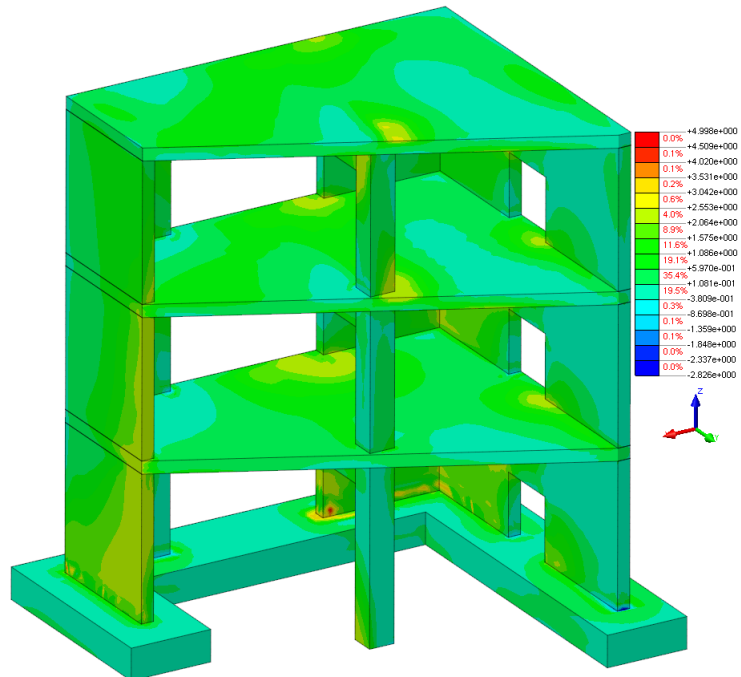
Figure 7.42: Tensile stresses in principle direction 1 in N/mm^2.

The two figures from above show that where the tensile stresses in the model are high (and higher then the tensile strength of the model) the cracks occur in those places. This relation between the contour plots of the crack patterns and the stress distribution are shown further below for different views of the model.

Figure 7.43: Crack pattern.

Figure 7.44: Tensile stresses in principle direction 1 in N/mm^2.

Figure 7.45: Crack pattern.
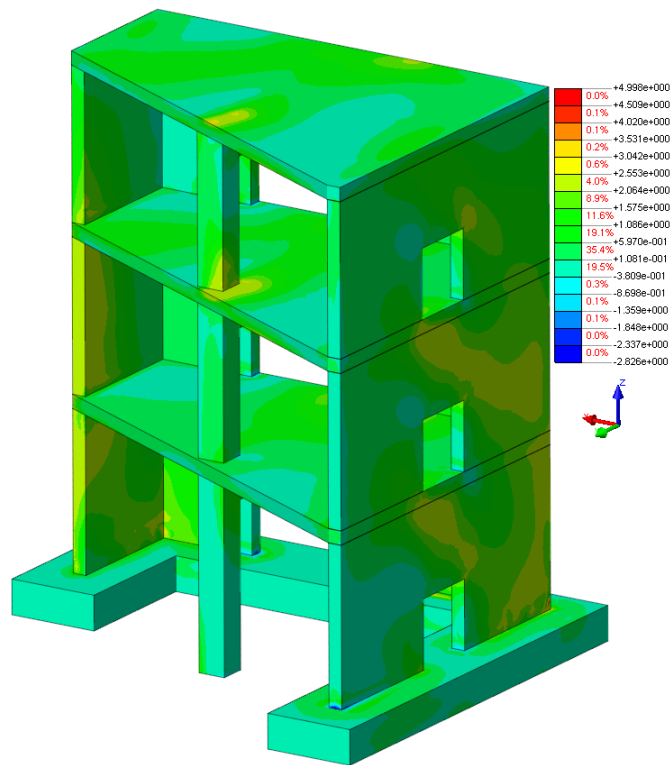
Figure 7.46: Tensile stresses in principle direction 1 in N/mm^2.

185
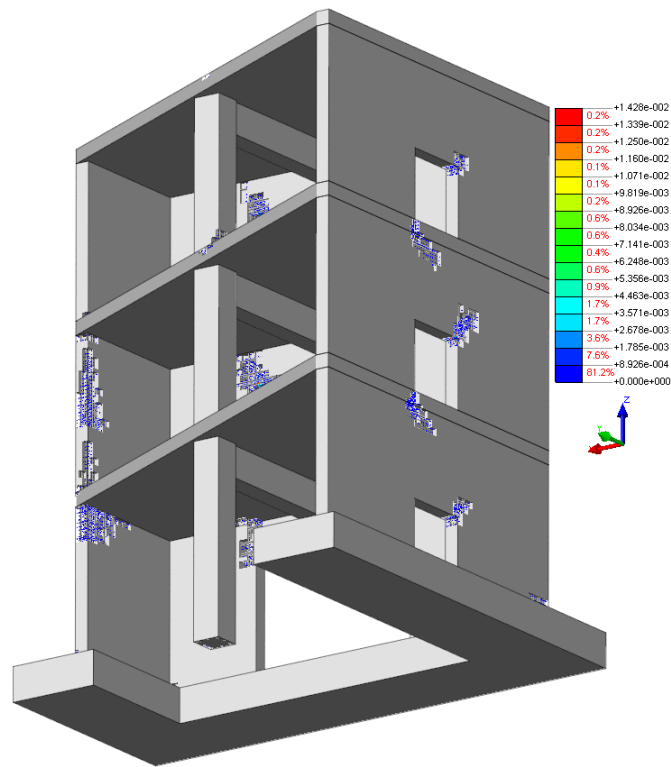
Figure 7.47: Crack pattern.
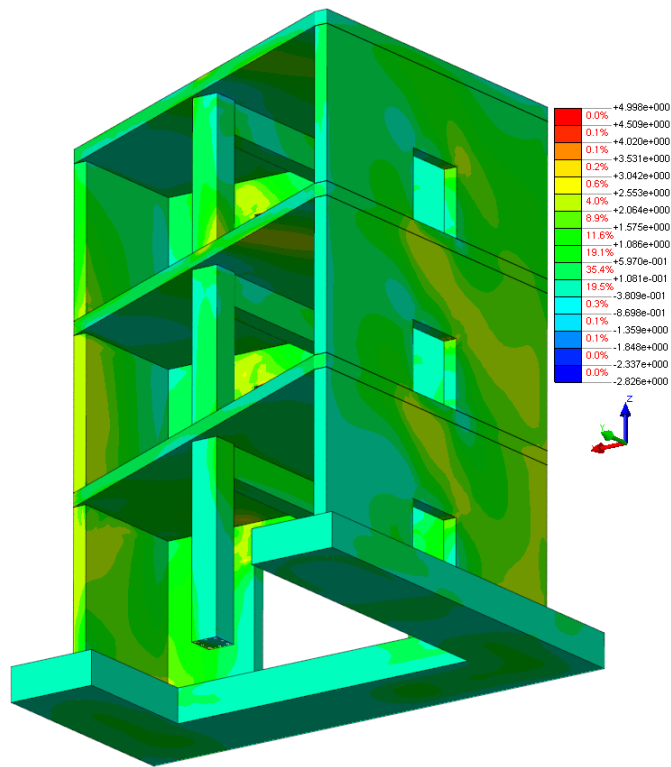
Figure 7.48: Tensile stresses in principle direction 1 in N/mm^2.
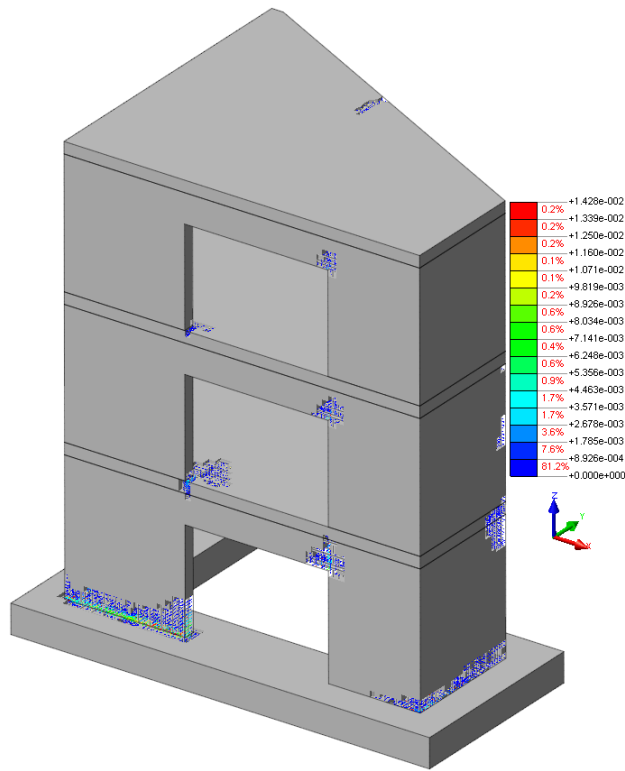
Figure 7.49: Crack pattern.
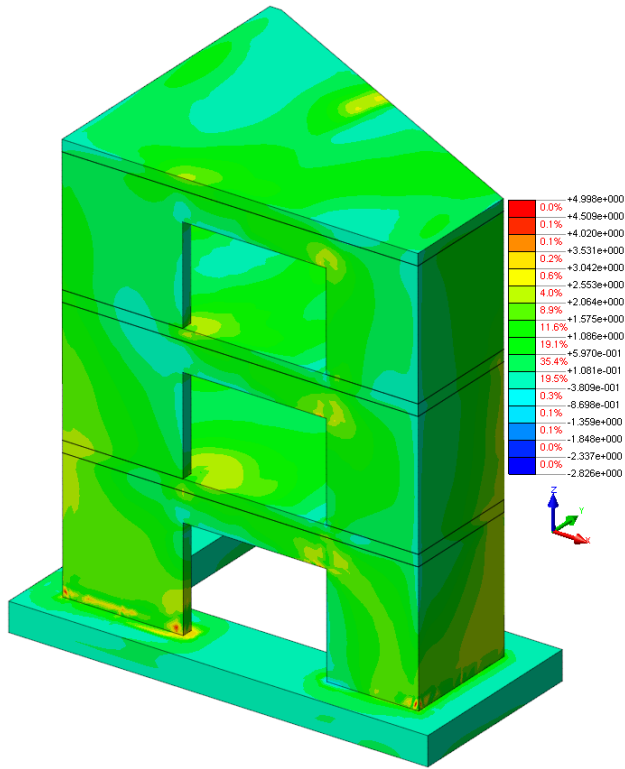
Figure 7.50: Tensile stresses in principle direction 1 in N/mm^2.

187

Here the cracks are focused at some edges of the openings and at the connection between the foundation and walls. Also the connection between the columns and the floor show some cracks together with the middle part of wall V04.

The interesting thing about the crack patterns from all three pushover analyses is that these cracks patterns have certain things in common. In all three pushover analyses, the cracks occur at the connections between the walls and the foundation. The edges of all openings show cracks in all three pushover analyses. Also the connections between the columns and the floors show cracks.

Further can be said the first pushover analysis shows the most cracks in comparison with the second and third pushover analysis. And the second pushover analysis shows the least amount of cracks. These observations can be explained by looking at the mode shapes of the model because the model is loaded according to its first three mode shapes in these pushover analyses.

The contour plots below shows what the stresses (S_{xx}) in the reinforcements are and where in the model the reinforcements are plastic (ϵ_{pxx}). The reinforcement in wall V01 near the foundation next to the opening yields.
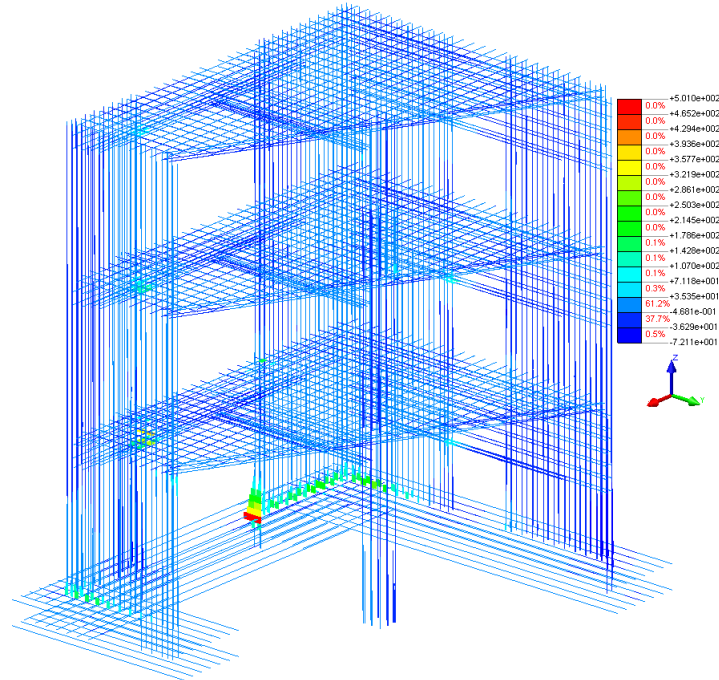
Figure 7.51: Stresses in the reinforcement.
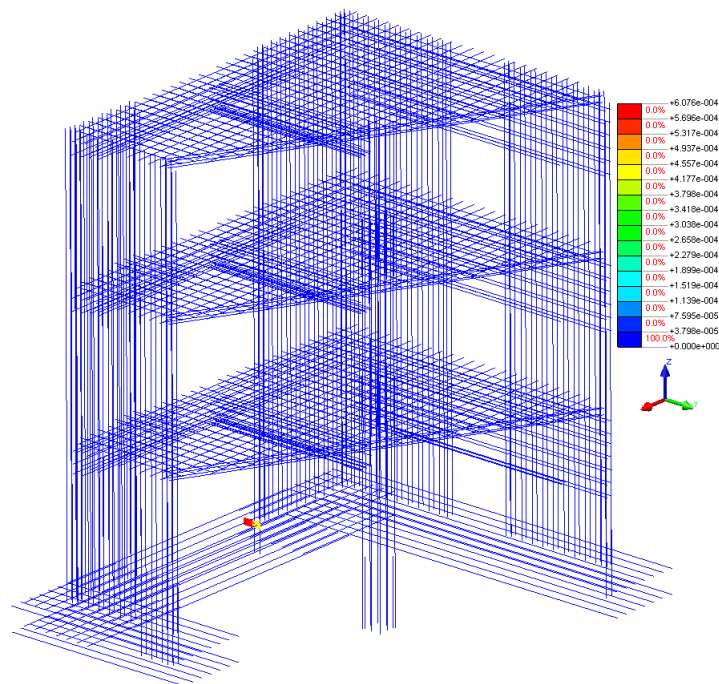
Figure 7.52: Plastic strains in the reinforcement.

According to the three pushover analyses the model can withstand, dependent of at which frequency the model vibrates, a PGA of 0.12 g, 0.14 g or 0.18 g, if the total mass of the model is taken into account. If the effective mass of the model is taken into account, then the model can withstand, dependent of at which frequency the model vibrates, a PGA of 0.22 g, 0.25 g or 1.41 g. The tables below give a nice overview of the estimated PGAs.

Table 7.7: Estimated PGA based on the total mass of the model.

Pushover	Estimated PGA [g] - total mass	Direction
1	0.12	x
2	0.14	y
3	0.18	y

Table 7.8: Estimated PGA based on the effective mass of the model.

Pushover	Estimated PGA [g] - effective mass	Direction
1	0.22	x
2	0.25	y
3	1.41	y

These estimated PGAs show what PGA (in x- and y-diraction) from a certain earthquake the model can withstand. If the total mass of the mock-up is taken into account, then the model can withstand a PGA of 0.12 g in x-direction and a PGA of 0.14/0.18 g in y-direction, dependent of at which frequency the model vibrates. When the effective mass of the model is considered, then the model can withstand a PGA of 0.22 g in x-direction and a PGA of 0.25/1.41 g in y-direction, dependent of at which frequency the model vibrates.

These estimated PGAs can be used to make predictions for the nonlinear transient analyses which will be performed in stage 3. For the prediction the following values are used.

Table 7.9: Estimated PGAs for the prediction.

Mass of the model	PGA x [g]	PGA y [g]
Total mass	0.12	0.18
Effective mass	0.22	1.41

Table 7.9 shows that for PGA y the estimated value of the third pushover analysis is chosen. The reason why the estimated PGA of the third pushover analysis is chosen above the estimated PGA of the second pushover analysis is because of the geometry of the model. Because of the geometry of the model, the model tends to twist in z-direction when it vibrates. As shown before, all three mode shapes showed that the model twists in z-direction where the torsion of the model is very dominant in the third mode. Also the third pushover analysis shows more cracks in comparison with the second pushover analysis.

According to the estimated PGAs of the pushover analyses, some RUNs for the nonlinear transient analysis will converge nicely and some RUNs will diverge because the PGA of these RUNs will exceed the capacity of the model. With exceeding the capacity of the model it means that the nonlinear transient analysis will diverge. The table below shows which RUNs will exceed the capacity of the model, according to the estimated PGAs, when taking the total mass of the model into account.

Table 7.10: Predictions of the pushover analysis - total mass.

RUN	PGA x [g]	Exceeds capacity	PGA y [g]	Exceeds capacity
9	0.25	Yes	0.35	Yes
11	0.22	Yes	0.18	No
13	0.42	Yes	0.32	Yes
17	0.63	Yes	0.44	Yes
19	1.11	Yes	1.03	Yes
21	0.15	Yes	0.20	No
23	0.65	Yes	0.46	Yes

When taking the effective mass of the mock-up into account, the following predictions hold.

Table 7.11: Predictions of the pushover analysis - effective mass.

RUN	PGA x [g]	Exceeds capacity	PGA y [g]	Exceeds capacity
9	0.25	Yes	0.35	No
11	0.22	No	0.18	No
13	0.42	Yes	0.32	No
17	0.63	Yes	0.44	No
19	1.11	Yes	1.03	No
21	0.15	No	0.20	No
23	0.65	Yes	0.46	No

Table 7.10 shows that the model can't withstand any of the RUNs but table 7.11 shows that the model can withstand RUN11 and RUN21 because the model can withstand the PGAs of these RUNs in x- and y-direction. It is important to know that when the model vibrates in a certain direction, a certain amount of the mass of the model will move in that certain direction and that is why it is convenient to use table 7.11 to predict the capacity of the model when performing nonlinear transient analyses.

As mentioned in the introduction of this stage, RUN17, RUN19 and RUN23 diverged. So what does diverging of the analysis actually mean? It could mean that the capacity of the model is reached and due to this some parts of the model maybe falling apart. When this happens, the analysis cannot proceed and it diverges. Having that said, the capacity estimations of the pushover analyses partially confirm this. The pushover analyses estimated that the model can only withstand RUN11 and RUN21 and indeed the model withstood RUN11 and RUN21. The model also withstood RUN9 and RUN13 while the pushover analyses estimated that the model cannot withstand RUN9 and RUN13. So how can this be explained? This can be explained by first mentioning that the predictions of the pushover analyses are estimations, which means that the predictions could not be completely true. A second reason could be the amplification factor that is used to estimate the capacity of the model. As mentioned before, the amplification factor that is used here holds for full scale buildings while the model in this thesis is scaled. And the last reason is that the pushover analysis is limited because it can only take one mode shape at a time. In the following sections a new amplification factor is calculated which is used to estimate the capacity of the model.

7.2 Non-linear Response with Respect to RUN9

The PGA of RUN9 in x-direction is 0.25 g, in y-direction it is 0.35 g, in z-direction it is 0.18 g and it has a duration of 8.99 seconds. First a comparison is made between the experimental response (red graphs) of the mock-up and the numerical response (blue graphs) of the model in terms of displacements in point D on floor 3. After that the contour plots of the crackwidth in (mm) together with the contour plots of the principle stresses in S1 from RSA are shown. The first graph shows the total responses and the second graph shows a piece of the total responses.
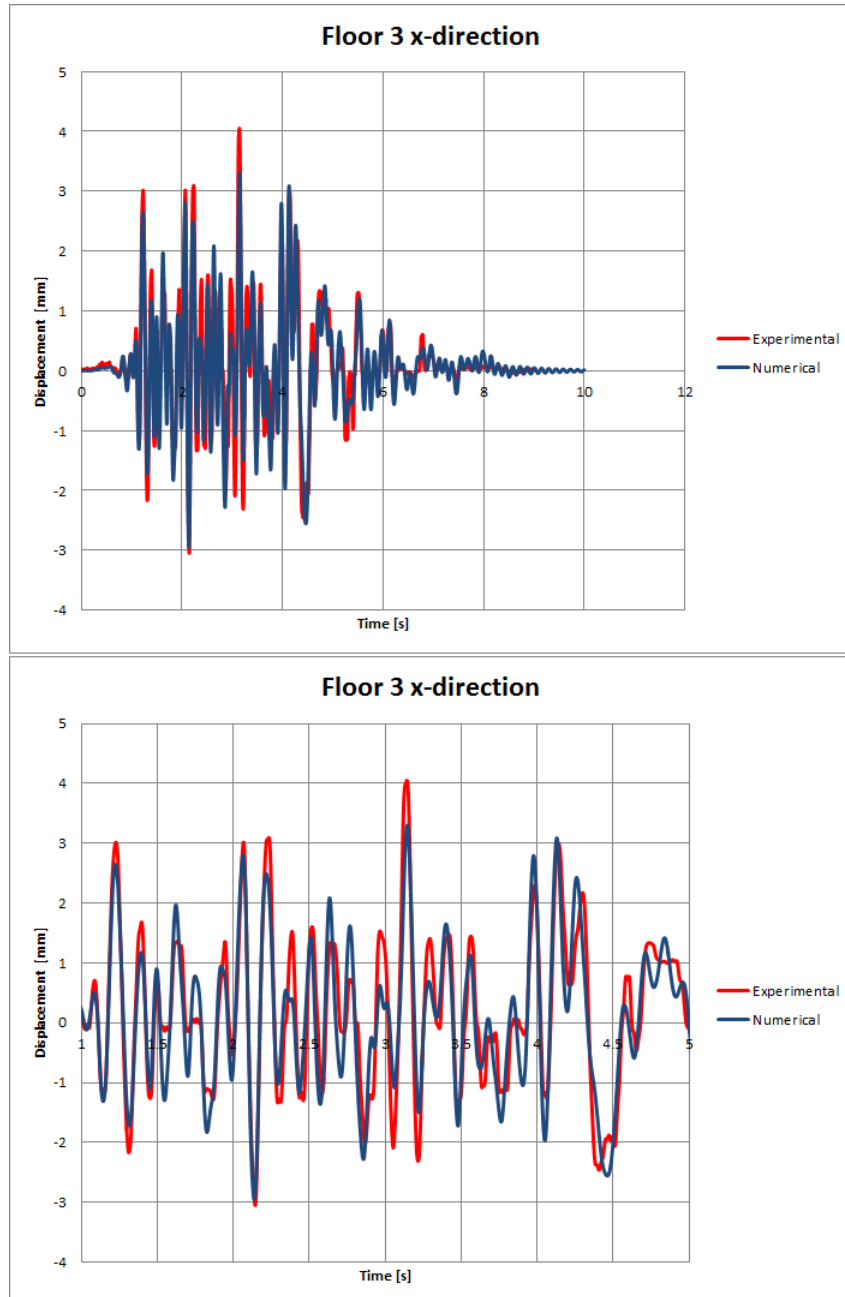
Figure 7.53: Experimental vs numerical displacement - RUN9.
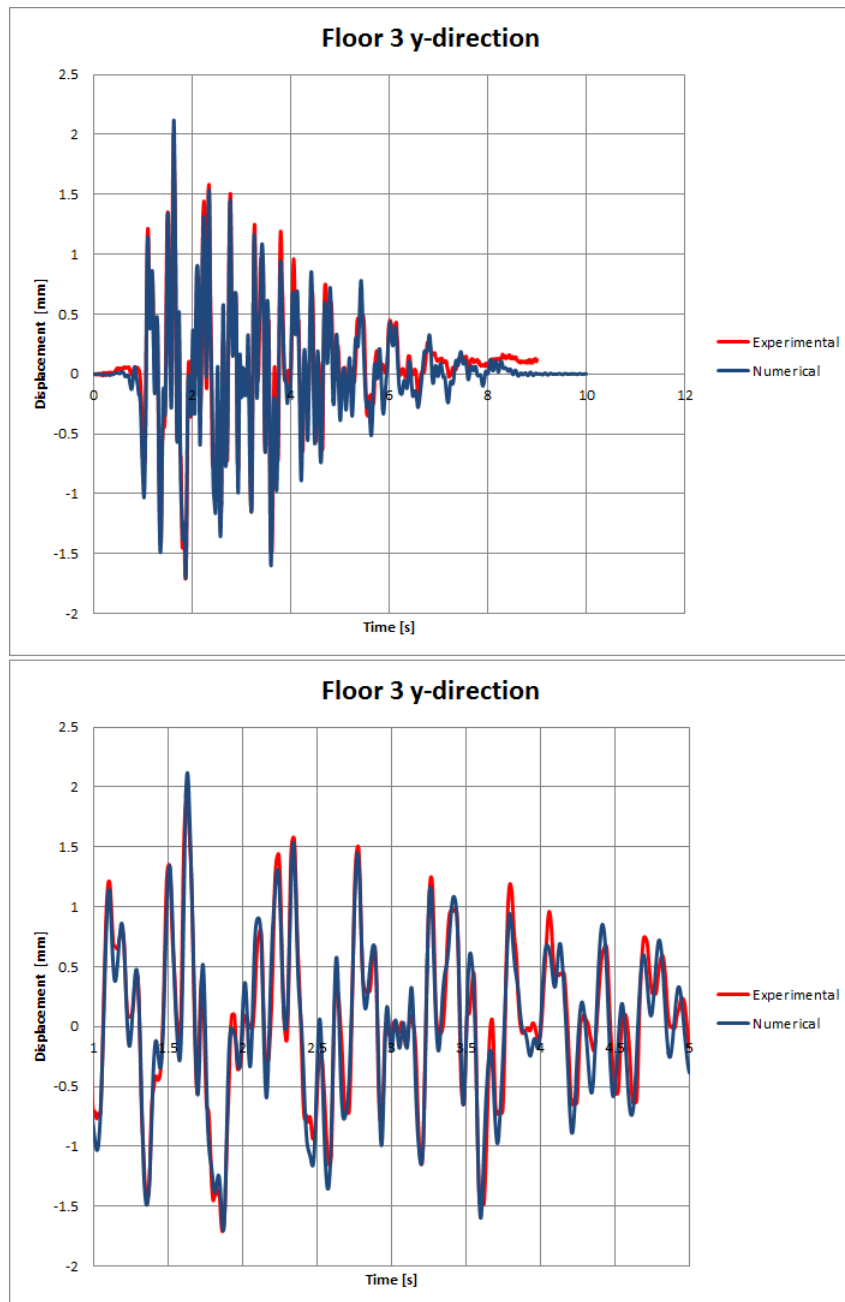
Figure 7.54: Experimental vs numerical displacement - RUN9.

The two figures from above show that there is a good match between the experimental response of the mock-up and the numerical response of the model in terms of displacements in x- and y-direction. In some points the amplitudes of the responses differ a bit and the responses are sometimes a little out-of-phase but in general the match is very good, especially in y-direction.

The contour plots look as follows.
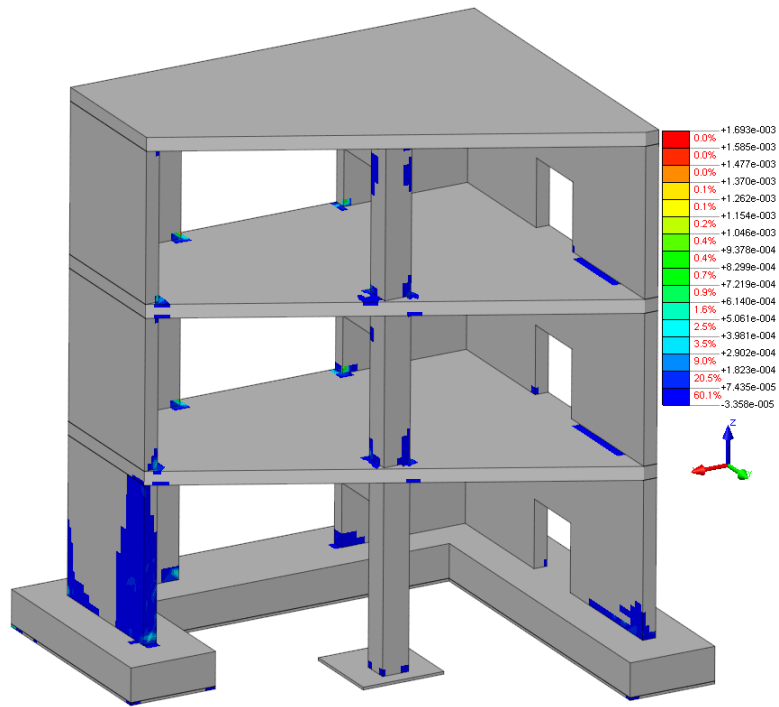
Figure 7.55: Crackwidth in mm.
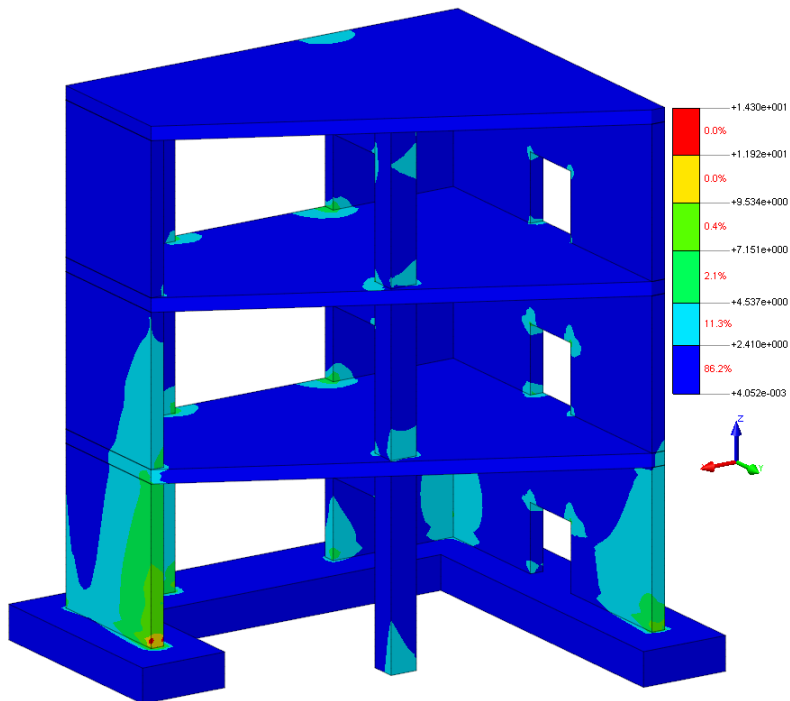
Figure 7.56: Principle stresses in S1 in N/mm^2 according to RSA.
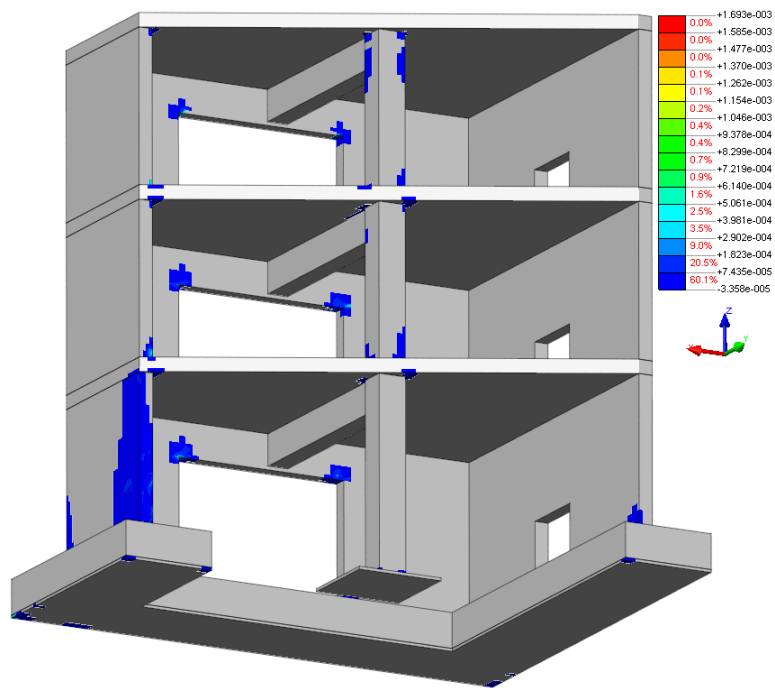
Figure 7.57: Crackwidth in mm.
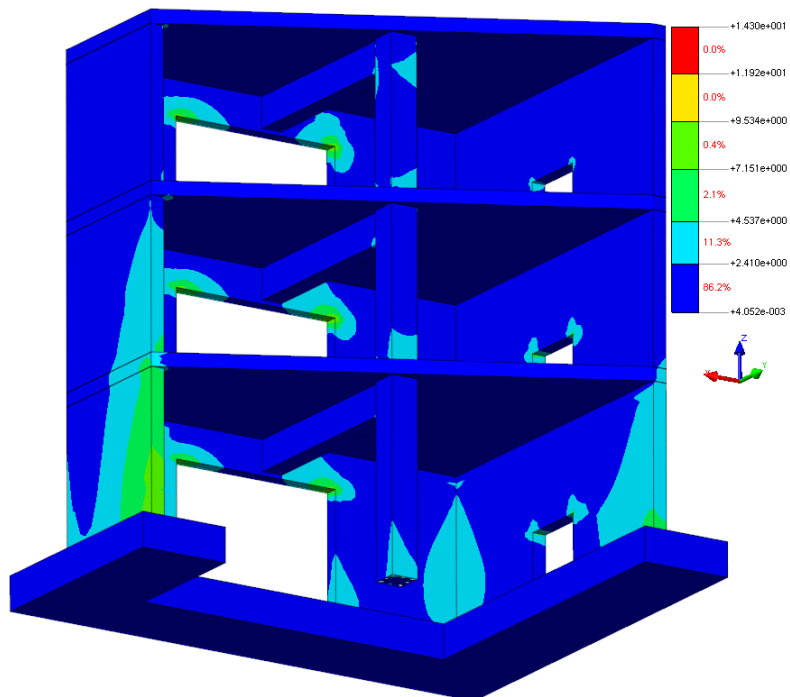
Figure 7.58: Principle stresses in S1 in N/mm^2 according to RSA.
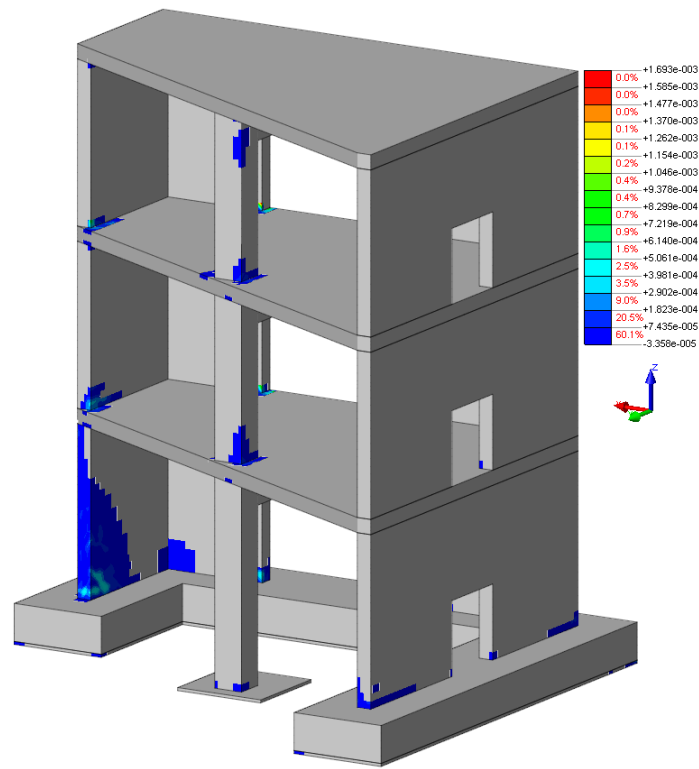
Figure 7.59: Crackwidth in mm.
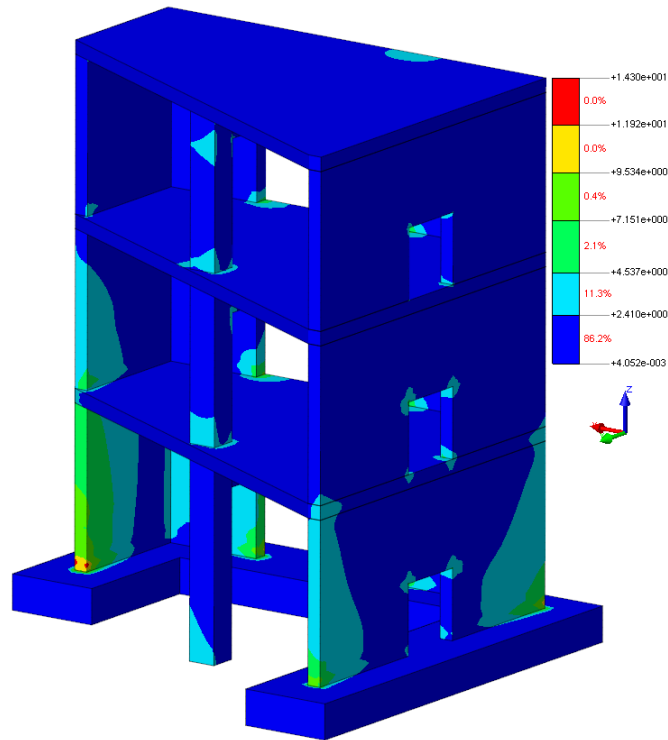
Figure 7.60: Principle stresses in S1 in N/mm^2 according to RSA.

Figure 7.61: Crackwidth in mm.
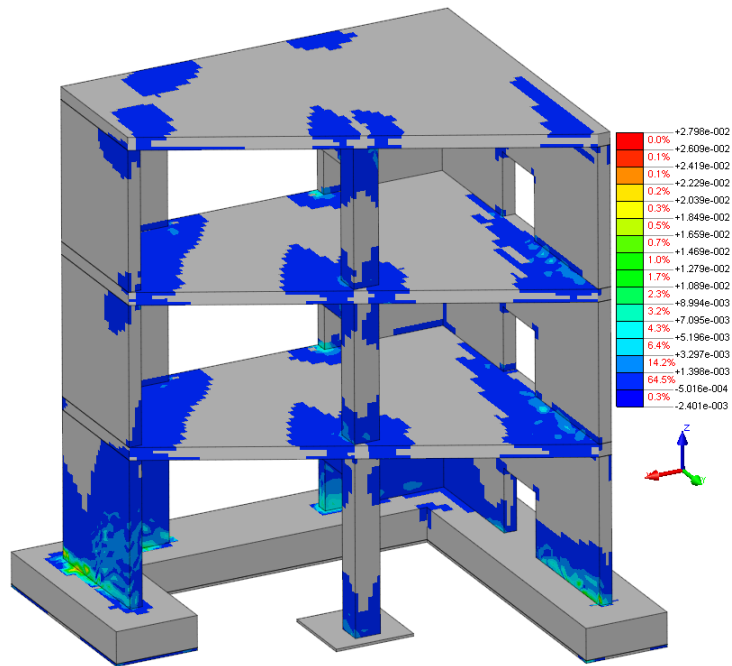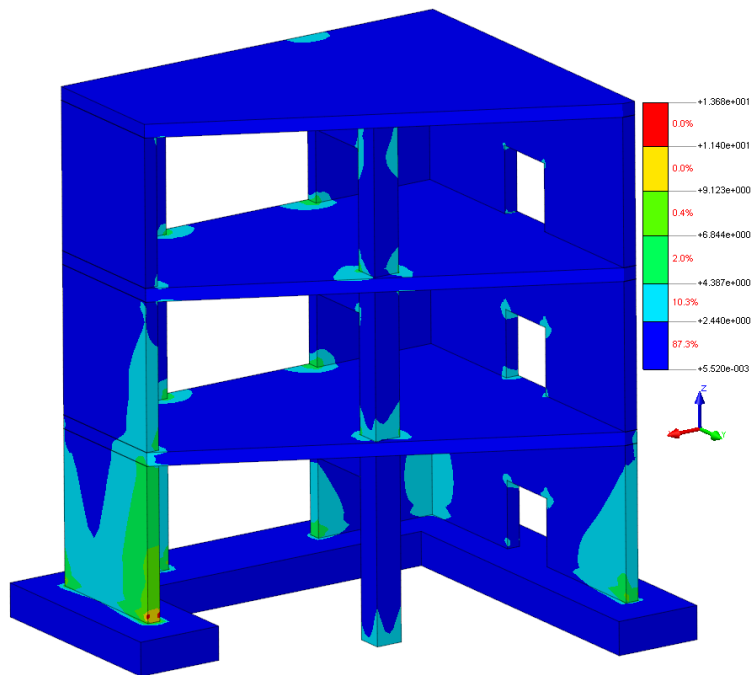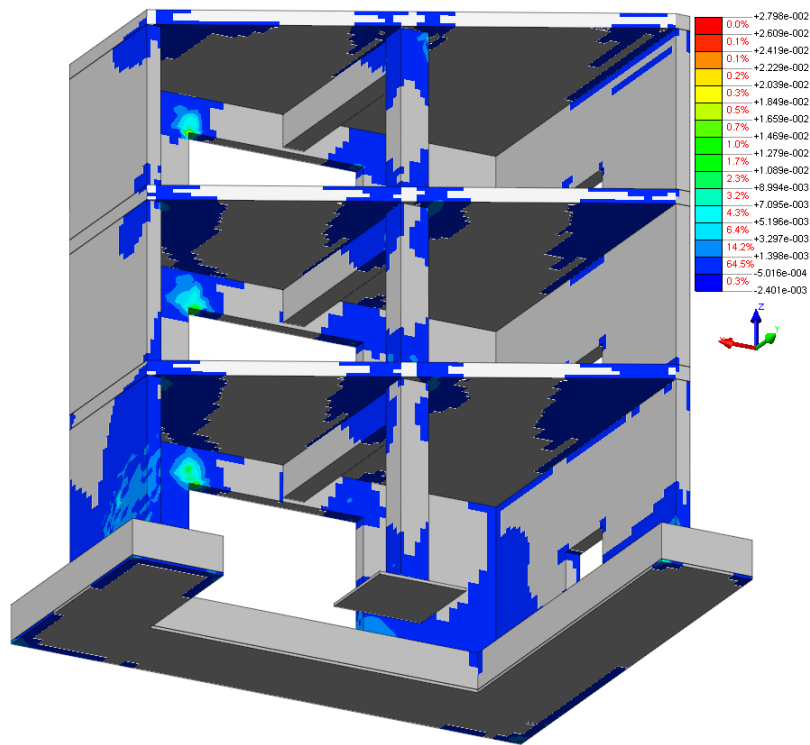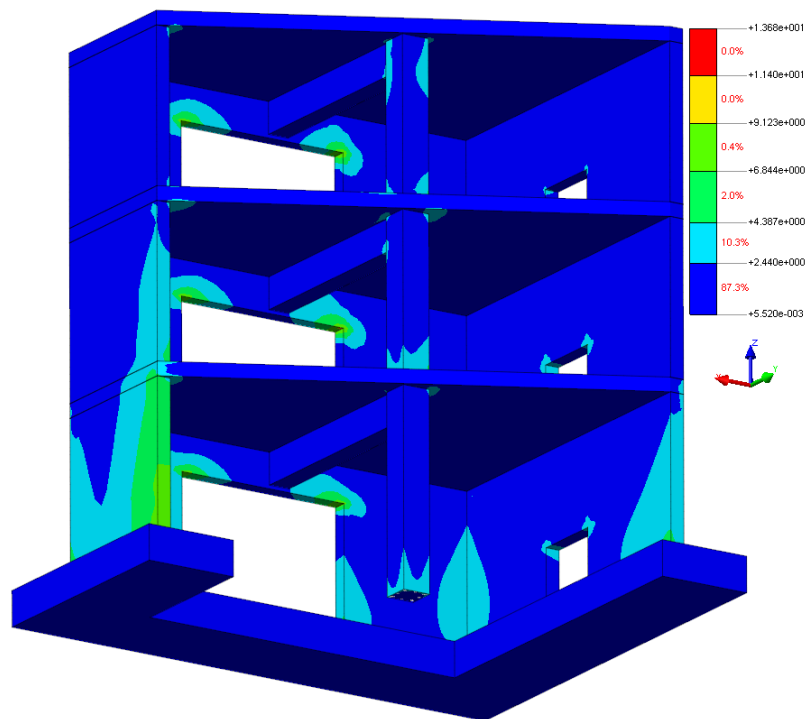

Figure 7.62: Principle stresses in S1 in N/mm^2 according to RSA.
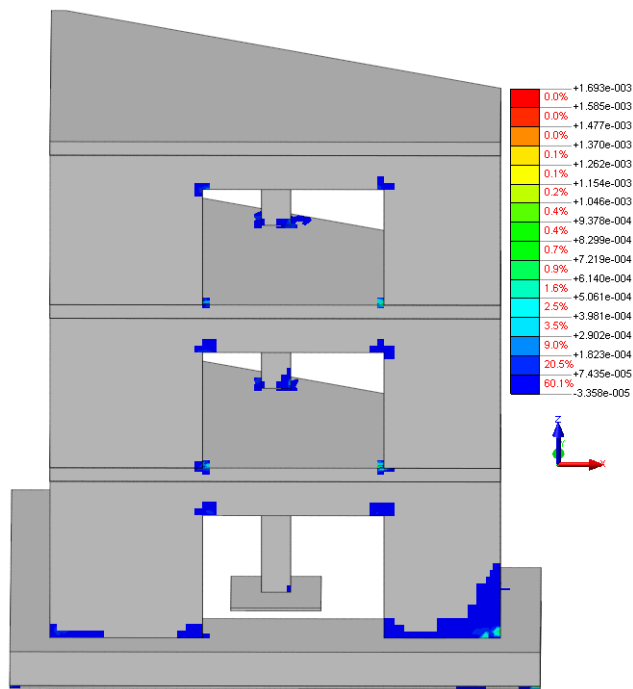
Figure 7.63: Crackwidth in mm.
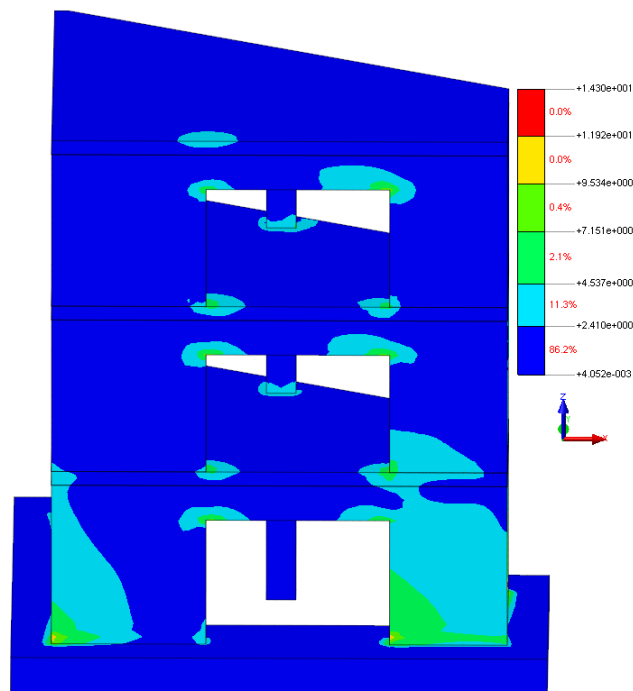
Figure 7.64: Principle stresses in S1 in N/mm^2 according to RSA.

The figures from above show that the contour plots from RSA are good in showing where the model might crack when performing nonlinear transient analysis. In the places where the tensile stresses are much higher then the tensile strength of concrete (according to RSA) the model shows cracks in the nonlinear transient analysis. The reason for this is that in RSA the concrete doesn't crack and because of this there will be high stress concentrations in some places of the model and from these high stress concentrations the stresses will spread out to other parts of the model. This phenomena is shown in the contour plots from above. The match between the contour plots of the stress distribution from RSA and the crackwidth is not 100% but it is good as can be seen. This same story holds also for all the other RUNs.

The RSA with the response spectrum of RUN9 as input, showed that the reinforcement will not yield. And indeed the reinforcement did not yield in the nonlinear transient analysis. The figure below shows that.
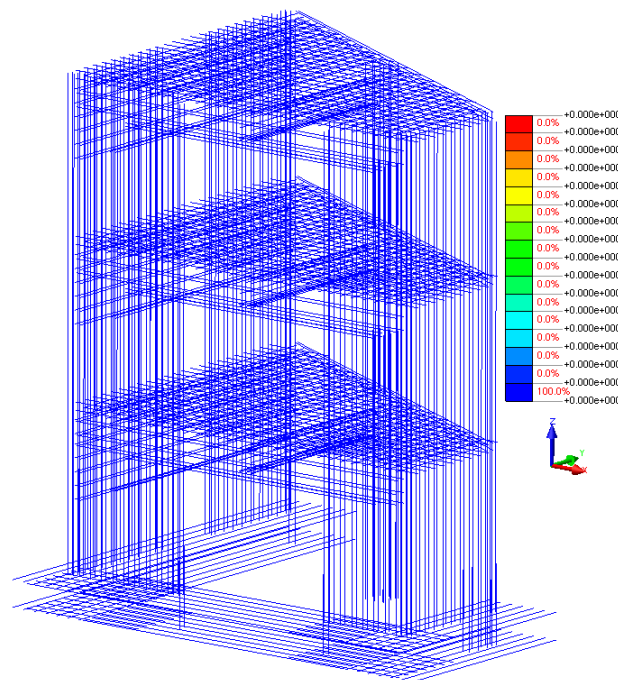
Figure 7.65: Plastic strains in the reinforcement.

The comparisons which are just made for RUN9 also hold for all other RUNs in the following sections.

7.3 Non-linear Response with Respect to RUN11

The PGA of RUN9 in x-direction is 0.22 g, in y-direction it is 0.18 g, in z-direction it is 0.09 g and it has a duration of 13.49 seconds. First a comparison is made between the experimental response of the mock-up and the numerical response of the model in terms of displacements and accelerations in point D on floor 3. After that the contour plots of the crackwidth in (mm) together with the contour plots of the principle stresses in S1 from RSA are shown. The first graph shows the total responses and the second graph shows a piece of the total responses.
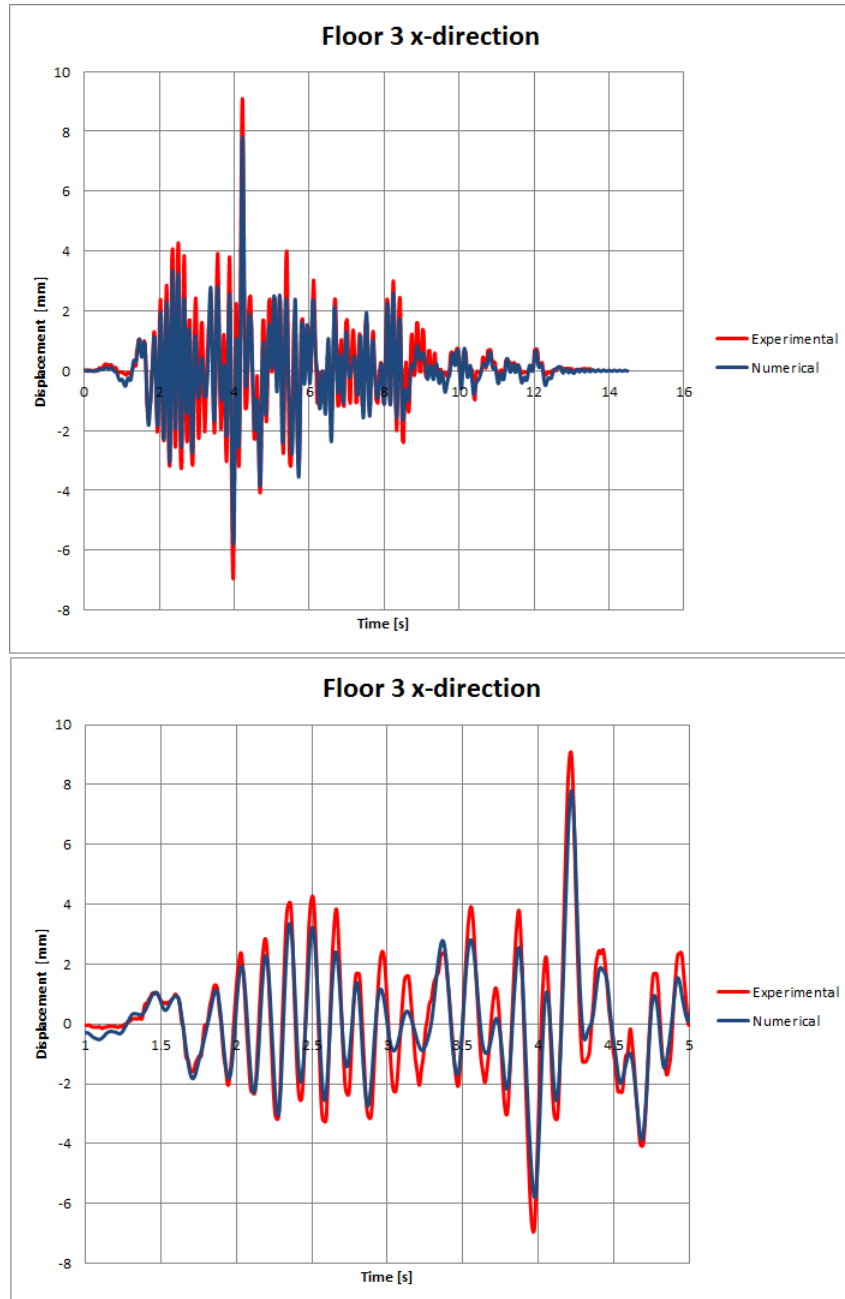
Figure 7.66: Experimental vs numerical displacement - RUN11.

200
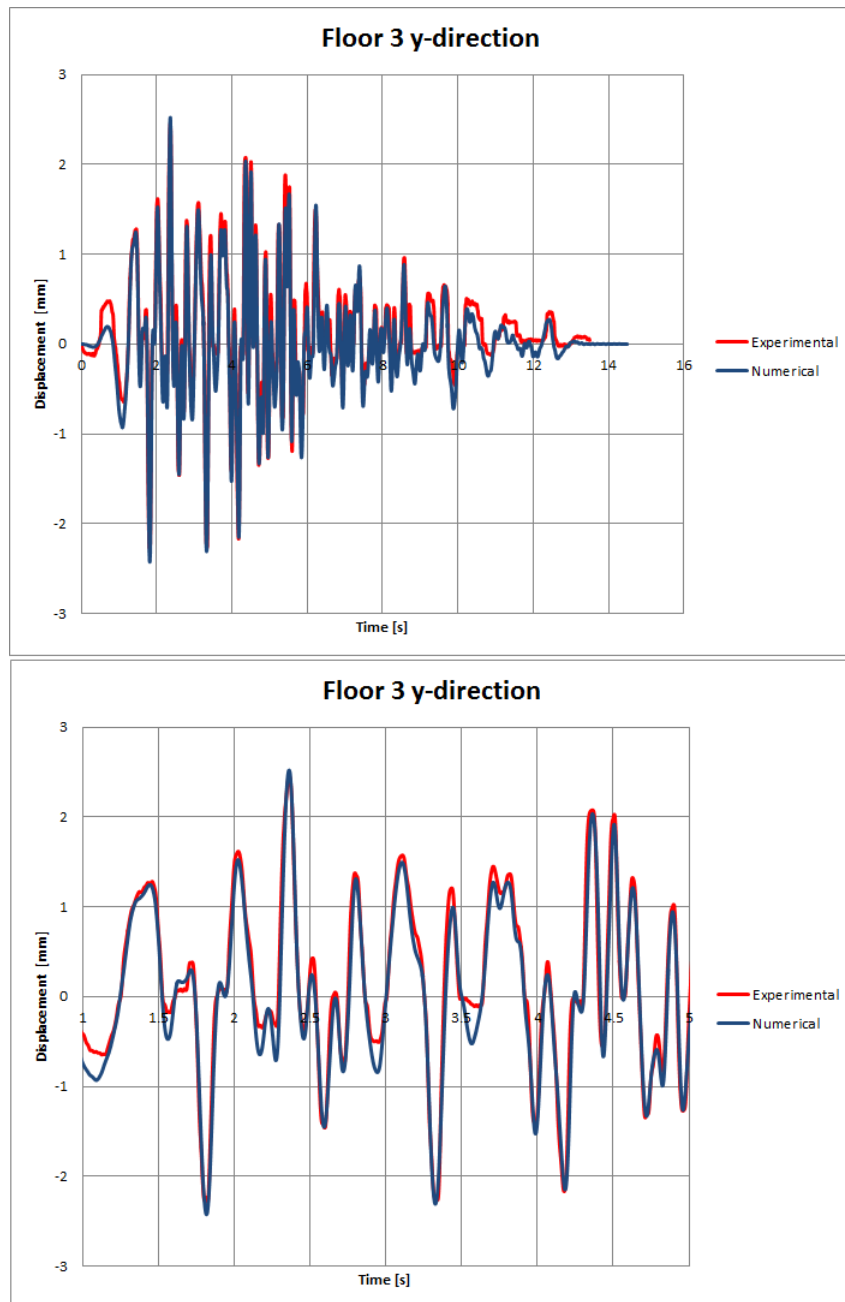
Figure 7.67: Experimental vs numerical displacement - RUN11.

The two figures from above show that there is a good match between the experimental response of the mock-up and the numerical response of the model in terms of displacements in x- and y-direction. In some points the amplitudes of the responses differ a bit and the responses are sometimes a little out-of-phase but in general the match is very good.

The contour plots look as follows.
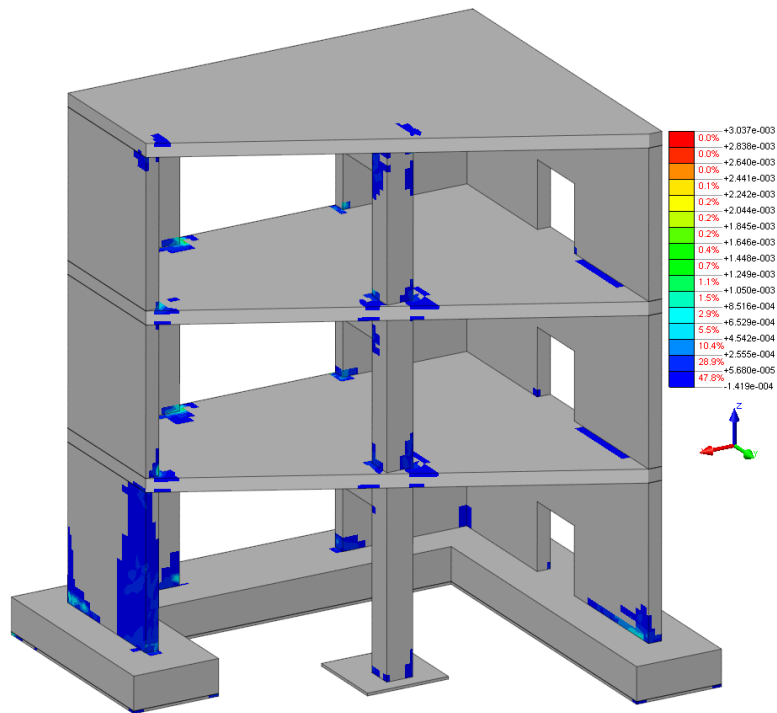
Figure 7.68: Crackwidth in mm.
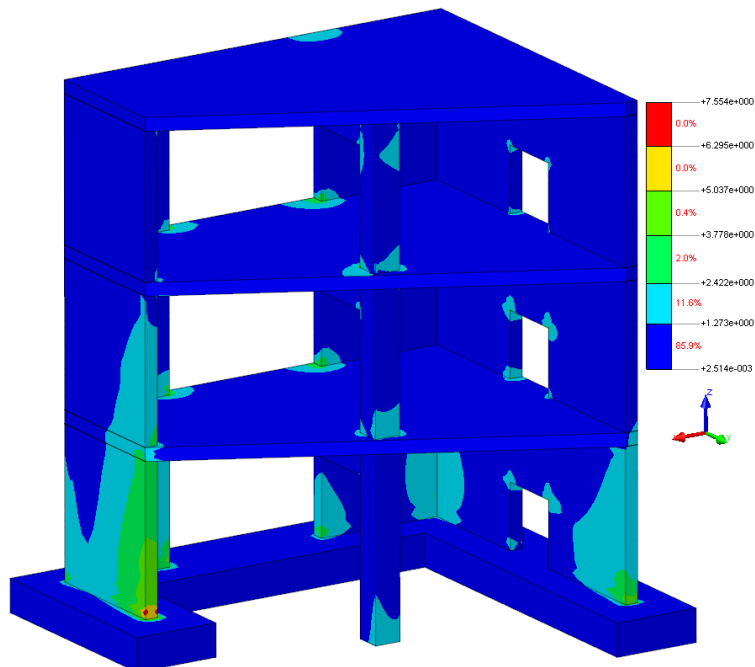
Figure 7.69: Principle stresses in S1 in N/mm^2 according to RSA.
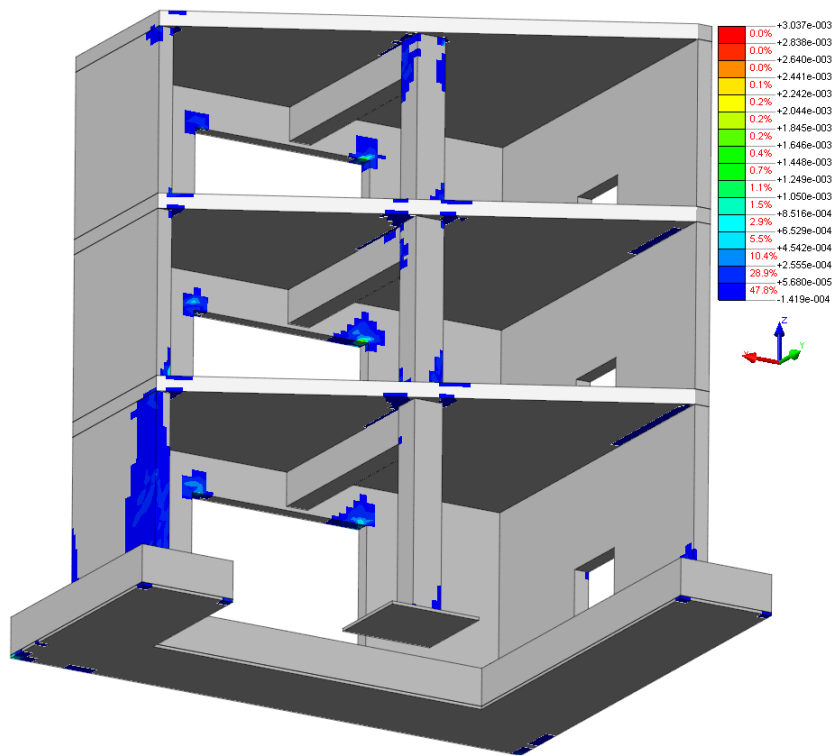
Figure 7.70: Crackwidth in mm.
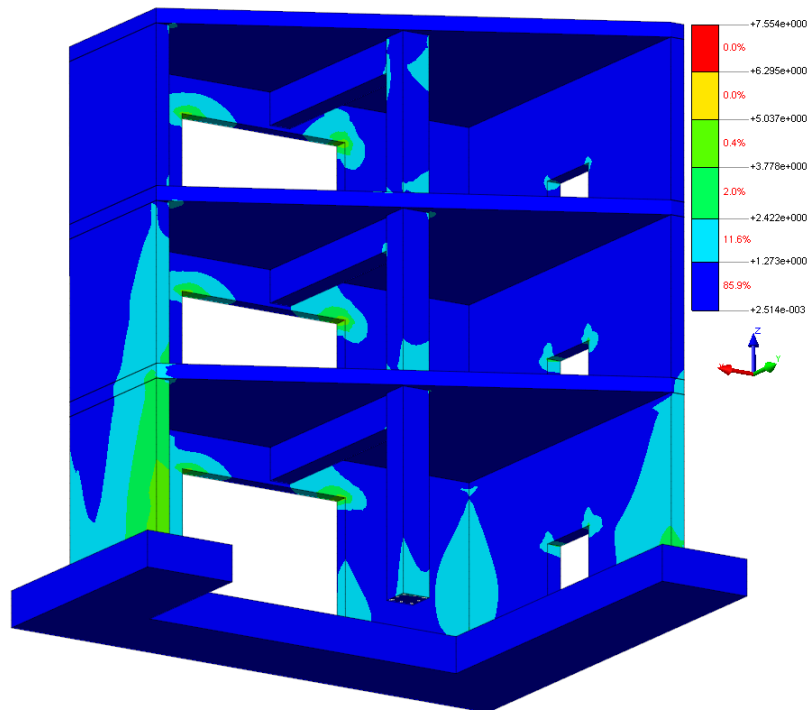
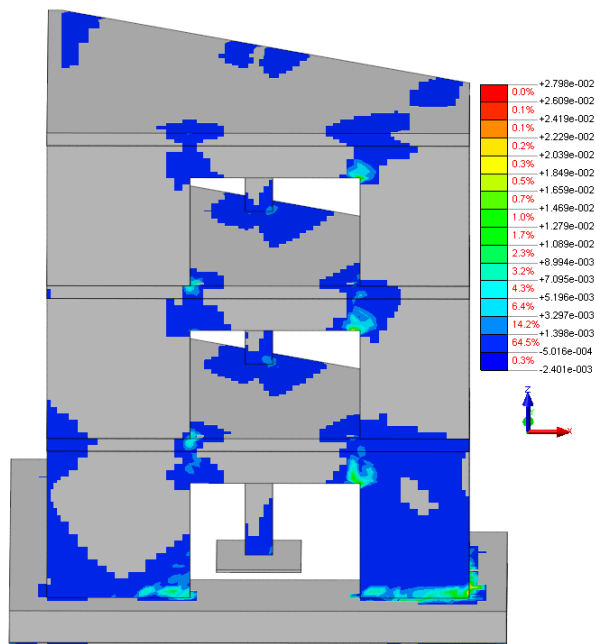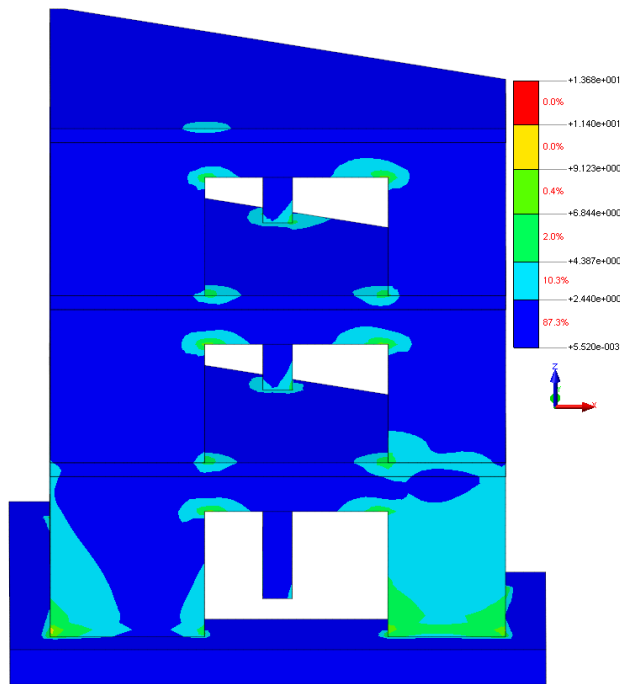Figure 7.71: Principle stresses in S1 in N/mm^2 according to RSA.
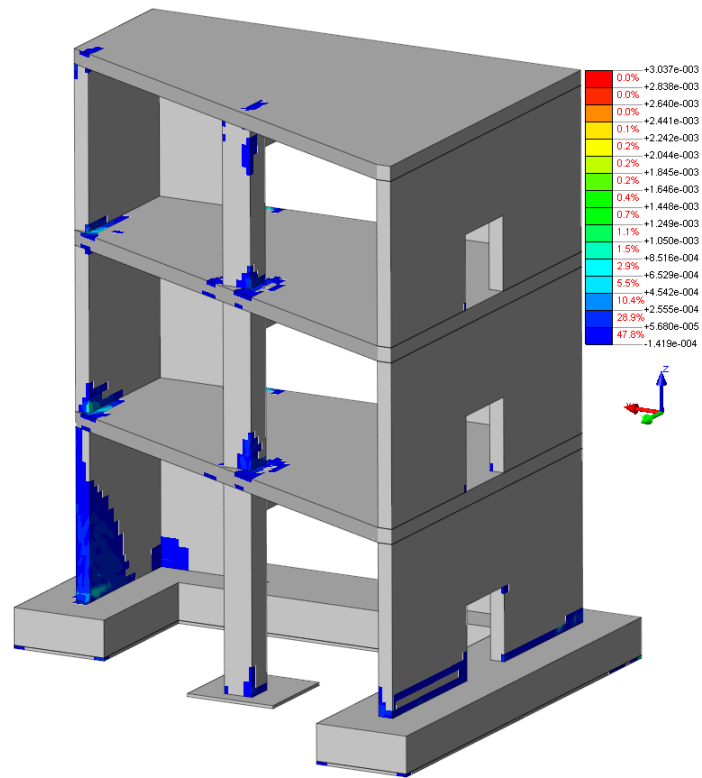
Figure 7.72: Crackwidth in mm.
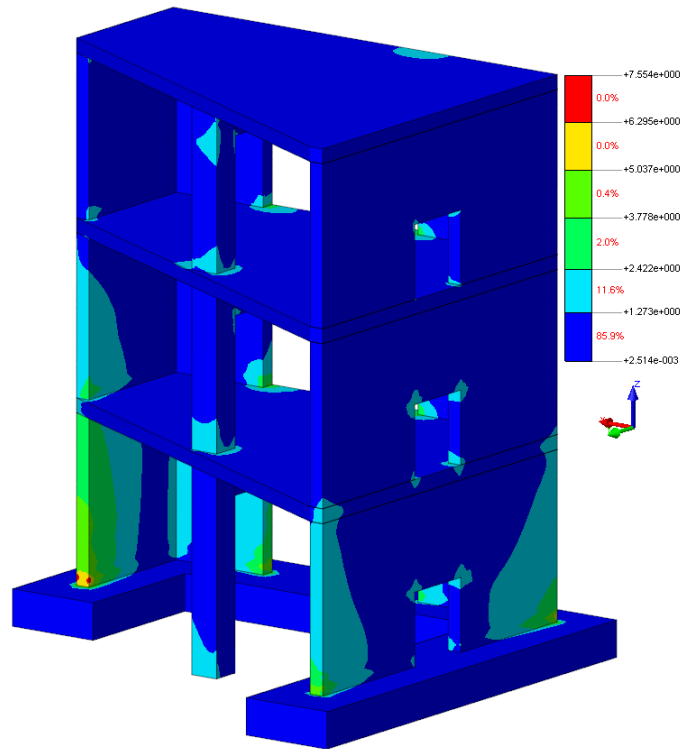
Figure 7.73: Principle stresses in S1 in N/mm^2 according to RSA.
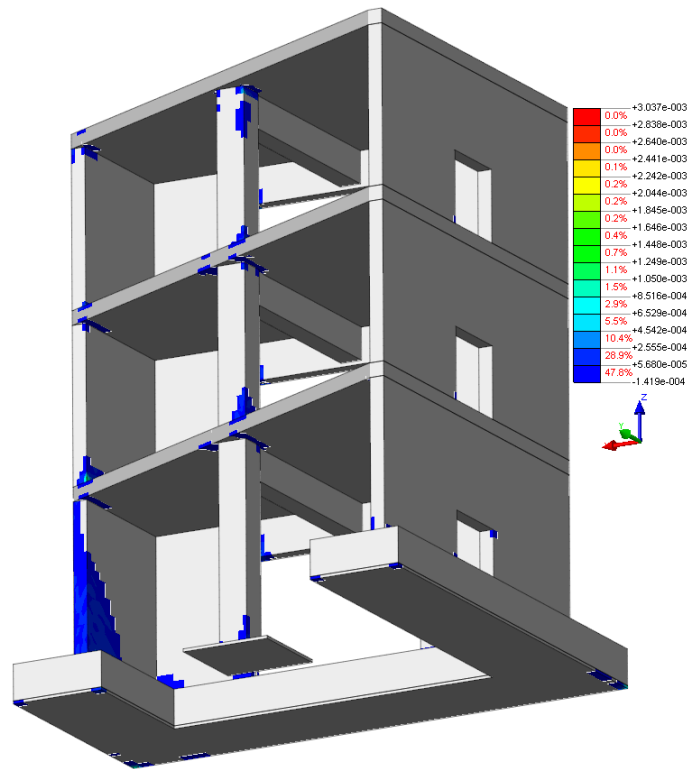
Figure 7.74: Crackwidth in mm.
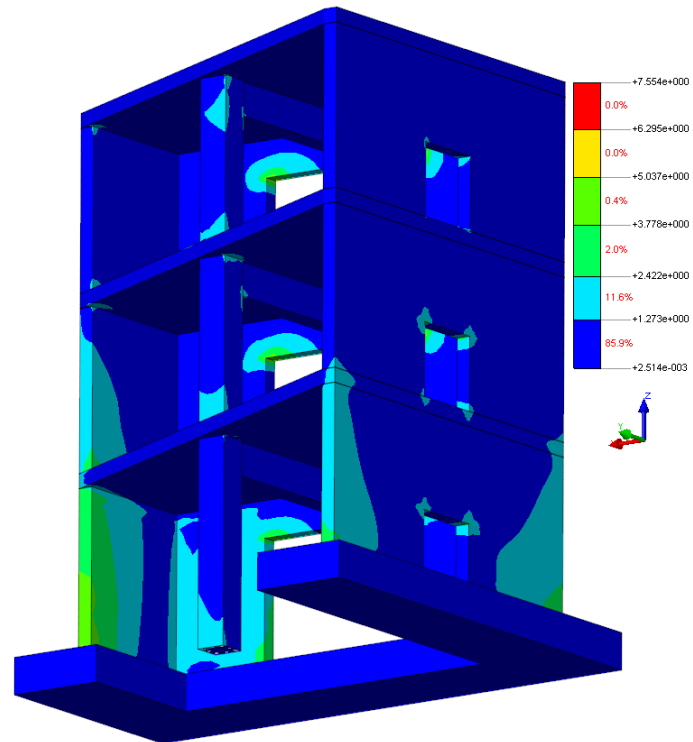
Figure 7.75: Principle stresses in S1 in N/mm^2 according to RSA.
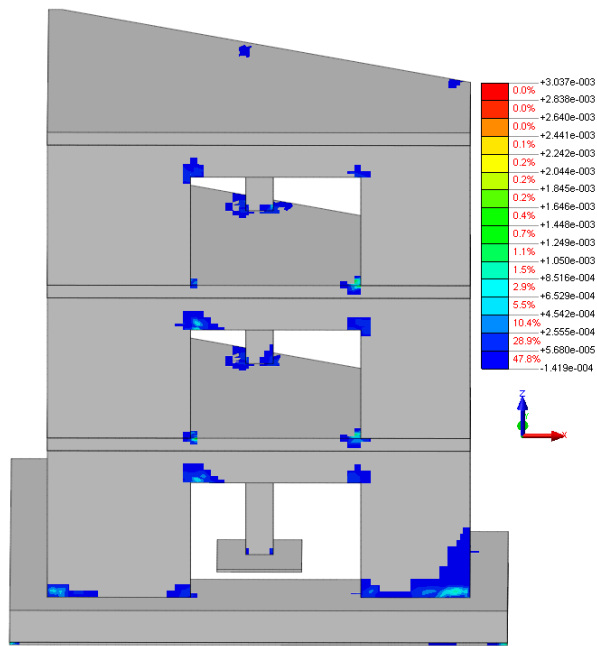
Figure 7.76: Crackwidth in mm.
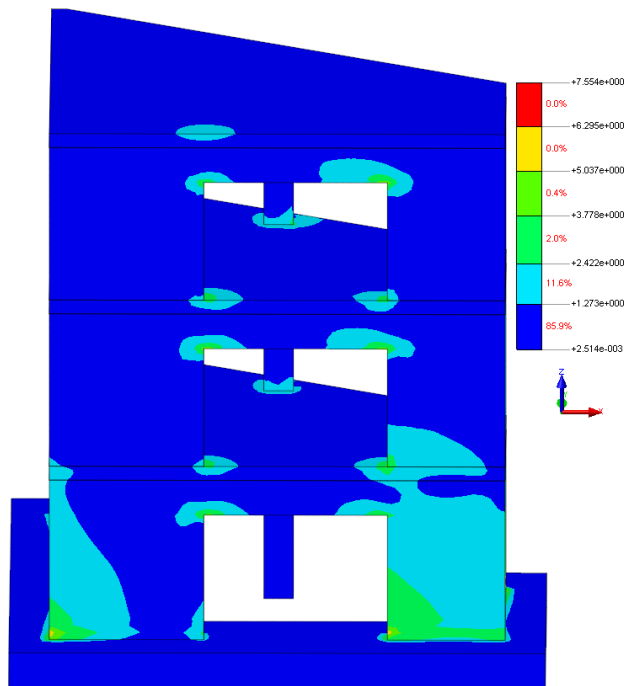
Figure 7.77: Principle stresses in S1 in N/mm^2 according to RSA.

There is no plasticity in the reinforcement. The plastic strains are everywhere zero.
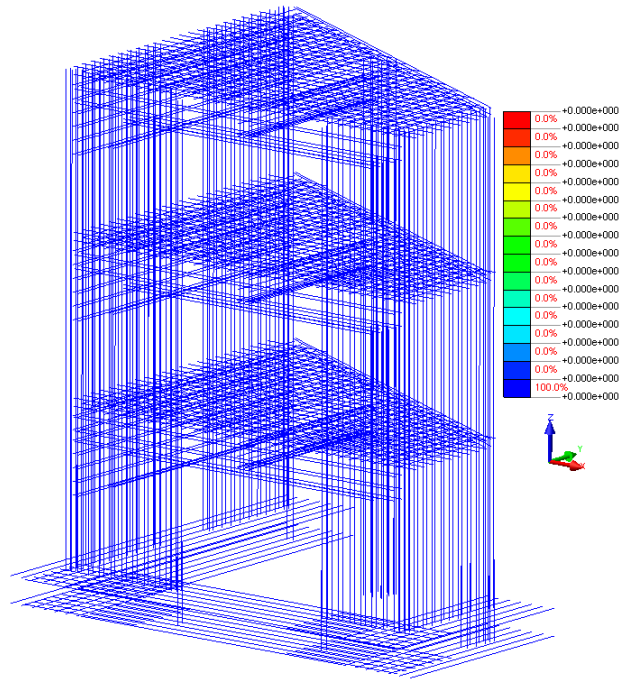
Figure 7.78: Plastic strains in the reinforcement.

7.4 Non-linear Response with Respect to RUN13

The PGA of RUN9 in x-direction is 0.42 g, in y-direction it is 0.32 g, in z-direction it is 0.24 g and it has a duration of 17.49 seconds. First a comparison is made between the experimental response of the mock-up and the numerical response of the model in terms of displacements and accelerations in point D on floor 3. After that the contour plots of the crackwidth in (mm) together with the contour plots of the principle stresses in S1 from RSA are shown. The first graph shows the total responses and the second graph shows a piece of the total responses.
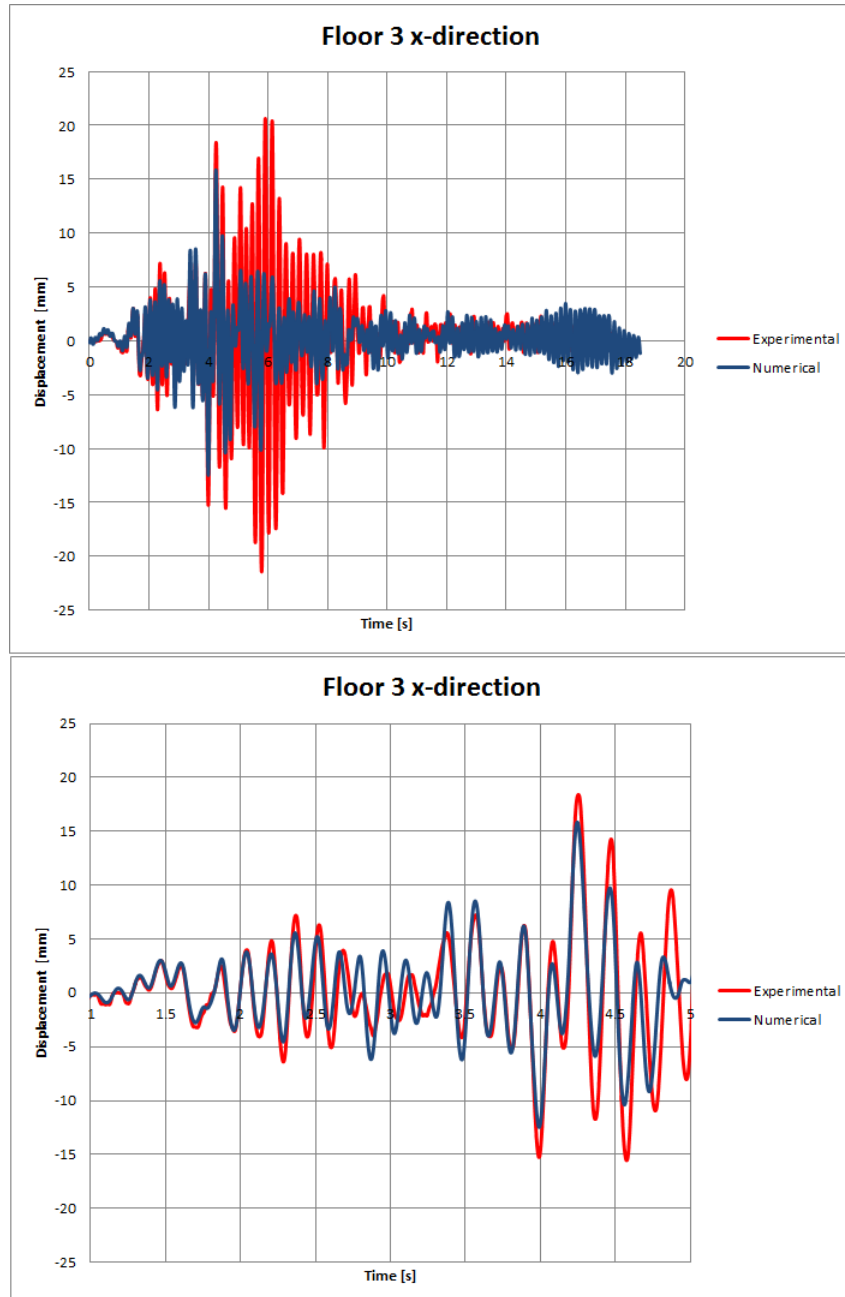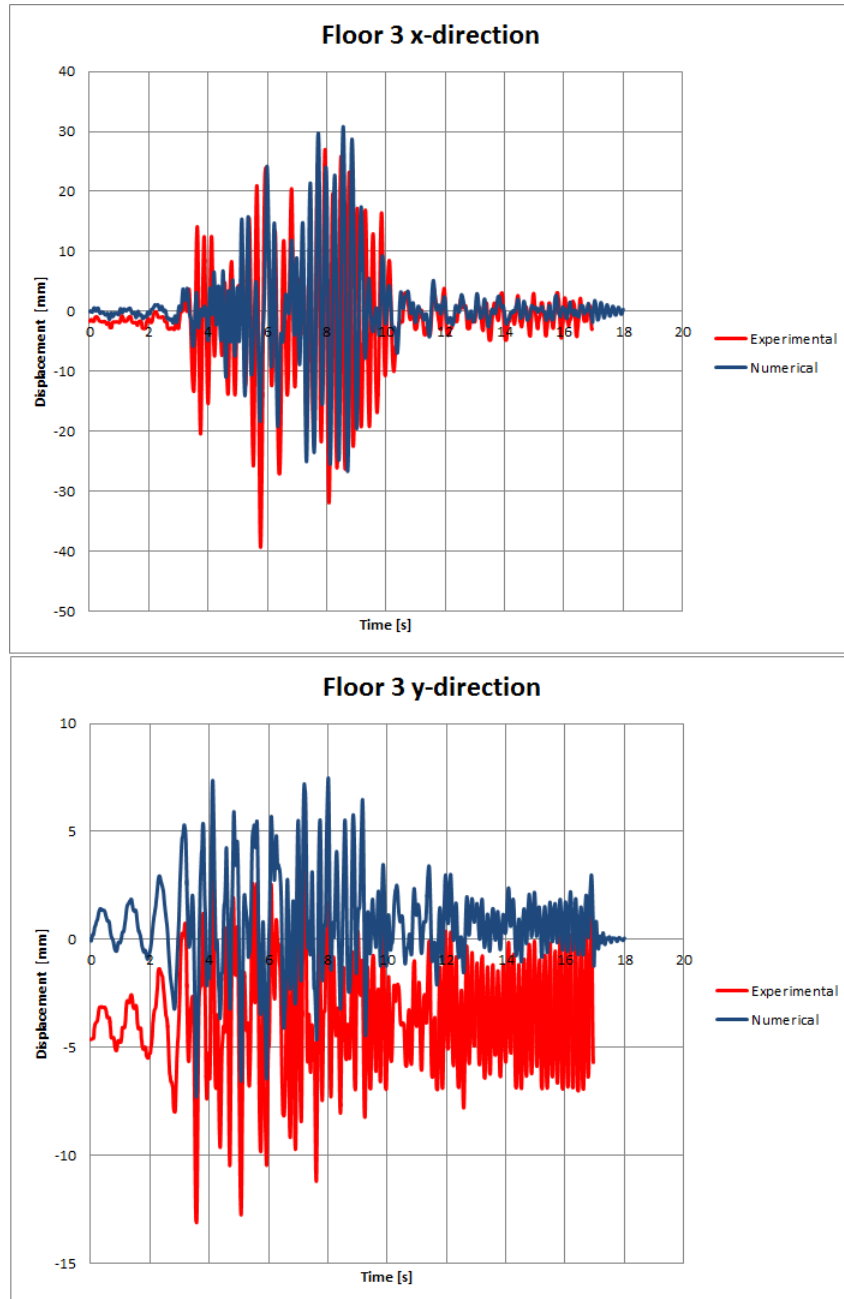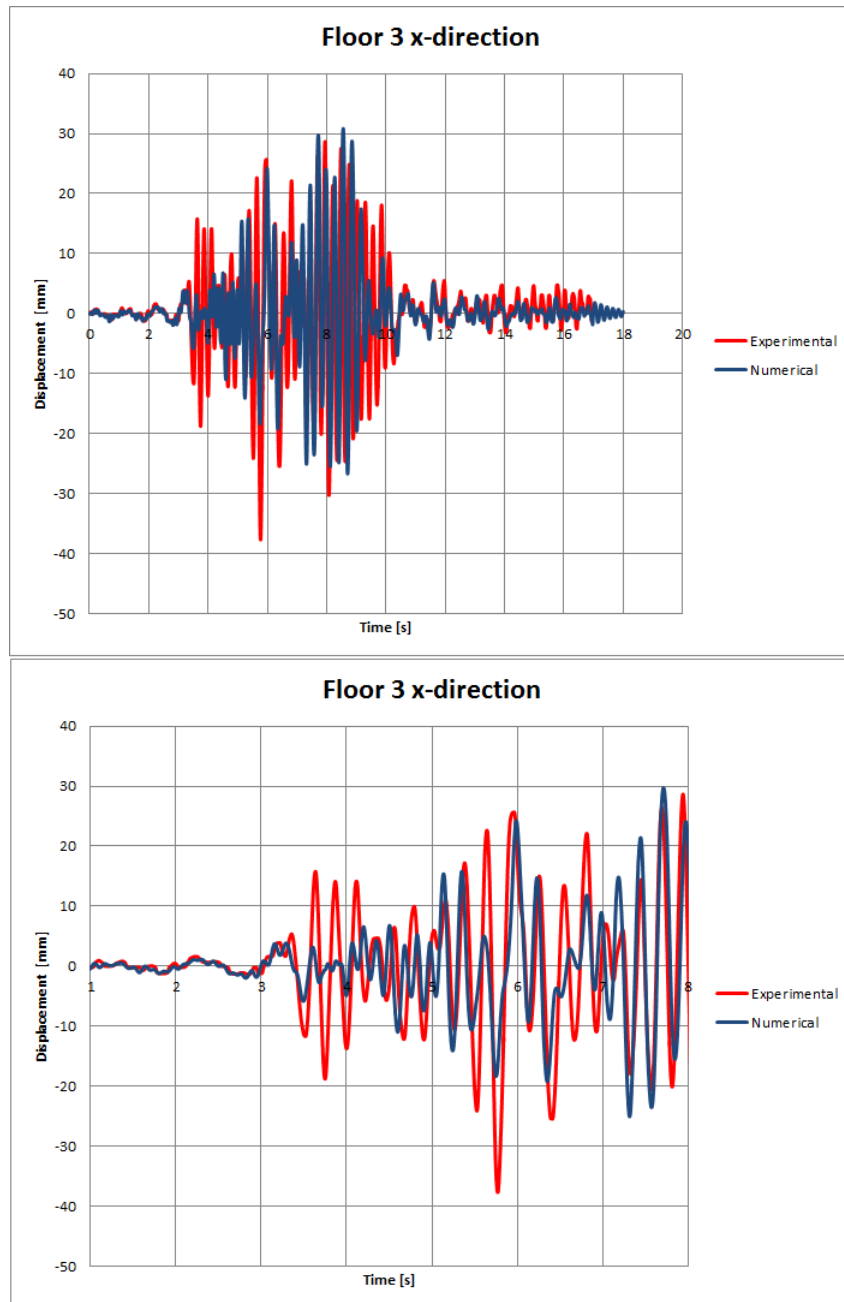

Figure 7.79: Experimental vs numerical displacement - RUN13.
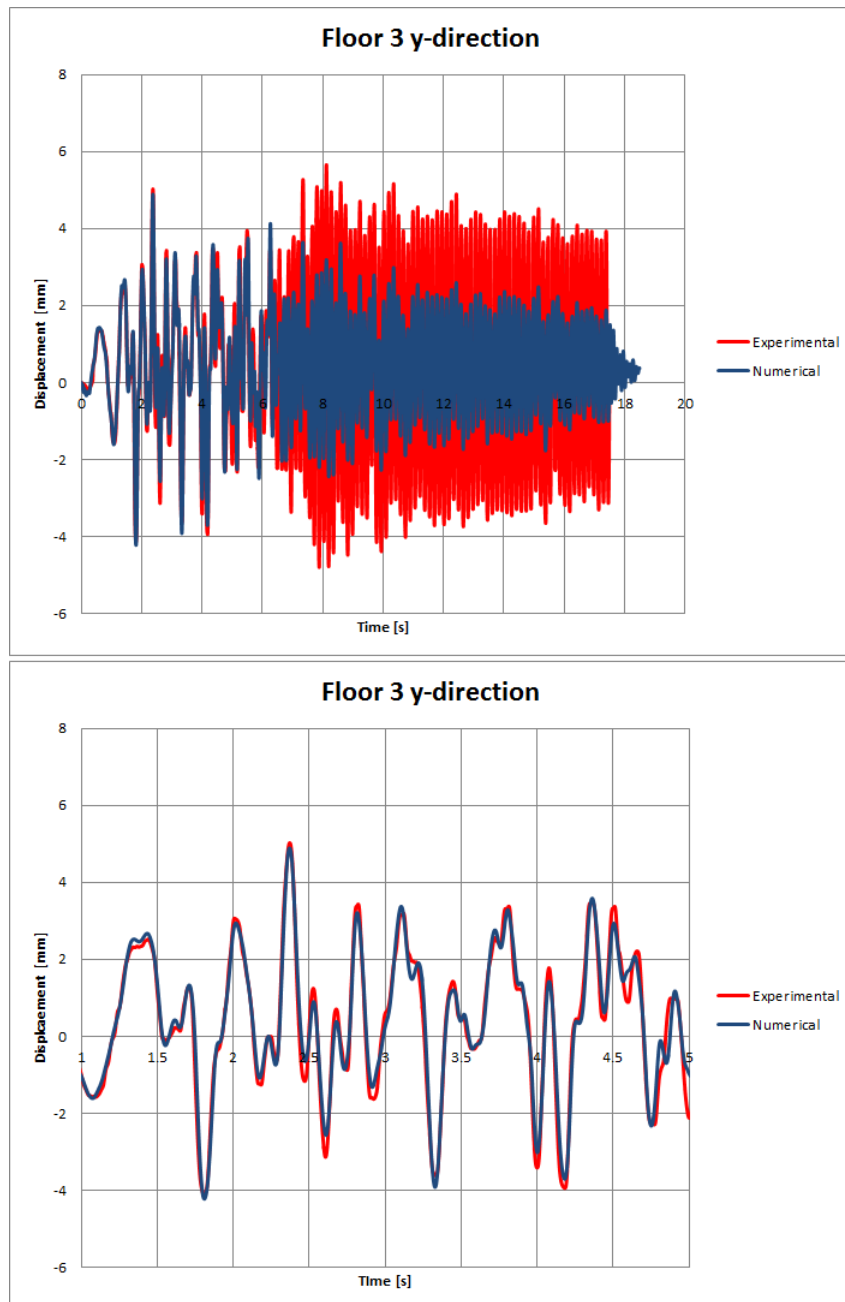
Figure 7.80: Experimental vs numerical displacement - RUN13.

The two figures from above show that there is a good match between the experimental response of the mock-up and the numerical response of the model in terms of displacements in x- and y-direction. The remarkable thing here is that after the sixth second, the experimental responses show much higher amplitudes in comparison with the numerical responses while the trend and the period of the graphs are almost the same. A reason for why the amplitudes of the experimental responses are so high, could be that after the sixth second the real mock-up is damaged a lot and can not resist the seismic loading much and thus shows these high responses in comparison with the numerical responses. Until now, the damage histories of the model and the mock-up are taken into account. Apparently, the mock-up is damaged more then the finite element model.

209

The contour plots look as follows.

Figure 7.81: Crackwidth in mm.

Figure 7.82: Principle stresses in S1 in N/mm^2 according to RSA.

Figure 7.83: Crackwidth in mm.

Figure 7.84: Principle stresses in S1 in N/mm^2 according to RSA.
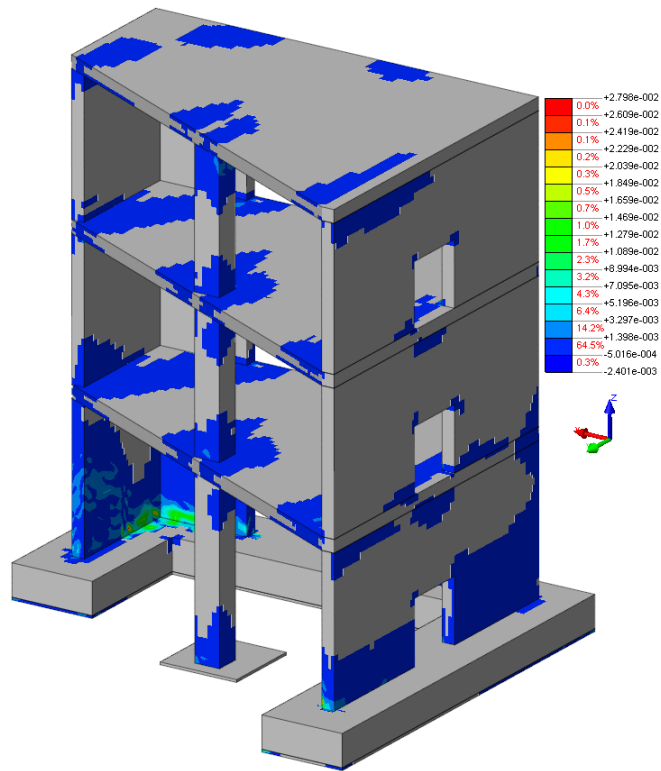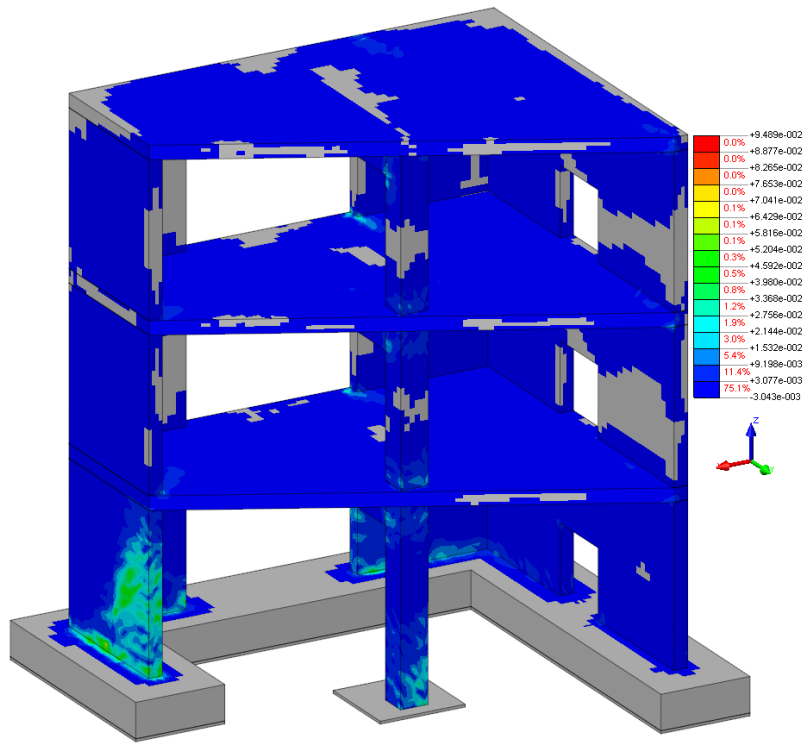
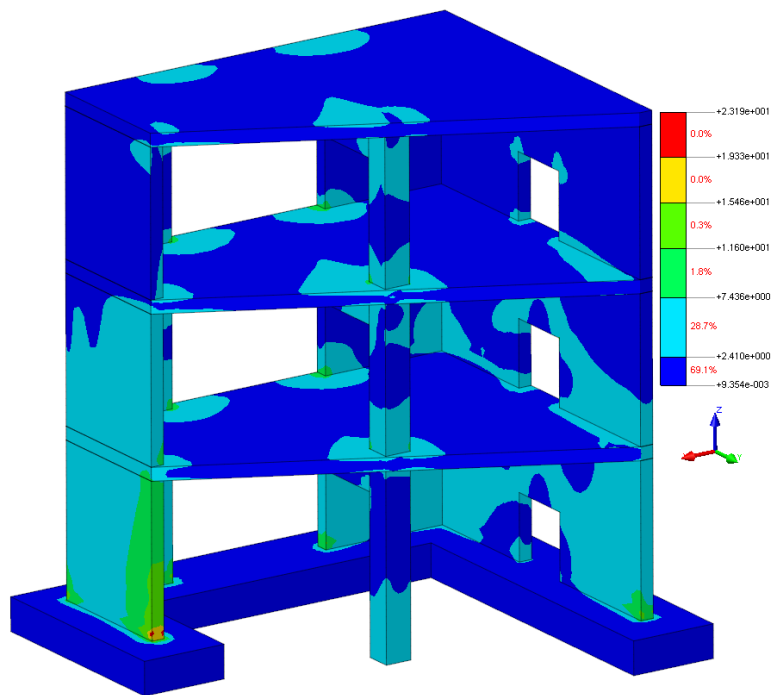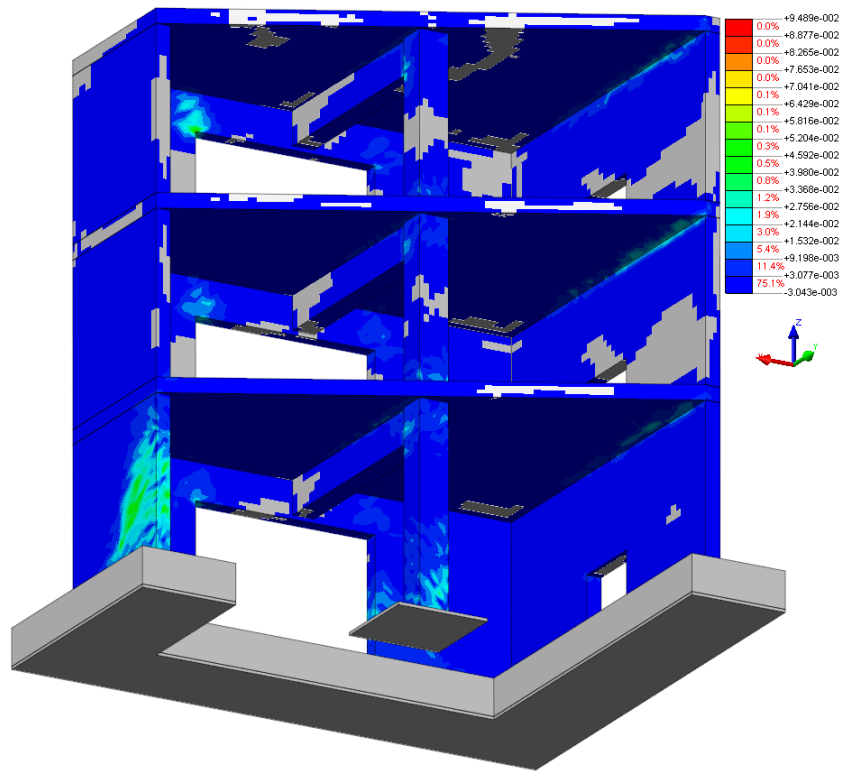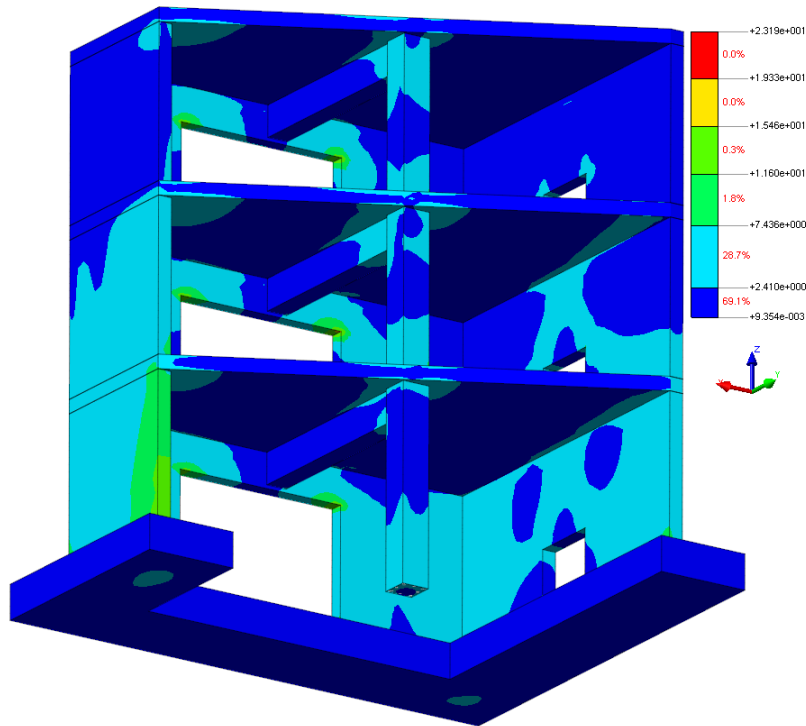Figure 7.85: Crackwidth in mm.
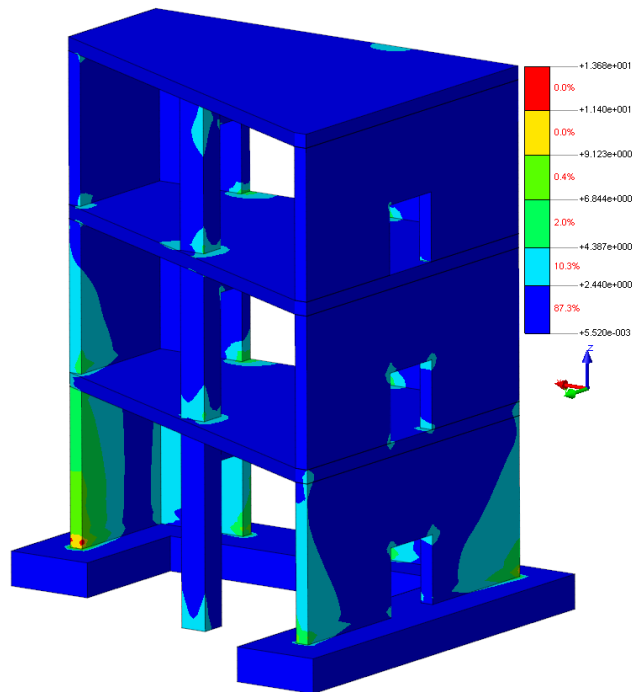
Figure 7.86: Principle stresses in S1 in N/mm^2 according to RSA.
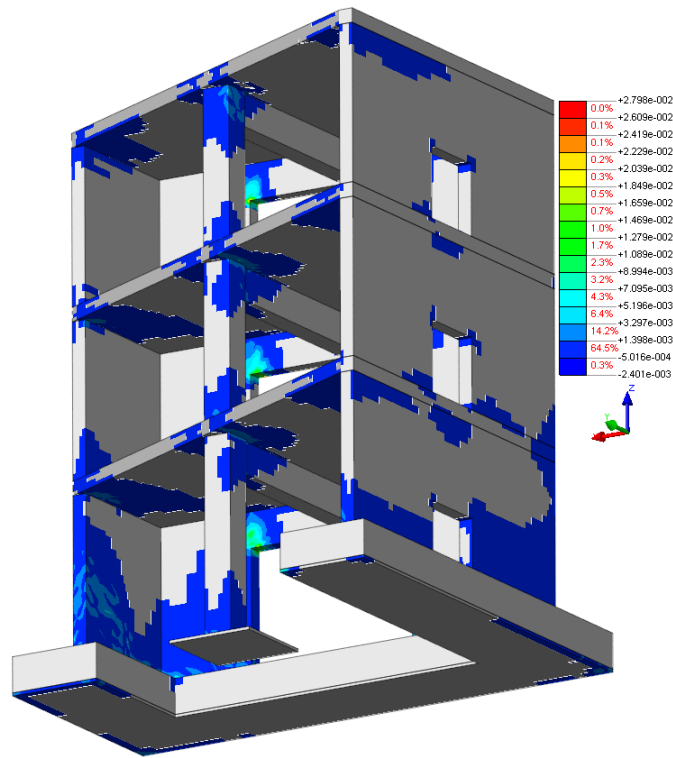
Figure 7.87: Crackwidth in mm.
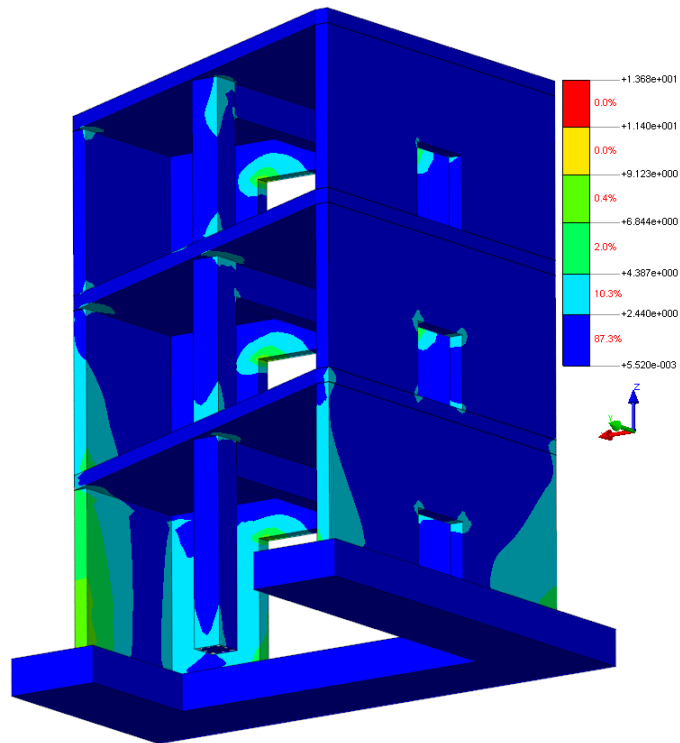
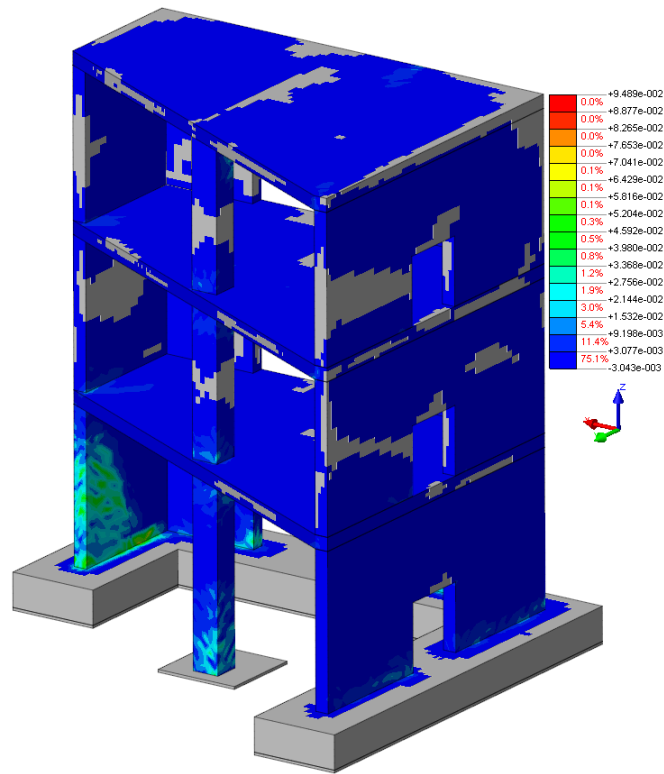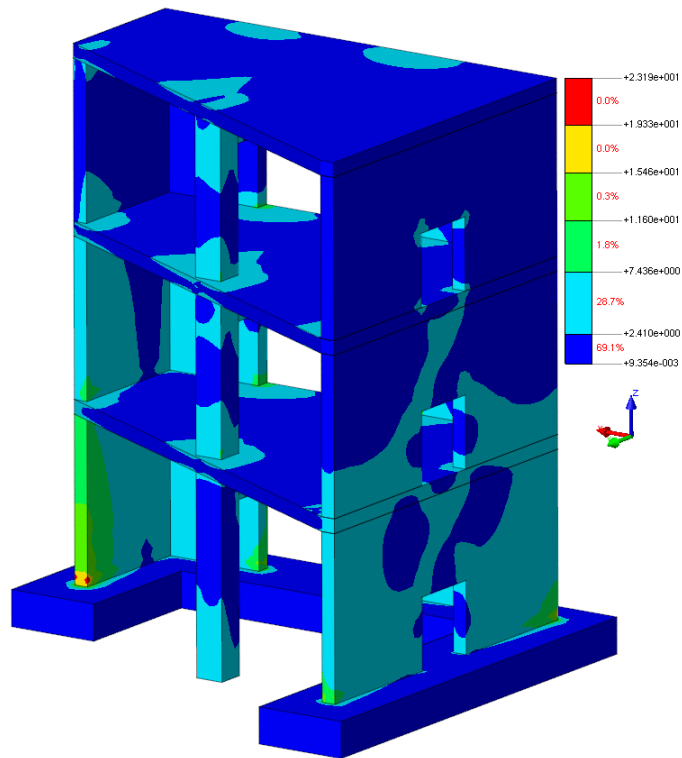Figure 7.88: Principle stresses in S1 in N/mm^2 according to RSA.

Figure 7.89: Crackwidth in mm.

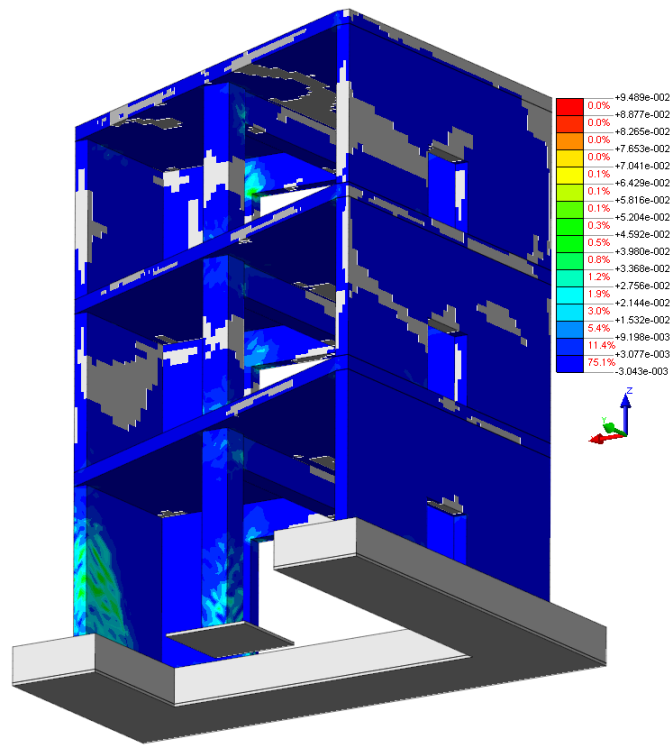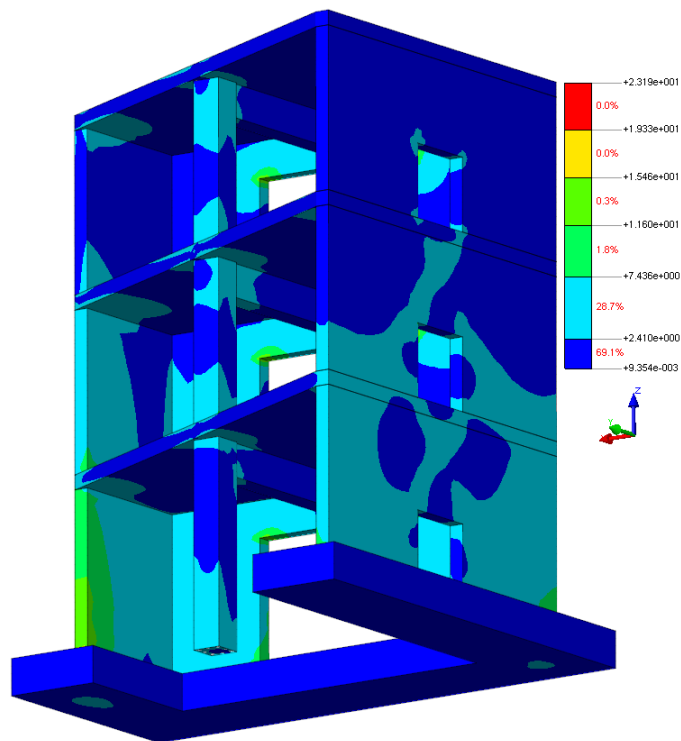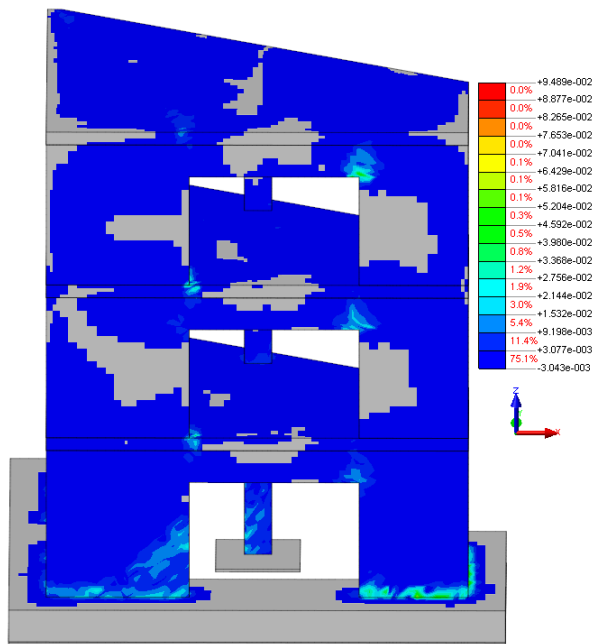Figure 7.90: Principle stresses in S1 in N/mm^2 according to RSA.

Some reinforcement bars near the foundation, in wall V04, become plastic due to RUN13.
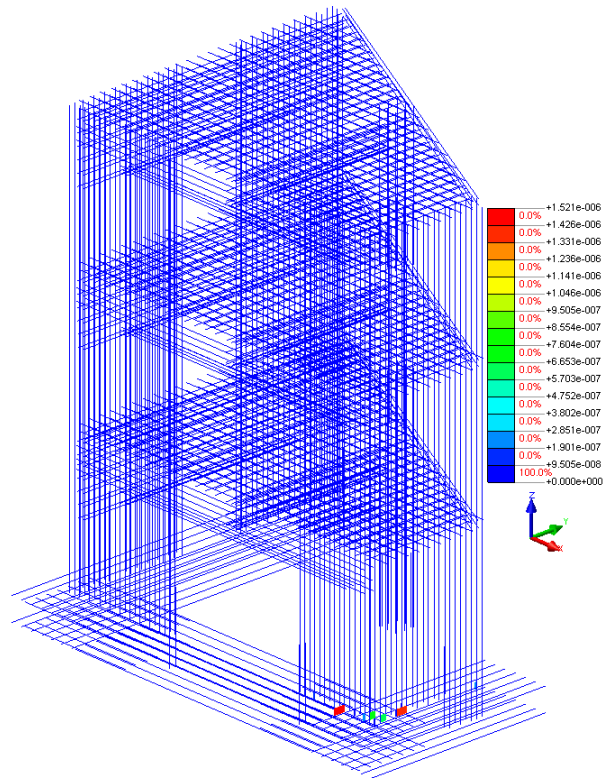
Figure 7.91: Plastic strains in the reinforcement.

7.5 Non-linear Response with Respect to RUN17

The PGA of RUN9 in x-direction is 0.63 g, in y-direction it is 0.44 g, in z-direction it is 0.41 g and it has a duration of 16.95 seconds. First a comparison is made between the experimental response of the mock-up and the numerical response of the model in terms of displacements and accelerations in point D on floor 3. After that the contour plots of the crackwidth in (mm) together with the contour plots of the principle stresses in S1 from RSA are shown. The first graph shows the total responses and the second graph shows a piece of the total responses.

Figure 7.92: Experimental vs numerical displacement - RUN17.

It seems like there is a shift in the provided experimental displacements in x- and y-direction. When undoing the shift, the following graphs are obtained.
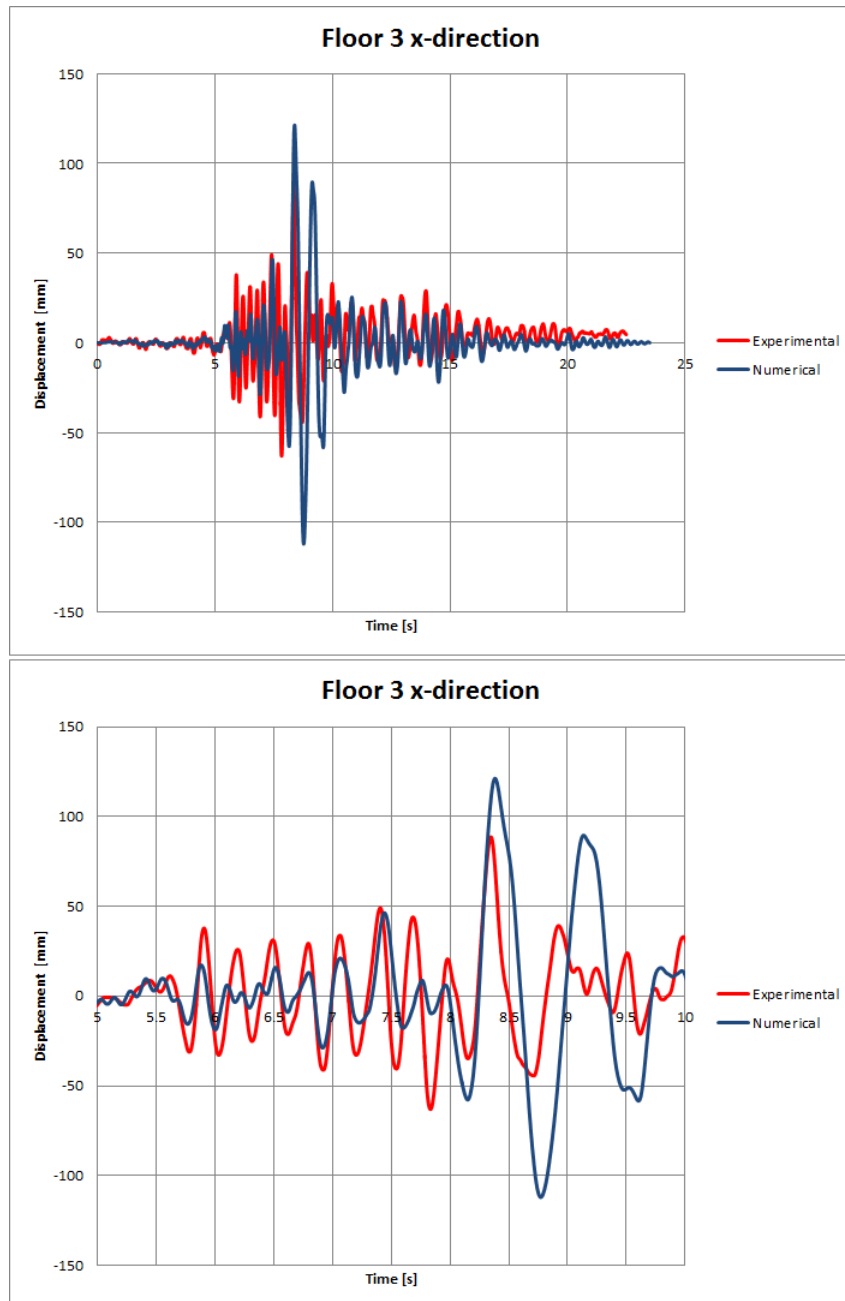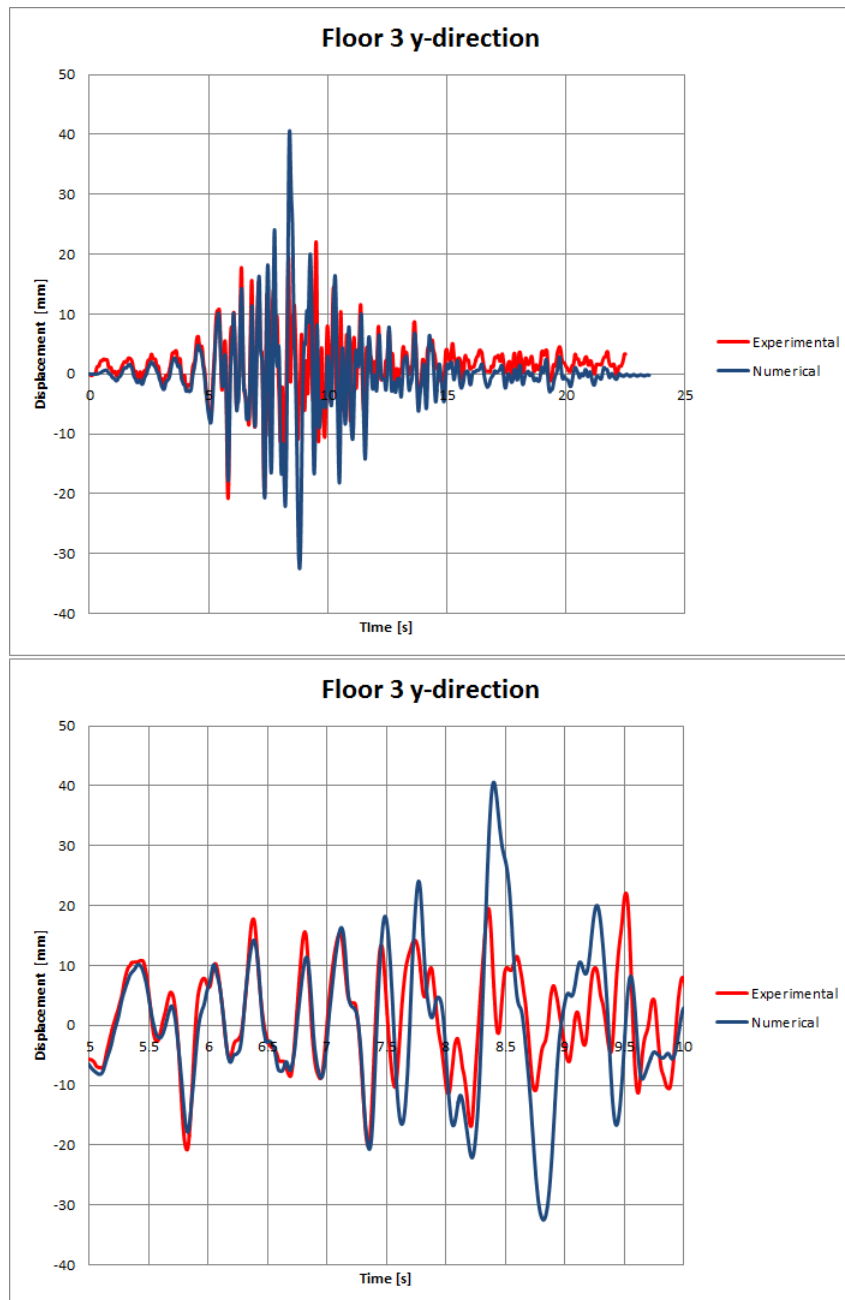

Figure 7.93: Experimental vs numerical displacement - RUN17.
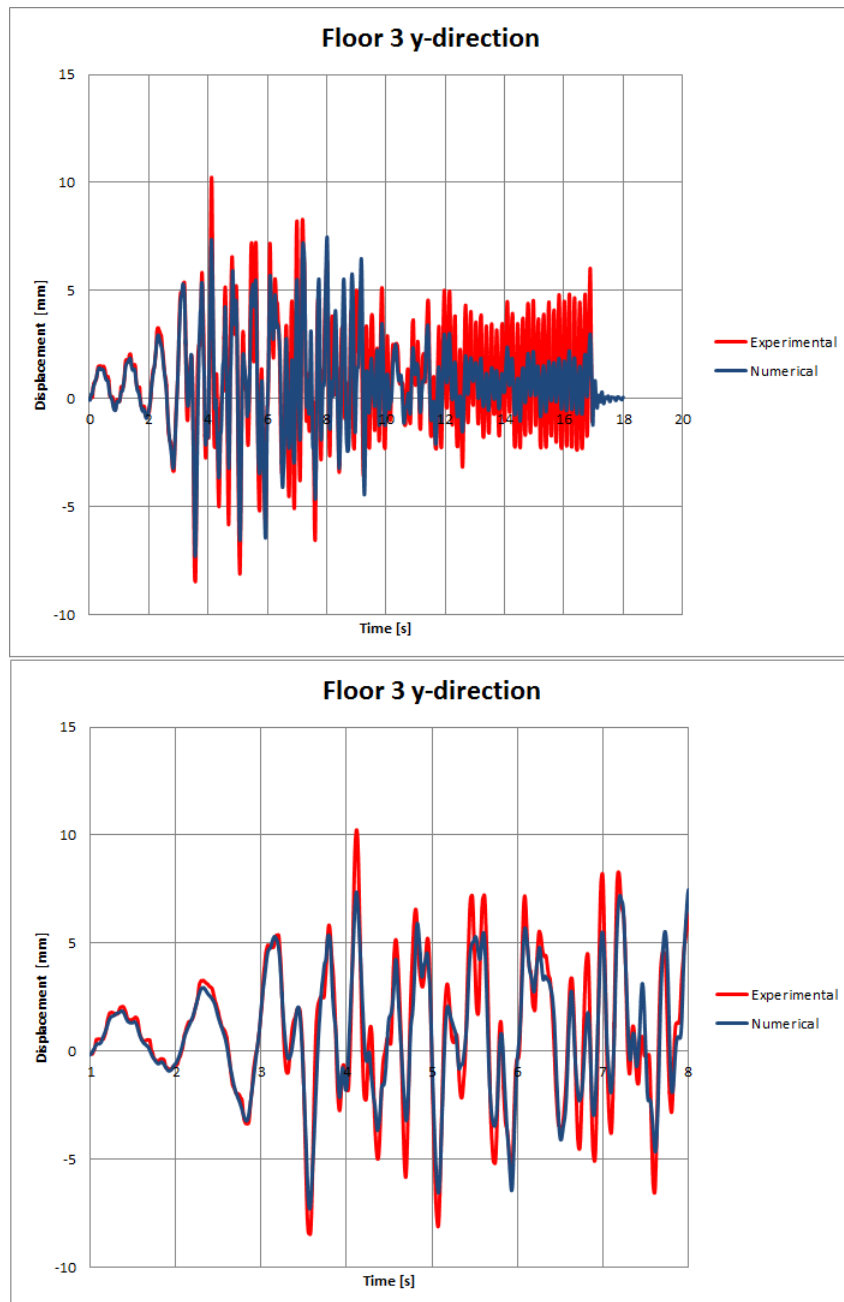
Figure 7.94: Experimental vs numerical displacement - RUN17.

The damage history is not taken into account here for the numerical response with respect to RUN17 because the nonlinear transient analysis with RUN17 diverged in the first attempts, as explained earlier, and thus performed separately. The numerical and experimental responses show nice matches and again at some moments the amplitudes of the experimental responses are much higher then the numerical responses. A reason could be that the real mock-up is damaged much more then the finite element model and thus can't resists the seismic loading as in for example RUN9 when the structure was not damaged much.

The contour plots look as follows.

Figure 7.95: Crackwidth in mm.

Figure 7.96: Principle stresses in S1 in N/mm^2 according to RSA.

Figure 7.97: Crackwidth in mm.

Figure 7.98: Principle stresses in S1 in N/mm^2 according to RSA.

Figure 7.99: Crackwidth in mm.

Figure 7.100: Principle stresses in S1 in N/mm^2 according to RSA.
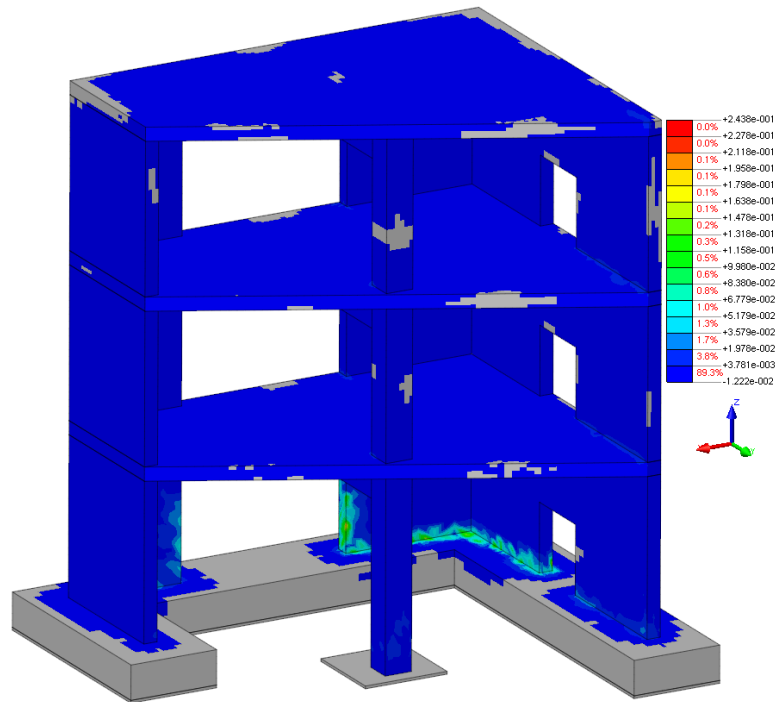
Figure 7.101: Crackwidth in mm.

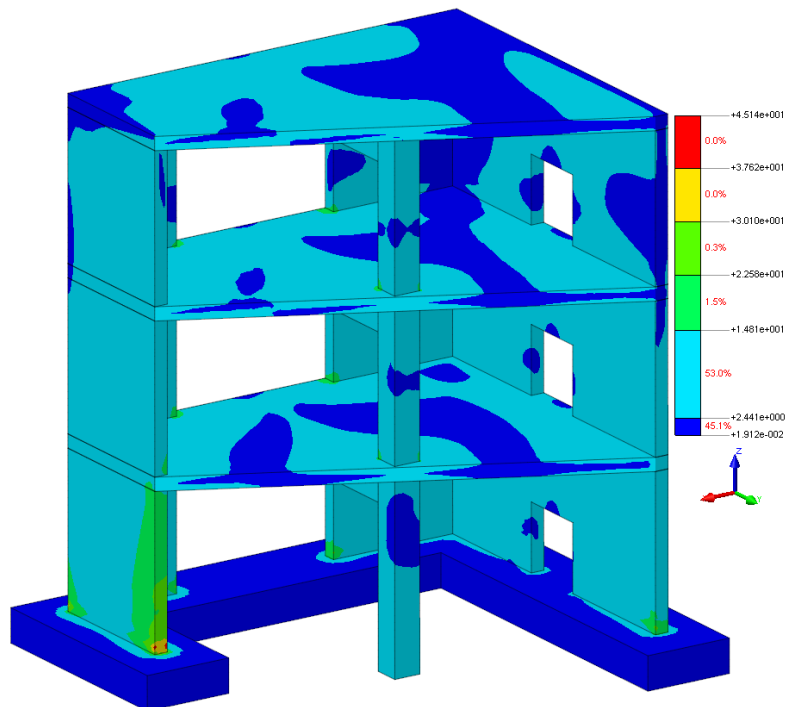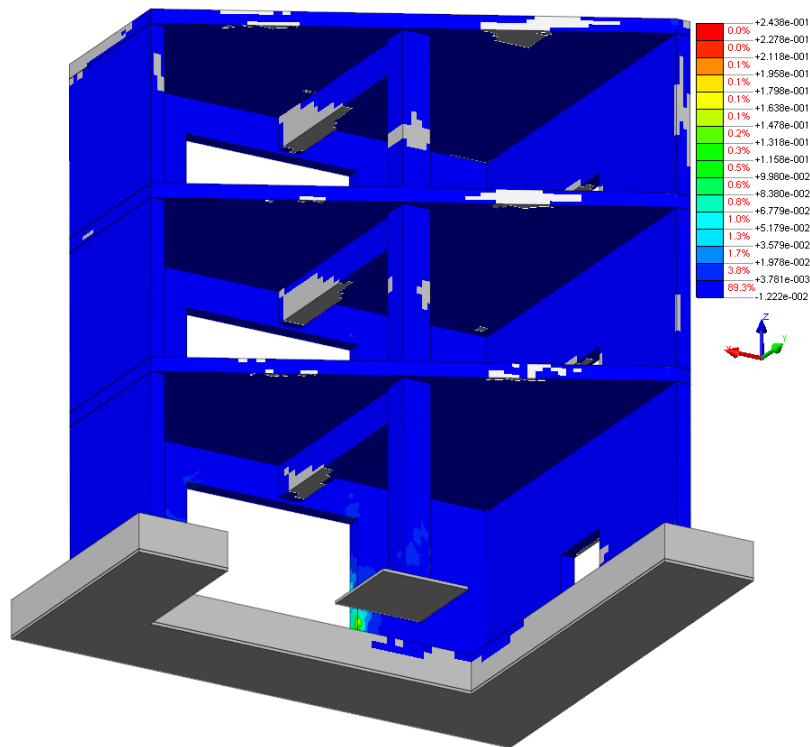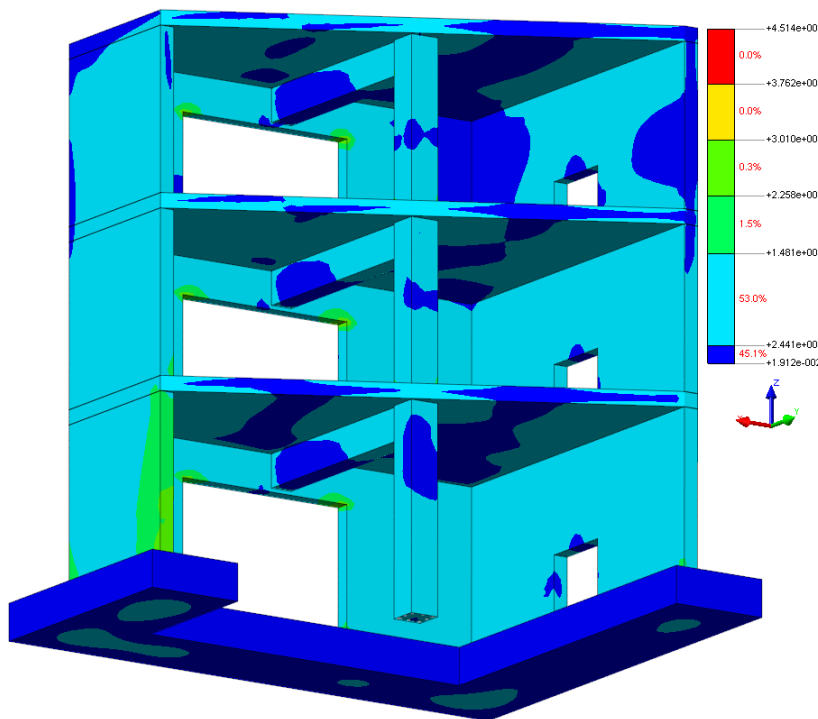Figure 7.102: Principle stresses in S1 in N/mm^2 according to RSA.

Figure 7.103: Crackwidth in mm.
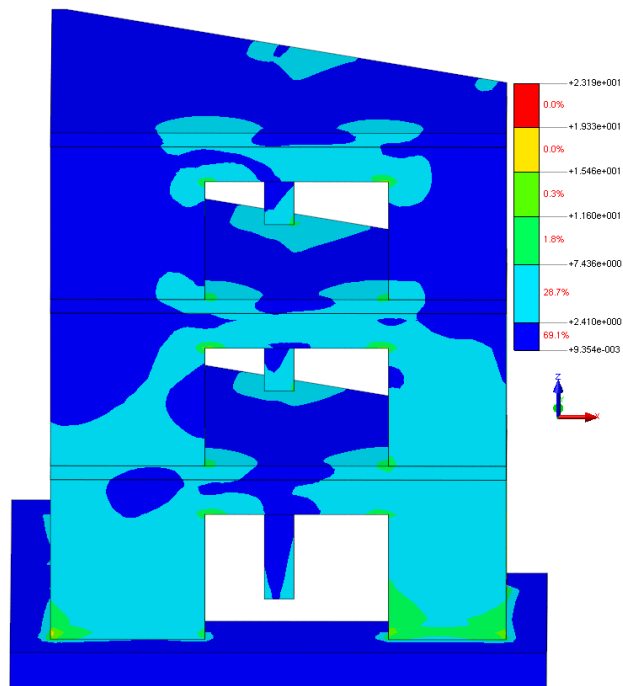
Figure 7.104: Principle stresses in S1 in N/mm^2 according to RSA.

The contour plot for the stress distribution of the reinforcement cannot be given because FX$^+$ could not show it for this RUN. The reason for this is that the embedded reinforcement was replaced by bond-slip-reinforcement because the analysis with RUN17 diverged in the beginning.

7.6 Non-linear Response with Respect to RUN19

The PGA of RUN9 in x-direction is 0.1.11 g, in y-direction it is 1.03 g, in z-direction it is 0.49 g and it has a duration of 22.49 seconds. First a comparison is made between the experimental response of the mock-up and the numerical response of the model in terms of displacements and accelerations in point D on floor 3. After that the contour plots of the crackwidth in (mm) together with the contour plots of the principle stresses in S1 from RSA are shown. The first graph shows the total responses and the second graph shows a piece of the total responses.

Figure 7.105: Experimental vs numerical displacement - RUN19.

Figure 7.106: Experimental vs numerical displacement - RUN19.

In RUN19, the damage history is again not taken in account for the finite element model for the same reason as mentioned before. When comparing the response of a *new* finite element model with the response of a damaged mock-up, the responses from above are obtained. At some moments both responses correspond to each other but most of the time their amplitudes differ and they are a bit out-of-phase.

The contour plots look as follows.

Figure 7.107: Crackwidth in mm.

Figure 7.108: Principle stresses in S1 in N/mm^2 according to RSA.

Figure 7.109: Crackwidth in mm.

Figure 7.110: Principle stresses in S1 in N/mm^2 according to RSA.
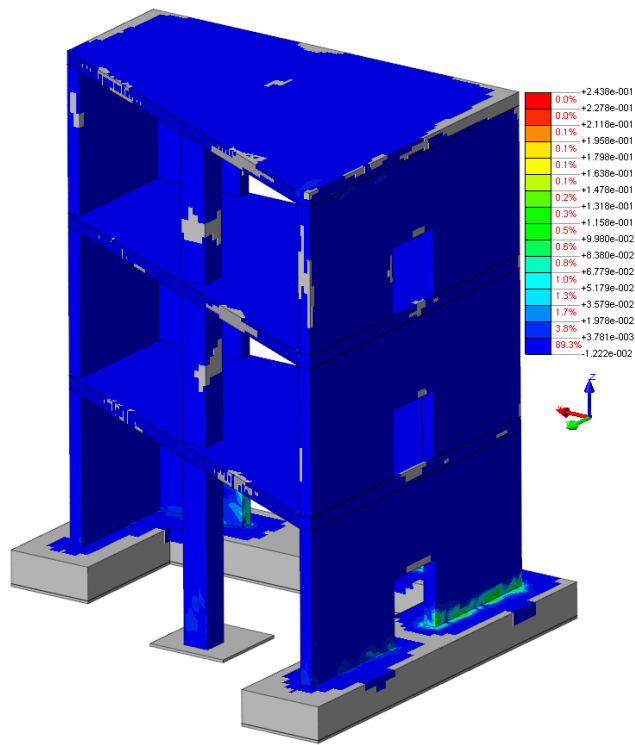
Figure 7.111: Crackwidth in mm.
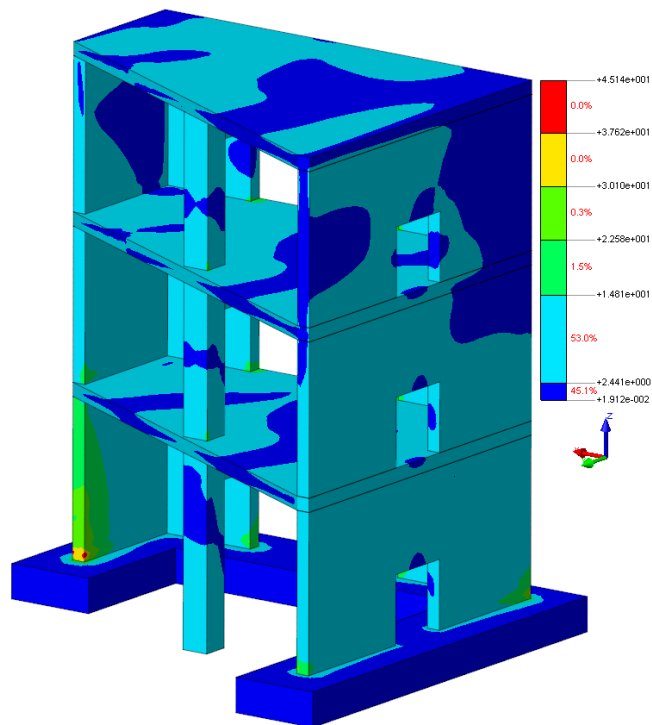
Figure 7.112: Principle stresses in S1 in N/mm^2 according to RSA.
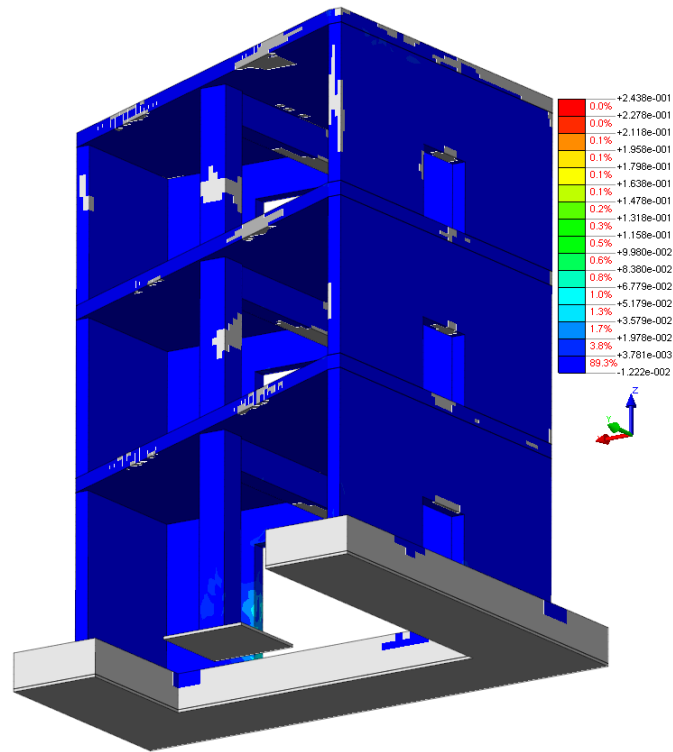
Figure 7.113: Crackwidth in mm.
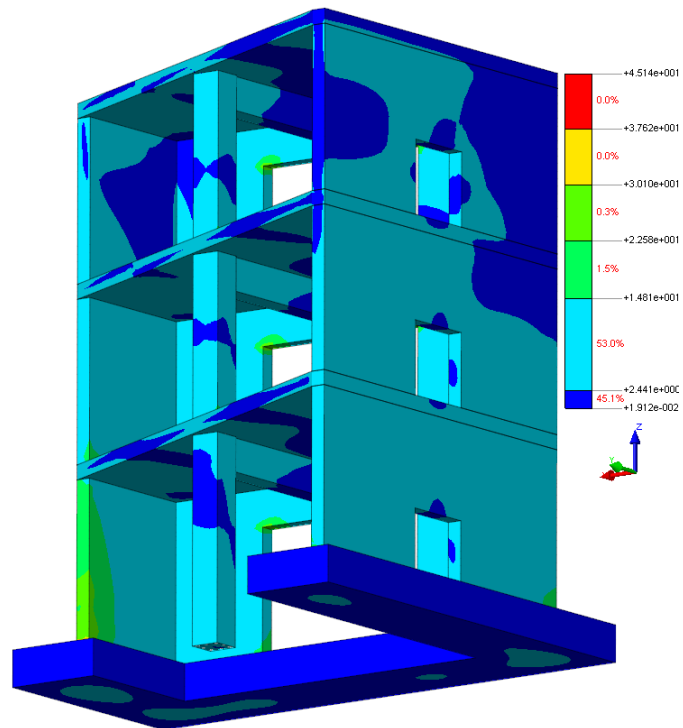
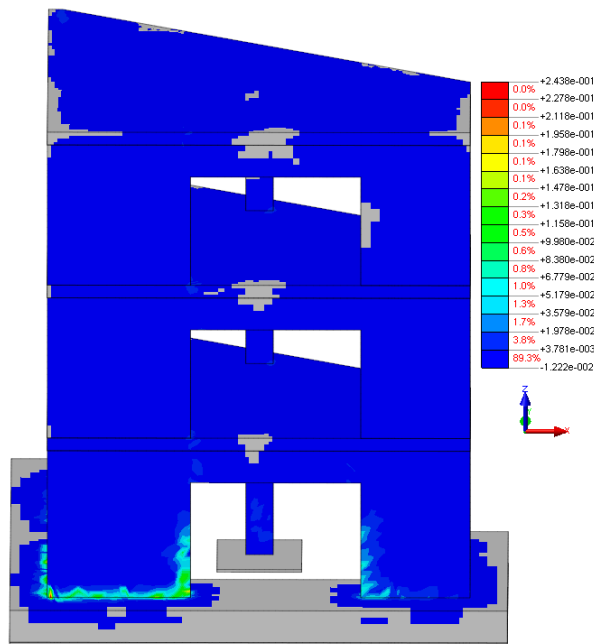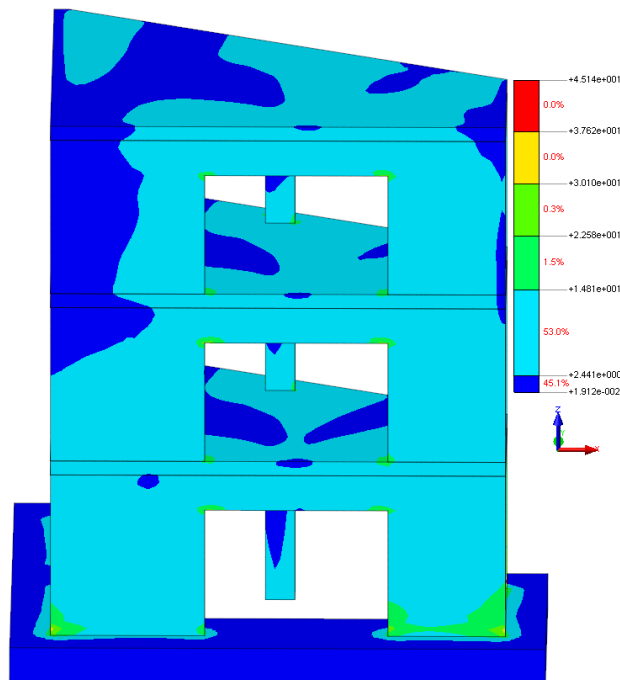Figure 7.114: Principle stresses in S1 in N/mm^2 according to RSA.

Figure 7.115: Crackwidth in mm.

Figure 7.116: Principle stresses in S1 in N/mm^2 according to RSA.

The contour plot for the stress distribution of the reinforcement cannot be given because FX$^+$ could not show it for this RUN. The reason for this is that the embedded reinforcement was replaced by bond-slip-reinforcement because the analysis with RUN19 diverged in the beginning.

7.7 Non-linear Response with Respect to RUN21

The PGA of RUN9 in x-direction is 0.15 g, in y-direction it is 0.20 g, in z-direction it is 0.09 g and it has a duration of 7.99 seconds. First a comparison is made between the experimental response of the mock-up and the numerical response of the model in terms of displacements and accelerations in point D on floor 3. After that the contour plots of the crackwidth in (mm) together with the contour plots of the principle stresses in S1 from RSA are shown. The first graph shows the total responses and the second graph shows a piece of the total responses.
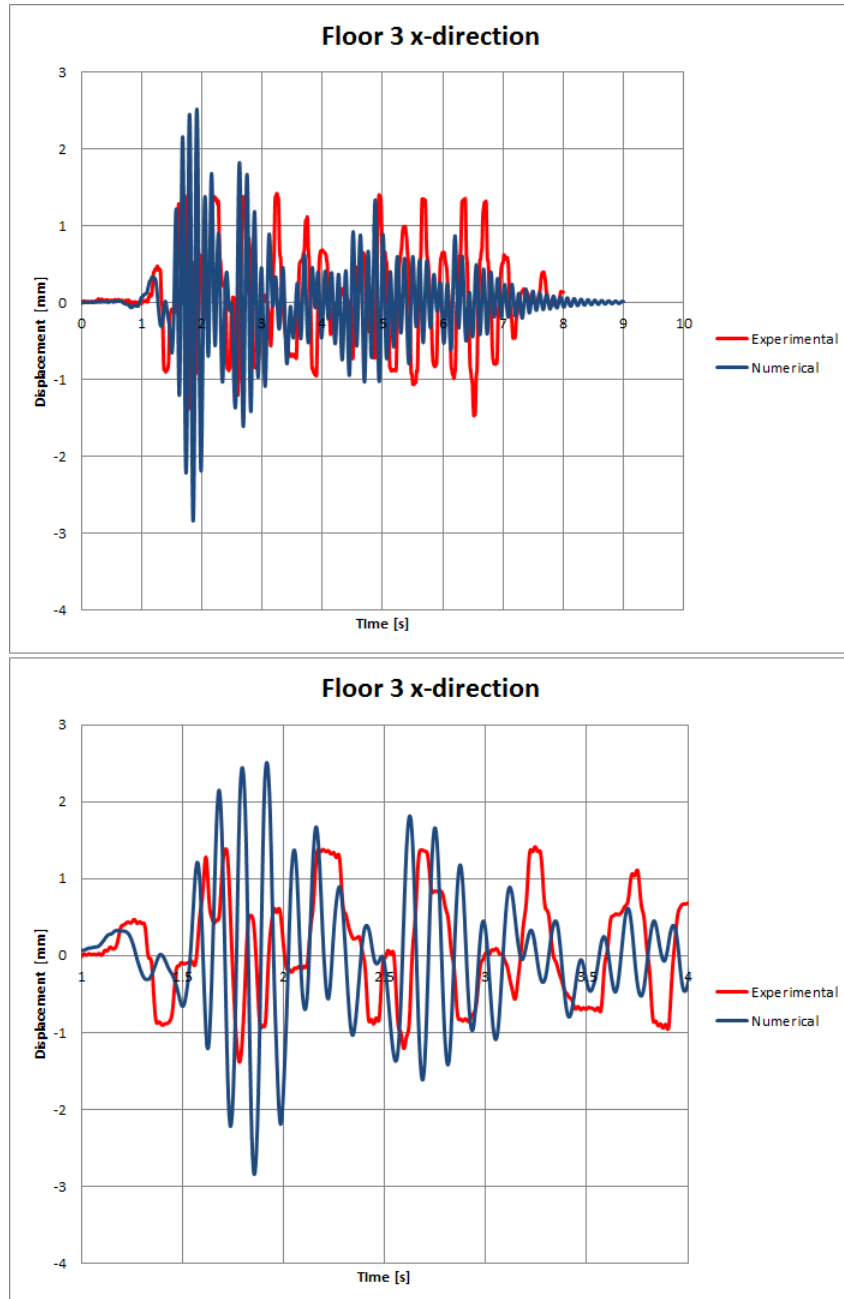
Figure 7.117: Experimental vs numerical displacement - RUN21.
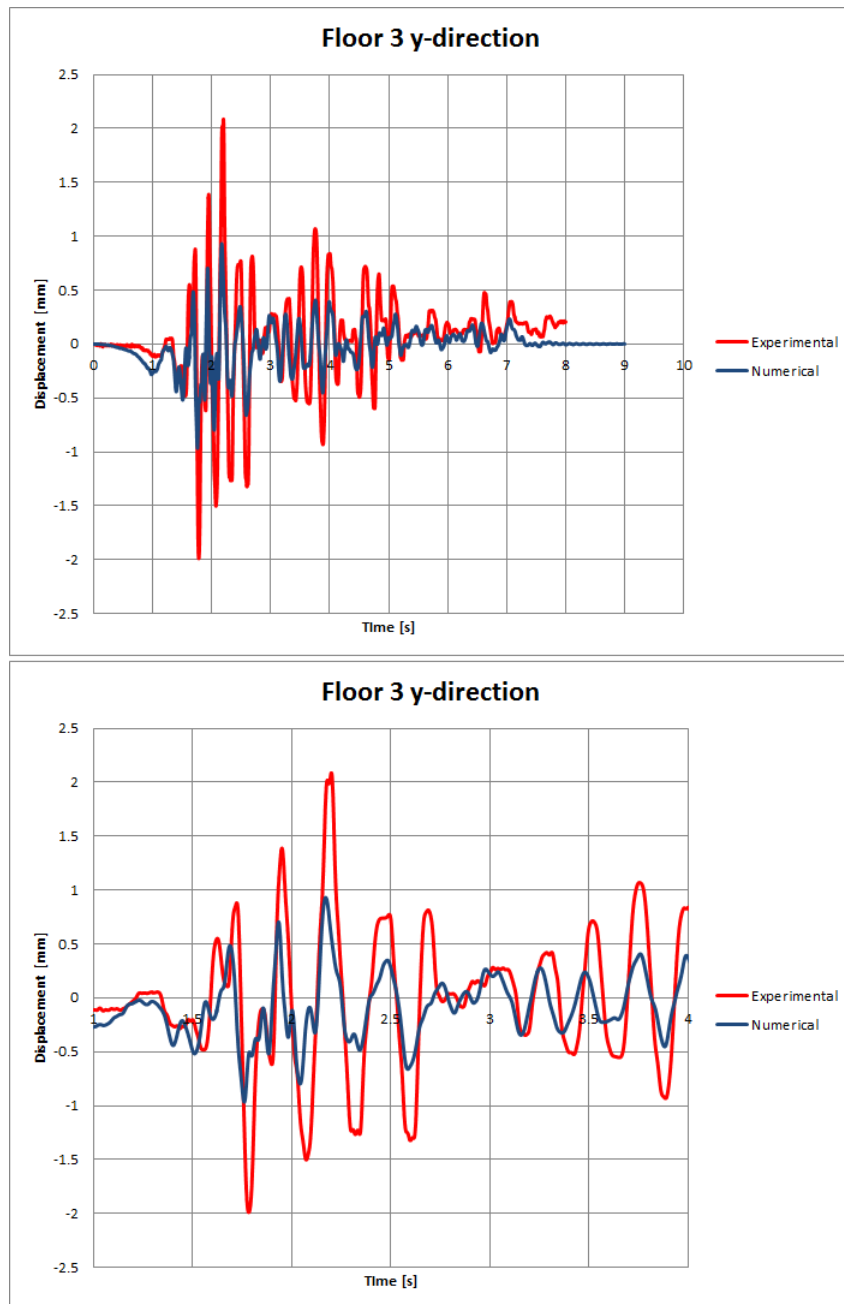
Figure 7.118: Experimental vs numerical displacement - RUN21.

At this point the real mock-up is damaged very much and the finite element model is not damaged at all because the damage history is not taken into account here. The experimental responses show the mock-up is damaged very much because the experimental responses are not high-frequent as the numerical responses. But both responses do follow the same trend, this can be clearly seen in the graphs of the displacements in y-direction.

The contour plots look as follows.
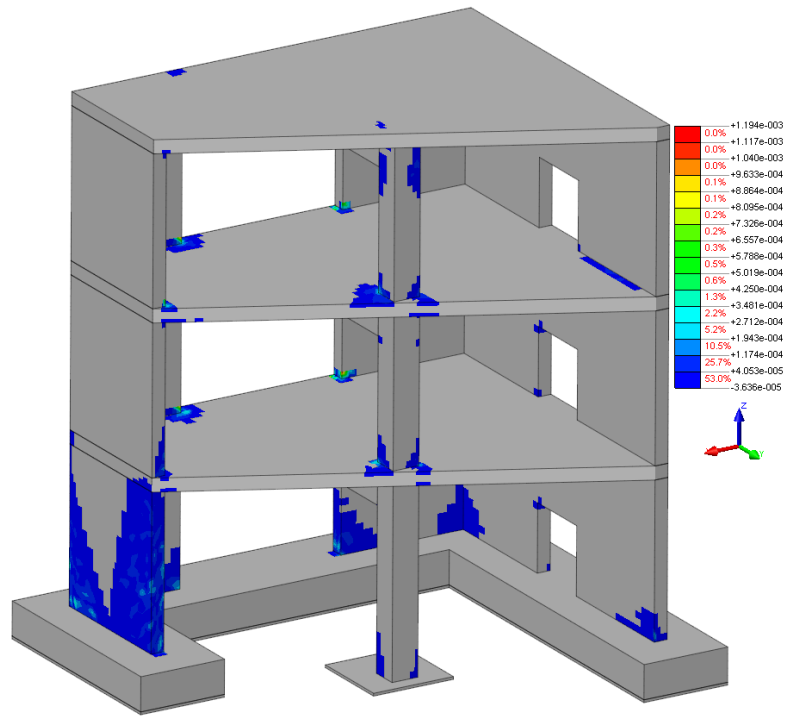
Figure 7.119: Crackwidth in mm.
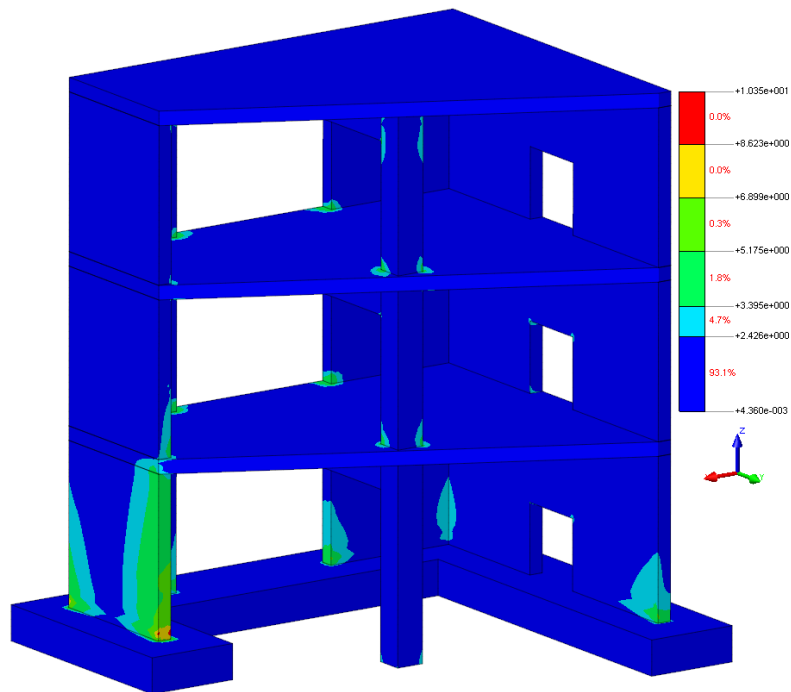
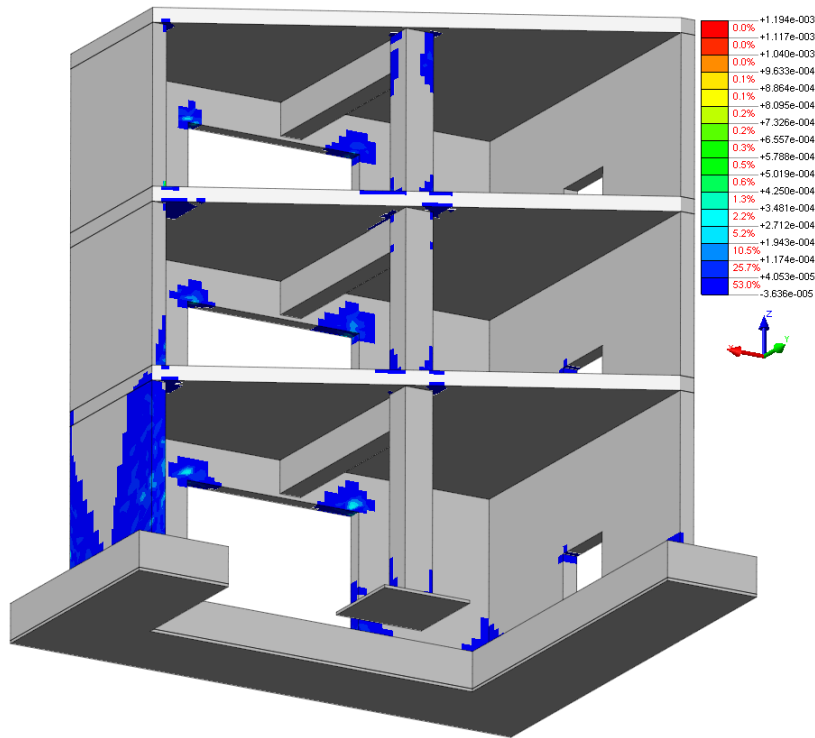Figure 7.120: Principle stresses in S1 in N/mm^2 according to RSA.
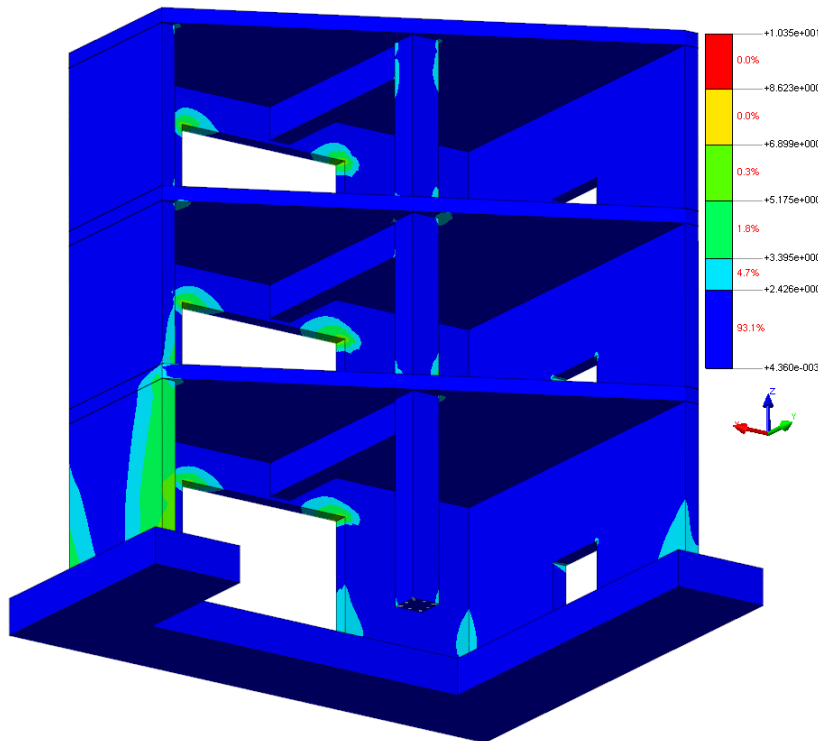
Figure 7.121: Crackwidth in mm.

Figure 7.122: Principle stresses in S1 in N/mm^2 according to RSA.
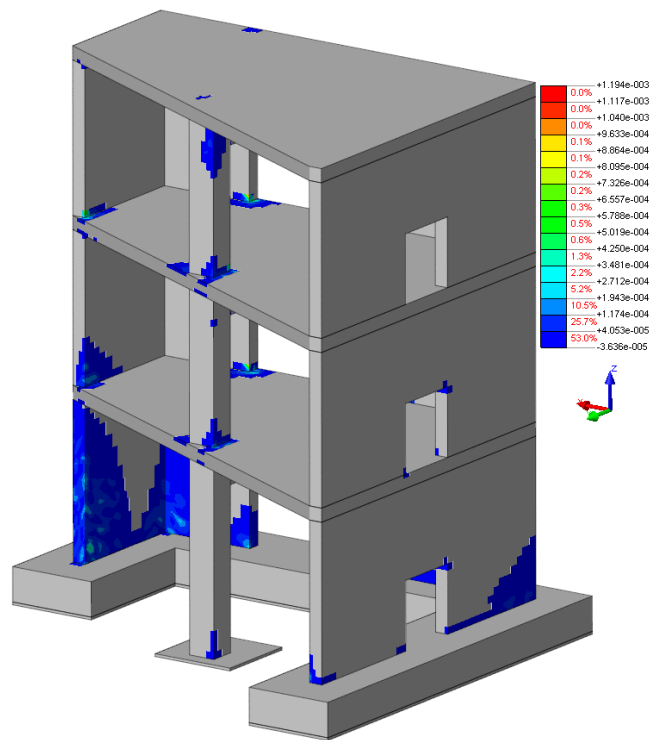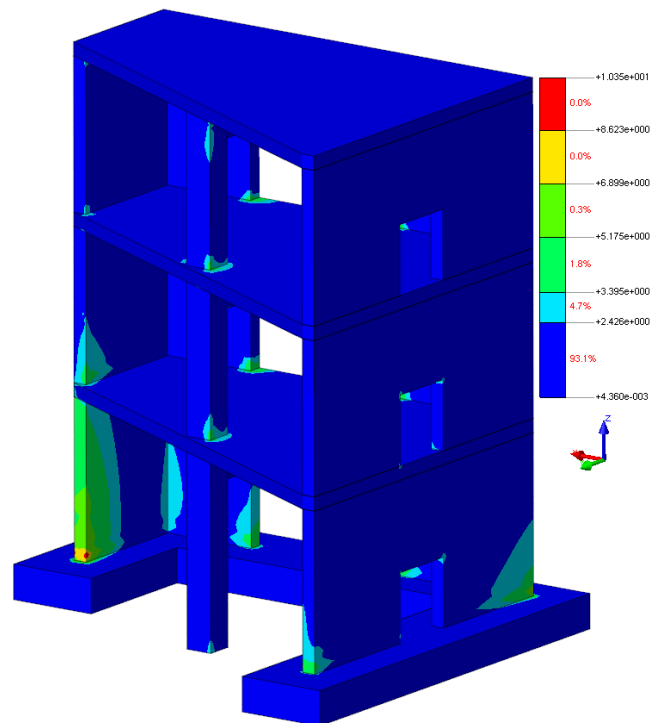
Figure 7.123: Crackwidth in mm.

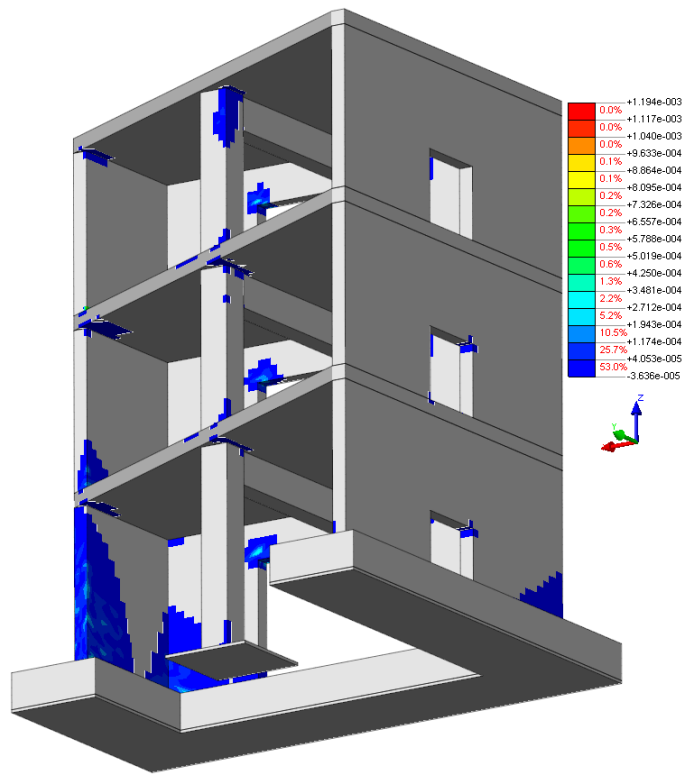Figure 7.124: Principle stresses in S1 in N/mm^2 according to RSA.

Figure 7.125: Crackwidth in mm.

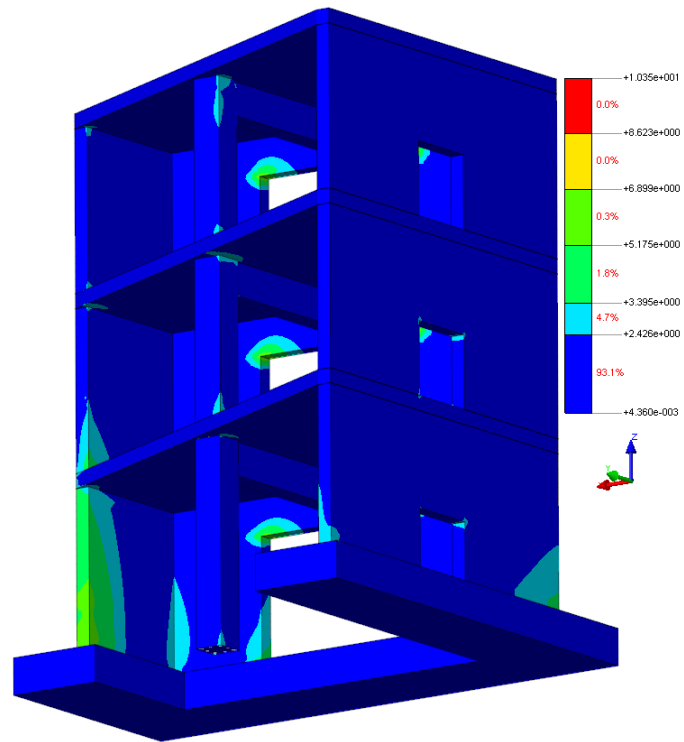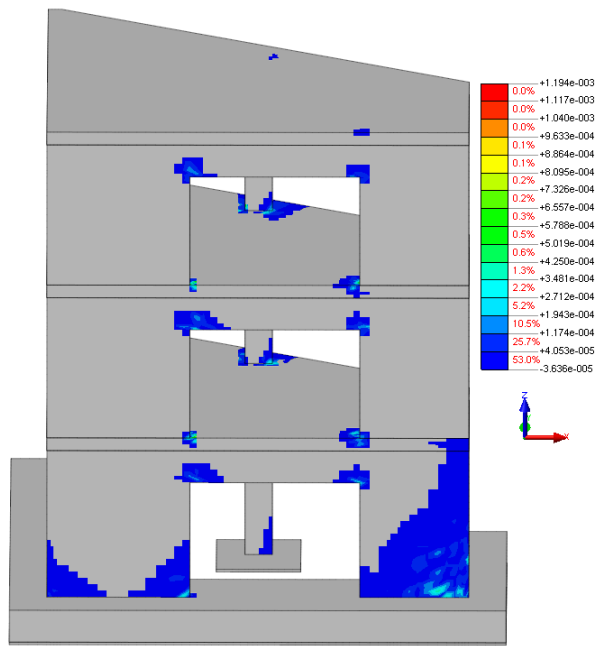Figure 7.126: Principle stresses in S1 in N/mm^2 according to RSA.

Figure 7.127: Crackwidth in mm.

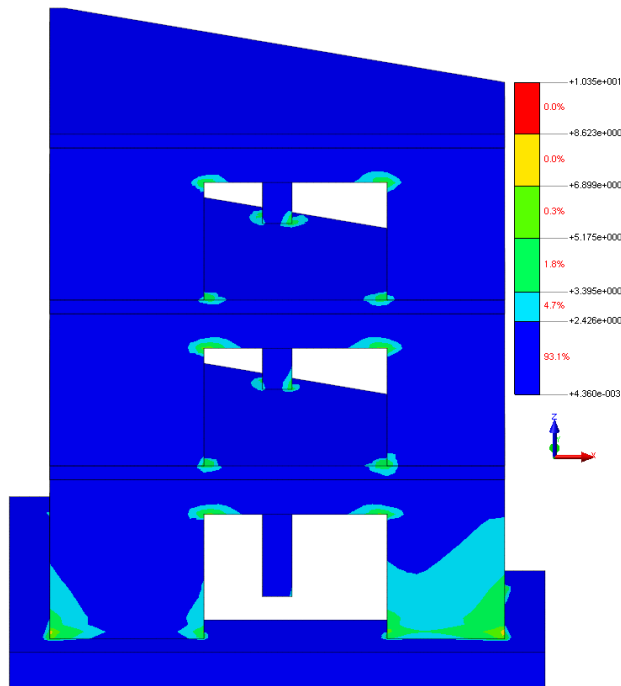Figure 7.128: Principle stresses in S1 in N/mm^2 according to RSA.

There is no plasticity in the reinforcement. The plastic strains are everywhere zero.

Figure 7.129: Plastic strains in the reinforcement.

7.8 Non-linear Response with Respect to RUN23

The PGA of RUN9 in x-direction is 0.65 g, in y-direction it is 0.46 g, in z-direction it is 0.25 g and it has a duration of 7.99 seconds. First a comparison is made between the experimental response of the mock-up and the numerical response of the model in terms of displacements and accelerations in point D on floor 3. After that the contour plots of the crackwidth in (mm) together with the contour plots of the principle stresses in S1 from RSA are shown. The first graph shows the total responses and the second graph shows a piece of the total responses.
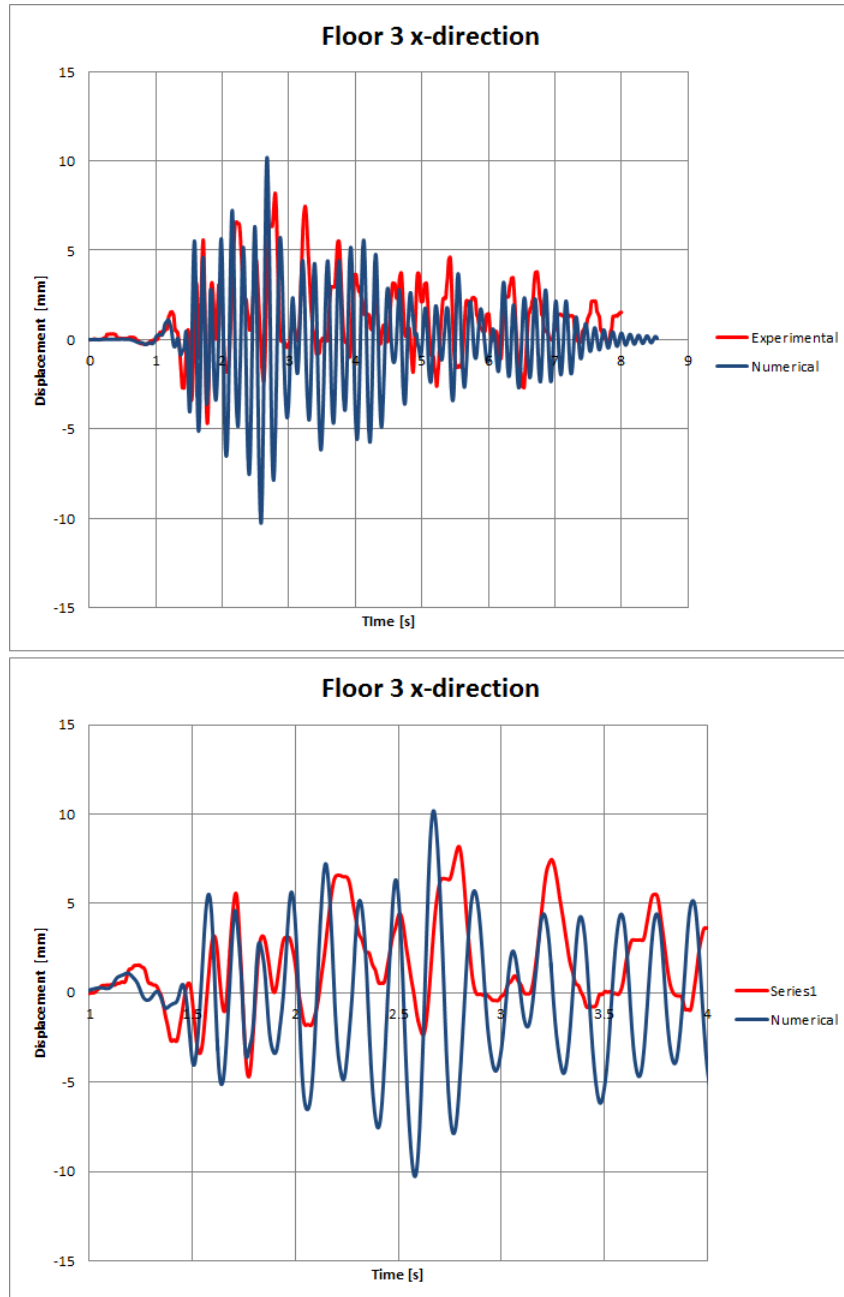

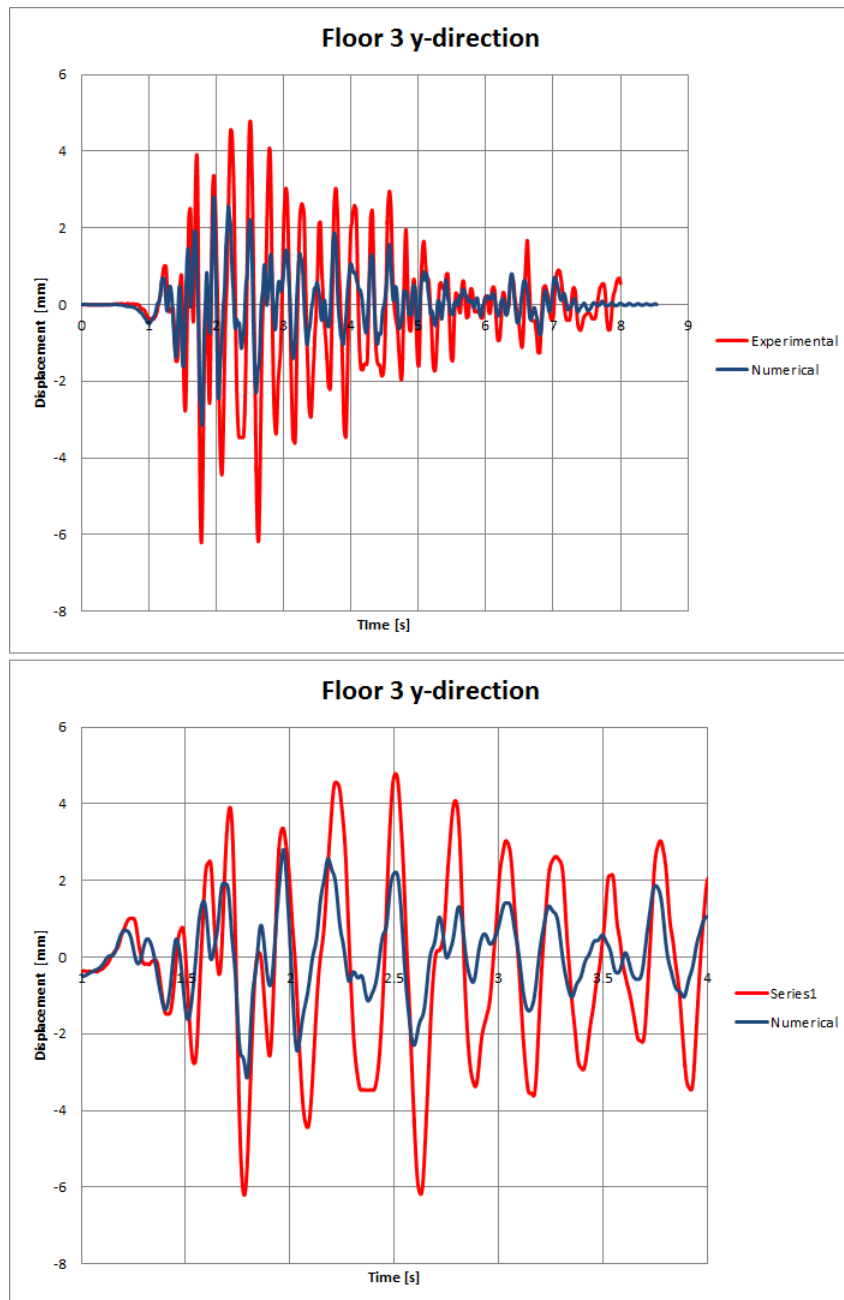Figure 7.130: Experimental vs numerical displacement - RUN23.

239

Figure 7.131: Experimental vs numerical displacement - RUN23.

Like in RUN21 (which is a scaled version of RUN23), the match between the experimental and numerical displacements are not very good. In x-direction, they are out-of-phase, the numerical displacements show higher frequency movements and the amplitudes differ a lot. In y-direction, the they have the same trend and are almost in-phase but the amplitudes of the experimental displacement are everywhere higher. This is all because of the damage history is not taken into account in the finite element model.
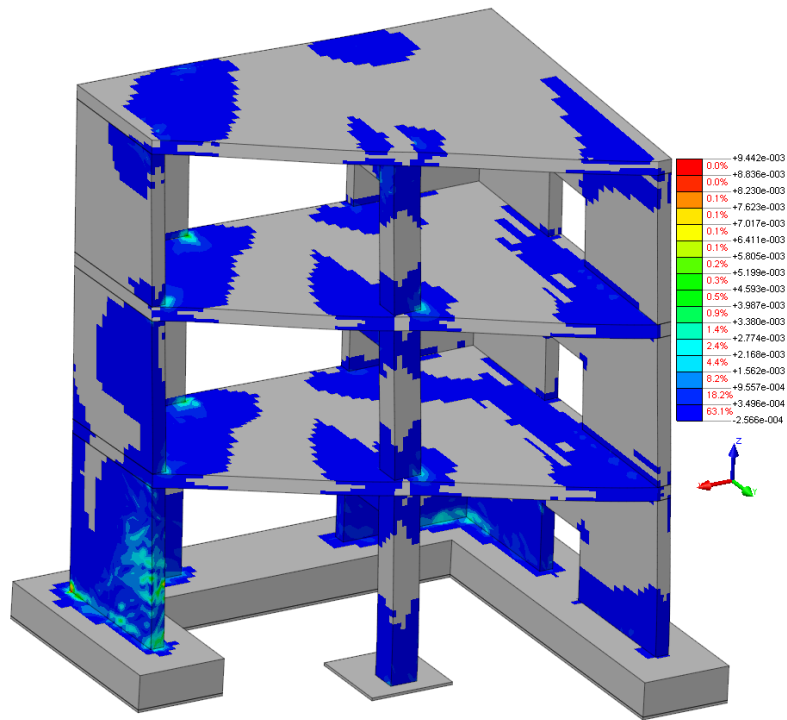
The contour plots look as follows.

Figure 7.132: Crackwidth in mm.

Figure 7.133: Principle stresses in S1 in N/mm^2 according to RSA.

Figure 7.134: Crackwidth in mm.

Figure 7.135: Principle stresses in S1 in N/mm² according to RSA.
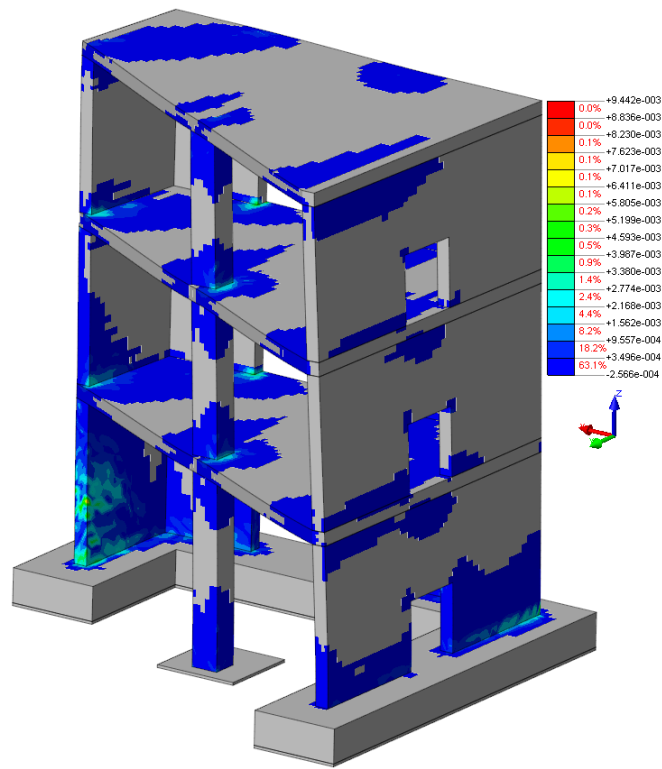
Figure 7.136: Crackwidth in mm.

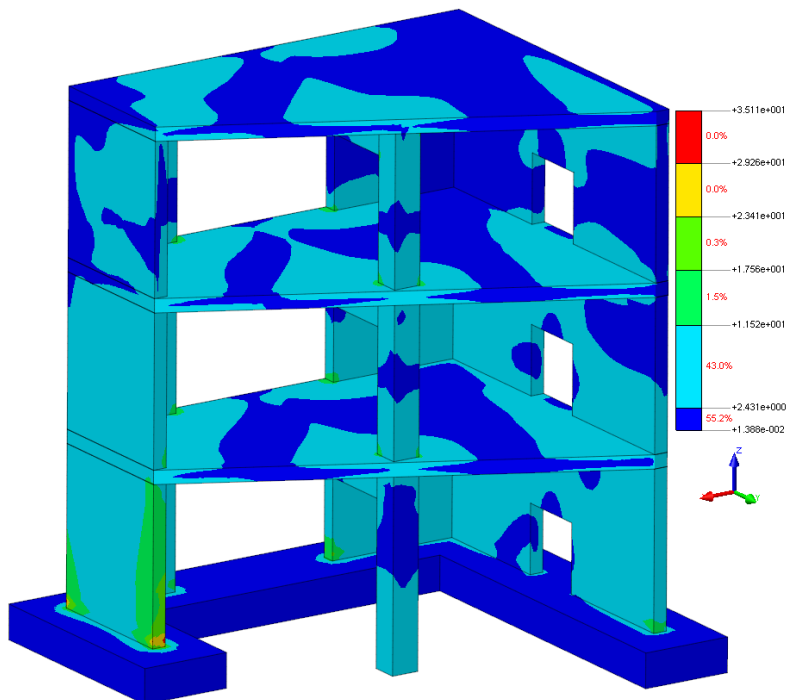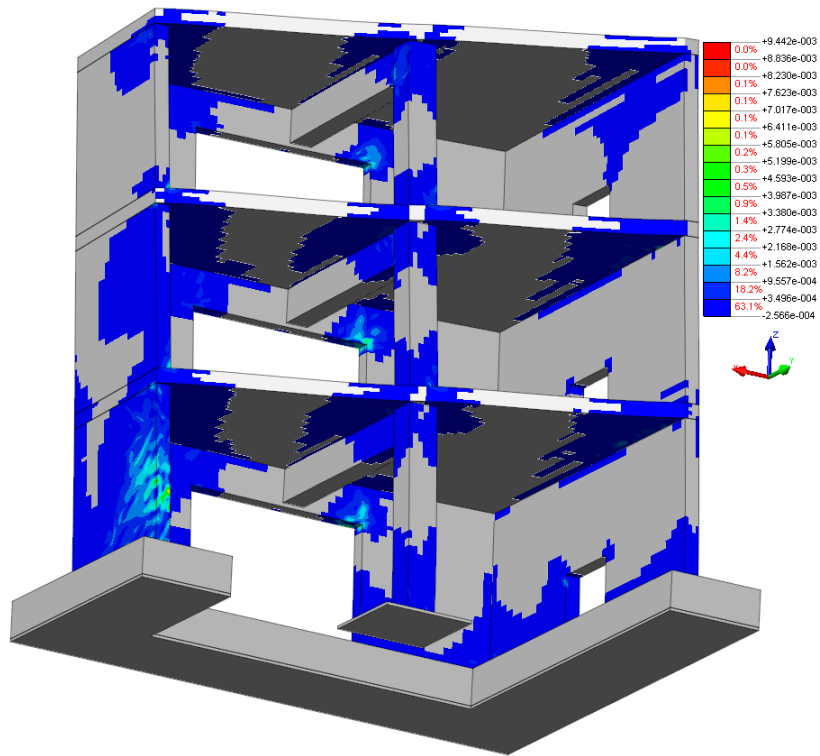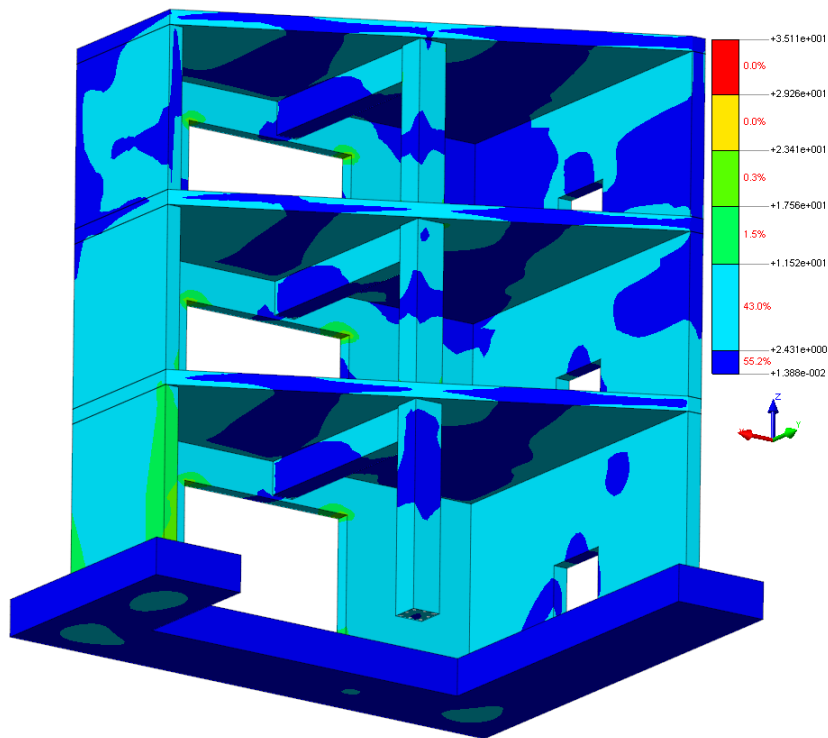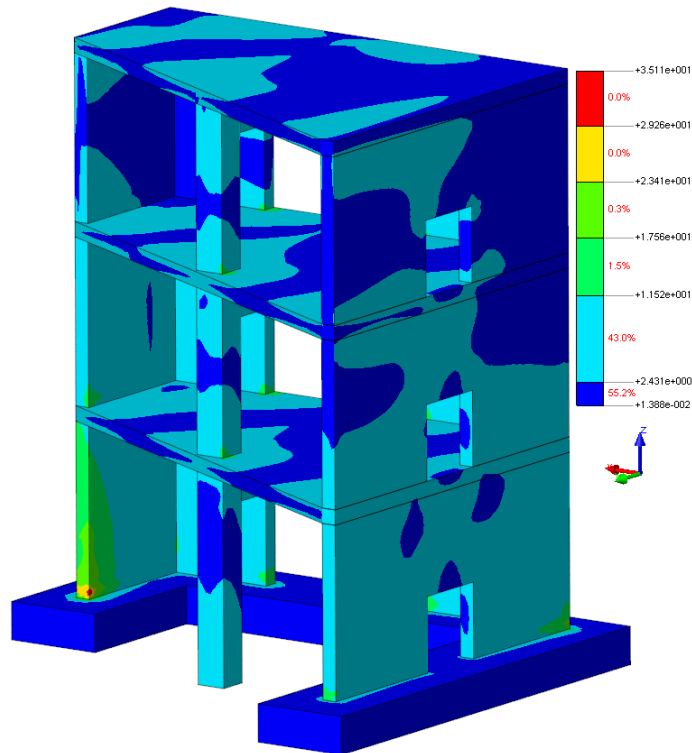Figure 7.137: Principle stresses in S1 in N/mm^2 according to RSA.
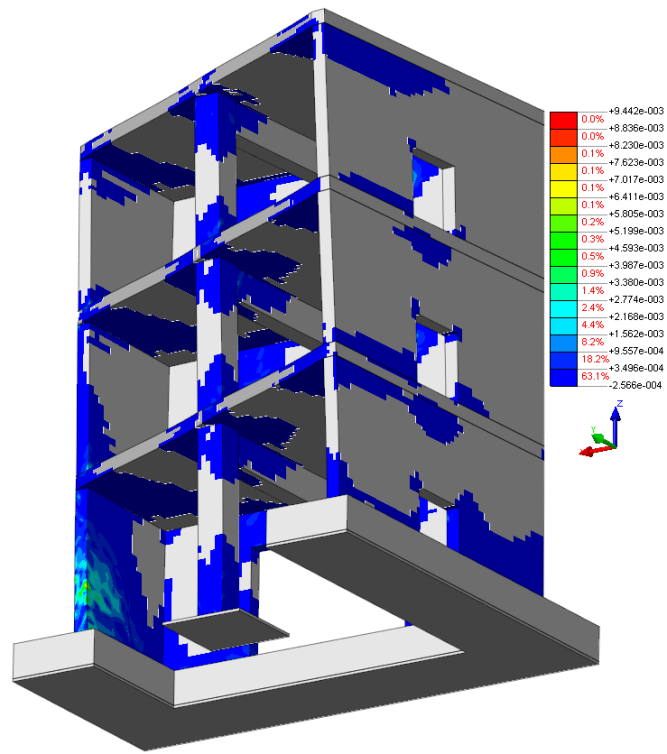
Figure 7.138: Crackwidth in mm.
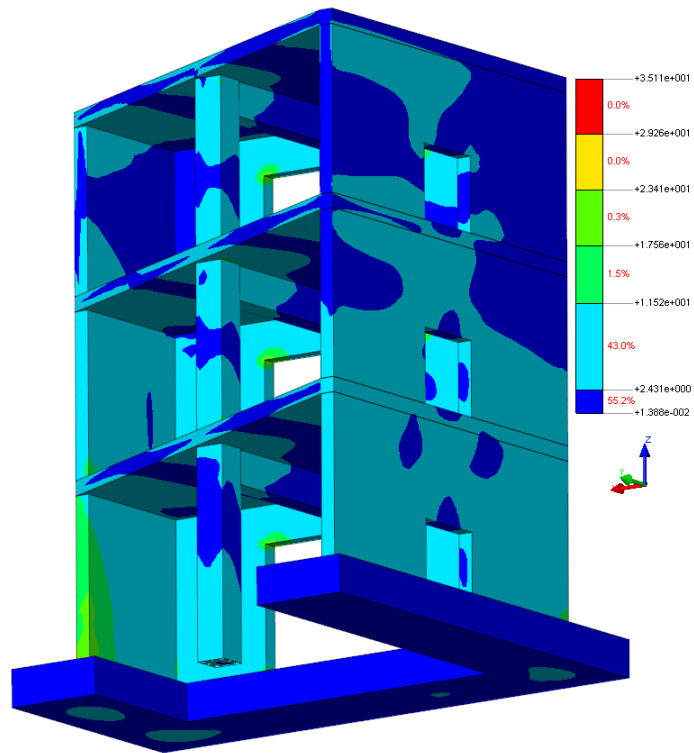
Figure 7.139: Principle stresses in S1 in N/mm^2 according to RSA.

Figure 7.140: Crackwidth in mm.

Figure 7.141: Principle stresses in S1 in N/mm^2 according to RSA.

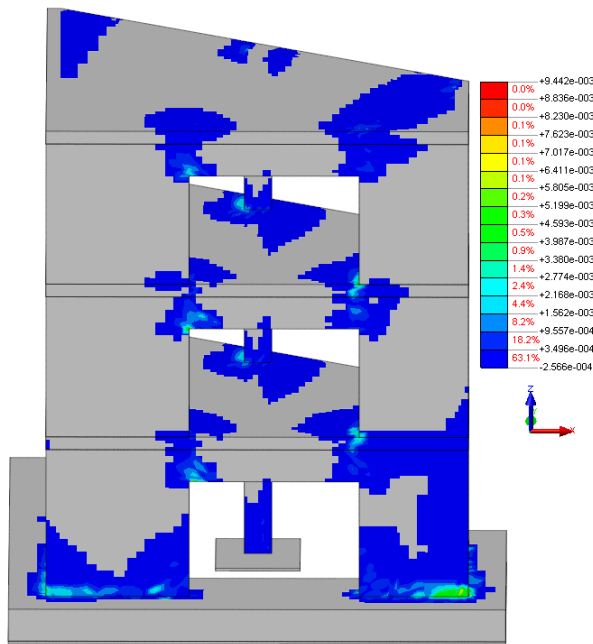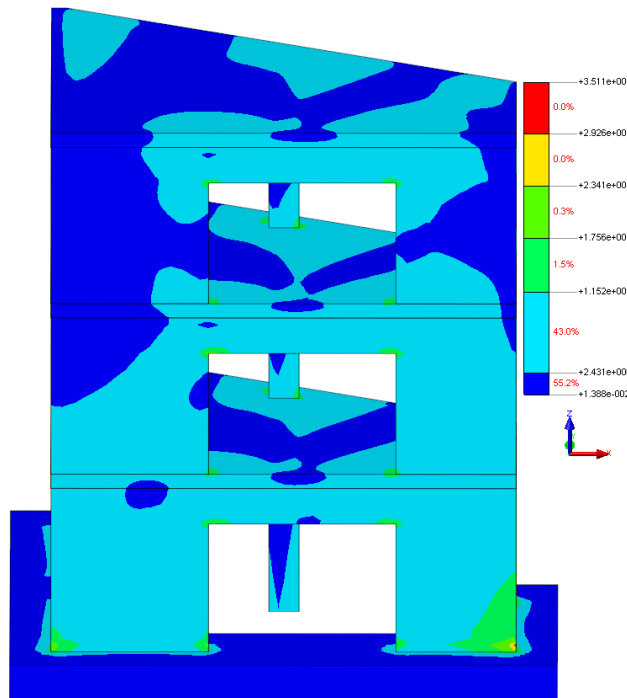The contour plot for the stress distribution of the reinforcement cannot be given because FX$^+$ could not show it for this RUN. The reason for this is that the embedded reinforcement was replaced by bond-slip-reinforcement because the analysis with RUN23 diverged in the beginning.

7.9 Amplification Factor

In section 7.1 the *floor acceleration amplification factor* was determined using equation 19, which was found by performing a non-linear time history dynamic analysis on full scale steel moment-resisting frame buildings [SOURCE]. The amplification factor for the third floor in x- and y-direction that was calculated was equal to 3. In this section the floor acceleration amplification factor for floor 3 is calculated, based on the response (in this case, response = acceleration) of the model with respect to all RUNs, which describes the relation between the PHFA and PGA (PGA = maximum seismic input) to see if the amplification factor from equation 19 also holds for the model of this thesis.

The amplification factor in this section is calculated using the response of the model, with respect to all RUNs, in all 5 points on the third floor and the PGA of each RUN. So how is this factor determined? First, the maximum response in all 5 points on floor 3 with respect to each RUN in x- and y-direction is determined. Then the PGA of each RUN in x- and y-direction is determined. After that, the ratio between the maximum response in all 5 points on the third floor and the PGA for each RUN is calculated. Then the average ratio of all 5 points on the third floor for all RUNs is calculated. At last, the average of the *average ratios* of all RUNs is taken to get the amplification factor.

The average ratios between the response of the model on floor 3 and the maximum seismic input for each RUN are given in the table below.

Table 7.12: Average ratios of all points on floor 3.

RUN	x-direction	y-direction
6	2.18	2.21
7	1.58	1.72
9	1.61	1.87
11	2.12	2.70
13	1.95	2.73
17	1.99	2.81
19	1.24	1.74
21	3.87	4.49
23	1.69	2.95

The get the amplification factor, the average of the *average ratios* of all RUNs is calculated which is given in the table below.

Table 7.13: Amplification factor.

Amplification factor	x-direction	y-direction
All RUNs	2.03	2.58

In section 7.1 the amplification factor in x- and y-direction were the same and equal to 3. According to table 7.13, which is based on the response of the model with respect to all RUNs, the amplification factor is equal to 2.03 in x-direction and 2.58 in y-direction.

The calculated amplification factors, based on the response of the model, in x- and y-direction are both smaller than 3 as calculated in section 7.1. Now these calculated amplification factors will be used to estimate the PGA as has been done in section 7.1 for the pushover analysis in order to show what PGA the model can withstand.

The PHFA on floor 3 from the first pushover analysis, based on the total mass of the model, is given in the table below.

Table 7.14: PHFA based on the total mass of the model.

Total mass [kg]	Maximum force [N]	Acceleration [m/s^2]	PHFA [g]
45300	162410	3.59	0.37

The PHFA on floor 3 from the first pushover analysis, based on the effective mass of the model, is given in the table below.

Table 7.15: PHFA based on the effective mass of the model.

Effective mass [kg]	Maximum force [N]	Acceleration [m/s^2]	PHFA [g]
25018	162410	6.49	0.66

By taking the total mass of the mock-up into account, the PGA will be as follows:

$$PGA = \frac{PHFA}{\Omega} = \frac{0.37}{2.03} = 0.18 \text{ g} \tag{27}$$

By taking the effective mass of the mock-up into account, the PGA will be as follows:

$$PGA = \frac{PHFA}{\Omega} = \frac{0.66}{2.03} = 0.33 \text{ g} \tag{28}$$

The PHFA on floor 3 from the second pushover analysis, based on the total mass of the model, is given in the table below.

Table 7.16: PHFA based on the total mass of the model.

Total mass [kg]	Maximum force [N]	Acceleration [m/s^2]	PHFA [g]
45300	181770	4.01	0.41

The PHFA on floor 3 from the first pushover analysis, based on the effective mass of the model, is given in the table below.

Table 7.17: PHFA based on the effective mass of the model.

Effective mass [kg]	Maximum force [N]	Acceleration [m/s^2]	PHFA [g]
24566	181770	7.39	0.75

By taking the total mass of the mock-up into account, the PGA will be as follows:

$$PGA = \frac{PHFA}{\Omega} = \frac{0.41}{2.58} = 0.16 \text{ g} \tag{29}$$

By taking the effective mass of the mock-up into account, the PGA will be as follows:

$$PGA = \frac{PHFA}{\Omega} = \frac{0.75}{2.58} = 0.29 \text{ g} \tag{30}$$

The PHFA on floor 3 from the third pushover analysis, based on the total mass of the model, is given in the table below.

Table 7.18: PHFA based on the total mass of the model.

Total mass [kg]	Maximum force [N]	Acceleration [m/s^2]	PHFA [g]
45300	243360	5.37	0.56

The PHFA on floor 3 from the third pushover analysis, based on the effective mass of the model, is given in the table below.

Table 7.19: PHFA based on the effective mass of the model.

Effective mass [kg]	Maximum force [N]	Acceleration [m/s^2]	PHFA [g]
5879	243360	41.39	4.22

By taking the total mass of the mock-up into account, the PGA will be as follows:

$$PGA = \frac{PHFA}{\Omega} = \frac{0.56}{2.58} = 0.22 \text{ g} \tag{31}$$

By taking the effective mass of the mock-up into account, the PGA will be as follows:

$$PGA = \frac{PHFA}{\Omega} = \frac{4.22}{2.58} = 1.64 \text{ g} \tag{32}$$

According to the calculated floor amplification factor (based on the response of the model with respect to all RUNs) the model can withstand, dependent of at which mode the model vibrates, a PGA of 0.16 g, 0.18 g or 0.25 g, if the total mass of the mock-up is taken into account. If the effective mass of the model is taken into account, then the model can withstand, dependent of at which mode the model vibrates, a PGA of 0.29 g, 0.33 g or 1.86 g. The tables below give an overview of the estimated PGAs.

Table 7.20: Estimated PGA based on the total mass of the model.

Pushover	Estimated PGA [g] - total mass	Direction
1	0.18	x
2	0.16	y
3	0.25	y

Table 7.21: Estimated PGA based on the effective mass of the model.

Pushover	Estimated PGA [g] - effective mass	Direction
1	0.33	x
2	0.29	y
3	1.86	y

Lets compare the estimated PGAs of the pushover analyses from section 7.1 with the estimated PGA from this section using the amplification factors from table 7.13. The tables below give a comparison of the estimated PGAs.

Table 7.22: Pushover analysis 1.

Amplification factor	PGA [g] - total mass	PGA [g] - effective mass
3	0.12	0.22
2.03	0.18	0.33

Table 7.23: Pushover analysis 2.

Amplification factor	PGA [g] - total mass	PGA [g] - effective mass
3	0.14	0.25
2.58	0.16	0.29

Table 7.24: Pushover analysis 3.

Amplification factor	PGA [g] - total mass	PGA [g] - effective mass
3	0.22	1.66
2.58	0.25	1.86

The three tables from above show that the model can withstand higher PGAs when using the calculated amplification factors which are based on the response of the model due to all RUNs. In section 7.1 it was mentioned that it is convenient to use the effective mass of the model when estimating the capacity of the model in terms of PGA. Now to estimate which RUNs will exceed the capacity of the model and which RUNs don't, the estimated PGAs (using the calculated amplification factors) based on the effective mass of the model will be used. The table below shows which RUNs will exceed the capacity of the model and which RUNs don't, according to the results of the pushover analyses.

Table 7.25: Prediction of the pushover analyses - effective mass.

RUN	PGA x [g]	Exceeds capacity	PGA y [g]	Exceeds capacity
9	0.25	No	0.35	No
11	0.22	No	0.18	No
13	0.42	Yes	0.32	No
17	0.63	Yes	0.44	No
19	1.11	Yes	1.03	No
21	0.15	No	0.20	No
23	0.65	Yes	0.46	No

Now according to the pushover analyses, the model can withstand RUN9, RUN11 and RUN21. Indeed the model withstood these three RUNs in the nonlinear transient analyses. The model also withstood RUN13 while it is predicted that the model can not withstand RUN13. The reason why the pushover analysis is not correct about RUN13 is because the pushover analysis made an estimation of the capacity of the model and it is known that estimations are not 100% right. The fact that the pushover analysis is right about RUN9, RUN11 and RUN21 is very good and at least it is now known why RUN17, RUN19 and RUN23 diverged.

The following graphs show graphical representations of table 7.25 which show which RUNs exceed the capacity of the model and which RUNs don't.
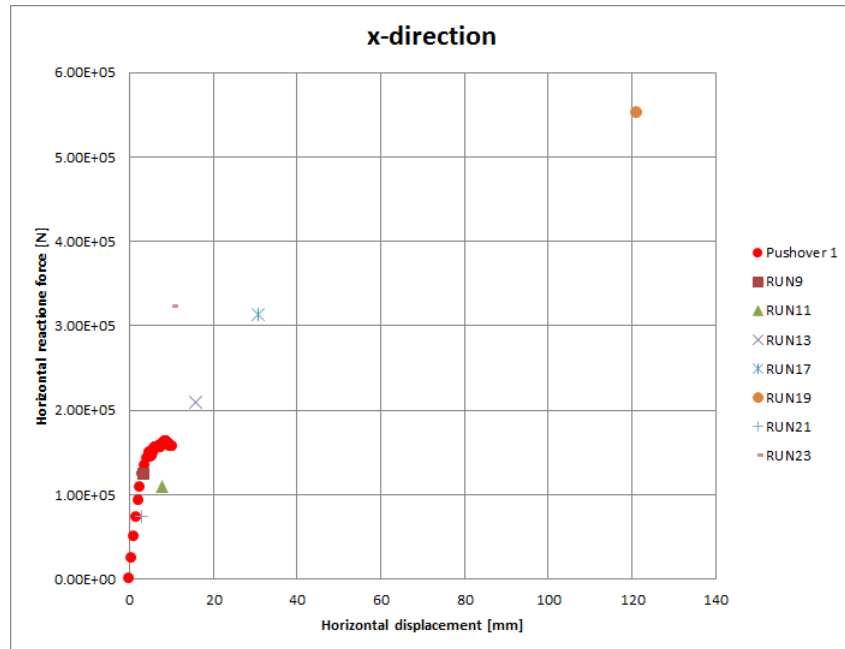

Figure 7.142: Force-displacement diagram in x-direction.

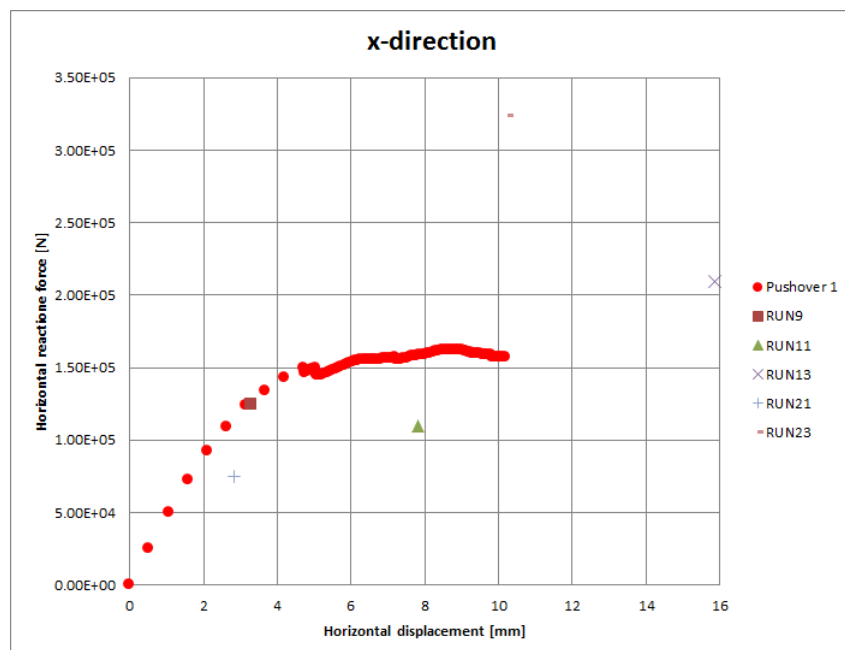By taking away RUN17 and RUN19 a more clear figure is obtained.

Figure 7.143: Force-displacement diagram in x-direction.

These figures show that the model can withstand RUN9, RUN11 and RUN21 in x-direction,
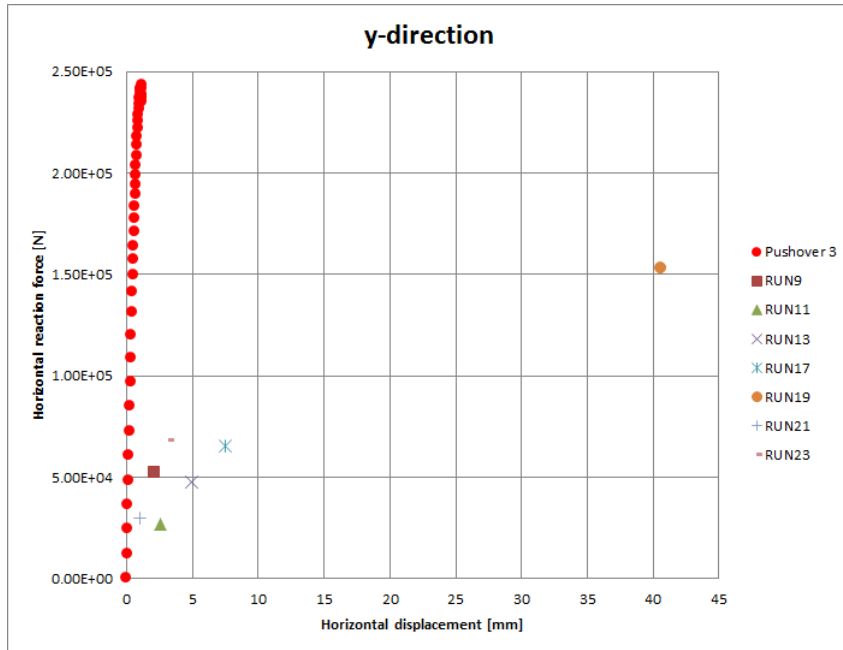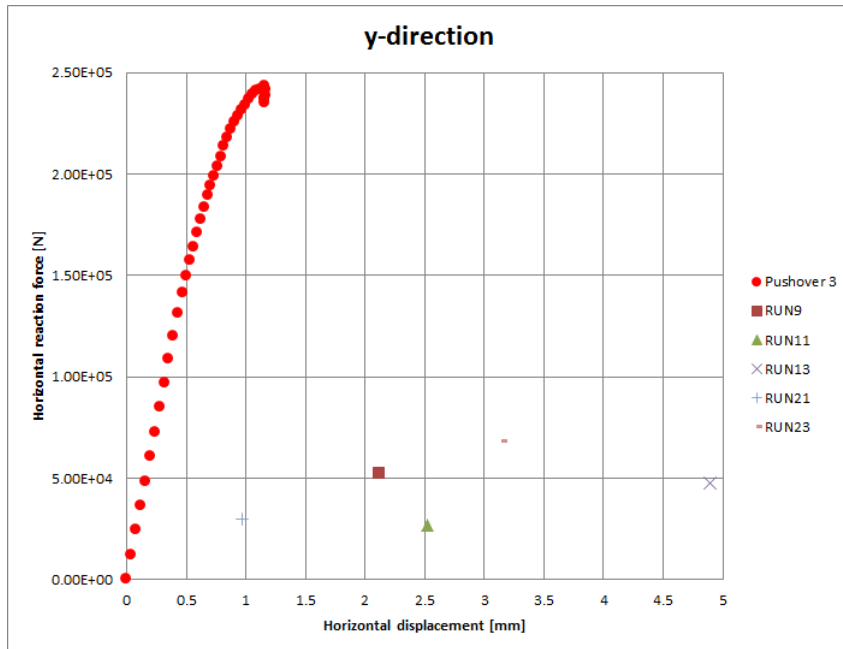
as mentioned before.

Figure 7.144: Force-displacement diagram in y-direction.

By taking away RUN17 and RUN19 a more clear figure is obtained.

Figure 7.145: Force-displacement diagram in y-direction.

These figures show that the model can withstand all RUNs in y-direction, as mentioned before. Because the model can only withstand RUN9, RUN11 and RUN21 in x-direction it can be said that the model can withstand only RUN9, RUN11 and RUN21.

How are the points for each RUN from the figures above obtained? First the PGAs in x- and y-direction for RUN are determined. After that the corresponding forces are estimated according to F = m*a by considering the effective mass of the model in x- or y-direction. The tables below show that.

Table 7.26: Estimation of the horizontal forces in x-direction.

RUN	PGA x [g]	PHFA x [g]	Effective mass [kg]	Force [N]
9	0.25	0.51	25018	124554
11	0.22	0.45	25018	109608
13	0.42	0.85	25018	209251
17	0.63	1.28	25018	313876
19	1.11	2.25	25018	553020
21	0.15	0.30	25018	74732
23	0.65	1.32	25018	323840

Table 7.27: Estimation of the horizontal forces in y-direction.

RUN	PGA y [g]	PHFA y [g]	Effective mass [kg]	Force [N]
9	0.35	0.90	5879	52079
11	0.18	0.46	5879	26783
13	0.32	0.83	5879	47615
17	0.44	1.14	5879	65470
19	1.03	2.66	5879	153260
21	0.2	0.52	5879	29759
23	0.46	1.19	5879	68446

After estimating the forces for each RUN, the maximum displacements for each RUN are determined. The maximum horizontal displacement for each RUN is given below.

Table 7.28: Maximum displacements in x-direction.

RUN	PGA x [g]	Displacement x-direction [mm]
9	0.25	3.3
11	0.22	7.8
13	0.42	15.85
17	0.63	30.82
19	1.11	121.2
21	0.15	2.84
23	0.65	10.27

Table 7.29: Maximum displacements in y-direction.

RUN	PGA y [g]	Displacement y-direction [mm]
9	0.35	2.12
11	0.18	2.52
13	0.32	4.89
17	0.44	7.48
19	1.03	40.61
21	0.2	0.97
23	0.46	3.15

At last the the estimated forces are plotted against the maximum horizontal displacements for each RUN to get the figures from above.

It is important to mentioned that the calculated amplification factors 2.03 and 2.58 are used to calculate the PHFA. It is also important to know that the calculated forces using F = m*a are estimations which means that these forces have uncertainties and are not exact. But once again, it a nice way to graphically represent the capacity of the model.

7.10 Summary Stage 3

In this stage the nonlinear dynamic response of the model is evaluated by performing nonlinear transient analyses and pushover analyses. For the nonlinear transient analyses different seismic excitations are used where for the pushover analyses only the first three mode shapes are taken into account.

The pushover analyses predicted that the model can withstand RUN9, RUN11 and RUN21. And indeed, these predictions were right. Because of the pushover analysis it is known why RUN17, RUN19 and RUN23 diverged. These RUNs diverged because the model could not withstand these RUNs. The pushover analyses showed where the model would crack (as a result of high tensile stresses) when the model is loaded to its capacity according to its first three mode shapes by giving the crack patterns. These crack patterns give an indication of where the model might crack when performing nonlinear transient analyses. The pushover analyses also showed where the reinforcement will yield which give an indication of where the reinforcement might yield when the reinforcement yields when performing nonlinear transient analyses. It is also important to mention that the predictions of the pushover analyses are not 100% accurate of how the model will behave when performing a nonlinear transient analysis. The reason for this is that when performing a nonlinear transient analysis, the model vibrates arbitrarily in every direction at various range of frequencies where in a pushover analysis the model is loaded only at one mode shape at a time. In this thesis, for the pushover analysis only the first three mode shapes are taken into account which also limits the prediction power of the pushover analysis. Having the previous said, a pushover analysis is a useful nonlinear dynamic analysis with certain limitations. This limitation may be reduced by taking more than three mode shapes into account.

During the study of the crack patterns of the nonlinear transient analyses, the stress distributions of the model according to the response spectrum analyses were considered to see if these stress distribution could say anything about the crack patterns of the model in the nonlinear transient analyses. These stress distributions were very useful and good in showing where the model might crack when performing nonlinear transient analysis. In places where the tensile stresses were much higher then the tensile strength of concrete in the contour plots from RSA, the model showed cracks in the contour plots from the nonlinear transient analyses. It is important to mention that the results of response spectrum analysis are less accurate in comparison with the results of the nonlinear transient analysis which is quite logical because a nonlinear transient analysis gives the exact response of the model due to seismic loading as a response spectrum analysis gives the maximum linear response of the model due to seismic loading. Because the RSA is a linear dynamic analysis, the model will not crack in this analysis. And the tensile stress contour plots which are shown in the previous sections of this stage show very high tensile stresses in areas where the model shows cracks in the nonlinear transient analysis. Also the tensile stresses spread which cover big areas of the model, from the area where the tensile stresses are much higher then the tensile strength of concrete. So a response spectrum analysis is also a useful dynamic analysis with certain limitations.

During the comparisons of the numerical responses of the model and the experimental responses of the mock-up with respect to all RUNs, there were some good matches between these two responses. The responses due to RUN9, RUN11 and RUN13 were close to each other. The match between the numerical and experimental responses due to RUN17 and RUN19 were quite good but after some time the amplitudes of the experimental responses became much higher then the numerical responses. A reason for this could be that the damage history of the finite element model was not taken into account while the damage history of the real mock-up was taken into account. Only the responses due to RUN21 and RUN23 did not show a good match. The is possibly because of the damage that is

experienced by the real mock-up with respect to RUN9, RUN11, RUN13, RUN17 and RUN19 while the damage history of the finite element model is not taken into account.

In this stage, research questions 5 - 8 are answered.

8 Conclusions

In stage 1 of this master thesis the finite element model is developed. This finite element model consists of a model of a reinforced concrete mock-up and a shaking table. The reinforced concrete mock-up is modeled with solid elements, the reinforcement bars are modeled with embedded reinforcement, the shaking table is modeled with curved shell elements and the additional masses with translational mass elements. In the figures of the model of the mock-up in stage 1 can be seen that the mesh of the model is quite fine. The thickness of the walls and the floors are for example divided into four elements. The reason why these types of elements are chosen to model the reinforced concrete mock-up and the shaking table and the chosen fine mesh is because it is tried to mimic the real structure as good as possible. Further can be said that all the elements that are used in the finite element model are linear elements. Linear elements are chosen because of the fine mesh and the computation time. If quadratic elements were chosen with this fine mesh, then the computation time would be at least twice as big as with linear elements.

After the development of the model, material models were assigned to each material. The total strain rotating crack model (with Hordijk softening and Thorenfeldt crushing) is used to model the concrete, the Menegotto-Pinto model is used to model the reinforcement bars and the Von Mises plasticity model is used to model the plates of the shaking table. These material models have proven in the past that they are suitable to model these materials when these materials undergo cyclic loading like earthquakes and that is why these material models are chosen in this thesis. It is possible that other material models are also suitable, or maybe more suitable, for earthquake loadings but that is not investigated here because that is not the focus of this thesis. It is a interesting to investigate different material models with different material parameters to find out which material models are more stuiable or optimal for earthquake loadings. These investigations can be done in further studies, outside this one.

In stage 2 eigenvalue analyses, linear transient analyses and response spectrum analyses are performed. The eigenvalue analyses are performed in order to calibrate the finite element model with the real mock-up. The eigenvalue analyses were performed for the following three cases:

1. the mock-up is fixed at the lower face of the foundation and is not loaded with additional masses,
2. the mock-up is fixed at the lower face of the foundation and is loaded with additional masses,
3. the mock-up is linked to the shaking table and is loaded with additional masses.

After performing and analyzing the results of the eigenvalue analyses for all three cases, it appeared that the case 3 made the match with the experimental natural frequencies as shown in the tables belows.

Table 8.1: Natural frequencies - total E-modulus.

Mode	Experimental [Hz]	Numerical [Hz]	Difference [%]
1	6.5	7.02	8
2	9.5	10.06	6
3	-	20.59	-

This table shows that the differences of 8% and 6% between the first two numerical and experimental natural frequencies arr so big. This difference can be further reduced by using

a reduced E-modulus of the model. According to Model Code 2010, 85% the E-modulus of the model should be used when performing an elastic linear analysis in order to account for initial plastic strain, causing some irreversible deformations. The natural refquencies of the model with reduced E-modulus are given below.

Table 8.2: Natural frequencies - 85% E-modulus.

Mode	Experimental [Hz]	Numerical [Hz]	Difference [%]
1	6.5	6.66	3
2	9.5	9.68	2
3	-	19.72	-

These experimental natural frequencies are obtained by performing a DFT on RUN7 and the response of the mock-up to RUN7 on floor 3 in point D. Lets consider table 8.2. The first and second natural frequencies are obtained but the third one couldn't be obtained. But looking at the first and second natural frequencies, it can be seen that the difference between the first numerical and experimental natural frequencies is 3% and the difference between the second numerical natural frequency and experimental natural frequency is 2%. The differences are not big and acceptable. It is also interesting to see how the mode shapes of the model looks like. The following figures show this. Please note that the mode shapes from below correspond to the model of the mock-up + shaking table but the shaking table is not shown.

Figure 8.1: Mode shape 1.
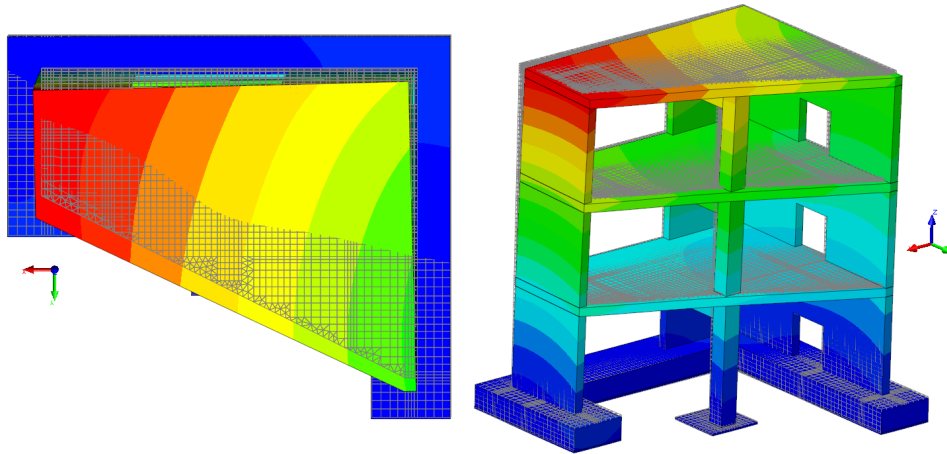
Figure 8.2: Mode shape 2.
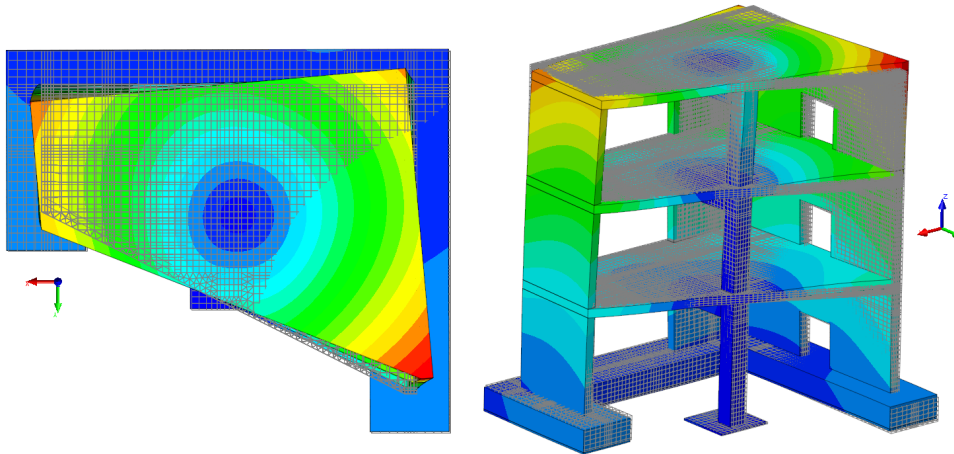
Figure 8.3: Mode shape 3.

For the calibration of the finite element model with the real mock-up the first three natural frequencies of the model are calculated with DIANA and then compared with the provided experimental natural frequencies of the mock-up. For a good calibration it is important that these natural frequencies are as close as possible to each other because in order to make reliable predictions for the dynamic bahavior of the mock-up the calibration of the finite element model (based on natural characteristics of the model) should be good. Only then the predictions of the dynamic behavior of the mock-up will be reliable. At the end the eigenvalue analyses for the three cases it appeared that it is important that the shaking table was also modeled along with the reinforced concrete mock-up because the numerical natural frequencies of case 3 were the closest to the experimental natural frequencies of the mock-up. The results of the eigenvalue analyses for each case can be found in stage 2 in section *Eigenvalue Analysis*.

After the eigenvalue analyses, linear transient analyses were performed using RUN6 and RUN7 as input. The responses of the model due to RUN6 and RUN7 were calculated in several points in the model. The benchmark committee provided the responses of the real mock-up due to RUN6 and RUN7 in several points of the mock-up. After the linear transient analyses were performed, comparisons were made between the numerical responses (in terms of displacements and accelerations) of the model and the experimental responses of the

mock-up on floor 3 in point D to see how good the finite element model predicts the dynamic response of the mock-up with respect to seismic loading. In stage 2 in section 6.4.1 it can be seen that the match between the numerical responses of the model and the experimental responses of the mock-up is quite good. In some points the amplitudes of the responses differ a bit and also the responses are sometimes a little bit out-of-phase. The reason why the previous mentioned differences occur is because the finite element model does not have the exact natural frequencies and stiffness as the real mock-up. Because of different natural frequencies, the responses are in some point a little bit out-of-phase and because of different stiffnesses the amplitudes of the responses are not the same in some points. If the natural characteristics of the finite element model were the same as the real mock-up together with the mass, stiffness and damping then the dynamic responses of the model would be the same as the dynamic responses of the mock-up. After comparing the experimental and numerical responses it can said that the finite element model did a nice prediction of the dynamic response of the mock-up with respect to RUN6 and RUN7.

The last type of dynamic analysis that is performed in stage 2 is the response spectrum analysis using the response spectrum of each RUN as input. These linear dynamic analyses were performed for each RUN to see where in the model the tensile stresses are higher then the tensile strength of the model. With this information it is possible to expect where the model might crack when performing nonlinear transient analyses for each RUN. The contour plots of the tensile stresses for each RUN, obtained from the RSA, are compared with the crack patterns, obtained from the nonlinear transient analyses, for each RUN in stage 3 to see how useful RSA really is. It appears that RSA is quite useful. As can be seen in for example section 7.2, the contour plots from RSA are good at showing where the model may crack. In the regions where the tensile stresses are much higher then the tensile strength of concrete, the nonlinear transient analysis shows cracks. This holds for all other nonlinear transient analyses. It is important to mention that the contour plots from RSA are not very accurate in comparison with the contour plots of the nonlinear transient analyses which is to be expected as the RSA is a linear and less advanced dynamic analysis. In RSA the concrete will not crack and the stresses build up to much higher values then the tensile strength of concrete, as shown in the contour plots of the stresses, and when performing an advanced nonlinear transient analysis, the concrete cracks in these high stressed regions. But the good thing about RSA is that it consumes much less computation time in comparison with the nonlinear transient analysis and it gives a good indication of the dynamic response of the model.

The first nonlinear dynamic analysis that is performed in this master thesis is the pushover analysis. With this nonlinear dynamic analysis it is possible to estimate the seismic capacity of the model by taking a certain mode shape of the model and then load the model according to this mode shape until the model collapses. Three pushover analyses are performed in stage 3 where the the first three mode shapes of the model are taken into account. The seismic capacity of the model is estimated in terms of PGAs in x- and y-direction by using the calculated maximum horizontal reaction forces for each pushover analysis. With these estimated PGAs it is possible to expect which RUNs from the nonlinear transient analysis the model can withstand and which RUNs it can't. The pushover analyses predicted that the model can withstand RUN9, RUN11 and RUN21. And indeed, these predictions were right. Because of the pushover analysis it is known why RUN17, RUN19 and RUN23 diverged. These RUNs diverged because the model could not withstand these RUNs. The pushover analyses showed where the model would crack (as a result of high tensile stresses) when the model is loaded to its capacity according to its first three mode shapes by giving the crack patterns. These crack patterns give an indication of where the model might crack when performing nonlinear transient analyses. The pushover analyses also showed where the reinforcement will yield when the reinforcement yields which give an indication of where the

reinforcement might yield when the reinforcement yields when performing nonlinear transient analyses. It is also important to mention that the predictions of the pushover analyses are not 100% accurate of how the model will behave when performing a nonlinear transient analysis. The reason for this is that when performing a nonlinear transient analysis, the model vibrates arbitrarily in every direction at various range of frequencies where in a pushover analysis the model is loaded only at one mode shape at a time and this is the limitation of the pushover analysis. In this thesis, for the pushover analysis only the first three mode shapes are taken into account which limits the prediction power of the pushover analysis. Having the previous said, a pushover analysis is a useful nonlinear dynamic analysis with certain limitations. This limitation may be reduced by taking more than three mode shapes into account.

At last the most advanced nonlinear dynamic analysis is performed, the nonlinear transient analysis. With this analysis the exact response of the model is calculated with respect to all RUNs. After calculating the response of the model, comparisons are made between the calculated numerical responses (in terms of displacements) and the provided experimental responses of the mock-up on floor 3 in point D. These comparison are given at the end of stage 3 for each RUN. The match between the numerical and experimental responses were good for RUN9, RUN11 and RUN13. The match between numerical and experimental responses due to RUN17 and RUN19 were also good but at some moments the experimental responses showed much higher amplitudes then the numerical responses. Only the match between the numerical and experimental responses due to RUN21 and RUN23 were not good, this is possibly because of the damage that is experienced by the real mock-up with respect to RUN9, RUN11, RUN13, RUN17 and RUN19 while the damage history of the finite element model is not taken into account. The numerical and experimental results of the nonlinear transient analyses are given in stage 3.

Hereby are all research questions which were given in section 3 answered.

9 Recommendations

Use instead of design values for the material parameters for concrete, measured values. With this it is possible to simulate the real structure better. The measured material parameters are given below.

Table 9.1: Measured material parameters for concrete.

Structural component	Young's modulus [MPa]	Poisson's ratio	f_c [MPa]	f_t [MPa]	G_f^I [J/m^2]	ρ_c [kg/m^3]
Foundation	25400	0.17	43.3	3.45	136	2300
Walls cast 1	28700	0.19	41.7	3.15	134	2300
Walls cast 2	25700	0.19	35.5	2.7	132	2300
Walls cast 3	29500	0.18	46.6	4.0	123	2300
Floor 1	28200	0.18	41.1	3.25	136	2300
Floor 2	24700	0.17	36.8	3.35	114	2300
Floor 3	24400	0.18	37.8	3.4	135	2300

Use a 2D finite element model instead of a 3D finite element model and perform the eigenvalue analyses and (non)linear transient analyses to see if a 3D finite model gives significantly better results or not. This is recommended because a 3D finite element model is expensive in computation time and if via this recommendation comes out that a 2D finite element model gives almost the same results as a 3D finite element model then it is better to use a 2D finite element model. This is handy in case of modeling much bigger structure then the scaled mock-up from this thesis.

Before performing a nonlinear transient analysis, perform a response spectrum analysis to see what can kind of response, in term of stresses, van be expected for the nonlinear transient analysis. This is recommended because a response spectrum analysis is way cheaper in computation time then a nonlinear transient analysis and according to this thesis a response spectrum analysis gives reliable results about the dynamic behavior of a structure.

It is worthwhile to perform a pushover analysis before performing a nonlinear transient analysis because with this analysis it is possible to estimate the seismic capacity of the structure, as shown in this thesis.

It is also recommended to perform a nonlinear transient analysis with bond-slip reinforcement (with measured material properties) to see if it is possible for the model to not diverge when taking the damage history of the model into account for all RUNs. With other words, combine all RUNs into one RUN and perform a nonlinear transient analysis with bond-slip reinforcement.

A   Appendix A

In this appendix the graphs of every RUN are shown. For the linear transient analysis, RUN6 and RUN7 are used. RUN6 is the synthetic white noise and RUN7 is a scaled design signal. The figures below show how RUN6 and RUN7 look like.
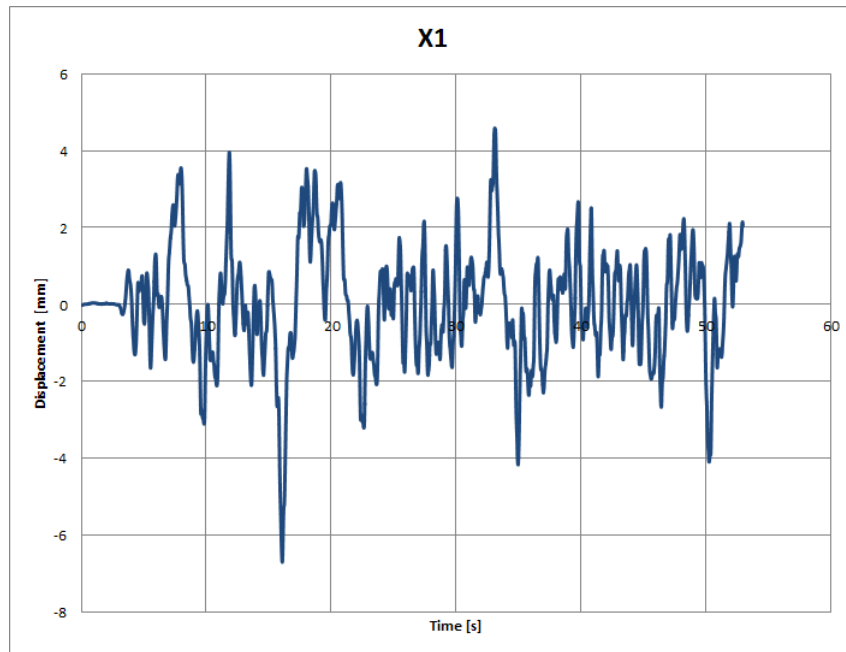
Figure A.1: RUN 6 - prescribed displacement at actuator X1.
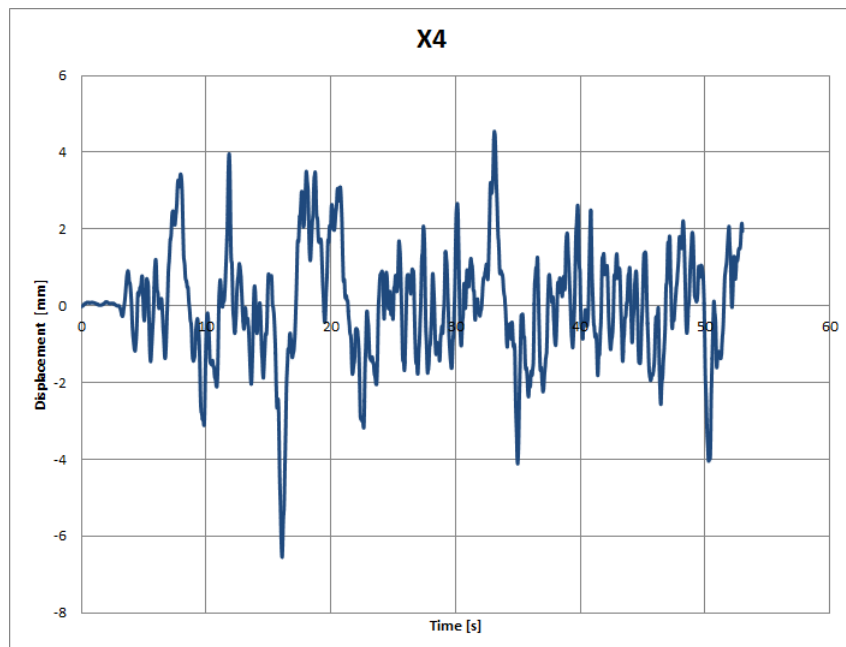
Figure A.2: RUN 6 - prescribed displacement at actuator X4.
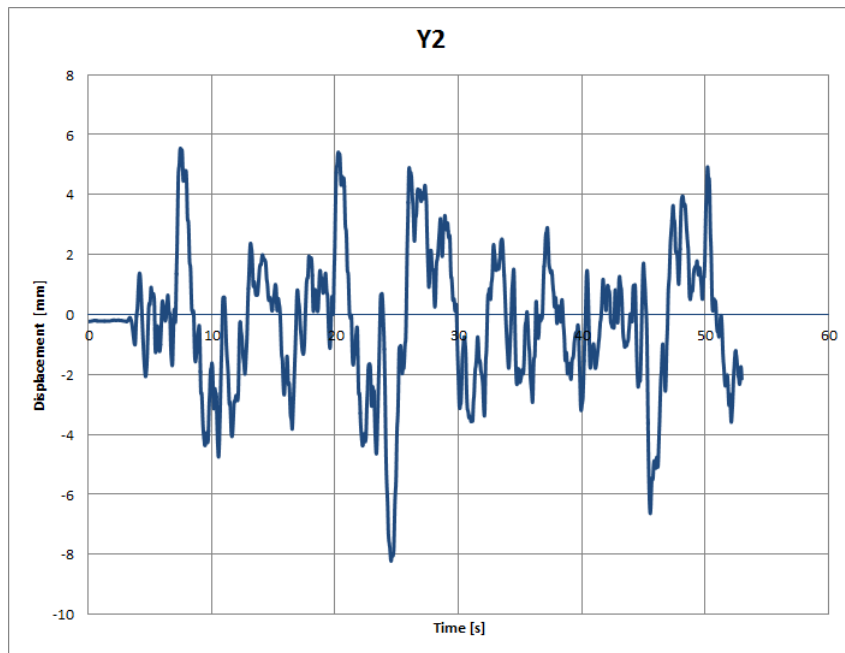
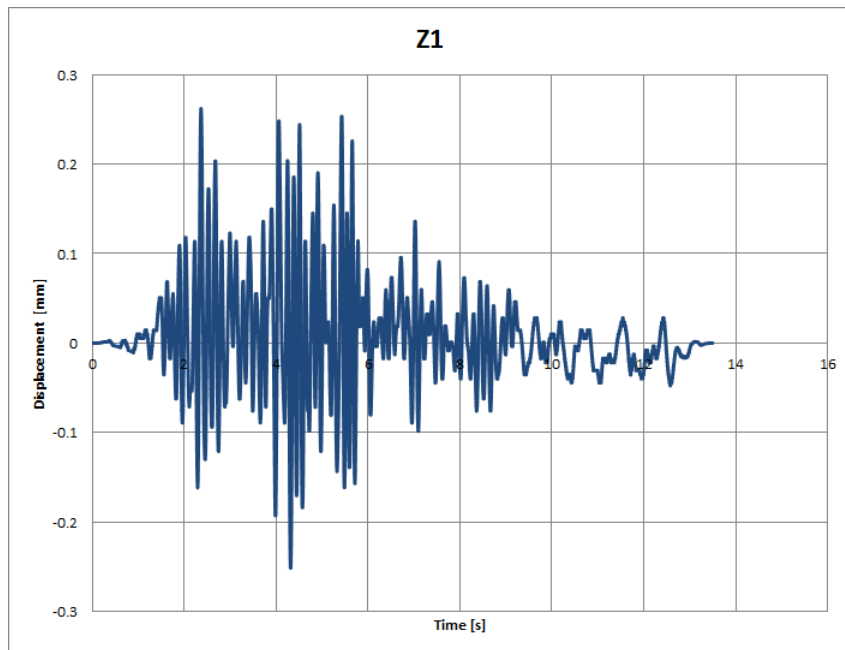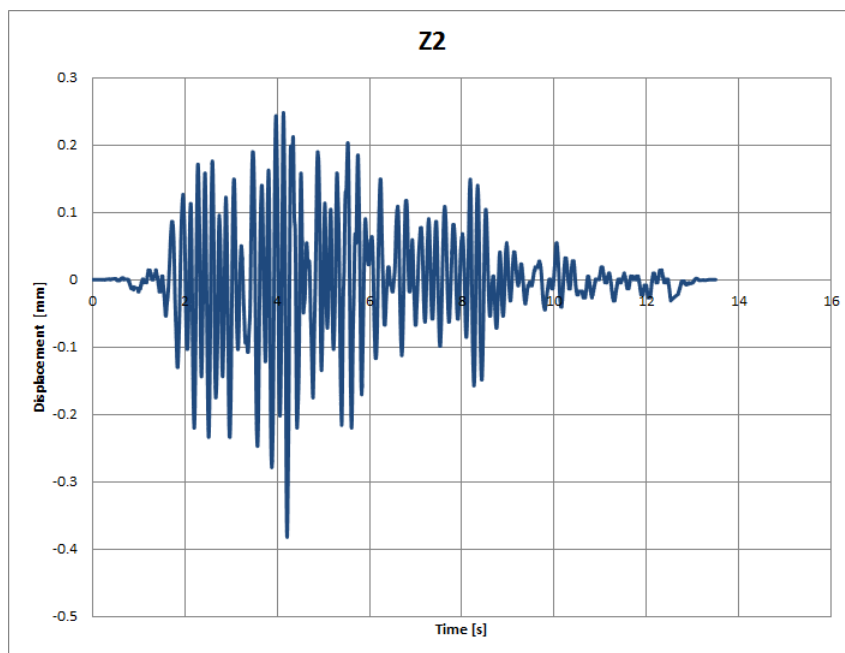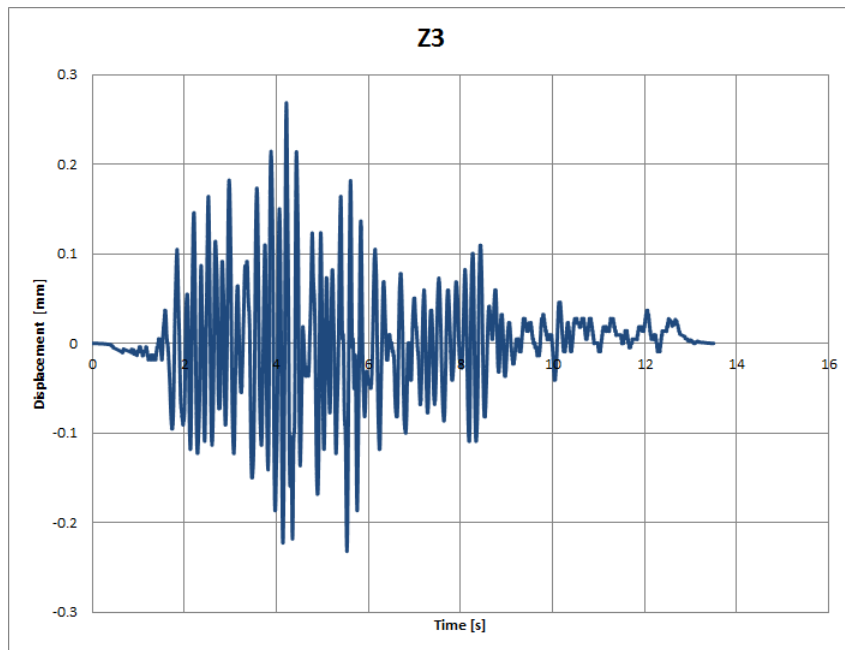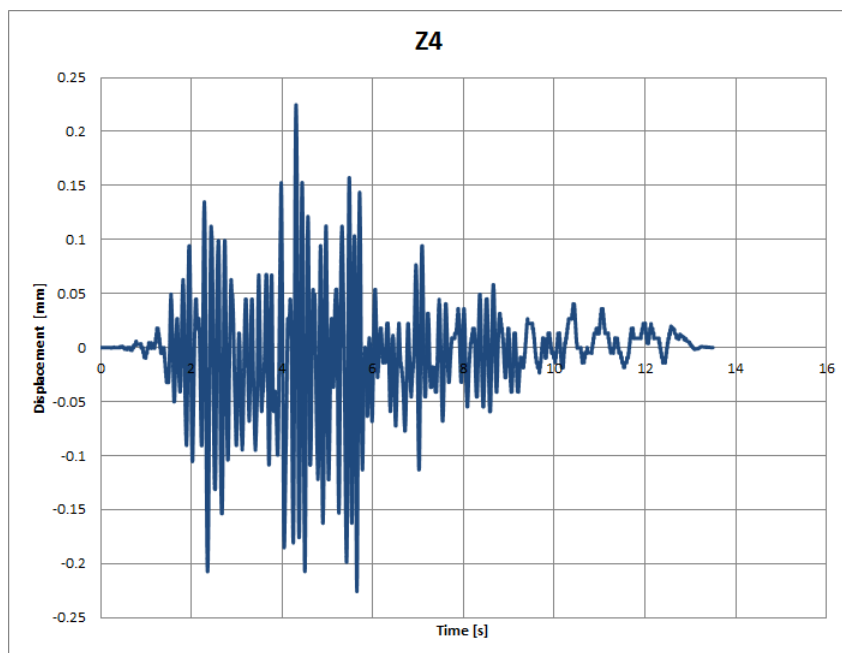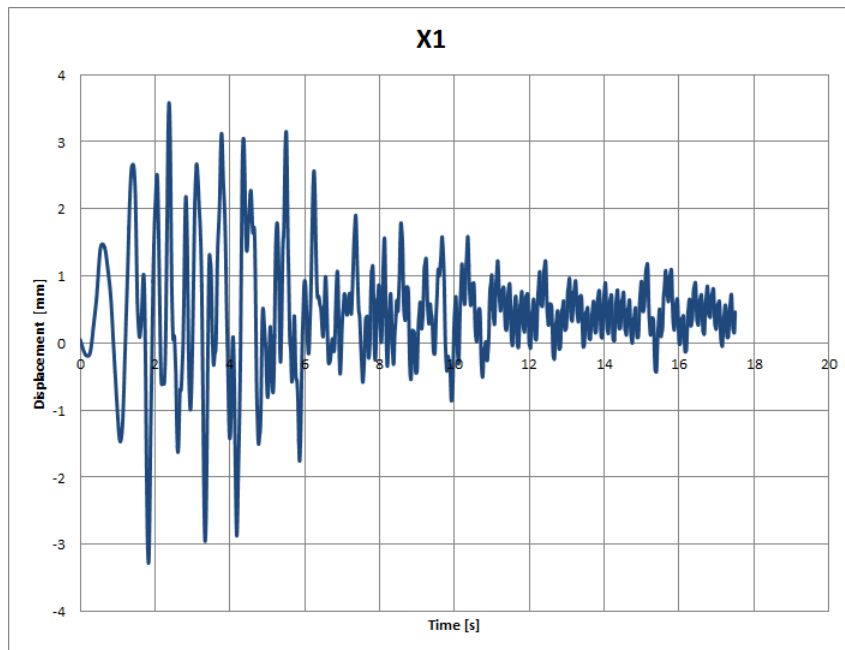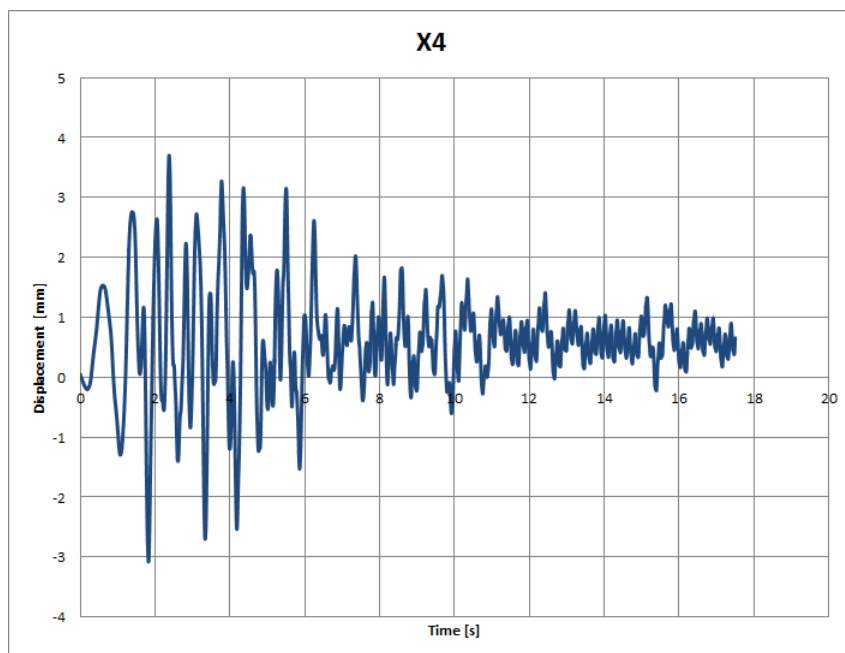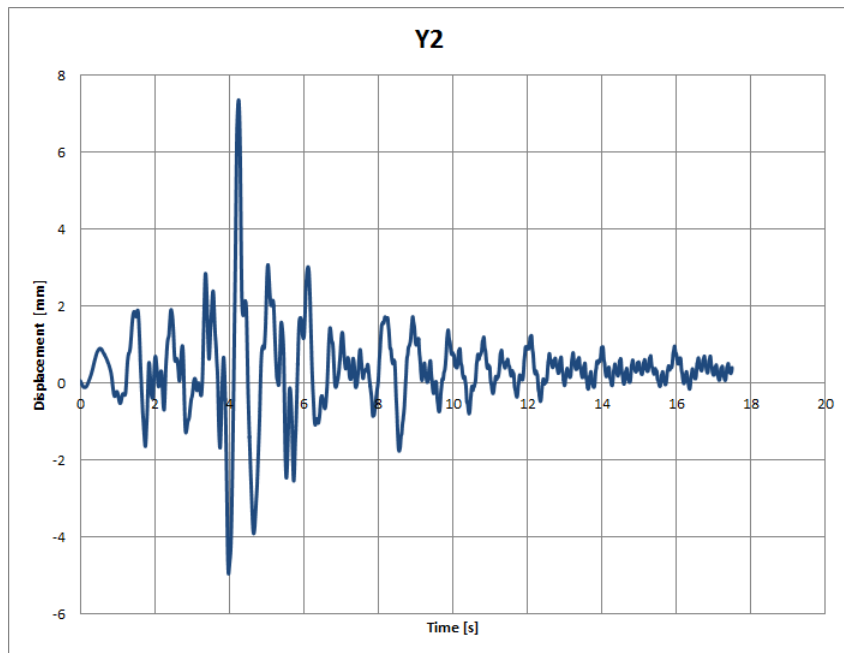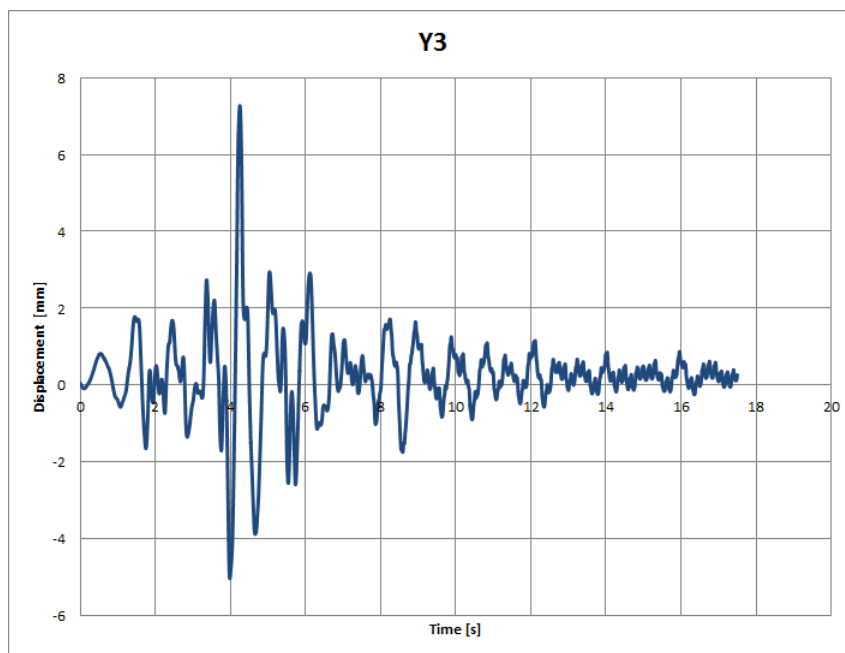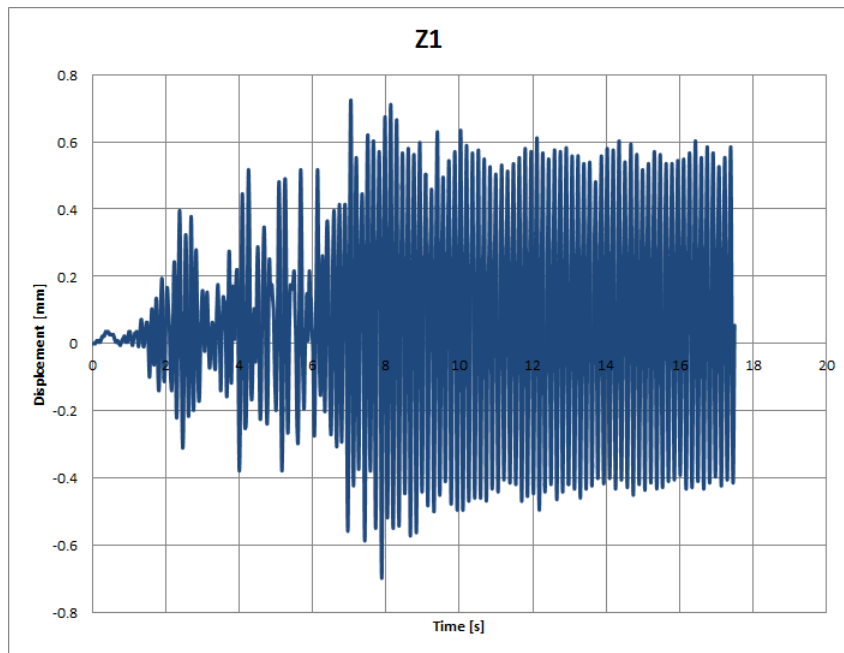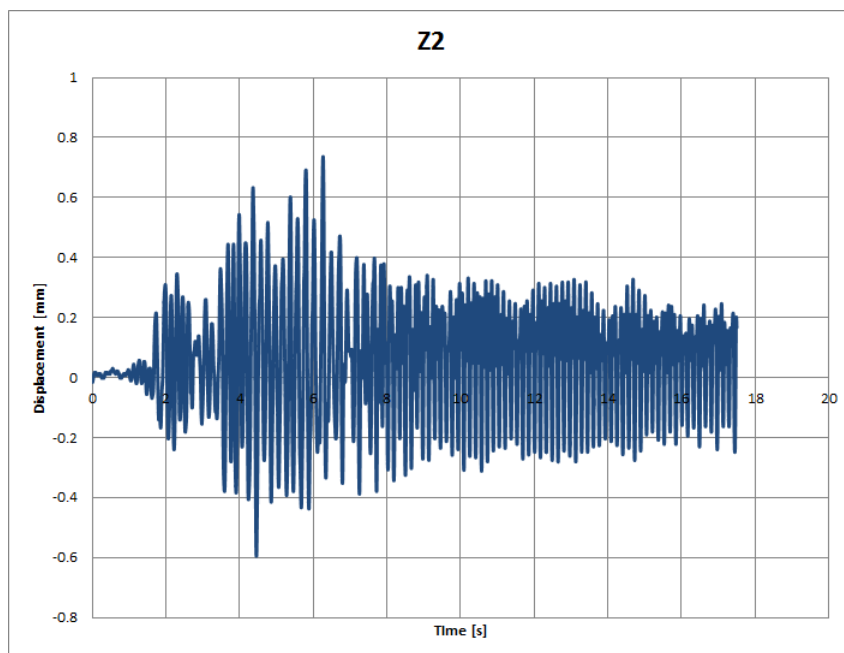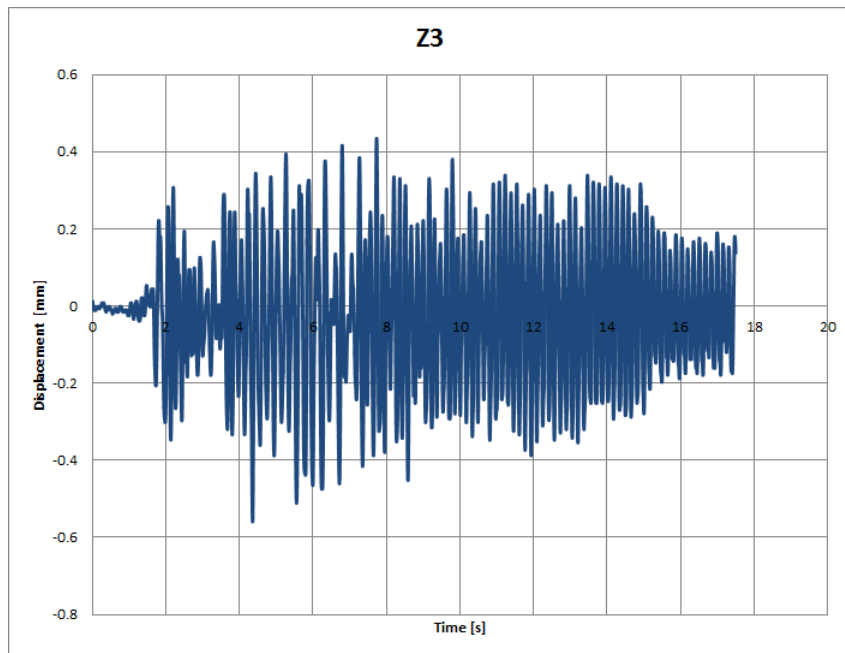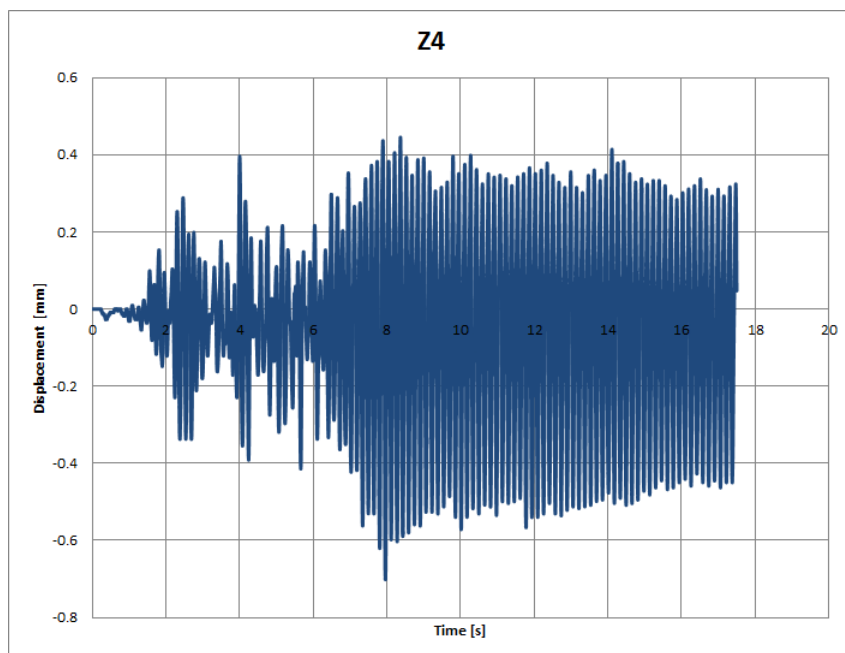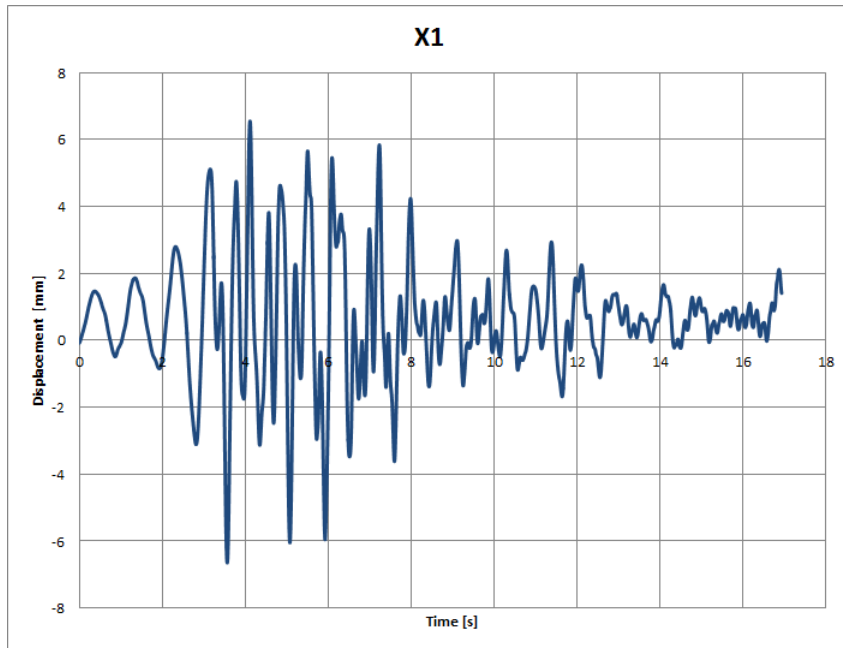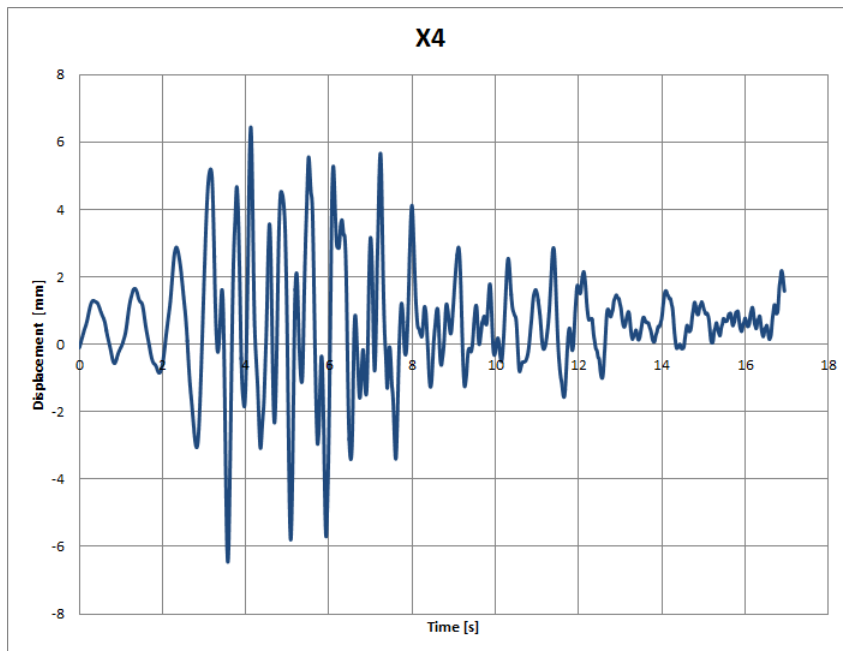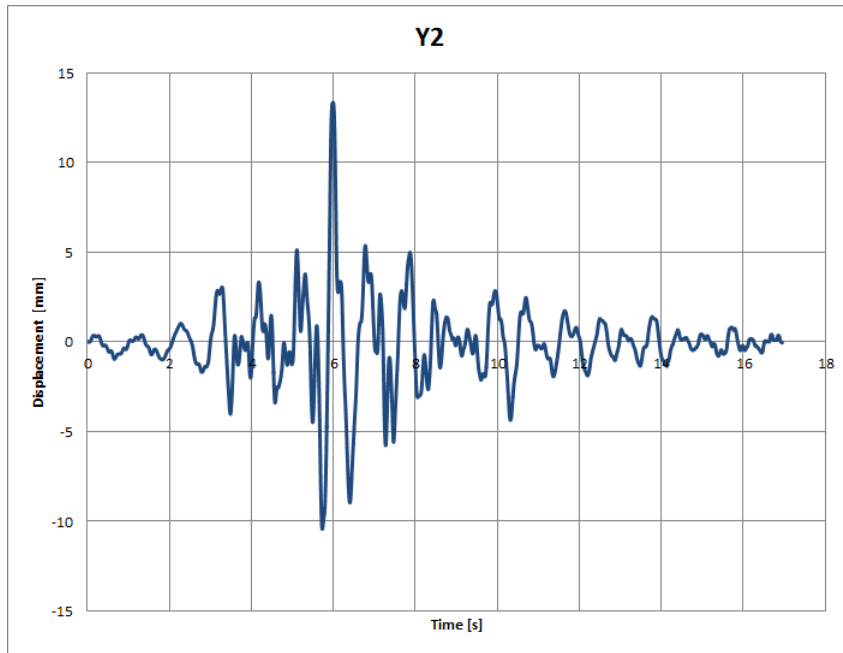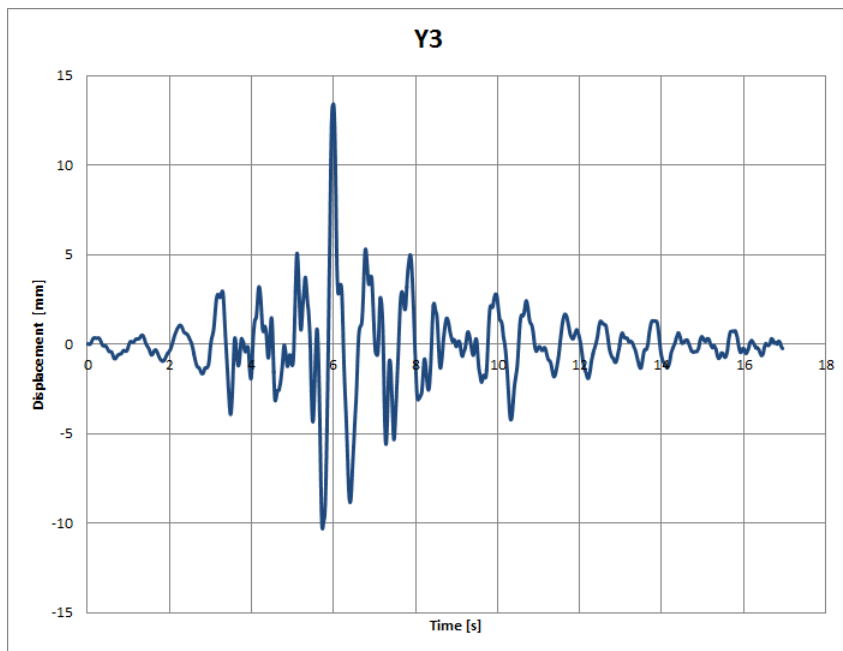Figure A.3: RUN 6 - prescribed displacement at actuator Y2.
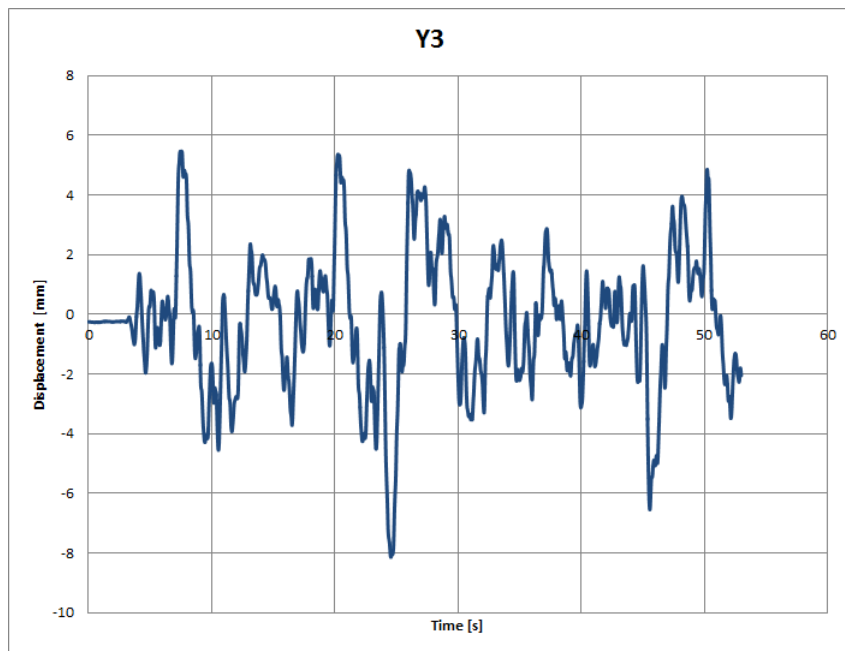
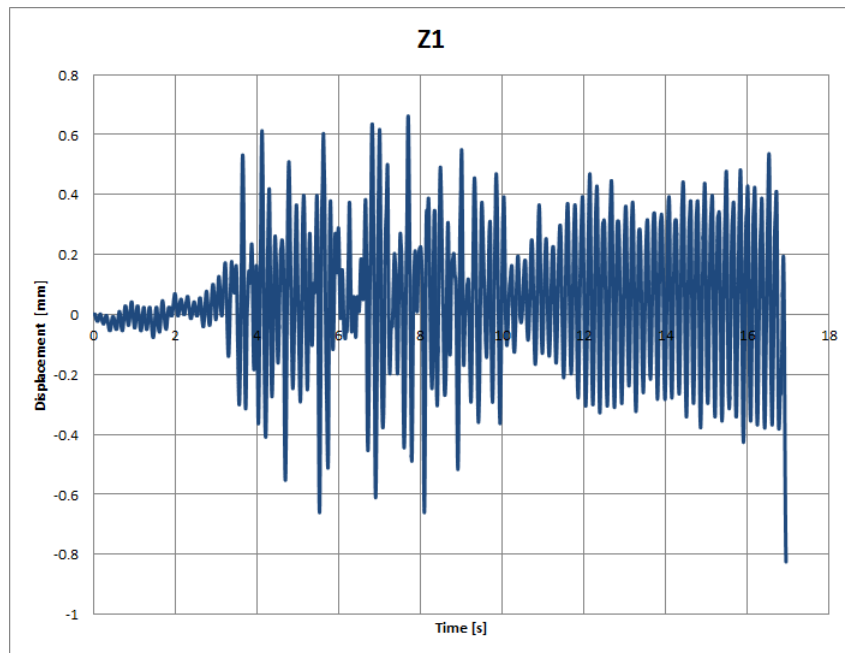Figure A.4: RUN 6 - prescribed displacement at actuator Y3.
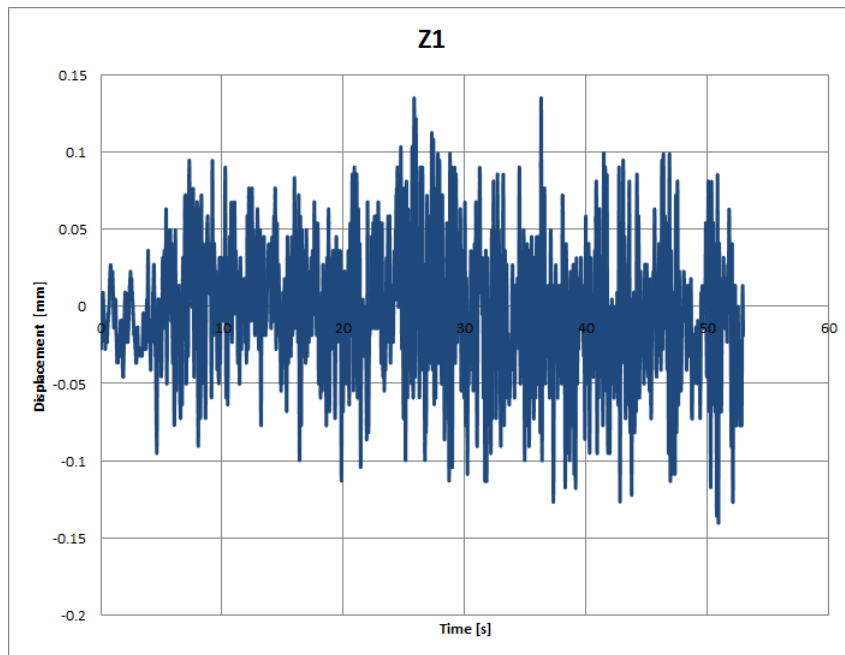
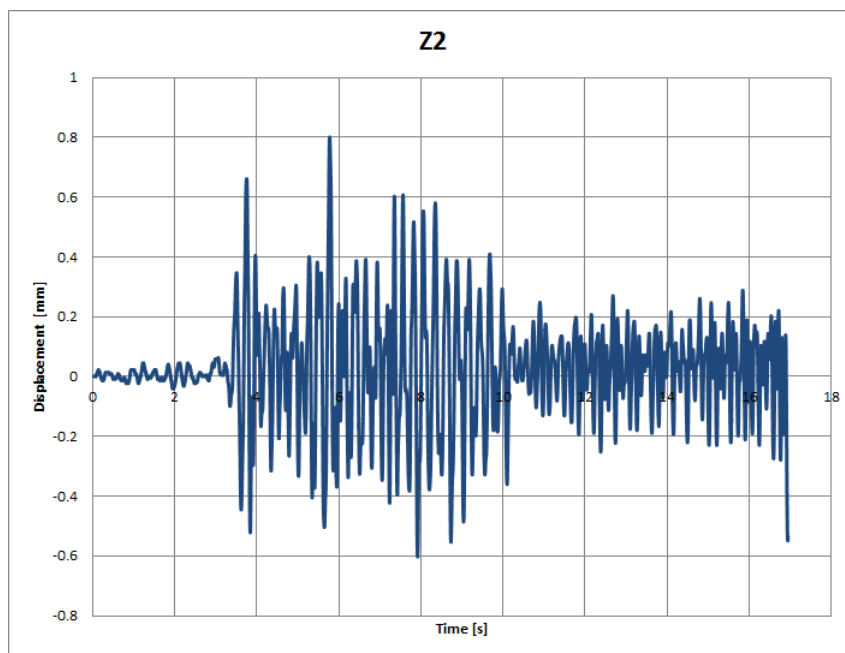Figure A.5: RUN 6 - prescribed displacement at actuator Z1.
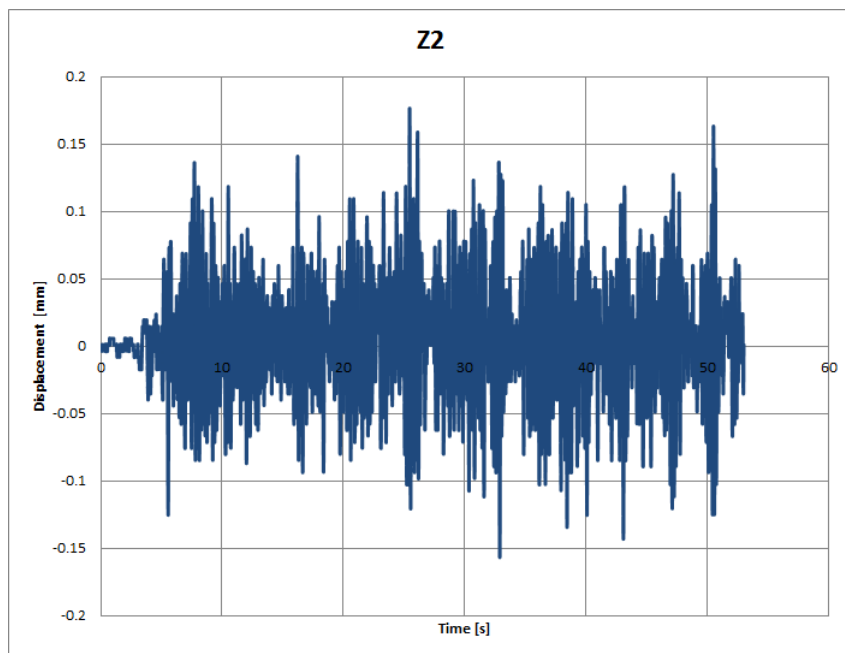
Figure A.6: RUN 6 - prescribed displacement at actuator Z2.
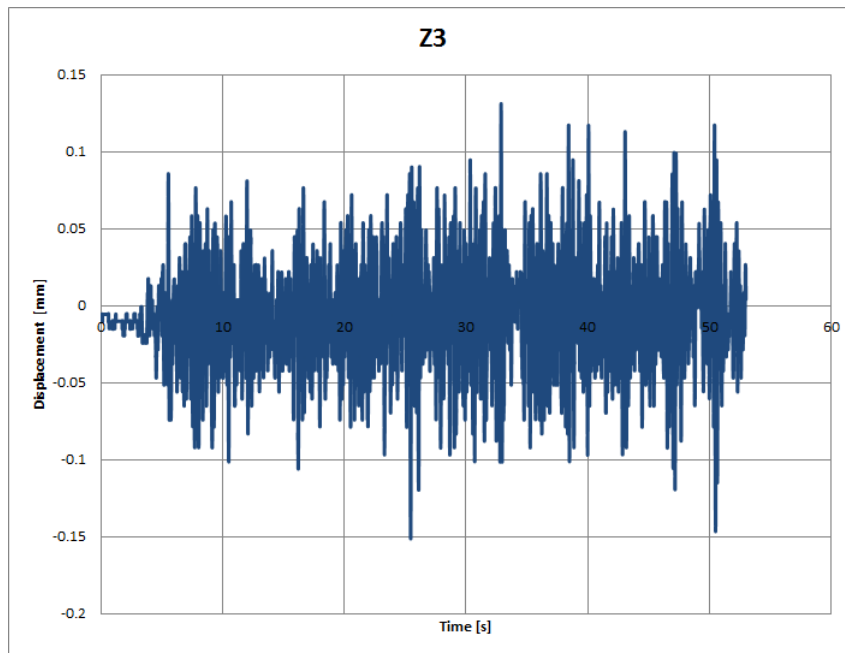
Figure A.7: RUN 6 - prescribed displacement at actuator Z3.
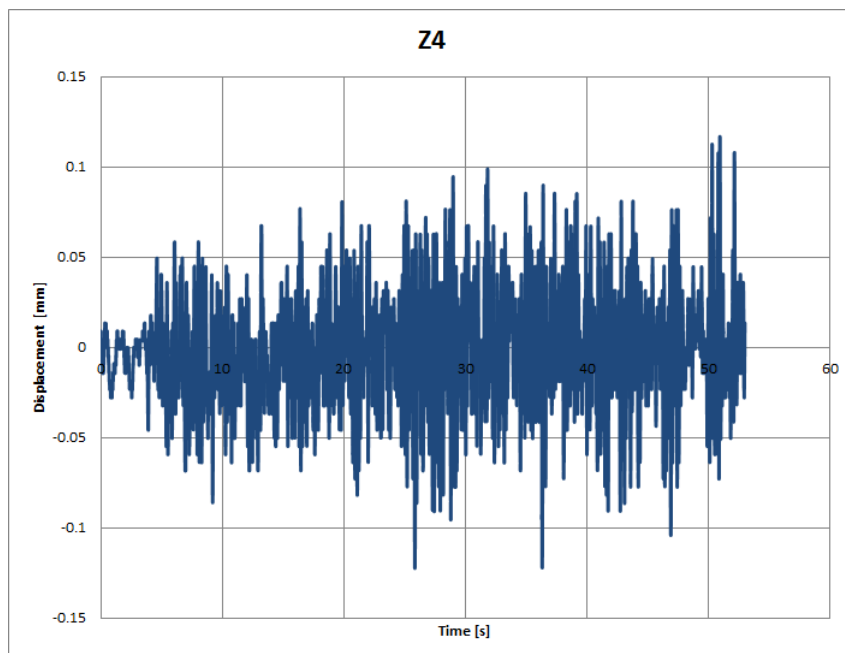
Figure A.8: RUN 6 - prescribed displacement at actuator Z4.
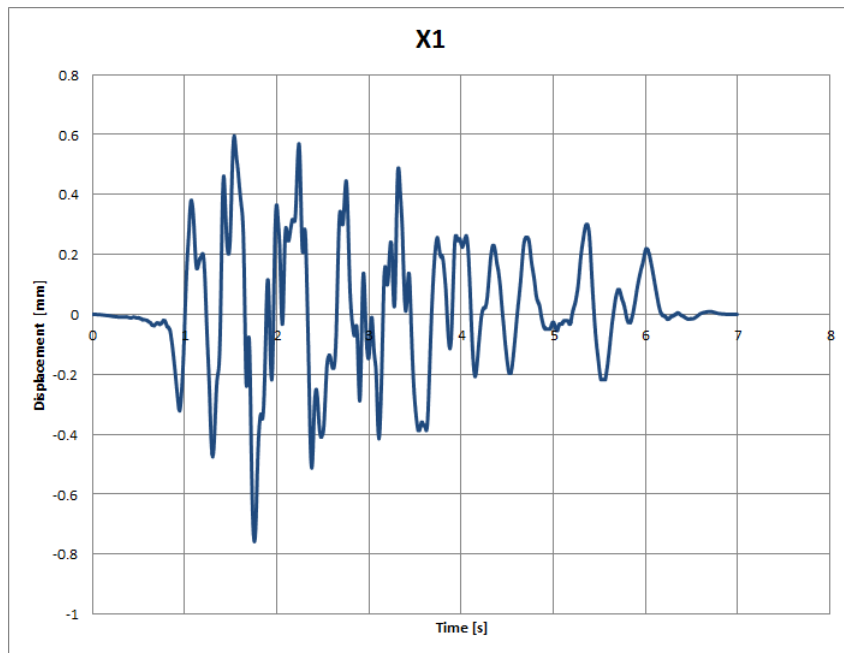
Figure A.9: RUN 7 - prescribed displacement at actuator X1.
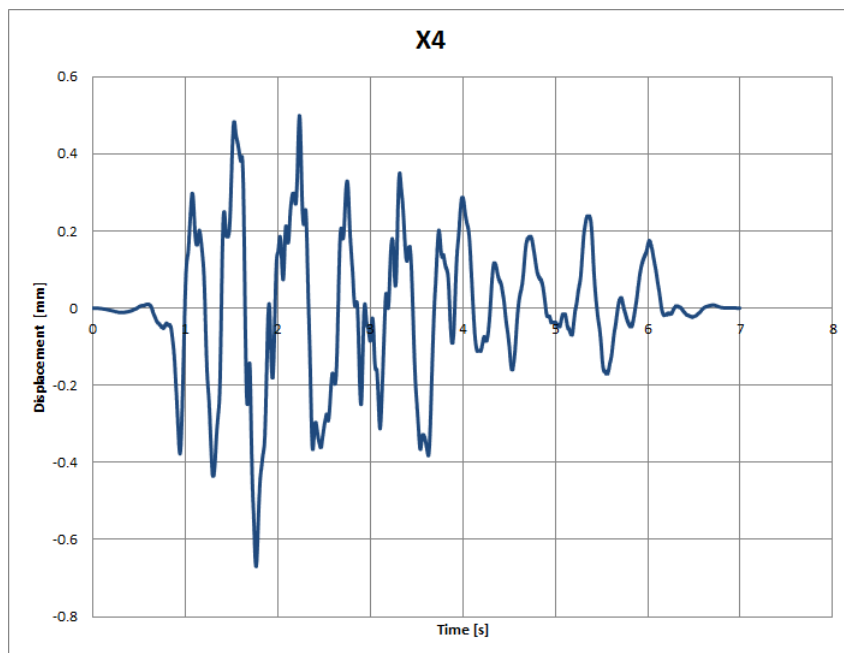
Figure A.10: RUN 7 - prescribed displacement at actuator X4.
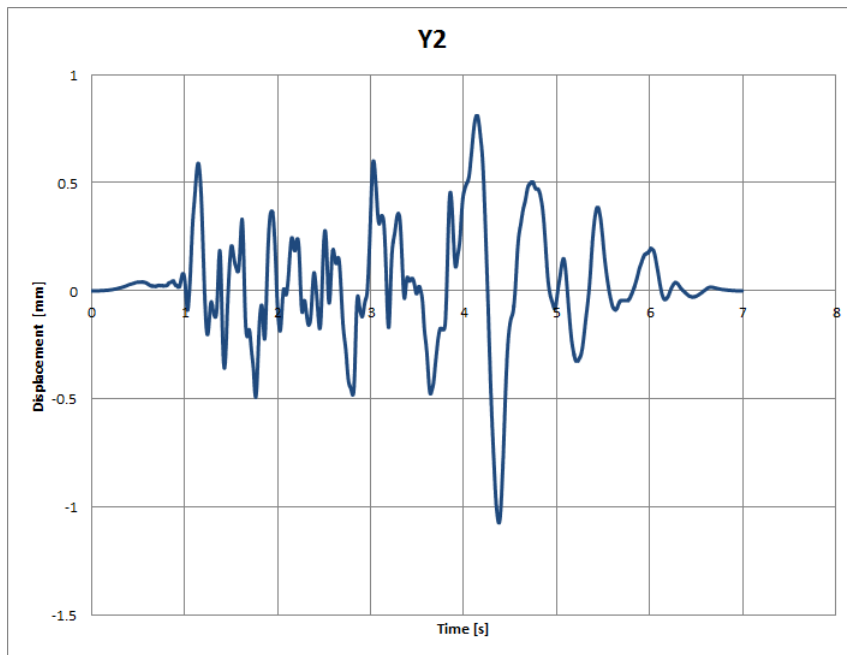
Figure A.11: RUN 7 - prescribed displacement at actuator Y2.
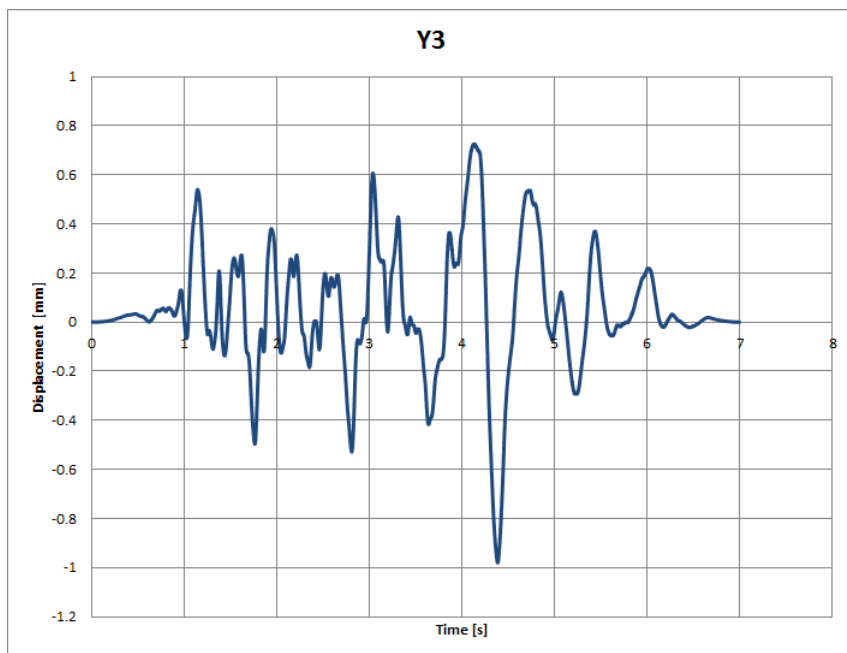
Figure A.12: RUN 7 - prescribed displacement at actuator Y3.
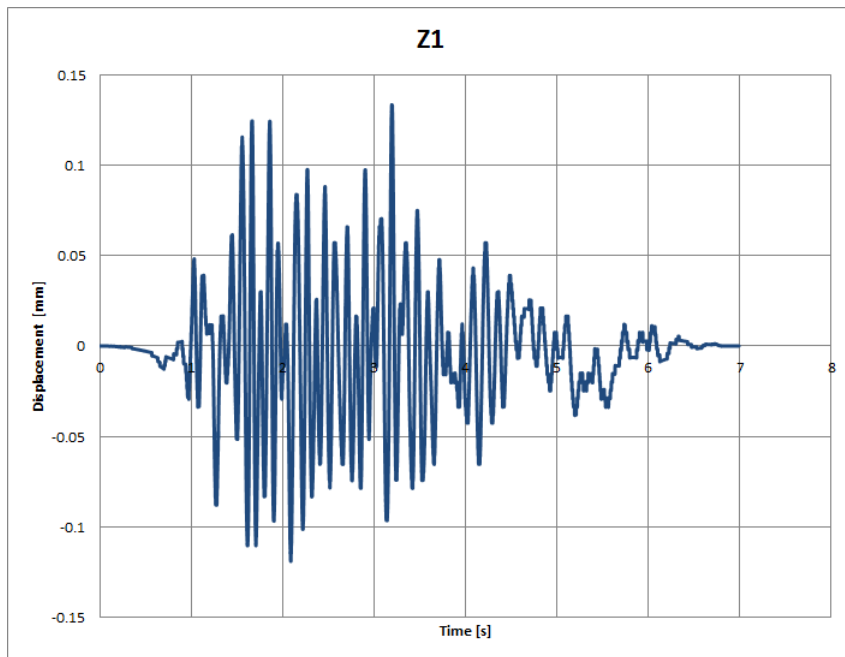
Figure A.13: RUN 7 - prescribed displacement at actuator Z1.
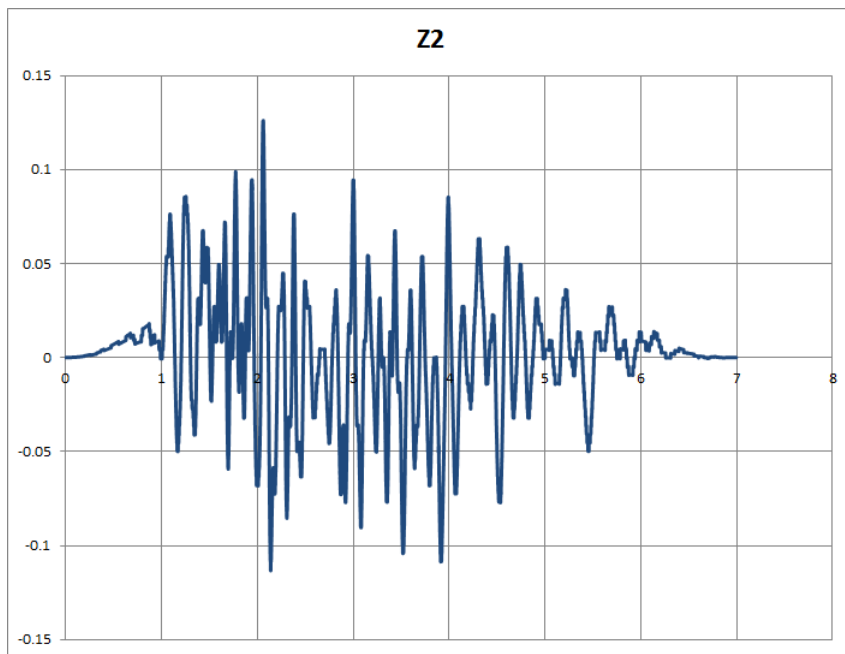
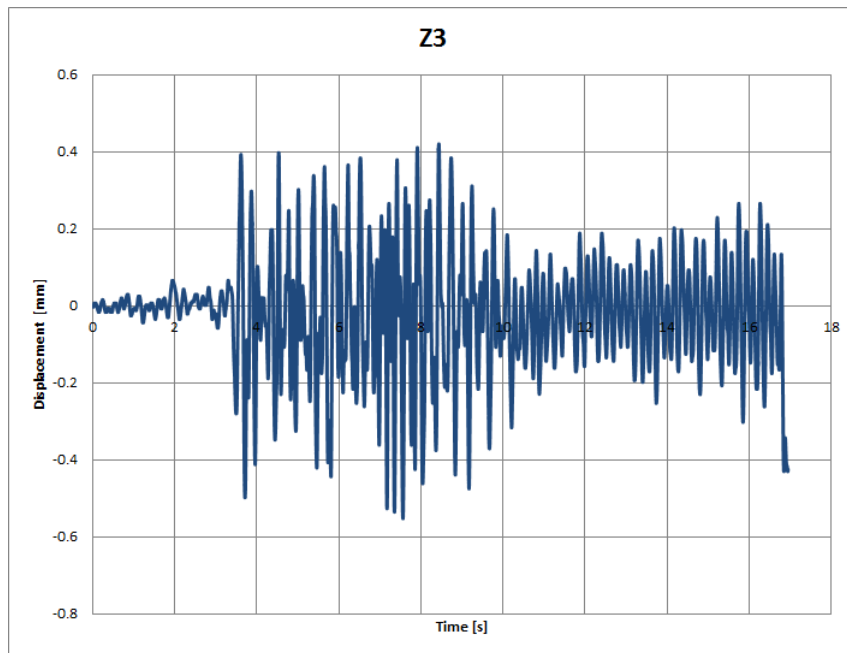Figure A.14: RUN 7 - prescribed displacement at actuator Z2.
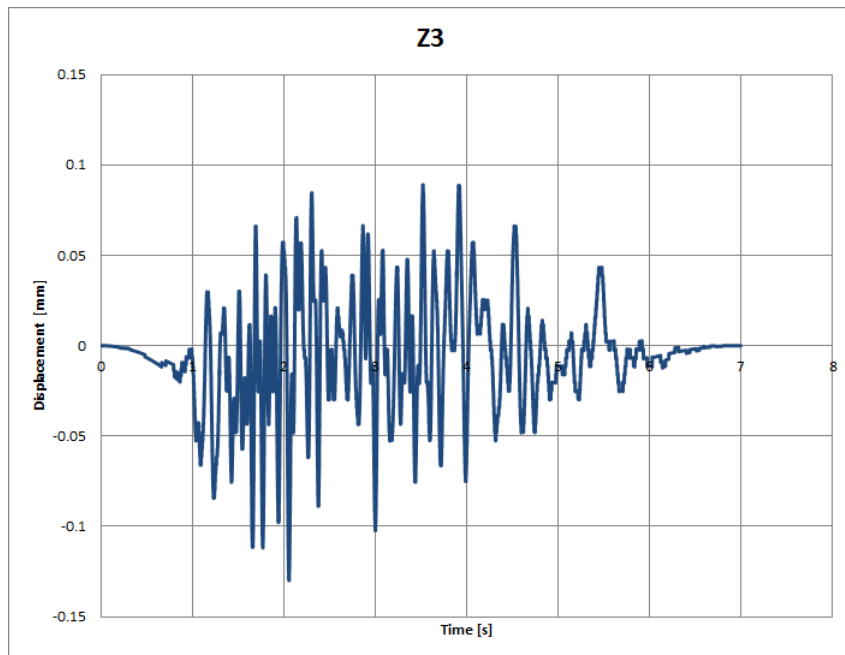
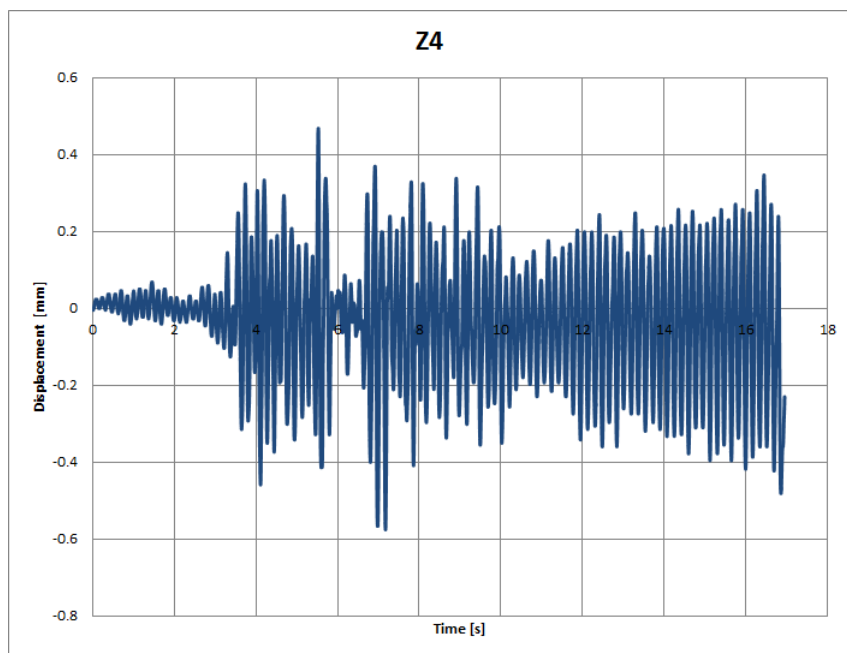Figure A.15: RUN 7 - prescribed displacement at actuator Z3.
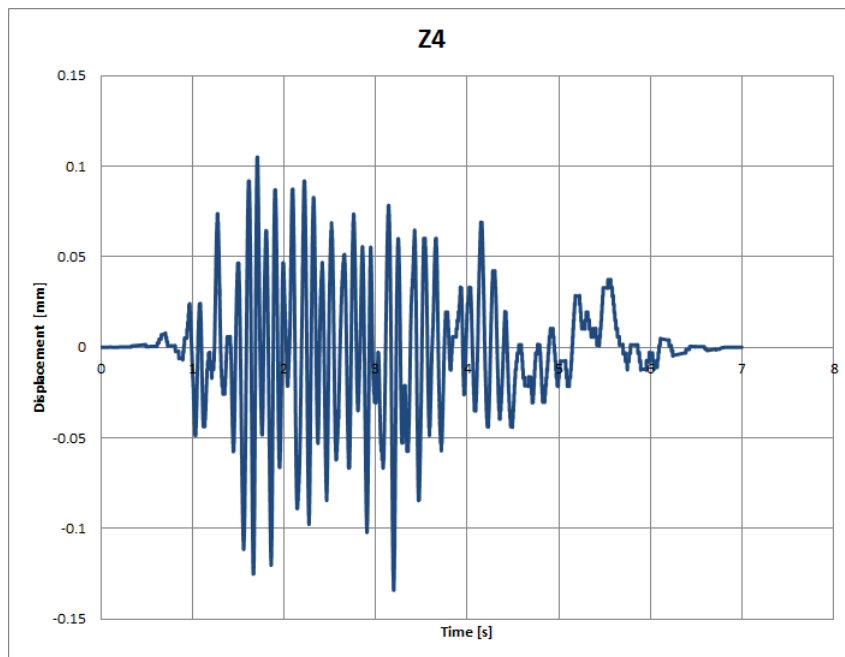
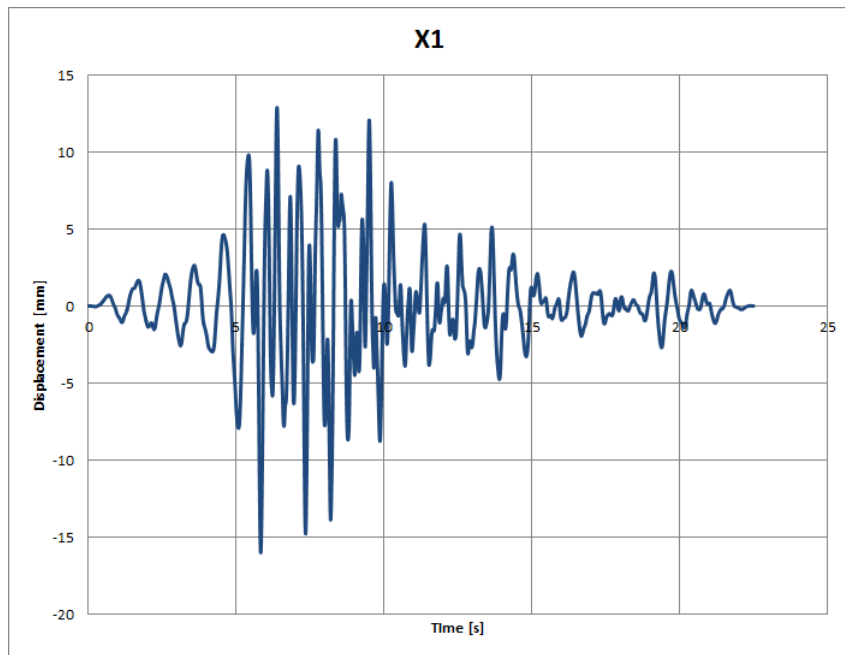Figure A.16: RUN 7 - prescribed displacement at actuator Z4.

For the nonlinear transient analysis RUN9, RUN11, RUN13, RUN17, RUN19, RUN21 and RUN23 are used. RUN9 is a real design signal, RUN11, RUN13 and RUN17 are scaled Northridge earthquakes. RUN19 is a real Northridge earthquake, RUN21 is a scaled Northridge after shock and RUN23 is a real Northridge after shock. The figures below show how the RUNs for the nonlinear analysis look like.
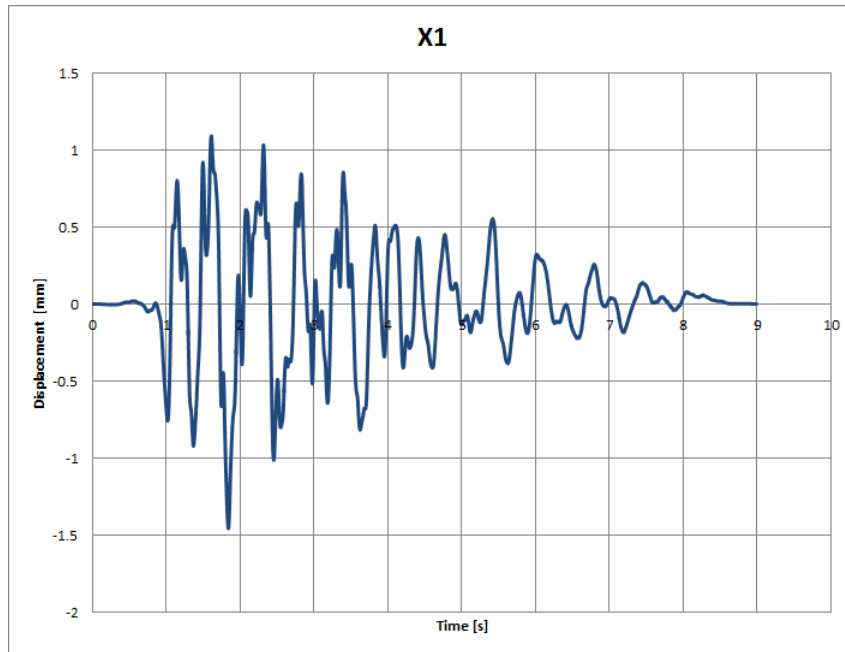
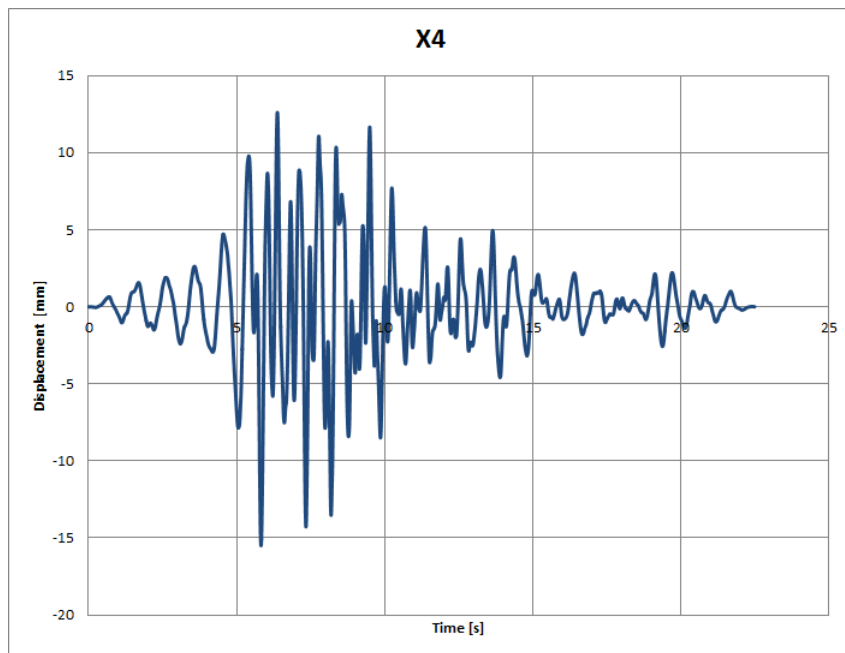Figure A.17: RUN 9 - prescribed displacements at actuator X1.
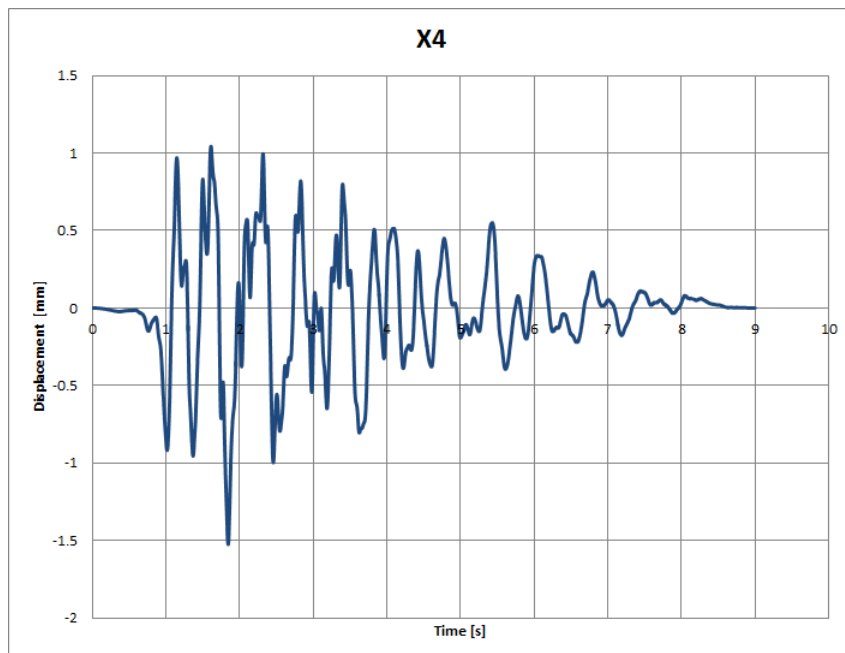
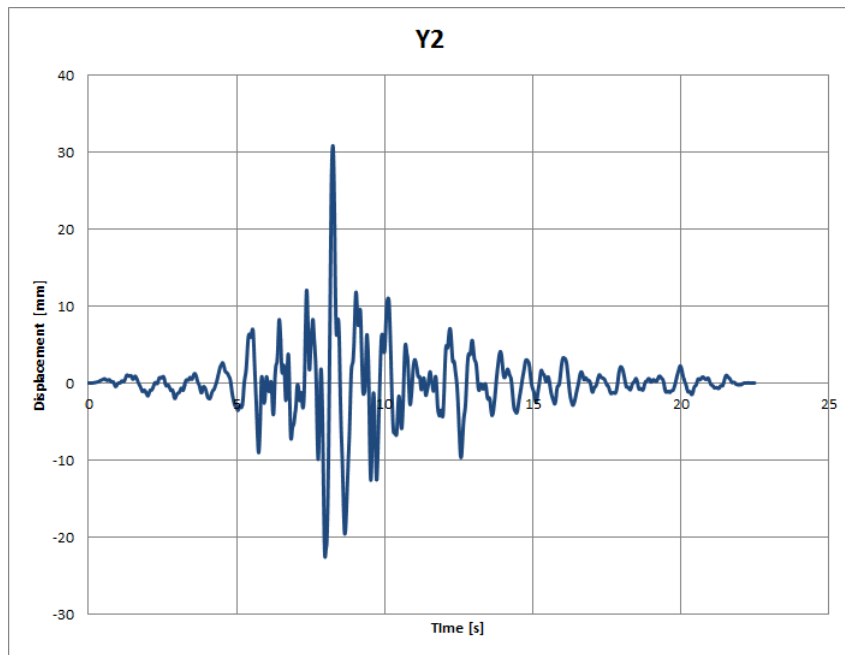Figure A.18: RUN 9 - prescribed displacements at actuator X4.
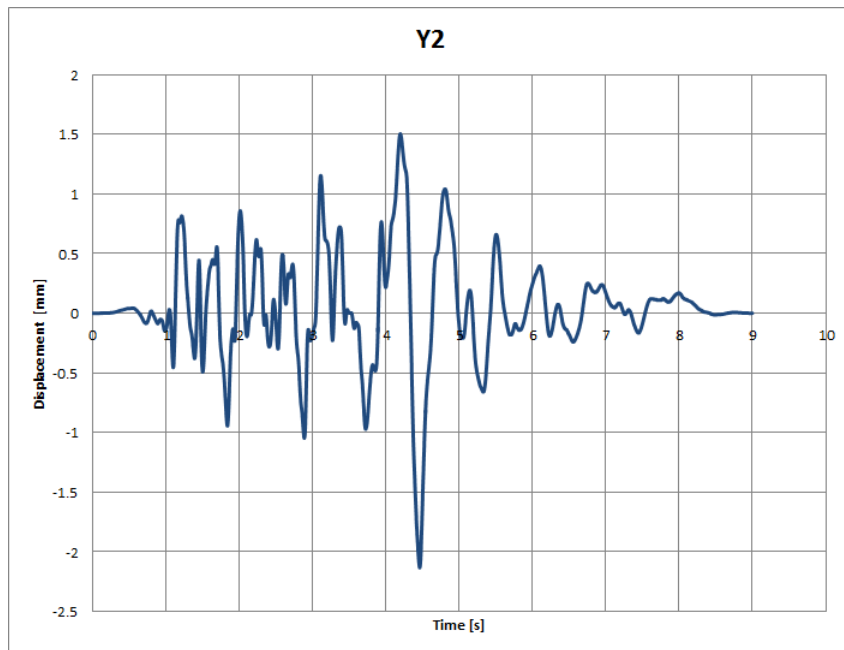
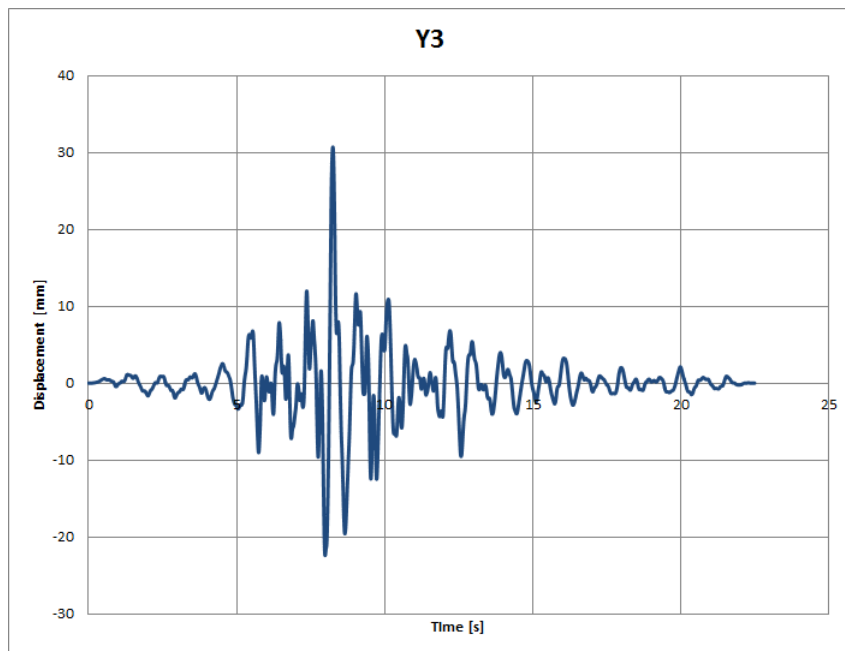Figure A.19: RUN 9 - prescribed displacements at actuator Y2.
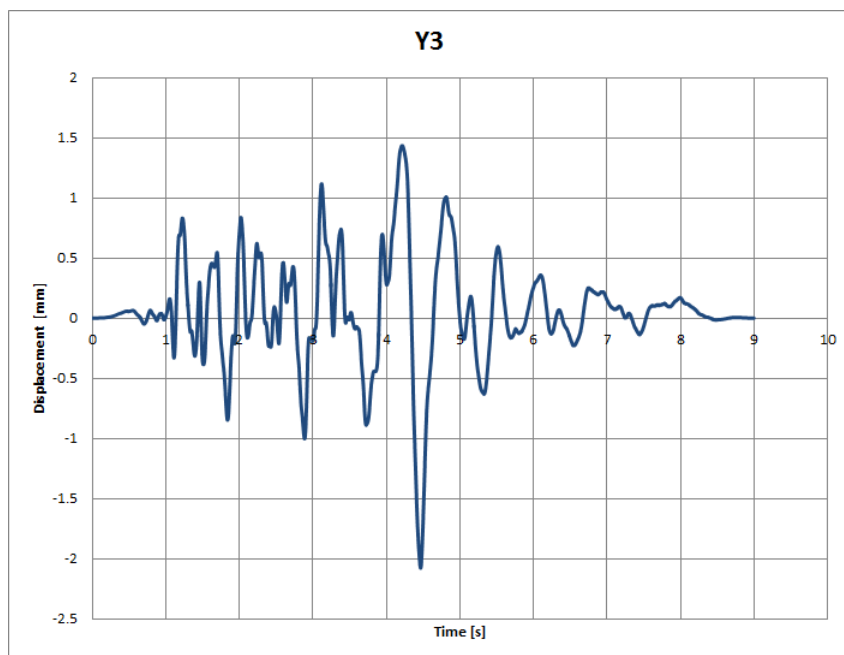
Figure A.20: RUN 9 - prescribed displacements at actuator Y3.
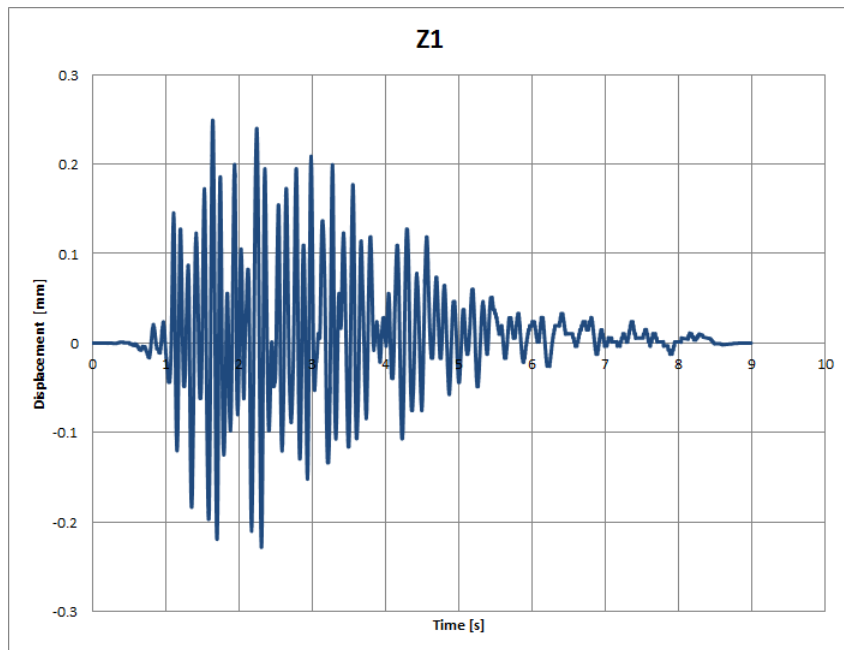
Figure A.21: RUN 9 - prescribed displacements at actuator Z1.
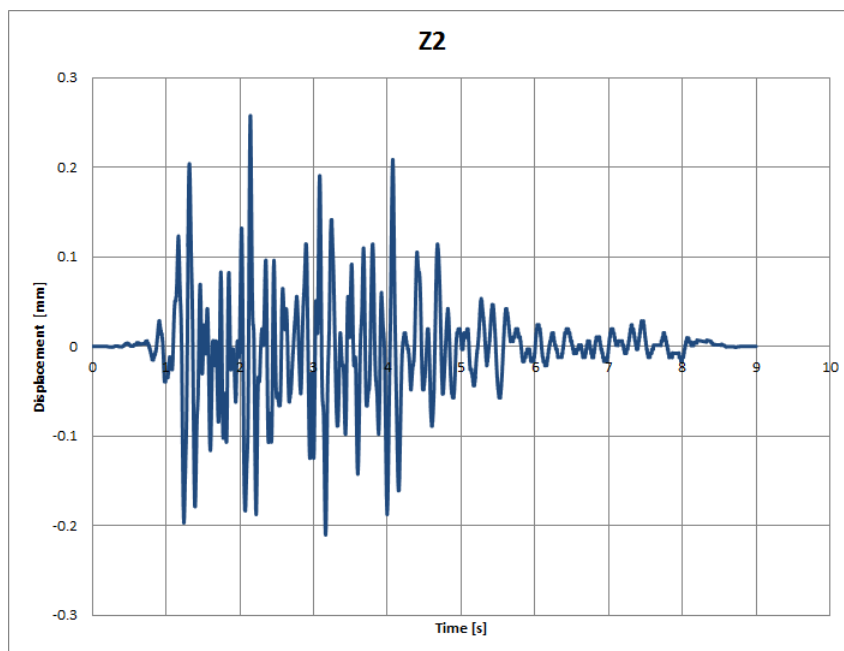
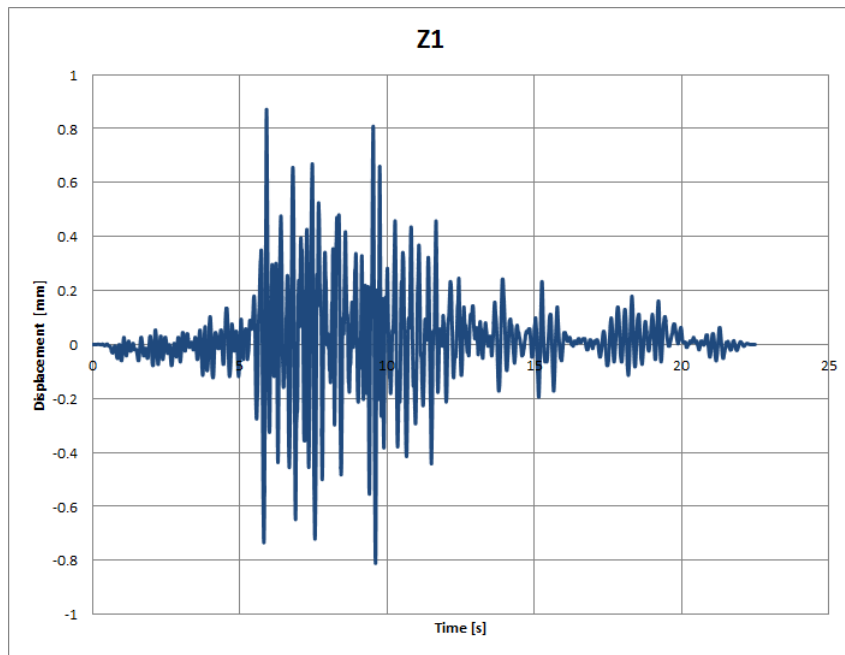Figure A.22: RUN 9 - prescribed displacements at actuator Z2.
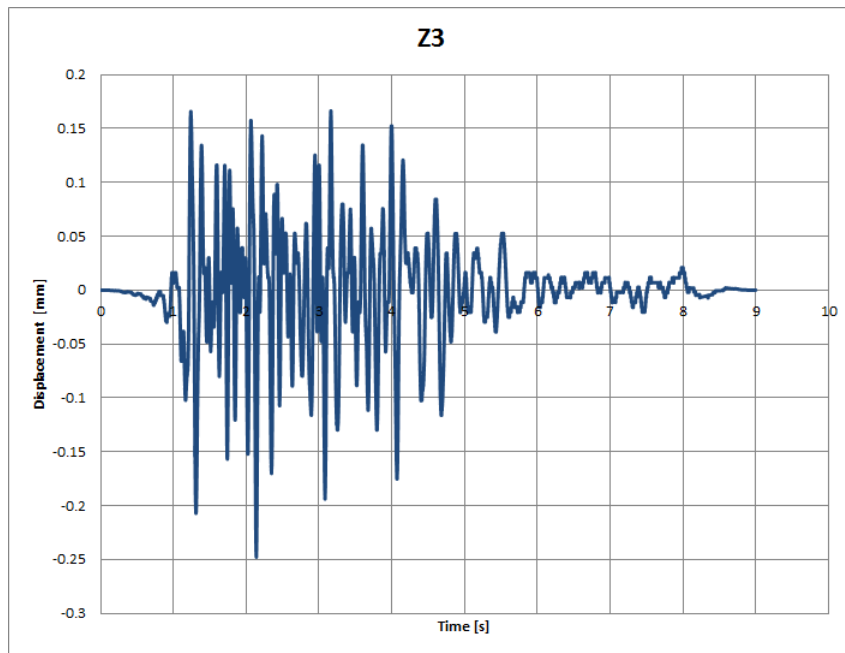
Figure A.23: RUN 9 - prescribed displacements at actuator Z3.
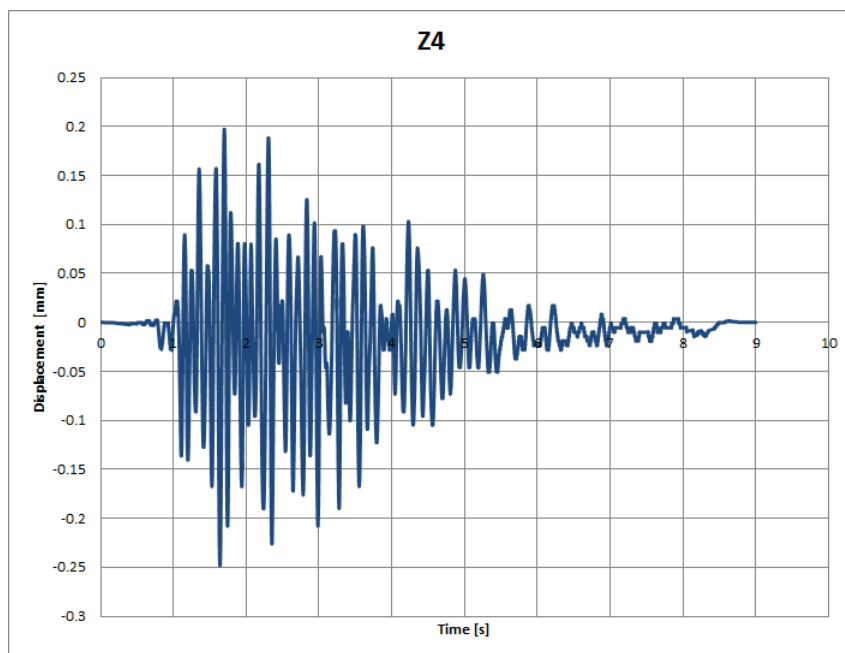
Figure A.24: RUN 9 - prescribed displacements at actuator Z4.
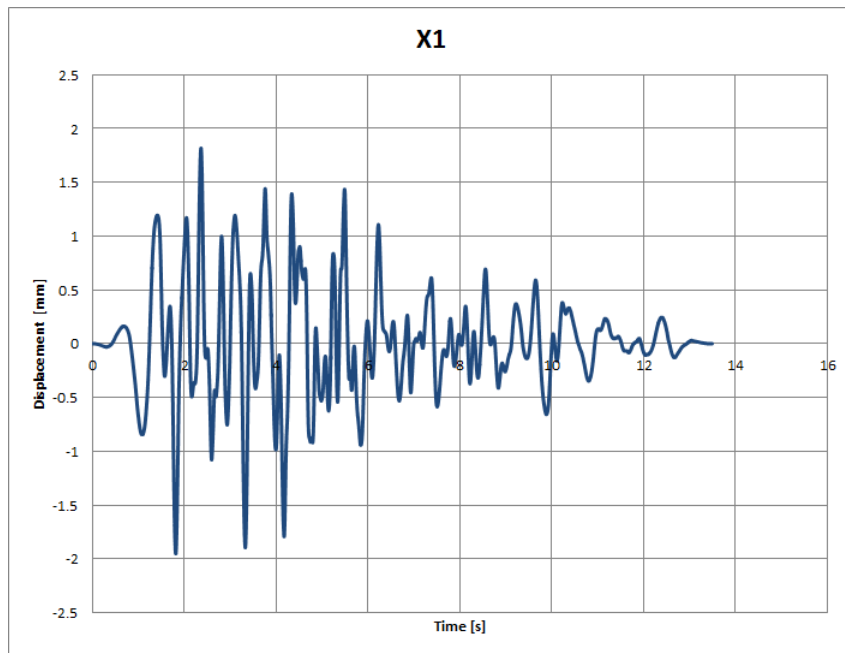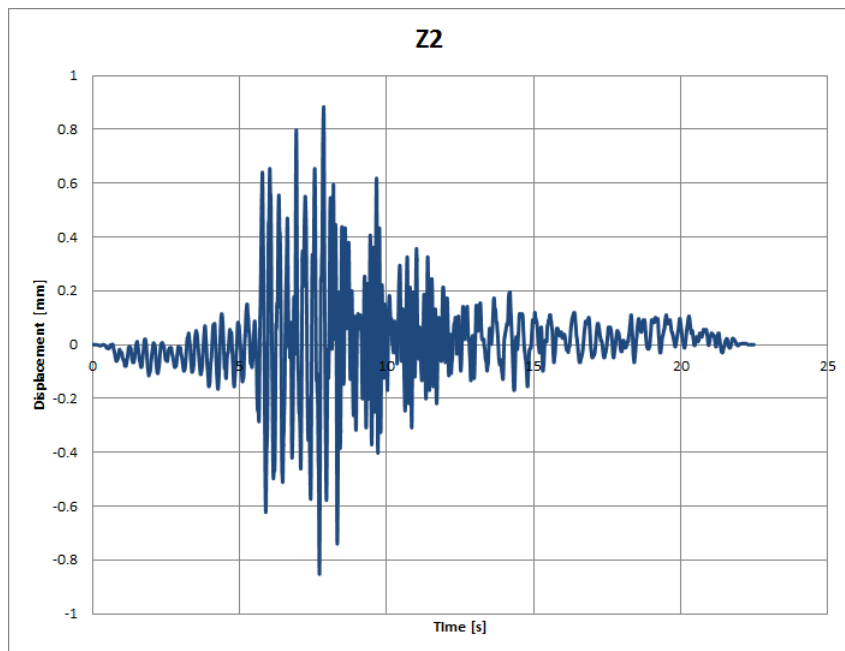
Figure A.25: RUN 11 - prescribed displacements at actuator X1.
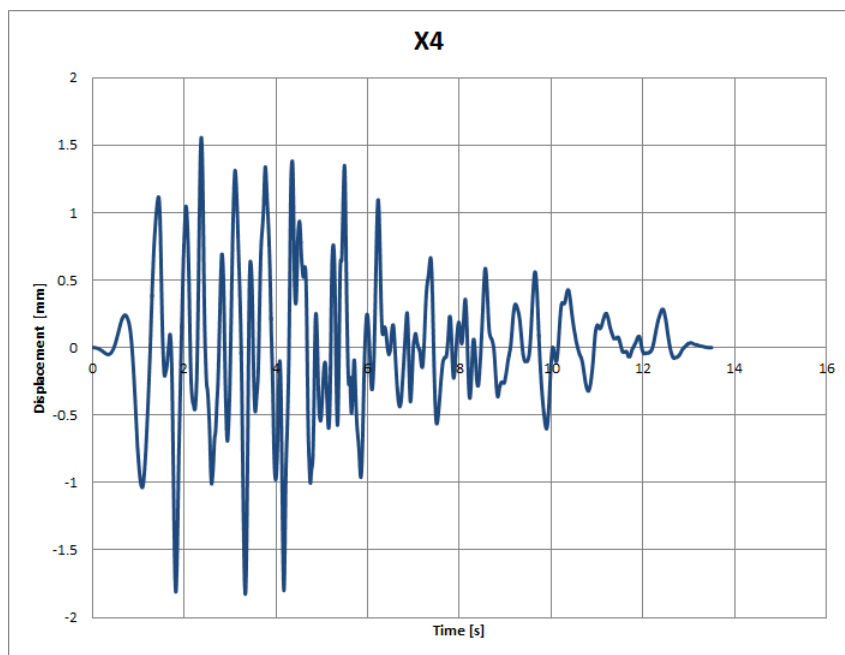
Figure A.26: RUN 11 - prescribed displacements at actuator X4.
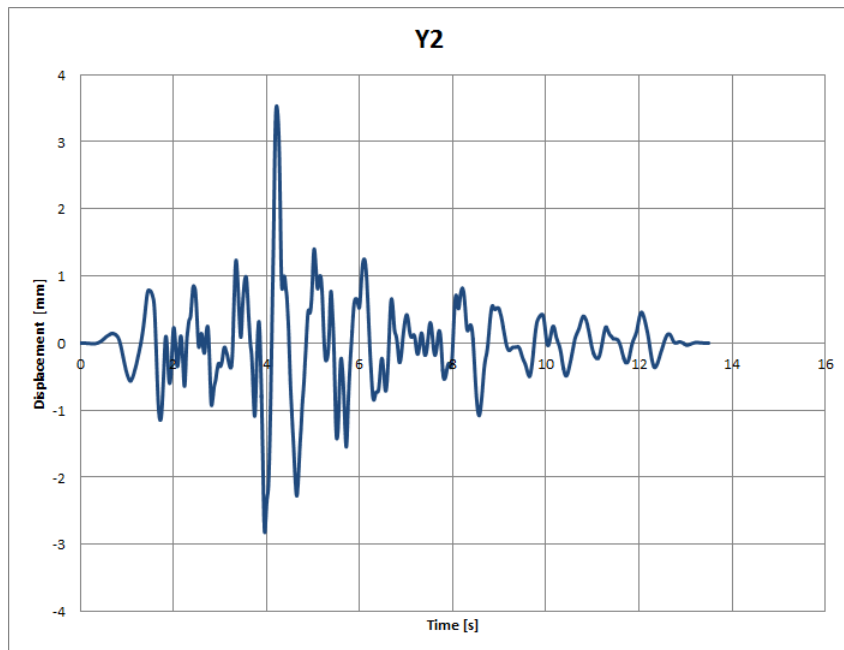
Figure A.27: RUN 11 - prescribed displacements at actuator Y2.
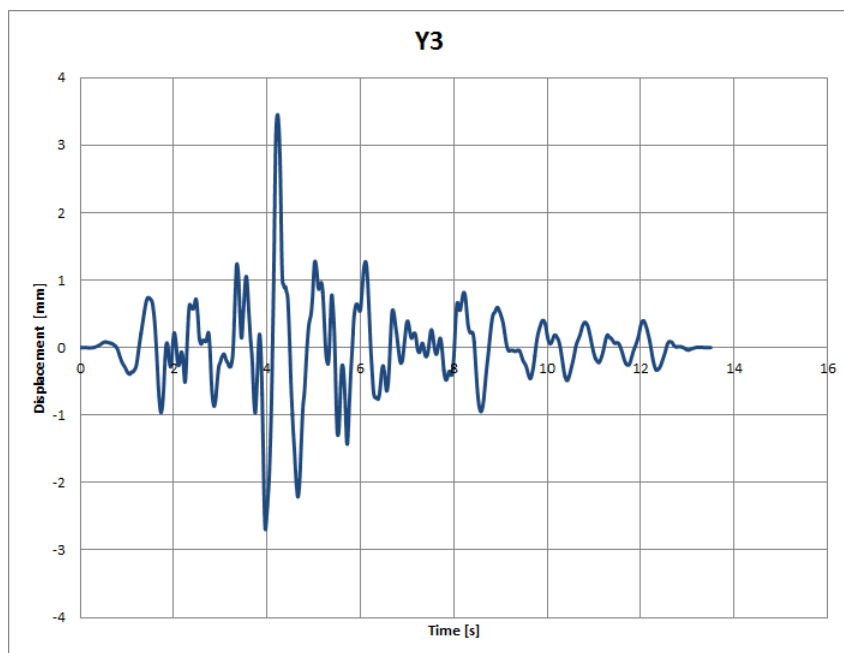
Figure A.28: RUN 11 - prescribed displacements at actuator Y3.

Figure A.29: RUN 11 - prescribed displacements at actuator Z1.

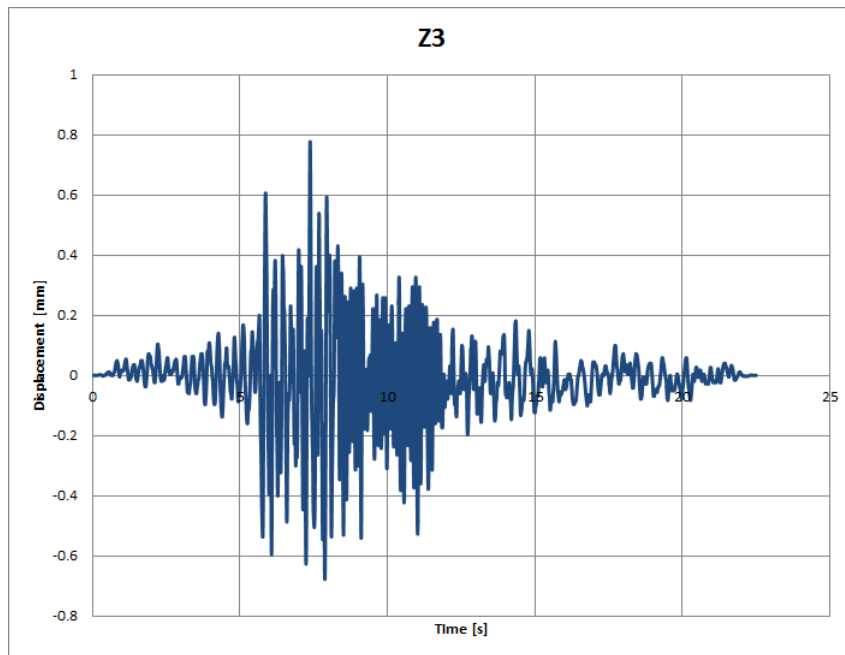Figure A.30: RUN 11 - prescribed displacements at actuator Z2.

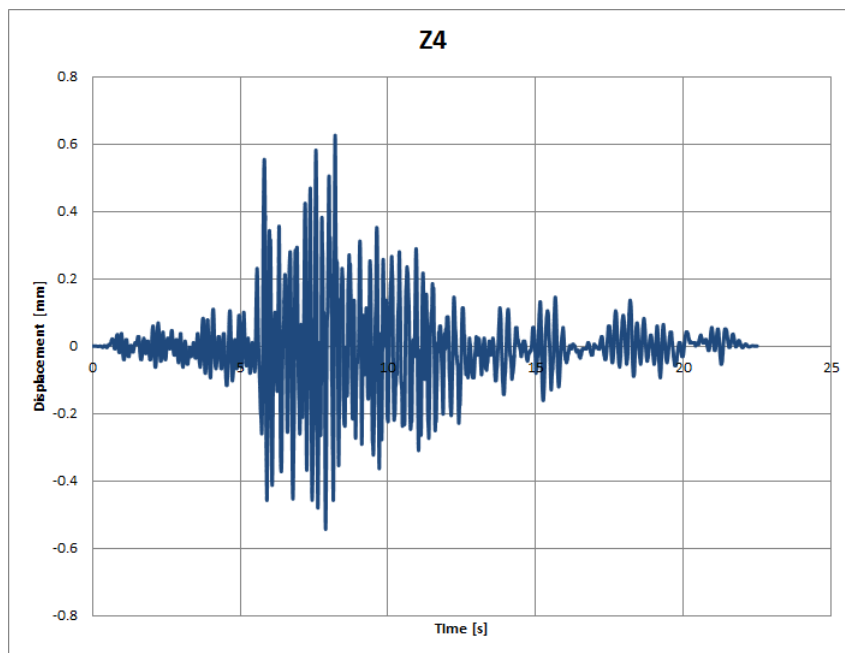Figure A.31: RUN 11 - prescribed displacements at actuator Z3.

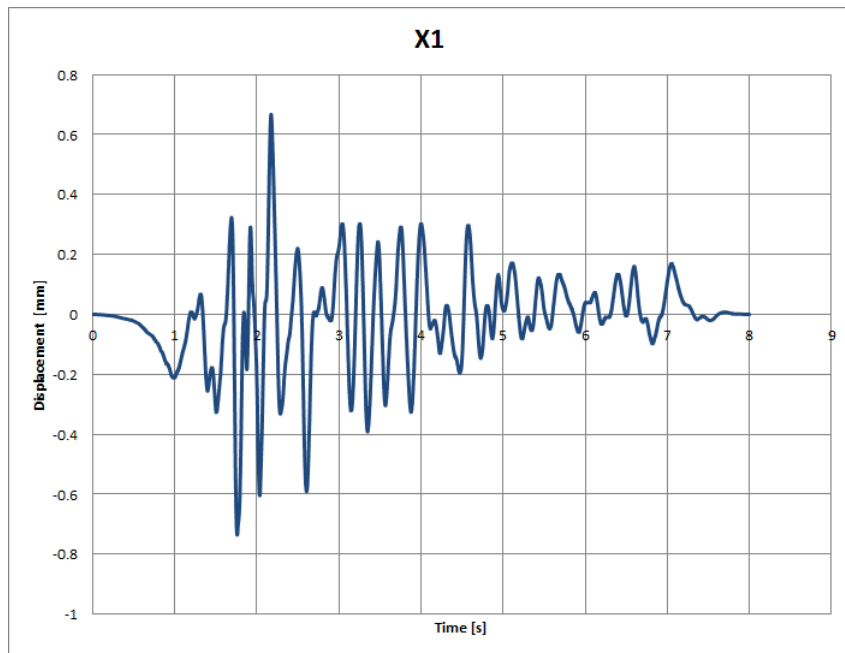Figure A.32: RUN 11 - prescribed displacements at actuator Z4.

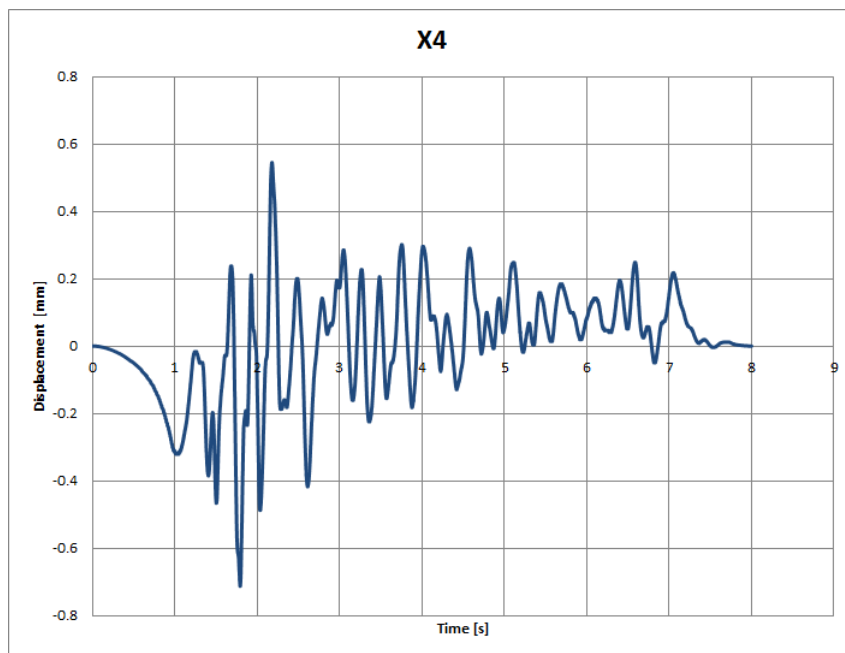Figure A.33: RUN 13 - prescribed displacements at actuator X1.

Figure A.34: RUN 13 - prescribed displacements at actuator X4.

Figure A.35: RUN 13 - prescribed displacements at actuator Y2.

Figure A.36: RUN 13 - prescribed displacements at actuator Y3.

Figure A.37: RUN 13 - prescribed displacements at actuator Z1.

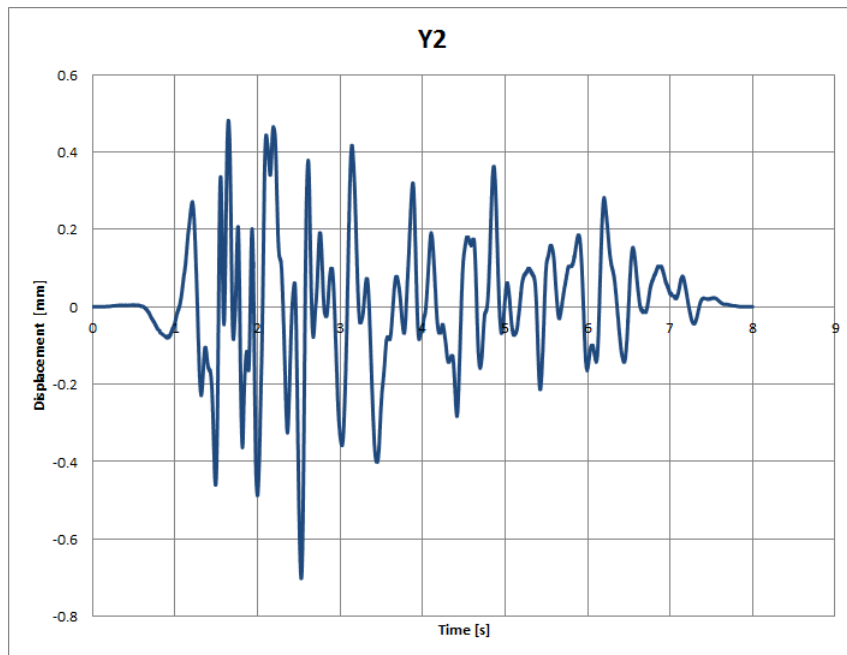Figure A.38: RUN 13 - prescribed displacements at actuator Z2.

Figure A.39: RUN 13 - prescribed displacements at actuator Z3.

Figure A.40: RUN 13 - prescribed displacements at actuator Z4.

Figure A.41: RUN 17 - prescribed displacements at actuator X1.

Figure A.42: RUN 17 - prescribed displacements at actuator X4.

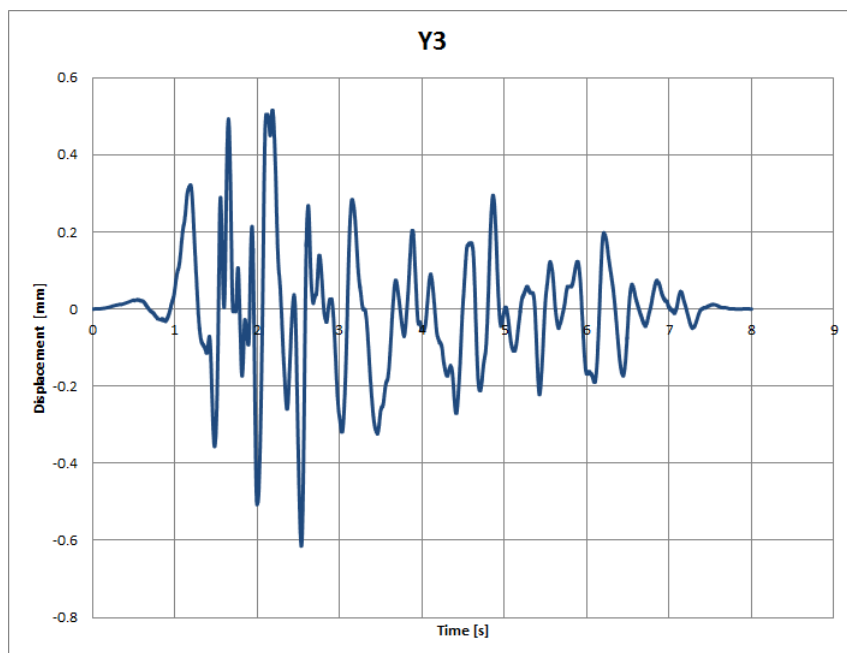Figure A.43: RUN 17 - prescribed displacements at actuator Y2.

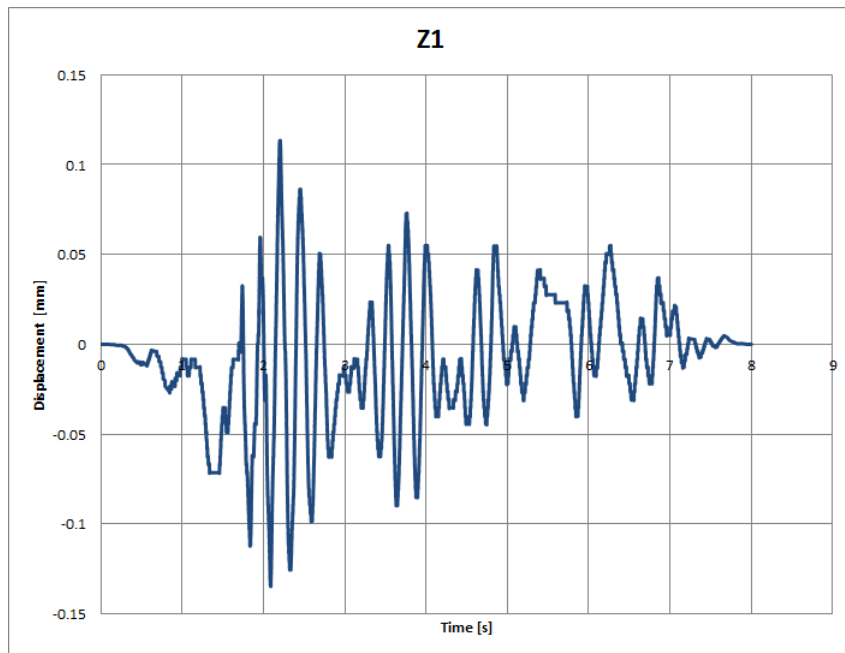Figure A.44: RUN 17 - prescribed displacements at actuator Y3.

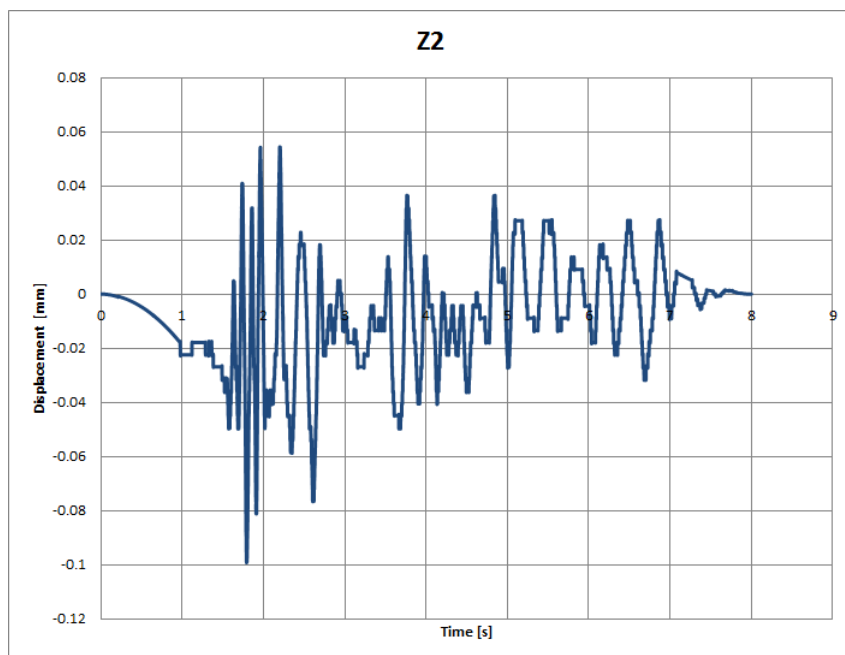Figure A.45: RUN 17 - prescribed displacements at actuator Z1.

Figure A.46: RUN 17 - prescribed displacements at actuator Z2.

Figure A.47: RUN 17 - prescribed displacements at actuator Z3.

Figure A.48: RUN 17 - prescribed displacements at actuator Z4.

Figure A.49: RUN 19 - prescribed displacements at actuator X1.
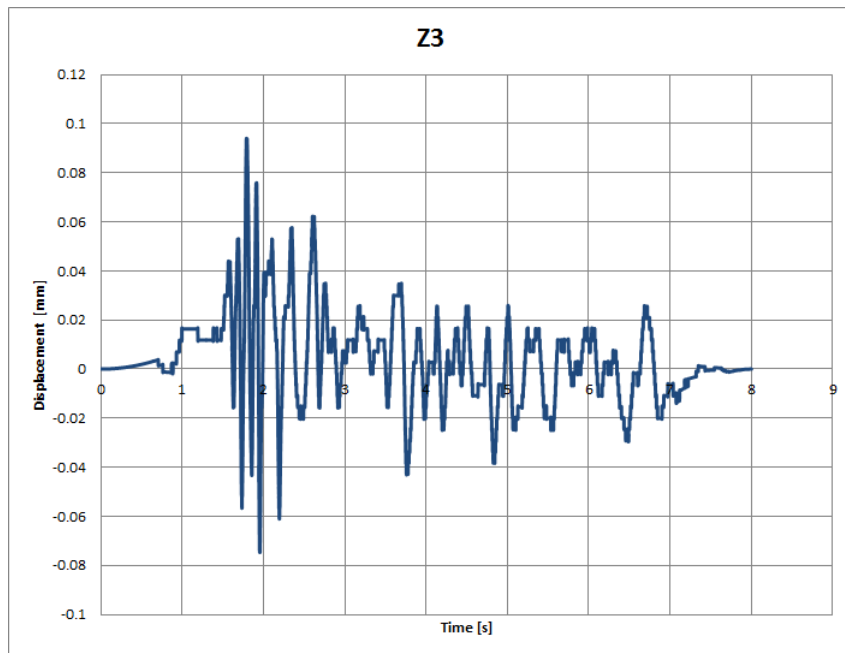

Figure A.50: RUN 19 - prescribed displacements at actuator X4.

Figure A.51: RUN 19 - prescribed displacements at actuator Y2.

Figure A.52: RUN 19 - prescribed displacements at actuator Y3.

Figure A.53: RUN 19 - prescribed displacements at actuator Z1.

Figure A.54: RUN 19 - prescribed displacements at actuator Z2.

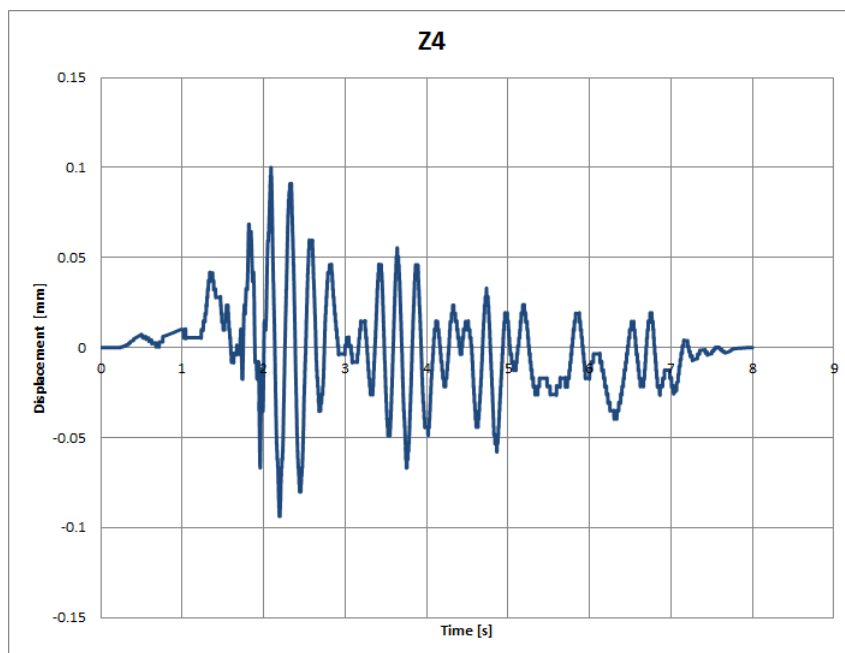Figure A.55: RUN 19 - prescribed displacements at actuator Z3.

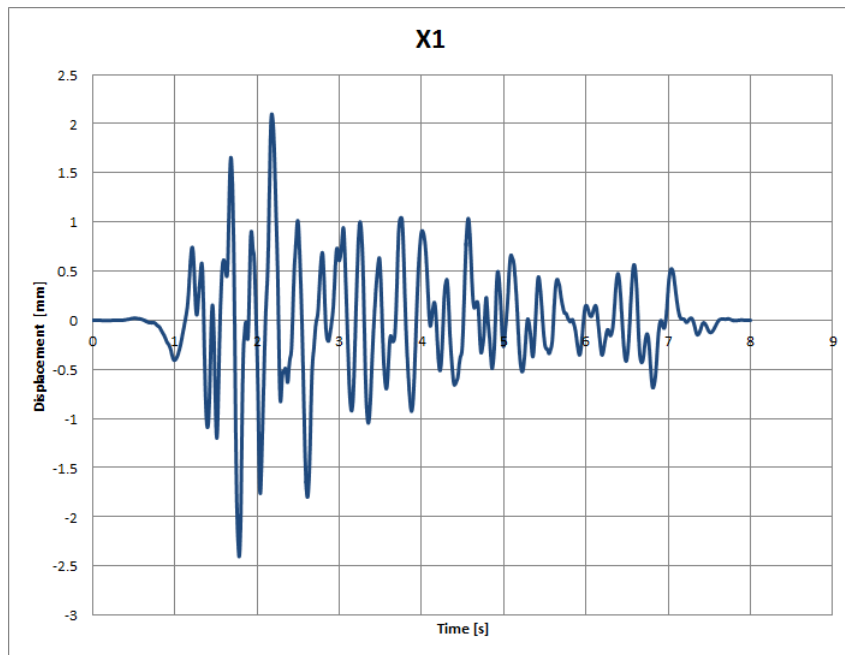Figure A.56: RUN 19 - prescribed displacements at actuator Z4.

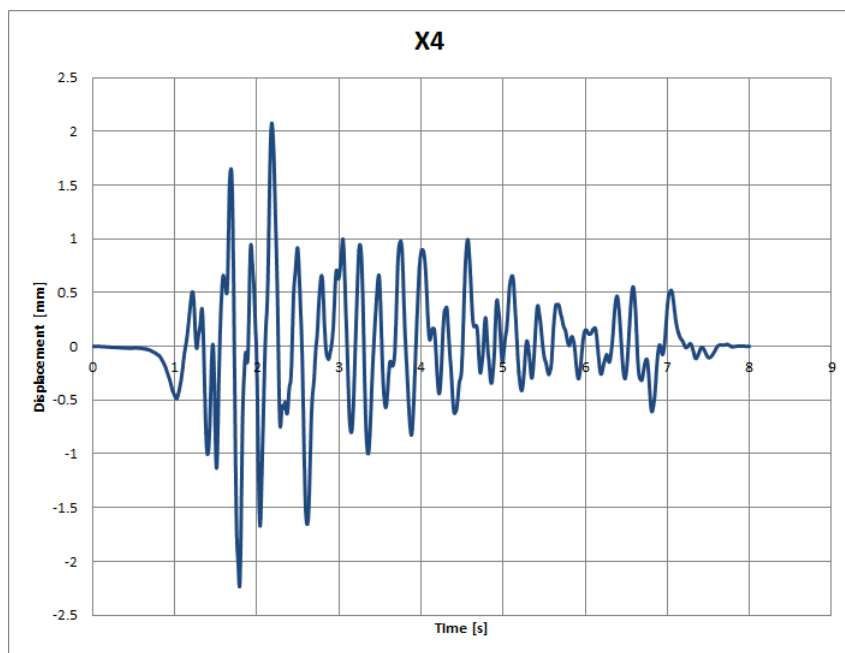Figure A.57: RUN 21 - prescribed displacements at actuator X1.

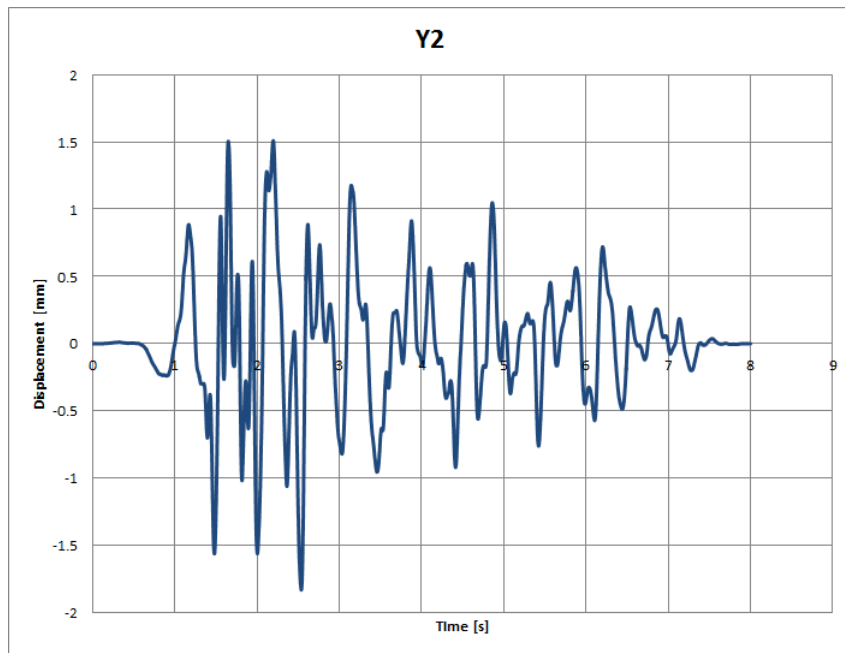Figure A.58: RUN 21 - prescribed displacements at actuator X4.

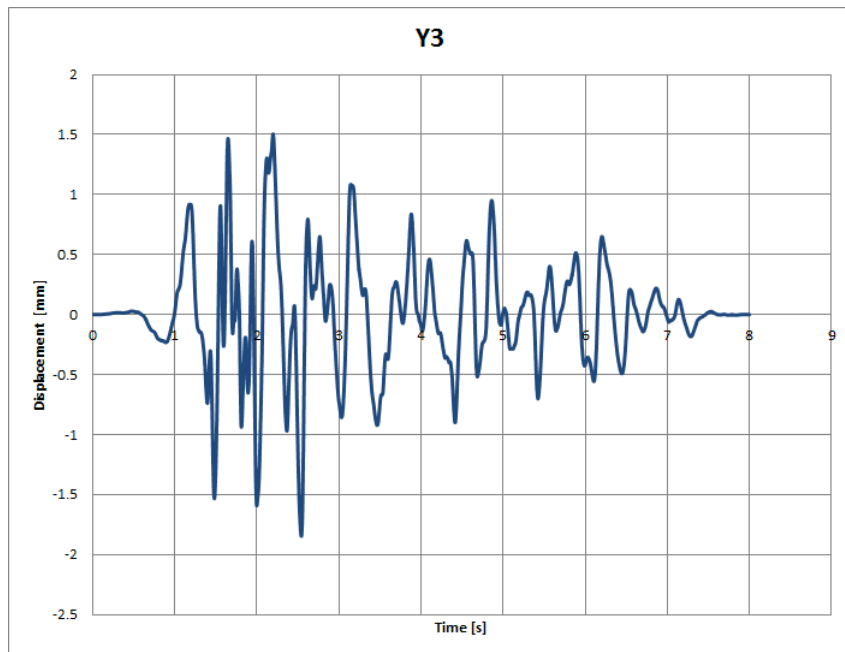Figure A.59: RUN 21 - prescribed displacements at actuator Y2.

Figure A.60: RUN21 - prescribed displacements at actuator Y3.

Figure A.61: RUN21 - prescribed displacements at actuator Z1.

Figure A.62: RUN21 - prescribed displacements at actuator Z2.

Figure A.63: RUN21 - prescribed displacements at actuator Z3.

Figure A.64: RUN21 - prescribed displacements at actuator Z4.

Figure A.65: RUN23 - prescribed displacements at actuator X1.

Figure A.66: RUN23 - prescribed displacements at actuator X4.

Figure A.67: RUN23 - prescribed displacements at actuator Y2.

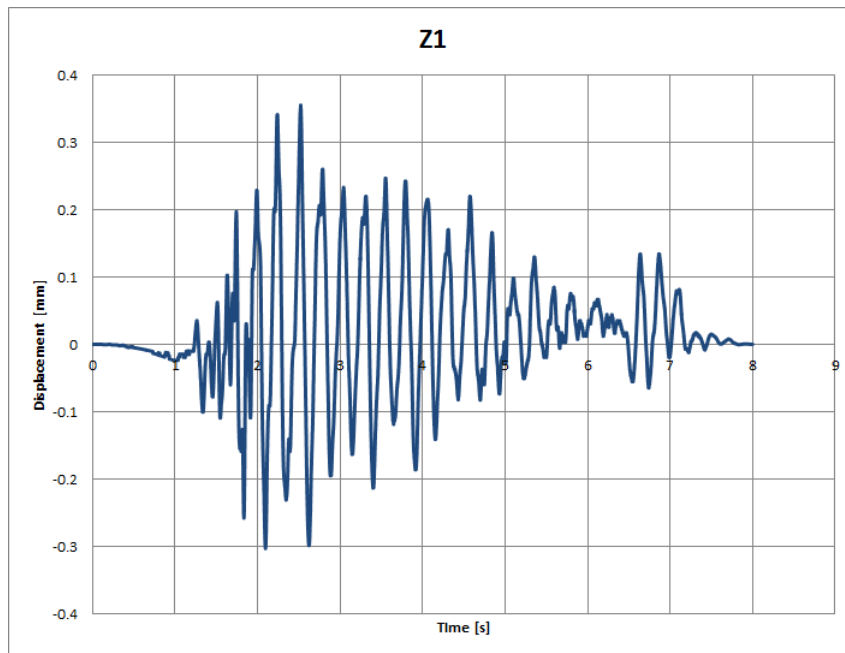Figure A.68: RUN23 - prescribed displacements at actuator Y3.

Figure A.69: RUN23 - prescribed displacements at actuator Z1.
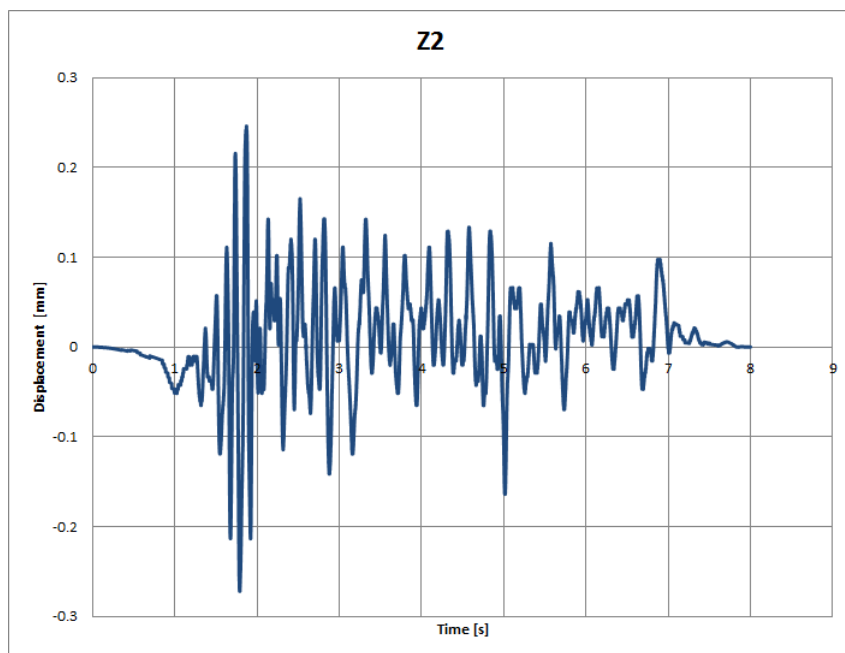

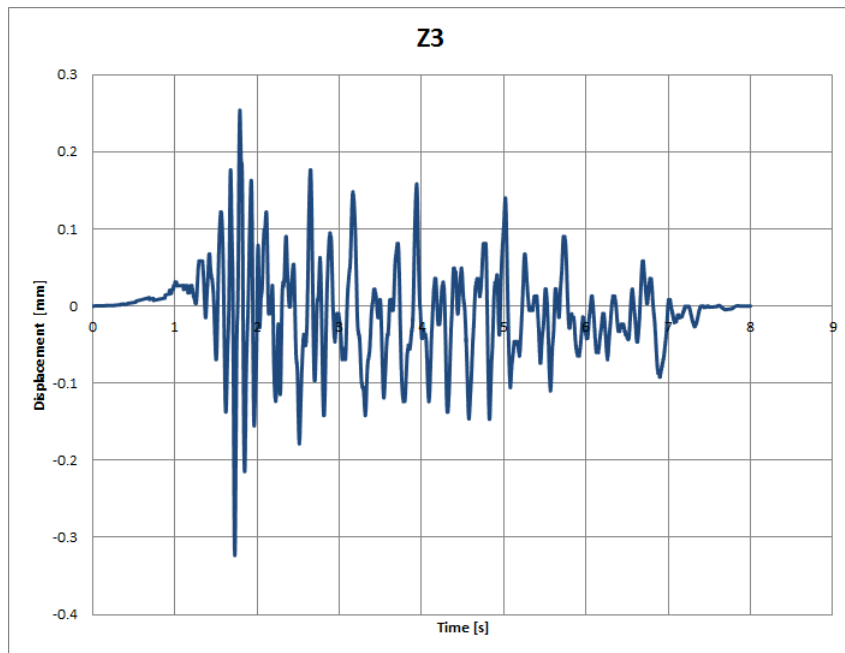Figure A.70: RUN23 - prescribed displacements at actuator Z2.

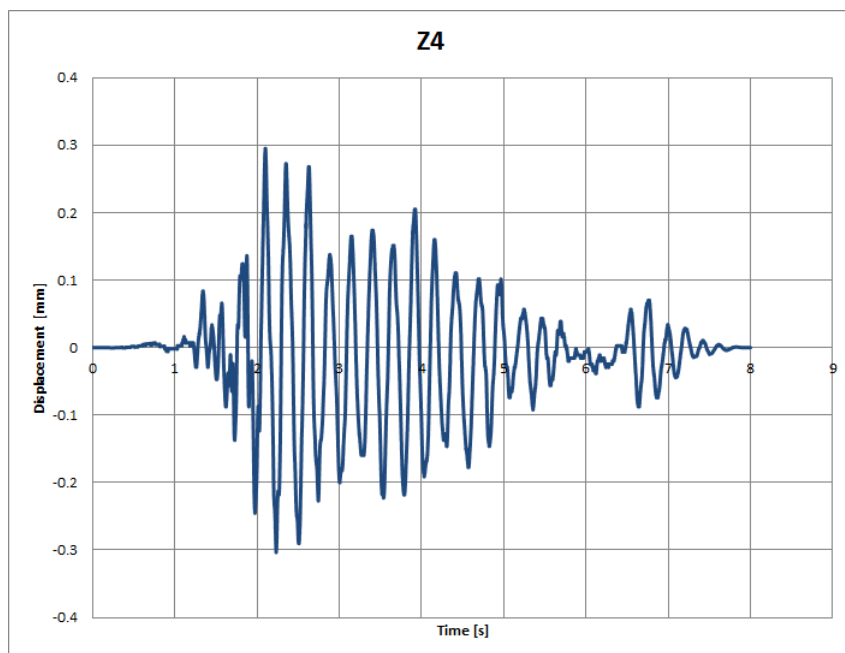Figure A.71: RUN23 - prescribed displacements at actuator Z3.

Figure A.72: RUN23 - prescribed displacements at actuator Z4.

References

[1] Ondej Kalny. Response Spectrum Analysis, 2014.

[2] H. Akhlaghi Moghadam and A.S. Height-Wise Distribution of Peak Horizontal Floor Acceleration (PHFA). 2008.

[3] Benjamin Richard and Thierry Chaudat. SMART 2013 International Benchmark. Technical report, 2013.

[4] TNO DIANA B.V. Element Library - Structural Elements, 2014.

[5] TNO DIANA B.V. Material Library - Structural Analysis, 2014.